Inaugural Dissertation

submitted to the
Combined Faculties for Natural Sciences and for Mathematics
of the Ruperto–Carola University of Heidelberg, Germany

for the degree of
Doctor of Natural Sciences

presented by

Dipl.–Phys. Andreas Müller

born in Jugenheim (Hessen), Germany

Oral examination: December 22nd, 2004

Black Hole Astrophysics:

Magnetohydrodynamics on the Kerr Geometry

Referees:

Prof. Dr. Max Camenzind
Prof. Dr. John Kirk

Astrophysik Schwarzer Löcher: Magnetohydrodynamik auf der Kerr-Geometrie

Diese Arbeit beschäftigt sich mit der Astrophysik von rotierenden Schwarzen Löchern. Schwerpunktthema ist die Akkretionsphysik im Regime der allgemein relativistischen Magnetohydrodynamik (GRMHD). Das Verhalten von Akkretionsflüssen und Ausflüssen auf der Kerr–Raumzeit ohne Strahlungseffekte wird analysiert. Die Grundgleichungen der GRMHD in Erhaltungsform und Aspekte numerischer Lösungsverfahren werden vorgestellt. Relativistische Codes und astrophysikalische Simulationen dienen einer Erörterung der Tauglichkeit unterschiedlicher numerischer Verfahren. Aus der Synopsis folgen Anforderungen an einen robusten GRMHD Code. Die Entwicklung im Forschungsfeld GRMHD wird eingeschätzt.
Ein weiterer Teil ist der Strahlung von Akkretionsscheiben gewidmet. Relativistisches Ray Tracing dient der Berechnung von relativistisch verbreiterten Emissionslinien von Aktiven Galaktischen Kernen und Röntgendoppelsternen. Es wird ein neues Modell – basierend auf trunkierten Standardscheiben – vorgestellt, dass der radialen Drift im Akkretionsfluss Rechnung trägt. Emissionslinien eignen sich als Diagnoseinstrumente, um unterschiedliche Parametermodelle zu vergleichen. Dabei wurde ein Klassifikations–schema nach Linienmorphologie entdeckt: Ein Linienprofil ist dreieckig, doppelköpfig, buckelig, schulterartig oder doppelspitzig.
Beide Teile der vorliegenden Arbeit können in weiterer Forschungsarbeit aneinander gekoppelt werden: Die Resultate von GRMHD–Simulationen, die das Geschwindigkeitsfeld eines nicht–radiativen Akkretionsflusses liefern, können als Eingangsdaten für Kerr Ray Tracing benutzt werden. Aus dieser Verknüpfung folgen realistische Spektren, die in der Nähe Schwarzer Löcher emittiert werden.

Black Hole Astrophysics: Magnetohydrodynamics on the Kerr Geometry

This work is dedicated to the astrophysics of rotating black holes. The main topic concerns accretion physics in the regime of General Relativistic Magnetohydrodynamics (GRMHD). The behavior of non–radiative accretion flows and outflows on the Kerr space–time is analyzed. Basic equations of conservative GRMHD and aspects of numerical schemes are presented. Relativistic codes and astrophysical simulations validate numerical schemes. A synopsis gives requirements for a robuste GRMHD code. Further developments in GRMHD research are investigated.
Another part deals with radiation from accretion disks. Relativistically broadened emission lines from active galactic nuclei and X–ray binaries are calculated by relativistic ray tracing. A new model – based on truncated standard disks – is presented that considers radial drift in accretion flows. Emission lines serve as diagnostic tools to compare parameter studies. Thereby, a classification scheme by line morphology was found: A line profile is triangular, double–horned, bumpy, shoulder–like or double–peaked.
Both parts of the work can be connected in further research: results from GRMHD simulations e.g. the velocity field of the flow serve as an input for Kerr ray tracing. Then, realistic spectra are feasible that originate from the vicinity of black holes.

In Appreciation to the Beauty of the World

Contents

List of Figures

Notations and Conventions

- The fundamental constants or Relativity, the vacuum speed of light, c, and the gravitational constant, G, are set to unity. Then, we deal with so–called "geometrized units" that are introduced in [MTW73].
- Therefore the natural length scale of GR, the gravitational radius, holds

$$r_{\rm g} = \frac{GM}{c^2} \equiv M. \tag{0.1}$$

  Generally, the Schwarzschild radius, $R_{\rm S}$, is equal to 2 $r_{\rm g}$.
- The signature of the metric is $(-\ +\ +\ +)$ if not differently specified.
- Greek indices μ, ν, κ, λ, ... at tensors cycle the numbers 0 to 3 and Latin indices i, j, ... cycle only spatial coordinates from 1 to 3. The temporal index is denoted by t and number 0.
- *Einstein's summation convention*: Sum on any index that is repeated in a product.
- The typical mass scale in astrophysics is the solar mass:

$$1\,{\rm M}_\odot = 1.989 \times 10^{30}\ {\rm kg} = 1.989 \times 10^{33}\ {\rm g} \tag{0.2}$$

- Stellar size is usually given in terms of the solar radius:

$$1\,{\rm R}_\odot = 6.960 \times 10^{8}\ {\rm m} = 6.960 \times 10^{10}\ {\rm cm} \tag{0.3}$$

- A usual luminosity scale in astrophysics is the solar luminosity:

$$1\,{\rm L}_\odot = 3.853 \times 10^{26}\ {\rm W} = 3.853 \times 10^{33}\ {\rm erg/s} \tag{0.4}$$

- The typical length scale in the solar system is the Astronomical Unit (AU):

$$1\,{\rm AU} = 1.4959787 \times 10^{11}\ {\rm m} = 1.4959787 \times 10^{13}\ {\rm cm} \tag{0.5}$$

- Galactic length scales are given in terms of the light year (ly):

$$1\,{\rm ly} = 63240{\rm AU} = 9.4605 \times 10^{15}\ {\rm m} = 9.4605 \times 10^{17}\ {\rm cm} \tag{0.6}$$

  or the parsec (pc):

$$1\,{\rm pc} = 3.2615\ {\rm ly} = 206264.8{\rm AU} = 3.0856 \times 10^{16}\ {\rm m} = 3.0856 \times 10^{18}\ {\rm cm} \tag{0.7}$$

- The cgs unit for energy is

$$1\,\mathrm{erg} = 1\,\frac{\mathrm{g\,cm^2}}{\mathrm{s^2}} = 10^{-7}\,\mathrm{J}. \tag{0.8}$$

- In theory, the strength of magnetic fields is often given in terms of Gauss

$$1\,\mathrm{G} = 10^{-4}\,\mathrm{T}. \tag{0.9}$$

- The Lorentz factor satifies

$$\gamma = \frac{1}{\sqrt{1-(v/c)^2}} = \frac{1}{\sqrt{1-(u_i\,u^i/c^2)}}, \tag{0.10}$$

  with the relative velocity v or spatial 3–velocity u^i.

- The 4–velocity, U^μ, is normalized by the condition [MTW73]

$$\mathbf{g}_{\mu\nu}U^\mu U^\nu = U_\nu U^\nu = -1. \tag{0.11}$$

- Abbreviations used in text are Ch(s). for Chapter(s), Sec(s). for Section(s), Eq(s). for Equation(s) and Fig(s). for Figures(s).

1 Introduction

The sky is full of fascinating cosmic objects. One of the most exotic and intriguing object is a black hole. Mass is so concentrated on a tiny region of space that even light is trapped. Black holes are described in the framework of relativistic astrophysics. Albert Einstein's Theory of General Relativity (GR) is the approach to get insight and understanding of black hole physics. Astronomers observed many candidate objects for black holes indicated by their darkness and compactness. The center of the Milky Way is such a favored candidate. It is supposed that a supermassive black hole of a few million solar masses hides in the Galactic Center. Besides this giant hole of solar system size, many star–like black holes spread over the Milky Way. These Galactic Black Hole Candidates (GBHCs) appear as X–ray sources in binary systems. Black holes play a key role in engines of active galaxies. The extreme luminosity of Active Galactic Nuclei (AGN) is explained by an accreting central supermassive black hole. The accretion process provides a source for intense electromagnetic emission outperforming any emission process known in the universe. The fascinating fact is the spatial proximity of absolute darkness of the black hole and the brightness of the accretion flow.
From a mathematical point of view, black holes are solutions of the Einstein field equations of GR. The first and simplest black hole solution was found in 1916 by the German astronomer Karl Schwarzschild. This so–called (exterior) Schwarzschild solution describes the static and spherically symmetric space–time of an electrically neutral point mass. The location of the point mass coincides with an intrinsical singularity. Here, the curvature of space–time diverges. For a distant observer the singularity lies behind an event horizon. In the Schwarzschild solution the horizon is located at the Schwarzschild radius. Schwarzschild black holes are global vacuum solutions of the field equations. The right–hand side, the energy–stress tensor, vanishes. This feature also holds for rotating black holes found in 1963 by the Newzealand mathematician Roy P. Kerr. The source for the stationary and axisymmetric gravitational field is a ring mass also shielded by an event horizon. Up to now, only these two space–times, Schwarzschild and Kerr solution, are relevant in black hole astrophysics. The most general form of an electrically charged black hole, the Kerr–Newman solution, is rarely considered because electric currents in the vicinity of the hole may compensate any black hole charge. Hence, the relativistic ingredient for black hole astrophysics is in general the Kerr space–time.
The accretion flow in the environment of the black hole can be described by using hydrodynamics and its extension to magnetohydrodynamics (MHD). This is due to the fact that the particles in the flow interact pairwisely. This regime is still valid for a plasma that consists of electrons and ions. A physical model of an accreting black hole therefore touches the following branches of physics: General Relativity, fluid dynamics, electrodynamics and radiation physics. An understanding of black hole astrophysics requires a

connection of those research fields. Actual research is two–fold: On the one hand, radiation physics is studied in the framework of non–relativistic hydrodynamics and MHD; on the other hand the non–radiative accretion flow (NRAF) is studied on the background of curved space–time. Upcoming research tends to link these two fields. The challenge is to develop robust methods to solve the covariant radiation transfer problem. Another complication is that the computation is expensive and reaches the limits of software and hardware.

This work is organized as follows: At first, rotating black holes are introduced as solutions in GR in Ch. 2. Their properties and the morphology are presented in detail. In Ch. 3, black holes are discussed as objects in astrophysics. After a pedagogical introduction to black hole astrophysics following historical cornerstones, observational techniques to detect black holes are presented and classified. The relevance of black holes in several astrophysical branches are reviewed. The main part concerns the astrophysics of rotating black holes and ergospheric processes. As an aside, modern black hole research with respect to the vacuum structure is discussed. Ch. 4 gives a brief review on accretion physics of black holes. Essential accretion solutions are presented and compared to each other. Hydrodynamical issues are opposed to MHD schemes. The truncation of standard accretion disks is considered in detail. There is a tendency that this property explains many observed features, especially the lack of broad relativistic emission lines in most AGN. The generation of relativistic jets due to the interaction of rotating black holes with the magnetosphere of the accretion flow is pointed out. The framework of General Relativistic Magnetohydrodynamics (GRMHD) is presented in Ch. 5. The basic set of differential equations is shown that connects magnetohydrodynamics and GR. Suited coordinate frames are presented that capture the physics of rotating black holes. Concepts of numerical Relativity like the splitting scheme of space–time (3+1) are summarized. Recent research demonstrated the relevance of MHD instabilities. Of special interest is the magneto–rotational instability (MRI) that efficiently drives magnetic turbulence in the accretion flow. MHD plus GR results in efficient mechanisms to drive outflows with high Lorentz factors. The so–called Poynting flux is also described mathematically in this chapter as well as today available GRMHD codes. General requirements, advantages and disadvantages are discussed in direct comparison. This analysis provides essential properties of future GRMHD codes. The decay of an initial plasma torus configuration turned out to be a nice benchmark problem for black hole accretion physics. Within these simulations black hole feeding from a matter reservoir can be studied. The morphology and parameter space of inflows and outflows is an important research topic. Ch. 6 is dedicated to Kerr ray tracing, a technique that solves the problem of light propagation in curved Kerr space–time. In this work, the method is used to simulate broad relativistic emission lines originating from truncated standard disks (TSDs). Thereby, a new model is presented that considers radial drift in TSDs in both, the plasma velocity field and the radial emissivity. Finally, all results concerning black hole astrophysics presented in this work – in particular black hole accretion – are summarized and discussed in Ch. 7.

2 Rotating Black Holes

2.1 Astrophysical Motivation

Astronomical observations hint for many objects that are compact and dark. The acronym CDO for compact dark object is often used in this context. Different detection methods for black holes which will be presented in Sec. 3.4 prove unambiguously the existence of high masses concentrating in tiny regions. There are alternative propositions for CDOs apart from black holes: compact star clusters, bosons stars, fermion balls. Recently it turned out that these alternatives can often be excluded. Consequently, the black hole remains.

Rotation is a natural feature of many cosmic objects: planets, stars, even galaxies rotate. Stellar black holes originate from collapsing massive stars. The angular momentum of the progenitor star can not completely radiated away, e.g. by emission of gravitational waves. Therefore, it is strongly suggested that at least stellar black holes rotate. As will be demonstrated in Sec. 3.2, astrophysical black holes cover a mass range over tens of decades. At the high–mass limit there are supermassive black holes (SMBHs) that weight millions to billions of solar masses. Typically, SMBHs can be found in every galaxy and especially in Active Galactic Nuclei (AGN). Astronomers mostly agree in this hypothesis. However, there may be some exceptions but this can be a result by merging scenarios where the galaxy core is extracted.

The evidence for rotation is particularly proposed in the center of our own galaxy, the Milky Way. The compact radio source Sgr A* is associated with the putative SMBH in the Galactic Center. Recent flare observations in the vicinity of Sgr A* reinforce the existence of a *rotating* black hole. Both, NIR and X–ray flares plead for a high rotational state of the hole [Gen03, Por03].

This motivates the theoretical astrophysicist to study rotating black holes. The most general black hole belongs to the Kerr–Newman family. These space–times are fully determined by mass, angular momentum and electric charge of the black hole. The source of this gravitational field is a charged mass current. For astrophysical black holes, the electric charge is supposed to be unimportant. The reason is that an electric charge would be compensated by electric currents i.e. plasma flows in the environment of the black hole. Hence, astrophysicists focus on rotating electrically neutral black holes. They are described by the Kerr solution.

2.2 The Kerr Solution

Rotating black holes belong to a more general class of space–times. This is the class of axisymmetric and stationary space–times. Usually, axisymmetric and stationary space–times – in vacuum or non–vacuum – are written in the following notation ("*Papapetrou line element*")

$$ds^2 = \exp(2\Phi)\,dt^2 - \exp(2\psi)\,(d\phi - \omega\,dt)^2 - \exp(2\mu_2)\,(dx^2)^2 - \exp(2\mu_3)\,(dx^3)^2, \quad (2.1)$$

where coordinates $\{t, \phi, x^2, x^3\}$ are assumed. The five functions Φ, ψ, ω, μ_2, and μ_3 are only functions of the spatial coordinates x^2 and x^3. The functions μ_2 and μ_3 are interconnected by a gauge transformation.
Axisymmetry and stationarity can be viewed as two symmetries that enforce two conserved quantities according to the Noether theorem: total angular momentum, J, and total energy, E. In general, each symmetry of a space–time is associated with a Killing field. The higher the symmetry, the more Killing fields are available.[1] Axisymmetry and stationarity lead to two Killing vectors: axisymmetry requires an asymptotically space–like Killing field, ∂_ϕ, and stationarity requires an asymptotically time–like Killing field, ∂_t. Both Killing fields can be extracted from the Killing equation for the space–time. It follows from an isometry condition by considering the vanishing Lie derivative of the metric.
Rapidly rotating neutron stars also fit the metric type in Eq. (2.1). But there is a crucial distinction between neutron stars and black holes: black holes exhibit an event horizon, there is no solid surface. And there is yet another vital distinction: For black holes the energy–momentum tensor vanishes globally, $\mathbf{T}_{\mu\nu} = 0$. Kerr black holes are solutions of the vacuum field equations of GR, $\mathbf{G}_{\mu\nu} = 0$, where $\mathbf{G}_{\mu\nu}$ denotes the Einstein tensor.
Exercising the gauge freedom for the functions μ_2 and μ_3, one defines

$$e^{2(\mu_3 - \mu_2)} = \Delta(r). \quad (2.2)$$

Here the horizon function , Δ, is introduced which defines a null surface , i.e. the event horizon of a black hole. We will return to this function in Sec. 2.3.
The Kerr solution is one possible realization for an axisymmetric and stationary space–time. It was found in 1963 by the New Zealand mathematician Roy Patrick Kerr [Ker63]. The solution describes rotating black holes. The global structure of the Kerr space–time is fixed only by two properties: the mass and the spin of the black hole. Wheeler therefore outlined in his famous aphorism *"Black holes have no hair!"*. This **no–hair theorem** states that black holes have only few parameters that fix their properties. In contrast, progenitor stars that form black holes exhibit significantly more attributes.
The Kerr solution is asymptotically flat i.e. that for large radii, $r \to \infty$, the Kerr metric transmutates to the Minkowski metric. This is simply the far field approximation where the gravitational field becomes weak in large distances. The Robinson theorem [Rob75] states the Kerr solution to be **unique**:
Stationary axisymmetric solutions of the vacuum field equations of GR which exhibit

[1] The highly symmetric flat Minkowski metric possesses ten Killing fields.

- *asymptotical flatness,*
- *a smooth convex horizon,*
- *regularity outside the horizon*

are uniquely specified only by two parameters: mass, M, and angular momentum, J.

The historical form[2] of the solution was given in Cartesian coordinates $\{t, x, y, z\}$ [Cha83]

$$\begin{aligned} ds^2 &= dt^2 - dx^2 - dy^2 - dz^2 \\ &\quad - \frac{2Mr^3}{r^4 + a^2 z^2}\left(dt - \frac{1}{r^2 + a^2}\left[r(x\,dx + y\,dy) + a(x\,dy - y\,dx)\right] - \frac{z}{r}\,dz\right)^2, \end{aligned} \tag{2.3}$$

with the mass of the black hole, M, and the specific angular momentum, $a = J/M$. a is also called the Kerr parameter or spin parameter of a rotating black hole. For $a = 0$ the Kerr solution degenerates to the static Schwarzschild solution. In geometrized units the Kerr parameter satisfies $a \in [-M, M]$. Negative values of a denote retrograde and positive values prograde rotation of the black hole. The function r in Eq. (2.3) is given implicitly as depending on x, y, z and a

$$r^4 - r^2(x^2 + y^2 + z^2 - a^2) - a^2 z^2 = 0. \tag{2.4}$$

This Cartesian form is somewhat cumbersome for practical purposes. The widely used form of the Kerr solution is the pseudo–spherical **Boyer–Lindquist form** $\{t, r, \theta, \phi\}$ [Boy67]. The coordinate t measures the coordinate time, r is the radial coordinate, θ measures the poloidal angle and ϕ is the azimuthal angle. The axis of symmetry respective the axis of rotation, is equal to $\theta = 0$. Then, the line element of the Kerr solution takes the standard form

$$\boxed{ds^2 = -\alpha^2 dt^2 + \tilde{\omega}^2(d\phi - \omega dt)^2 + \rho^2/\Delta\; dr^2 + \rho^2 d\theta^2.} \tag{2.5}$$

According to the Robinson theorem respective no–hair theorem the metric depends essentially on two free parameters, black hole mass, M, and black hole spin, a. The canonical functions in the line element are simple functions of these two parameters:

$$\alpha = \frac{\rho\sqrt{\Delta}}{\Sigma}, \tag{2.6}$$

$$\Delta = r^2 - 2Mr + a^2, \tag{2.7}$$

$$\rho^2 = r^2 + a^2\cos^2\theta, \tag{2.8}$$

$$\Sigma^2 = (r^2 + a^2)^2 - a^2\Delta\sin^2\theta, \tag{2.9}$$

$$\omega = \frac{2aMr}{\Sigma^2}, \tag{2.10}$$

$$\tilde{\omega} = \frac{\Sigma}{\rho}\sin\theta. \tag{2.11}$$

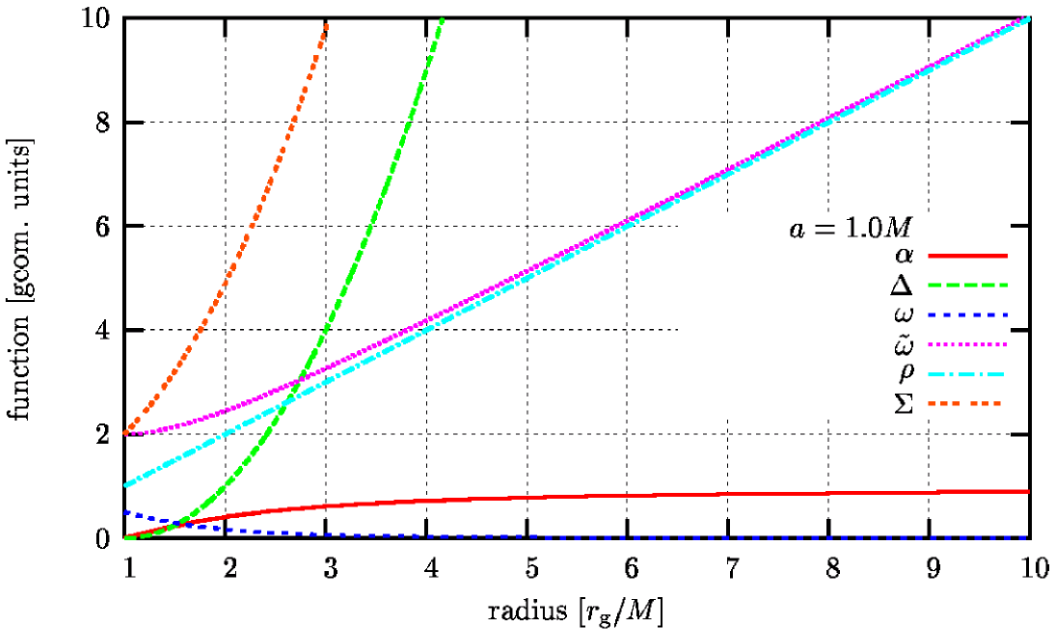

Figure 2.1: Radial profiles of canonical Boyer–Lindquist functions for extreme Kerr, $a = M$, restricted to the equatorial plane, $\theta = \pi/2$. The left–hand side marks the outer event horizon at r_{H}^{+}=M.

These functions satisfy the following nomenclature due to their physical or geometrical interpretation: α is the redshift factor or lapse function which measures the general relativistic time dilatation or gravitational redshift of local clocks as compared to infinity. ω is called the frame–dragging frequency or potential for angular momentum[3]. It falls off very rapidly with radius, $\omega \propto r^{-3}$. The frame–dragging frequency parametrizes the rotation of the Kerr space–time. More generally, it is defined as $\omega = -g_{t\phi}/g_{\phi\phi}$. For $a = 0$ the function ω vanishes identically. Then, the cross term $g_{t\phi} = g_{\phi t}$ disappears in the line element. The space–time becomes static and the metric is diagonal: The Schwarzschild metric is restored. In other words: In Boyer–Lindquist coordinates the off–diagonal element $g_{t\phi}$ contains the rotation of the space–time. The name of $\tilde{\omega}$ is cylindrical radius because $2\pi\tilde{\omega} = 2\pi\sqrt{-g_{\phi\phi}}$ equals the circumference of cylinders at radial position r that are concentric to the axis of symmetry. Δ and ρ are geometrical functions where Δ was already introduced as horizon function. This is due to the fact that Δ fixes two event horizons (as elaborated in Sec. 2.3). In the equatorial plane, $\theta = \pi/2$, ρ equals the radial

[2]Please note the deviating signature $(+ - - -)$.

[3]We will see in Sec. 3.5 that the shift vector $\vec{\beta}$, specifically the component $\beta^{\phi} = -\omega$ in Boyer–Lindquist coordinates serves as a potential which is associated with a gravitomagnetic field.

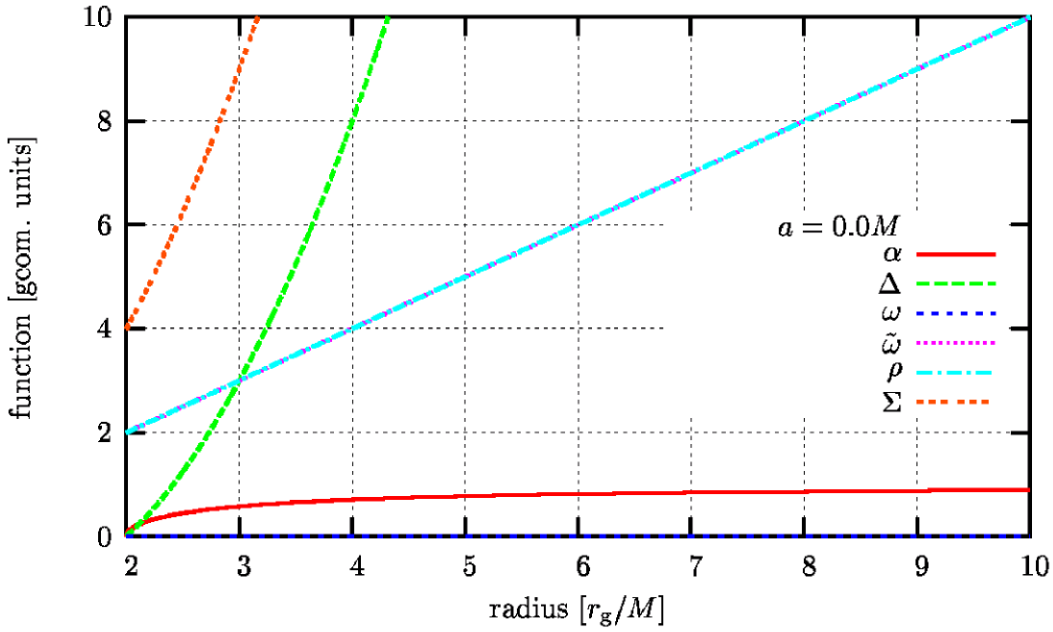

Figure 2.2: Radial profiles of canonical Boyer–Lindquist functions for Schwarzschild, $a = 0$, restricted to the equatorial plane, $\theta = \pi/2$. The left–hand side marks the event horizon of a non–rotating black hole, located at the Schwarzschild radius, $R_S = 2M$.

coordinate r. Fig. 2.1 and 2.2 illustrate the radial dependence of the Boyer–Lindquist functions given in Eqs. (2.6) to (2.11). In geometrized units, $G = c = 1$, the radius is given in terms of the mass of the black hole, M. In both cases, the lapse function α vanishes at the horizon. This is due to the fact that the horizon function Δ becomes zero. As can be seen in Fig. 2.1 the frame–dragging potential ω increases significantly only at small radii. In direct vicinity of the Kerr hole the rotation of space–time is enhanced. Of course, ω disappears in the Schwarzschild case as illustrated in Fig. 2.2.

2.3 Event Horizons

In general, an event horizon flags the point of no return for infalling matter, radiation and observers. This critical zone appears totally black as viewed from the outside because no light is able to escape. The notion of an *event horizon* is justified because events or in relativistic language world points that are located beyond the horizon radius cannot be

detected from outer observers. Like every horizon[4] the black hole event horizon separates observable from unobservable objects.
As anticipated in Sec. 2.2 the Kerr solution exhibits an event horizon. Due to the symmetries of the space–time this smooth two–dimensional null surface is spanned by two tangent vectors, the Killing vectors ∂_t and ∂_ϕ. The notion *null surface* means that this surface is light–like.
Exploiting the gauge freedom, the event horizon can be defined by using the horizon function Δ. The roots of this generally quadratic function define the position of the horizons :

$$\Delta = 0 \;\Leftrightarrow\; r_{\mathrm{H}}^{\pm} = M \pm \sqrt{M^2 - a^2}. \tag{2.12}$$

The astronomical important fact is that due to $\Delta(r_{\mathrm{H}}^{\pm}) = 0$, also the redshift factor α vanishes at the horizon, compare Eq. (2.6). In other words: the redshift z defined by

$$z = \frac{\lambda_{\mathrm{obs}} - \lambda_{\mathrm{em}}}{\lambda_{\mathrm{em}}} = 1/\alpha(r) - 1 \tag{2.13}$$

becomes infinite, $z \to \infty$. This behavior is the reason for the blackness of the black hole . Generally spoken, strongly curved space–times of compact objects (COs) damp local emission of radiation. Black holes represent the extreme version of those COs.
As can be seen from Eq. (2.12), there exist **two horizons** for arbitrary Kerr parameter, $a \neq 0$: The outer event horizon , r_{H}^{+}, and the inner event horizon or Cauchy horizon , r_{H}^{-}. The inner horizon is often neglected in discussing astrophysical black holes. The reason is that it is of subordinate importance for astronomy because observational features stop naturally at the outer horizon. A Cauchy surface is defined as a hypersurface of space–time that a causal curve can only intersect once. Hence, Cauchy horizons are somewhat like "semipermeable barriers". It is an interesting phenomenon that an observer who may reach the Cauchy surface witnesses in a flash the entire history of the external world. This is because of an infinite blueshift $dt/d\tau \to -\infty$ for $r \to r_{-} + 0$. Therefore, the observer will be additionally hit by an infinite flash of radiation. These strange and fantastic features of the black holes interior are a consequence of pure GR. It may signal that relativists enter here the domain of a quantum description of space–time. The idealized structure of the singularities which will be treated in the next section hint also for the need of embedding quantum concepts in GR.
For vanishing spin parameter, $a = 0$, these two horizons degenerate to only one horizon, the Schwarzschild radius $R_{\mathrm{S}} = 2M$. Generically, there is no dependence of any horizon radius on the poloidal angle θ. Hence, the horizons have in any cases spherical symmetry.

2.4 Singularities

Static and rotating electrically neutral black holes are global vacuum solutions of GR. If the energy–momentum tensor vanishes globally, $\mathbf{T}_{\mu\nu} = 0$, the question arises what is

[4]The notion originates from the Greek expression *όρίζωνν κύκλος*, i.e. 'limiting circle'.

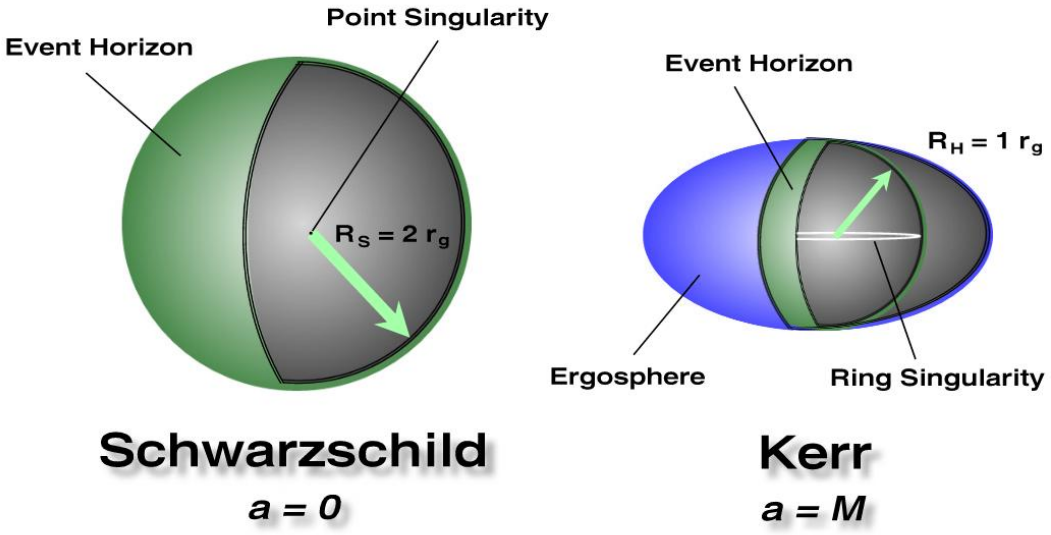

Figure 2.3: Direct comparison of the morphologies of a Schwarzschild black hole (*left*) vs. an extreme Kerr black hole (*right*). In the static case, a point mass generates the spherically symmetric gravitational field; in the rotating case a mass current generates the axisymmetric space–time. The outer horizons are illustrated (*green*). The oblate ergosphere (*blue*) wraps the event horizon at R_{H}. Additionally, the same mass, M, was assumed. Then Kerr black holes are smaller than Schwarzschild black holes as viewed from infinity.

the source of the gravitational field. The space–time of a black hole is strongly curved by an *intrinsical singularity* . These singularities exhibit infinite curvature, i.e. here the Riemann tensor diverges.
The intrinsical singularity of the Schwarzschild geometry is a point mass that is located at $r = 0$. In case of the Kerr geometry this point is blown up to a ring: The axisymmetric Kerr space–time is generated by a **ring mass current**. This ring is located in the equatorial plane at $z = 0$ respective $\theta = \pi/2$ and has a radius that equals the Kerr parameter in geometrized units, $r = a$. This can easily derived from Eq. (2.4), contained in the historical line element Eq. (2.3). Alternatively, in Boyer–Lindquist coordinates this condition is equivalent to $\rho(r, \theta) = \sqrt{r^2 + a^2 \cos^2 \theta} = 0$.
The ring singularity lies always inbetween the two horizons of the Kerr space–time as illustrated in Fig. 2.3. In contrast to these unavoidable singularities there are avoidable ones, the *coordinate singularities*. It is well–known that the Schwarzschild solution diverges at the Schwarzschild radius, R_{S}, in classical "Schwarzschild coordinates". In Schwarzschild, one can overcome this deficiency by a transformation to Kruskal–Szekeres coordinates [Kru60, Sze60] . These coordinates represent the maximally analytical extension. Similarly, the Kerr solution exhibits a coordinate singularity at both horizons

in Boyer–Lindquist form. Therefore, it is recommended to transform to suited well–behaved coordinates such as horizon adapted coordinates. It is astonishing that the pathological Boyer–Lindquist frame is widely used in black hole physics. Especially in GRMHD the Boyer–Lindquist coordinates pose a serious problem as debated in Sec. 5.3.
Another aspect treats the question of the existence of *singularities in nature*. From the viewpoint of modern physics the idealized point and ring singularities in classical GR are questionable and doubtful. We know from quantum theory that due to the Heisenberg uncertainty principle every idealized point or string must be smoothed to an extended object. The singularity theorems by Hawking and Penrose [Hawk69] state that under certain conditions intrinsical singularities must exist *mathematically*. But is this statement synonymous to an existence in nature? We conclude that there is a need that these theorems must be re–evaluated under the modern viewpoint.
The singularity problem intensifies under the pressure of alternative **regular** solutions that were found since the beginning of the millenium. They are called vacuum stars because a new kind of physical vacuum other than the relativistic vacuum of classical black holes is considered. Up to now, the vacuum star solutions are static as the Schwarzschild solution. In Sec. 3.6 the modern alternative models for classical Schwarzschild black holes – Gravastars and Holostars – are shortly presented. However, the lack of rotating generalizations of these proposals motivates to study the Kerr solution with classical "relativistic vacuum" .

2.5 Ergosphere

The Kerr geometry offers another feature that is missing in static black hole solutions: the *ergosphere*. This mathematical surface is defined by the vanishing component g_{tt} of the metric. Using the Boyer–Lindquist frame (see Eq. (2.5)) this leads to the condition

$$g_{\mathrm{tt}} = -\alpha^2 + \omega^2\tilde{\omega}^2 = 0 \;\Leftrightarrow\; r_{\mathrm{E}}(\theta) = M + \sqrt{M^2 - a^2\cos^2\theta}. \tag{2.14}$$

The eye–catching feature of this equation is the θ–dependence. Hence, the ergosphere depends on the poloidal angle and has oblate morphology, comparable to the Earth. At the poles of the black hole, the ergosphere touches the outer event horizon. At the equator the ergosphere has a bulge.
Fig. 2.4 shows the radial profile of the metric coefficient g_{tt} for parameters $a = M$ and $\theta = \pi/2$. At $r = 2\ r_{\mathrm{g}}$ the coordinate t switches from time–like to space–like. The zone between outer horizon and ergosphere, $r_H \leq r \leq r_E$, is called the ergoregion. The ergoregion has maximal size for extreme Kerr solutions, $a = \pm M$. In Fig. 2.1 it is shown that the radial profile of the frame–dragging frequency, ω, steeply increases in the ergoregion. This implies that the rotation of space–time becomes extraordinary strong. In Sec. 3.5 we will see that there are a number of processes operating only in the ergosphere.
The rotation of space–time is the key feature of the Kerr geometry. Interestingly, the dynamics implies that reference frames are dragged. It is not possible to sustain static observers. Hence, the ergosphere is also called the *static limit*. There is no globally

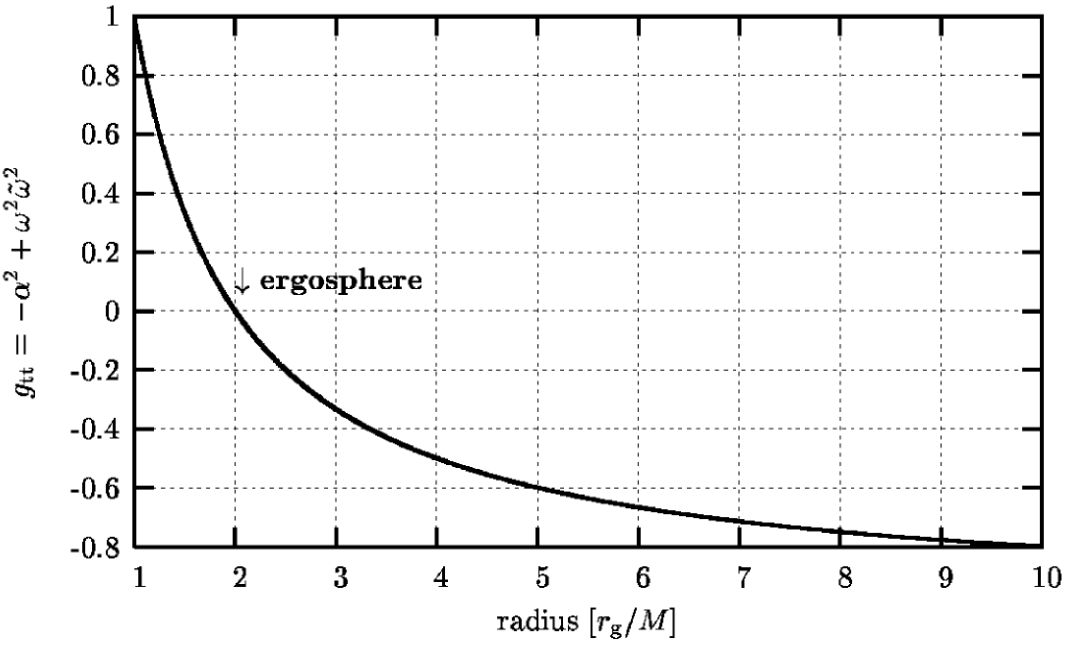

Figure 2.4: The ergospheric turnover. Parameters are fixed to maximum Kerr, $a = M$, and equatorial plane, $\theta = \pi/2$. Entering the ergosphere the metric coefficient g_{tt} flips the sign. The edge of the ergosphere is defined by $g_{tt} = 0$.

time–like non–rotating Killing field. Observers are also dragged by the rotating space–time. This called the **frame–dragging effect**.

In the Kerr space–time, the general expression for the angular frequency of a particle, Ω, with specific angular momentum, $\lambda = J/E$, is given by

$$\Omega = \omega + \frac{\alpha^2}{\tilde{\omega}^2} \frac{\lambda}{1 - \omega\lambda}, \tag{2.15}$$

with a dependence on the metric functions ω, α and $\tilde{\omega}$. Their influence becomes dominant at small radii. For radii greater than the orbit of marginal stability, r_{ms} (see Sec. 2.7), Keplerian rotation is established, $\Omega \to \Omega_K$ satisfying

$$\Omega_K = \pm \frac{\sqrt{M}}{\sqrt{r^3} \pm a\sqrt{M}} \text{ for } r \geq r_{ms}, \tag{2.16}$$

with upper sign for prograde and lower sign for retrograde (counter–rotating) orbits. The Boyer–Lindquist functions are now evaluated at the outer event horizon, $r = r_H^+$,

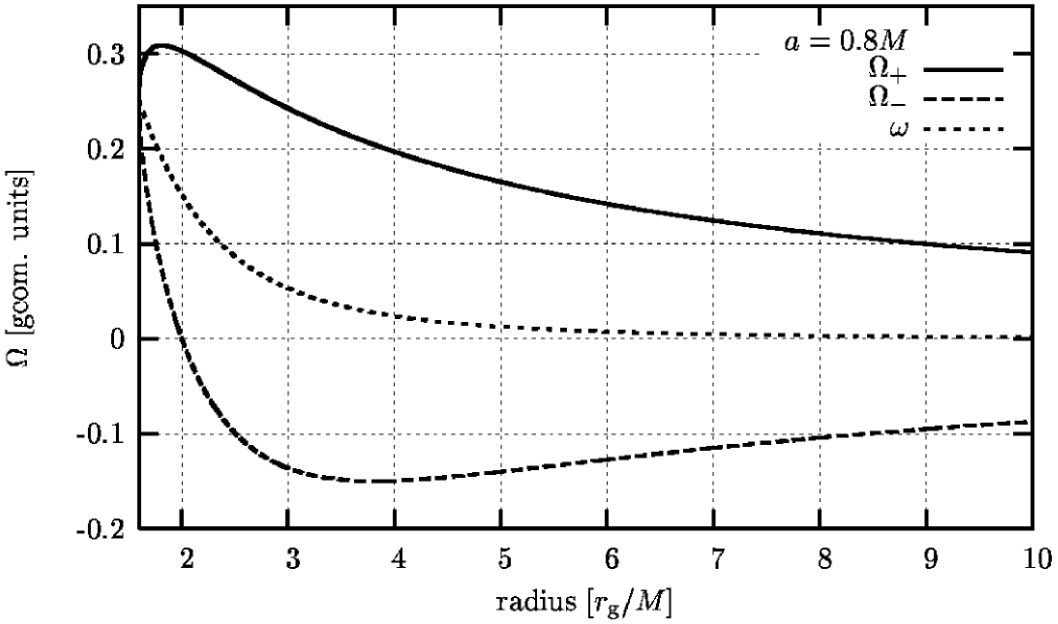

Figure 2.5: Frame–dragging illustrated for Kerr parameter $a = 0.8\,M$. The frame–dragging frequency, ω, is the central curve. The upper curve corresponds to the prograde limit of the angular velocity, Ω_+, whereas the lower curve corresponds to the retrograde limit of the angular velocity, Ω_-. At the outer event horizon, $r_{\rm H}^+(a = 0.8\ M) = 1.6\ r_{\rm g}$, all curves coincide: The black hole horizon forces anything to corotate with $\omega(r_{\rm H}^+)$!

and restricted to the equatorial plane, $\theta = \pi/2$:

$$\begin{aligned} \Delta(r_{\rm H}^+) &= 0, & \alpha(r_{\rm H}^+) &= 0, \\ \Sigma_{\pi/2}(r_{\rm H}^+) &= 2r_{\rm H}^+, & \tilde{\omega}_{\pi/2}(r_{\rm H}^+) &= 2, \\ \omega(r_{\rm H}^+) &= a/(2Mr_{\rm H}^+) \equiv \Omega_{\rm H}. \end{aligned} \tag{2.17}$$

The latter quantity is the angular frequency of the black hole horizon, $\Omega_{\rm H}$. Frame–dragging means that the Kerr black hole forces anything to rotate: observers, photons, light cones and magnetic field lines. The square of α goes rapidly to zero as approaching the horizon. Hence, the second term in Eq. (2.16) vanishes and $\Omega \to \Omega_{\rm H}$.
Assuming a time–like Killing field, ∂_t, and a space–like Killing field, ∂_ϕ, the velocity field of an observer takes the form

$$u = u^t(\partial_t + \Omega\ \partial_\phi), \quad \Omega = \frac{u^\phi}{u^t}. \tag{2.18}$$

A globally time–like velocity field fulfills the condition [MTW73]

$$g_{tt} + 2\,\Omega\,g_{t\phi} + \Omega^2\,g_{\phi\phi} > 0. \tag{2.19}$$

Therefore, the angular velocity, Ω, satisfies the limits

$$\Omega_- \leq \Omega \leq \Omega_+,\ \Omega_\pm = \omega \pm \frac{\alpha}{\tilde{\omega}}. \tag{2.20}$$

At the outer horizon, r_{H}^+, the space–time and anything else rotates with the angular velocity of the Kerr black hole

$$\Omega_{\mathrm{H}} \equiv \omega(r_{\mathrm{H}}^+) = \frac{a}{2Mr_{\mathrm{H}}^+} = \frac{a}{r_{\mathrm{H}}^{+2} + a^2}. \tag{2.21}$$

This behavior is displayed in Fig. 2.5.
Of course, this angular frequency, Ω_{H}, vanishes identically in the Schwarzschild case, $a = 0$. But it is necessary to say that frame–dragging holds also in this static case: Anything needs to stop rotation at the Schwarzschild radius, especially inspiraling matter from a rotating accretion disk! Hence, in Schwarzschild it is supposed that infalling matter forms a boundary layer. It has to stop rotation when overflowing from the accretion disk to the horizon. One may refer to this phenomenon as an **anti–frame–dragging**.

2.6 Photon Sphere

The photon sphere is another characteristic orbit of a Kerr black hole. This orbit follows from calculations in the framework of celestrial mechanics of a black hole [Bar72] using the particle momenta in the Kerr geometry [Car68]. At the radius

$$r_{\mathrm{ph}} = 2M\left[1 + \cos\left(\frac{2}{3}\arccos(-a/M)\right)\right], \tag{2.22}$$

it is possible for photons to circulate on unstable orbits. At the radius r_{ph} the energy per unit rest mass becomes infinite. Therefore, it is a photon orbit. In Schwarzschild, $a = 0$, the photon sphere amounts to $r_{\mathrm{ph}}(a = 0) = 3M$. For extreme Kerr, this radius coincides with the outer horizon in the prograde case and amounts $4M$ in the retrograde case.
To date, there are no hints that this sphere has ever been observed astronomically. But we will see in Sec. 3.5 that the photon sphere may play a certain role in the generation of a leptonic pair plasma.

2.7 Marginally Stable and Bound Orbit

Black holes are endowed with some further characteristic radii. These are the marginally stable orbit, r_{ms}, and the marginally bound orbit, r_{mb}.

The orbit of marginal stability marks the minimal radius in the equatorial plane where stable rotation around the hole is possible. The radius follows from a discussion of effective potentials in the Kerr geometry. As in classical mechanics, minima of the potential curve indicate stable trajectories of a particle. The specific angular momentum of the particle acts as a parameter for the potential curve.
The analysis of the extrema and the inflection points yield the marginally stable orbit as a *saddle point* in the potential curve

$$r_{\mathrm{ms}} = M\left(3 + Z_2 \mp \sqrt{(3 - Z_1)(3 + Z_1 + 2Z_2)}\right), \tag{2.23}$$

with auxiliary functions

$$Z_1 = 1 + \left(1 - \frac{a^2}{M^2}\right)^{1/3}\left(\left(1 + \frac{a}{M}\right)^{1/3} + \left(1 - \frac{a}{M}\right)^{1/3}\right),$$
$$Z_2 = \sqrt{3\frac{a^2}{M^2} + Z_1^2}.$$

The upper sign holds for prograde whereas the lower sign is used for retrograde orbits. The marginally stable orbit also called *innermost stable circular orbit*, **ISCO**, or *last stable circular orbit*. It depends only on the mass, M, and specific angular momentum, a, of the Kerr black hole. Limiting cases are extreme Kerr with retrograde rotation, $r_{\mathrm{ms}}(a = -M) = 9\ M$, extreme Kerr with prograde rotation, $r_{\mathrm{ms}}(a = M) = M$ and the intermediate Schwarzschild case, $r_{\mathrm{ms}}(a = 0) = 6\ M$.
We will return in the context of accretion physics to the innermost stable circular orbit in Sec. 4.2. This is due to the fact that standard accretion disks (SADs) also called Shakura–Sunyaev disks (SSDs) extend inwards down to the marginally stable orbit. For smaller radii, $r < r_{\mathrm{ms}}$, stable Keplerian rotation and hence stable disk rotation breaks down. It is remarkable that for prograde extreme Kerr, $a = M$, the ISCO touches the outer horizon! Theoretically spoken, a standard disk extends down to the event horizon.

Another characteristic radius in black hole physics is the **marginally bound orbit**, r_{mb}. Let us consider a test particle with rest mass, m. An unbound circular orbit is described by $E/m > 1$. They are all unstable. The discussion in [Bar72] and also revisited in [Cha83] leads to the conclusion that an outward perturbation on such a particle will provoke an escape to infinity. Now, the critical radius r_{mb} can be deduced by setting the total energy equal to the rest mass of the particle, $E = m$. This relativistic condition corresponds to the Newtonian analogue with a discussion of Keplerian orbits for $E = 0$. But here is a characteristic rest frame term that does not depend on the velocity. Hence, in black hole physics the condition is generalized to $E = m$. One can interprete this as a particle at rest at infinity that is just going to fall towards the black hole. The condition finally yields the marginally bound orbit to

$$r_{\mathrm{mb}} = 2M \mp a + 2\sqrt{M}\sqrt{M \mp a} = \left(\sqrt{M} + \sqrt{M \mp a}\right)^2 \tag{2.24}$$

Again, the upper sign means prograde, the lower sign retrograde orbits.

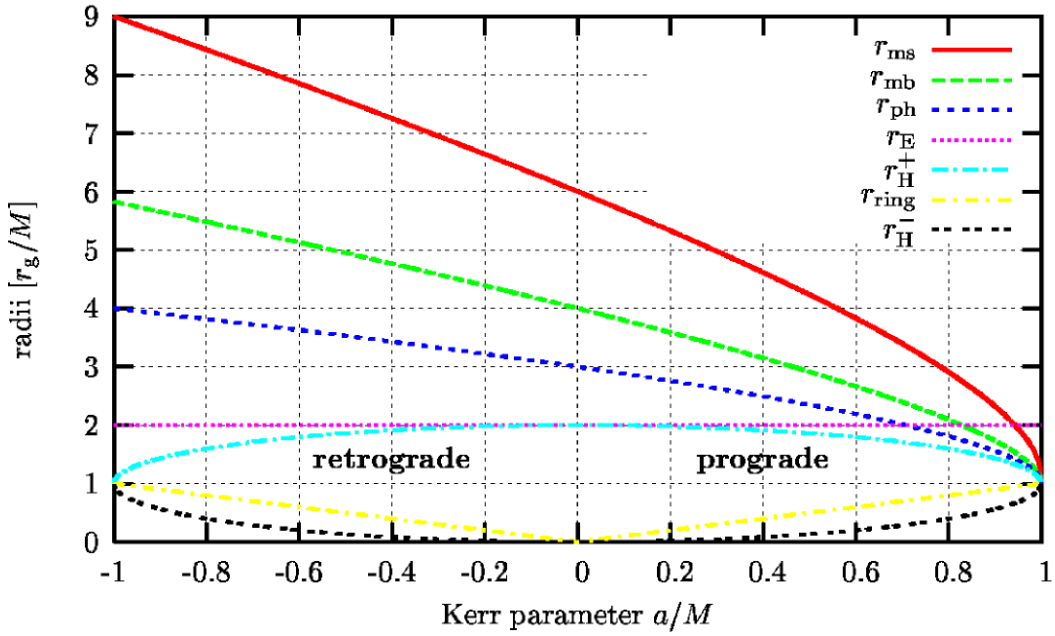

Figure 2.6: Characteristic radii of a Kerr black hole for the complete interval of the spin parameter, $a \in [-M, M]$. The left side represents the regime of retrograde rotation, $a < 0$, the right side is for prograde rotation, $a > 0$. The Schwarzschild case lies exactly in the center, $a = 0$. From top to bottom there is the marginally stable orbit (*red*), the marginally bound orbit (*green*), the photon sphere radius (*blue*), the radius of static limit (*purple*, in the equatorial plane), the outer horizon (*cyan*), the radius of the ring singularity (*yellow*) and the inner horizon radius (*black*).

All characeristic radii of a Kerr black hole as introduced before, inner and outer event horizon $r_{\mathrm{H}}^{\pm}$ in Sec. 2.3, the radius of the ring singularity r_{ring} in Sec. 2.4, the static limit respective the ergosphere r_{E} in Sec. 2.5, photon sphere r_{ph} from Sec. 2.6, finally r_{ms} and r_{mb} from this section, are now summarized in Fig. 2.6. Their dependence on the specific angular momentum of the black hole, $a \in [-M, M]$, shows the trend that all radii (apart from the static limit) come closer for higher values of a. A degeneracy is reached for maximum Kerr, $a = M$. Then, there is no distinction between the radii (except of r_{E}): *Any* radius lies at the event horizon, $r_{\mathrm{ms}} = r_{\mathrm{mb}} = r_{\mathrm{ph}} = r_{\mathrm{H}}^{+} = r_{\mathrm{ring}} = r_{\mathrm{H}}^{-} = r_{\mathrm{g}} = M$.

3 Astrophysics of Black Holes

3.1 Historical Overview

As an introduction to the topic of this chapter it is interesting to follow the historical cornerstones of black hole physics. 221 years of black hole history are characterized by some first conjectures that change into a reliable theory. The purely theoretical existence turn into a strong believe that nature permits black holes. Rather late – in the course of astrophysical developments – the notion of the *black hole* was born. Nowadays, astrophysics requires the existence of black holes – or something that look like black holes.
The timeline of black hole physics is now presented in a some detail[1]:

- The **first speculations** for the existence of black hole–like objects are ascribed to Reverend John Michell (1724–1793) [Tho94]. The British natural philosopher, geologist and astronomer wrote in his publication to the Royal Society (1783):
  "*If the semi-diameter of a sphere of the same density as the Sun in the proportion of five hundred to one, and by supposing light to be attracted by the same force in proportion to its mass with other bodies, all light emitted from such a body would be made to return towards it, by its own proper gravity.*"
  Therefore, he speculated about a body so dense that its escape velocity is equal to the speed of light. These bodies must be absolutely dark.

- Twelve years later, in 1795, Pierre Simon de Laplace (1749–1827) wrote down similar thoughts in *Exposition du Système du Monde*. On the basis of Newtonian gravity and corpuscular theory of light Laplace noted that light cannot escape from a sufficiently massive object [MTW73].

- Albert Einstein (1879–1955) invented the Theory of Relativity. The first step, Special Relativity (1905) [Ein05], revolutionized the ideas of motion, length, space and time. The second step, **General Relativity** (1915) [Ein15a, Ein15b, Ein15c], revealed a deeper understanding of space, time, mass and energy than Newtonian gravity. The next cornerstone proves that the concepts of GR are of outstanding relevance to capture black holes as space–times.

- In 1916, the German astronomer Karl Schwarzschild (1873–1916) discovered the **first solution** of Einstein's field equations of GR [Sch16a]. It describes the static vacuum space–time of a point mass (compare Sec. 2.4). Besides, Schwarzschild

[1] Of course, this overview lays no claim to be complete.

found another solution: the internal Schwarzschild solution that is created by a sphere of an incompressible fluid [Sch16b].

- Hans Jacob Reissner (1874 - 1967) [Rei16] and Gunnar Nordstrøm [Nor18] succeeded in generalizing the Schwarzschild solution: They discovered the spherically symmetric gravitational field of a point charge. Both, internal Schwarzschild and this **Reissner-Nordstrøm solution** are non–vacuum space–times.

- In the twenties, the mathematician Theodor F.E. Kaluza (1885–1954) and the chemist Oskar Klein (1894–1977) invented a new fivedimensional field theory [Kal21, Kle26]. This **Kaluza–Klein theory** connects Relativity and electromagnetism under the assumption of a **spatial extra dimension**. The field theory was superseded by quantum theory, but revived in the nineties.

- In 1923, George Birkhoff proved that the Schwarzschild space–time is the unique spherically symmetric solution of Einstein's vacuum field equations [Bir23] (**Birkhoff theorem**).

- The Indian astrophysicist Subrahmanyan Chandrasekhar (1910–1995) discovered in 1930 that white dwarfs – the compact relic configurations of sun–like stars – are not stable for arbitrary mass. The description of relativistic matter as a Fermi gas led to a critical mass limit [Cha31a, Cha31b]. Exceeding this limiting **Chandrasekhar mass** of about 1.46 $M_\odot$, nothing can stop the matter undergoing gravitational collapse.

- The English astrophysicist and relativist Sir Arthur S. Eddington (1882–1944) speculated in 1935 – inspired by Chandrasekhar's mass limit – about relativistic stars that collapse to such a dense object that they could capture radiation. In his opinion, this concept was absurd.

- Julius Robert Oppenheimer (1904–1967) and Hartland Snyder (1913–1962) published in 1939 a paper that exposed the relativistic gravitational collapse of a homogeneous pressureless fluid sphere [Opp39a]. This first calculation showed that in the collapsed object is shilded by an **event horizon** (compare Sec. 2.3) that formed in the collapse.

- In the same year, 1939, Oppenheimer and George Michael Volkoff (1914–2000) posed the basic relativistic equations for a neutron star [Opp39b]. The authors referred to the analytical approach of Richard Chase Tolman (1881–1948) [Tol39]. The set of equations is nowadays known as Tolman–Oppenheimer–Volkoff equations (**TOV equations**) and fundamental in the theory of relativistic stars.

- In 1956, the relativist Wolfgang Rindler proposes the notion and definition of a **horizon** [Rin56].

- In 1958, David Finkelstein invented a coordinate frame that removes the Schwarzschild coordinate singularity at the Schwarzschild radius [Fin58]. This frame is known

as **Eddington–Finkelstein coordinates** because also Eddington contributed to that in earlier times.

- The Newzealand mathematician Roy Patrick Kerr (* 1934) found in 1963 the generalization of the static and spherically symmetric Schwarzschild solution to a stationary and axisymmetric space–time [Ker63]. The **Kerr solution** (see also Sec. 2.2) describes rotating black holes.

- The British mathematician and relativist Roger Penrose speculated about intrinsical singularities in black holes. 1965 he published a paper about **gravitational collapse and singularities** [Pen65]. In the following years, Penrose and Stephen W. Hawking (* 1942) developed the **singularity theorems** [Hawk69]. These theorems prove the *mathematical* existence of singularities.

- The most general form of a black hole was discovered in 1965 by Ezra T. Newman, E. Couch, K. Chinnapared, A. Exton, A. Prakash and R. Torrence [New65]. This **Kerr–Newman solution** has the maximal set of parameters: mass, angular momentum and electric charge.

- In 1967, R. H. Boyer and R. W. Lindquist found the standard coordinate frame for Kerr black holes, the **Boyer–Lindquist form** as presented in Eq. (2.5).

- The relativist and astronomer John Archibald Wheeler (* 1911) invented in 1967 **the term "black hole"** [Tho94]. Since then, people world–wide used this famous expression.[2]

- Wheeler also invented the **no–hair theorem** [Tho94]. This theorem states that black holes have very few properties. In the maximal case there are mass, angular momentum and charge determining the Kerr–Newman black hole. Wheeler paraphrased: "*A black hole has no hair.*" In this context *hair* has to be interpreted as anything that might stick out of the black hole that gives an information about its formation history. The no–hair theorem was proven by Werner Israel in 1967 (Israel theorem).

- Penrose discovered in 1969 the **cosmic censorship conjectrue** [Pen69]. According to that hypothesis any intrinsical singularity is hidden from an event horizon. *Naked singularities* are forbidden.

- In 1970, James Bardeen devised a suitable observer frame to study the physics of rotating black holes, the **locally non–rotating frame**, **LNRF** [Bar70]. In modern language, an observer in the LNRF (*Bardeen observer*) is called the **ZAMO**, a zero angular momentum observer. ZAMOs corotate with the space–time so that local effects caused by frame–dragging are essentially removed. However, as viewed from infinity the ZAMO rotates with the frame–dragging frequency.

[2] Before that time, scientists used the notion singularity or collapsed star instead of black hole. 51 years after the discovery of the first black hole solution, black holes obtained their name.

- The relativists J.M. Cohen and Robert M. Wald (* 1947) described electric point charges in the vicinity of black holes [Coh71]. In the year 1974, Wald discovered a new solution of Einstein's equations. The **Wald solution** represents a rotating black hole that is immersed in a uniform magnetic field [Wal74]. Therefore, it is a non–vacuum black hole solution.

- After a long purely theoretical treatment of black holes, the Canadian astronomer Tom Bolton identified in 1971 the **first candidate object** for a black hole in nature: the X–ray source Cyg X–1 [Bol72]. This X–ray binary consists of a normal star and a stellar black hole of about ten solar masses.

- Hawking et al. discovered in the early seventies that the black hole horizon increases via accretion or black hole merging scenarios [Bar73]. A **thermodynamical analogue** in black hole physics was found.

- In 1974, Hawking considered quantum effects in black hole physics [Hawk75]. He described a quantum scalar field on the background of the (non–quantized) curved space–time. He found that there are non–vanishing expectation values and concluded that black holes are not absolutely black! Black holes can emit particles that originate from the horizon region, the **Hawking radiation**.
  Due to the Hawking effect black holes can decay via emission of particles. A detailed calculation shows that especially light black holes e.g. primordial black holes can decay on short time scales via emission of Hawking radiation. Until today, Hawking radiation was not confirmed experimentally.

- William G. Unruh revisited evaporation of black holes in 1975 [Unr76]. Later, Unruh and Wald discovered in 1984 the counterpart of Hawking radiation in flat space–times [Unr84]. According to the **Unruh effect**, an accelerated observer moving in the Minkowski vacuum will detect *acceleration radiation*. Hawking radiation and acceleration radiation are related effects due to the equivalence principle.

- In the mid–eighties, the theorists Abhay Ashtekar and Amitaba Sen worked out an **alternative formulation of GR** with new variables [Sen82, Ash86, Ash87].

- In the same year, 1986, Ted Jacobson and Lee Smolin reformulated the Wheeler–DeWitt equation in these new so–called *Ashtekar variables* [Jac87, Jac88]. They found a class of exact solutions, the **Wilson loops**. These loops give the name for the **loop quantum gravity** (LQG). LQG is a theory that unifies the concepts of GR and quantum mechanics. The loop theory permits new insights in the nature of gravitation, cosmology and black hole physics. But LQG must prove to be a powerful theory to describe nature.

- In 1990, the optical space–telescope *Hubble*, HST, was deployed in space. In 1994, astronomers found evidence for a **supermassive black hole** harboring in the AGN M87.

- In the same year, 1990, I. Antoniadis at CERN revived the Kaluza–Klein theory and the idea of an **extra dimension** in perturbative string theories [Ant90].

- In 1997, Ashtekar and Jerzy Lewandowski developed a non–perturbative approach to quantum gravity. They introduced self-adjoint operators corresponding to areas of 2–surfaces, the **area operators** [Ash97]. It turned out that quantum geometry is *not continuous* than rather granular. The formalism is later extended to volume operators. Due to this theory the grains of space–time are volume quanta that have a size of the cube of the Planck length, $10^{-99}\,\mathrm{cm}^3$.

- The speculations about the **formation of mini black holes** in terrestrial particle accelerators became more substantial in 1999. On the basis of the ADD scenario the Planck scale ($\approx\ 10^{19}$ GeV) is reduced to the electroweak scale (≈ 1 TeV) [Ark98]. A reduced Planck scale is supposed to permit the creation of **TeV black holes** in modern particle accelerators.

- In the new millennium, G. Chapline, E. Hohlfeld, R.B. Laughlin and D.I. Santiago proposed that a black hole event horizon is a **quantum phase transition** of a vacuum state of space–time to a Bose–Einstein condensate state of gravity [Cha03]. The metric inside the horizon is different from classical GR and suggested to be de Sitter space. Therefore, the notion of **Schwarzschild–de Sitter interfaces** was born.

- In 2000, there were first indications for the existence of **mid–mass black holes**. Astronomers found with the X–ray space observatory *Chandra* a 500 $\mathrm{M}_\odot$ mass black hole [Kaa00]. It harbors off the center of the star burst galaxy M82. The interesting aspect of mid–mass black holes is that they close the mass gap between stellar and supermassive black holes.

- The hypothesis of the existence of massive black holes with 10^3 to 10^5 $\mathrm{M}_\odot$ was strengthened by HST observations in 2002. Astronomers found weak evidence for intermediate–mass black holes that may be located in the dynamical centers of **globular clusters**. One candidate object is a globular cluster in the Milky Way, M15, that may harbor a central black hole of 4000 $\mathrm{M}_\odot$ [vdM02, Ger02]. Another candidate is G1, a globular cluster in the Andromeda galaxy. The dark central mass is kinematically measured to 20000 $\mathrm{M}_\odot$ [Geb02].

- A new static solution of Einstein's field equations of GR was proposed [Maz01, Maz01]. The **gravastar** consists of a dark energy core. This "de Sitter bubble" supports a thin matter shell by negative pressure. The exterior metric is identical to the Schwarzschild solution. Gravastars have fascinating features: there is no intrinsical singularity, no horizon, and they possess a global time (see also Sec. 3.6).

- In 2002, Asthtekar and Badri Krishnan invented a new notion of horizon: the **dynamical horizon** [Ash02]. They argued that the classical apparent horizon

has a non–local character. In simulations, e.g. merging scenarios of two neutron stars, a *local* notion of a horizon is needed to decide whether a horizon has formed or not.

- Also **dwarf galaxies** became favored to have central massive black holes. There are two examples for dwarf galaxies with a Seyfert core, NGC 4395 and POX 52. The supermassive black hole of NGC 4395 has either a mass of 10^4 to 10^5 $M_\odot$ [Shi03] or maximally 6.2×10^6 $M_\odot$ [Fil03]. POX 52 shows evidence for a central massive black hole with 1.6×10^5 $M_\odot$; this is rather comparable to the putative globular cluster black holes.

- The center of the Milky Way associated with the compact radio source Sgr A* was long before supposed to be a good candidate for a supermassive black hole. In 2003, astronomers detected near–infrared flares with typical durations of tens of seconds using the Very Large Telescope, VLT [Gen03]. If one assumes stable rotation of the flare emitter on circular Keplerian orbits, the **black hole rotates** with a Kerr parameter of $a \simeq 0.52\, M$. The resulting mass determination confirmed other results that the black hole weighs of about three million solar masses. This was the first discovery of black hole rotation!

- Also in 2003, X–ray astronomers also detected flares of Sgr A* with XMM [Por03]. The measurements led to a comparable mass but a much higher black hole rotation, $a \simeq 0.99\, M$, i.e. black hole rotation at its **extreme limit**.

- A spectacular observation was done in 2004: In an elliptical galaxy with $z = 0.05$, $RXJ1242 - 1119$, a X–ray flare was detected that was interpreted as a **tidal disruption event of a star** [Komo04]. The star was disrupted by tidal forces of a nearby supermassive black hole (see Sec. 3.4).

- The interior of the black hole was discussed in the light of brane respective string physics [Mat04]. Mathur argued that behind the horizon there might exist a **fuzzball** that contains information of the black holes progenitor state. Then, the **information loss paradox** would not exist because the interior stringy degrees of freedom can pick up information.

- Another alternative for static black holes was proposed: the **holostar** [Pet03a]. Like gravastars these new solutions are globally regular and have a thin matter surface, but no horizon. The interior of holostars is completely different: Michael Petri adopted Mathur's fuzzball idea that the interior is filled with strings [Pet04]. An anisotropic negative pressure originating from radial strings balances the gravitational collapse forces of the compact object. The negative pressure supports the thin matter shell made of bosons. The exterior metric is identical to Schwarzschild – just as for gravastars (compare Sec. 3.6).

- The latest result of black hole physics concerns the **information loss paradox** [Hawk04]. After three decades where no solution for this paradox was found,

Hawking himself – who formulated the problem in 1975 – solved the problem.[3] Heisenberg's uncertainty principle allows all the information inside the black hole i.e. beyond the event horizon to leak out. Therefore, quantum mechanical information is also preserved in black holes and the information loss paradox is non–existent.

3.2 Mass Scale

The most important parameter of a black hole is its mass, M. From the viewpoint of GR, there are no limits for the black hole mass. As demonstrated in Sec. 2.3 the Schwarzschild radius increases linearly with mass, $R_S \propto M$. Therefore, mass regulates also the size of a black hole as viewed from infinity.
Considering quantum effects and the Planck scale, the Planck mass, M_P, imposes a lower mass limit for classical black holes. At the minimum mass, $M_P = 1.2 \times 10^{19}$ GeV $= 2.14 \times 10^{-5}$ g, quantum theory comes into play and may change classical black hole physics significantly.

Black holes can be devided into certain classes depending on their mass:

- **TeV black holes** with masses around 1 TeV, i.e. $\approx 10^{-21}$ g.
- **Primordial black holes** (PBH) possess masses of $\approx 10^{15}$ g.
- **Stellar black holes** have masses between 1 and 100 $M_\odot$.
- **Massive black holes** (MBH) weigh about 10^2 to 10^6 $M_\odot$.
- **Supermassive black holes** (SMBH) have masses between 10^6 and 10^{10} $M_\odot$.

The terminology for primordial, stellar and supermassive black holes is well established in astrophysics. The expression to denote massive black holes varies: MBHs are also termed as intermediate–mass black holes or mid–mass black holes. TeV black holes are non–conservative and only discussed in a certain branch of high–energy physics.
There are no indications for black holes in the intermediate mass range between primordial and stellar black holes.
The next paragraphs give an overview to each black hole type presented above.

TeV black holes are supposed to emerge in TeV quantum gravity [Cav02, Cav04]. They are also named mini black holes. The vital assumption for their creation is the existence of spatial extra dimensions. String theories and also the Kaluza–Klein theory suggest that there are more spatial dimensions than three. These extra dimensions may be toroidally compactified so that Newtonian physics changes only on small length scales. Experimental analysis restricts the compactification scale to the order of few

[3] ...and lost a wager for the benefit of John Preskill.

microns or Fermis (*ADD scenario*) [Ant90, Ark98]. But also non–compactification with a complicated warping is disussed (*RS brane world scenario*) [Ran99a, Ran99b].
One favored scenario is that the standard model physics is restricted to a hypersurface, the so–called *brane*, whereas gravitons can also propagate into the extra dimensions, the so–called *bulk*. Hence, a number of n extra dimensions should modify the classical Planck scale of 10^{19} GeV: It is reduced to the electroweak scale of 1 TeV. Modern particle accelerators grasp this energy regime. A huge amount of deposited energy density results in a strong curvature of the space–time. Probably this object is a mini black hole. Shortly after the creation of the TeV black hole it is expected that it will decay by emission of Hawking radiation [Hawk75]. The annihilation scenario is outlined as follows [Gid02]: (1) *balding phase* with emission of gravity waves and SM fields; (2) evaporation due to Hawking emission with *spin–down phase* and *Schwarzschild phase*; (3) end of the black hole in the *Planck phase* accompanied by particle emission with reduced Planck scale energies. This decay process is very rapid for tiny black holes: The short life of TeV black holes lasts only 10^{-24} to 10^{-22} seconds. In such a short time, the mini holes have few opportunity to accrete and grow. Therefore, TeV black holes are not dangerous for the Earth and the terrestrial life. It will be interesting to see if these hypothetical particle–like black holes form in modern particle colliders.

Primordial black holes (PBH) were introduced in cosmology. They should have masses comparable to a mountain, $M_{\mathrm{PBH}} \simeq 10^{15}$ g. It is supposed that these light black holes formed in early phases of the universe. The early universe in the post–inflation era provides suited energy and density regimes to form PBHs. Additionally, inhomogeneities are needed that have a characteristic length scale that undergoes the particle horizon at given cosmic time [Bek04]. If the concept of Hawking radiation holds, then PBHs are died out due to evaporation. Hence, their existence in the local universe is excluded. Evaporating PBHs enrich the background of γ–rays in the recombination era. Therefore, the entropy of the cosmic microwave background (CMB) received a contribution from Hawking radiation of annihilating PBHs. PBH searches still failed up to now.

Stellar black holes are formed in gravitational collapses of massive stars. Hence, their mass is comparable to the sun. Stars are nothing else than "plasma balls" in hydrostatic equilibrium. On the one hand, gas pressure, radiation pressure and pressure from centrifugal forces blow up the star; on the other hand gravitational pressure from the star's own weigth compresses it. The hydrostatic equilibrium states that all these forces are balanced at each point in the star's interior. But, when nuclear burning stops this equilibrium is disturbed and gravitation overtops all other kinds of pressure. For sun–like and light progenitor stars the gravitational collapse may be stopped by fermionic degeneracy pressure. But exceeding a critical mass limit, even degeneracy pressure does not stabilize the collapsar: A stellar black hole is formed.
The gravitational collapse of massive stars is naturally accompanied by an explosion. Depending on the mass of the progenitor star, the explosion can be observed as a supernova (type II) with a deposited energy of $E_{\mathrm{SN}} \simeq 10^{51}$ erg or a hypernova (a long–term

GRB) with typically $E_{\mathrm{HN}} \simeq 10^{53}$ erg . Stellar black holes as relics of these explosions can be found in some X–ray binaries, especially in microquasars.

To understand when a stellar black hole is created, the zoo of compact objects (COs) is outlined here. Astrophysicists distinguish white dwarfs, neutron stars, quark stars and stellar black holes. The theory of stellar evolution teaches that the resulting CO type depends mainly on the mass of the progenitor star:

- A sun–like star is rather light if compared to all existing stars. In the red giant phase such stars expand and lose a significant amount of mass from strong stellar winds. This material forms a planetary nebulae in the environment of the red giant. At the end of stellar evolution the core of the red giant collapses to a **white dwarf**. White dwarfs are very hot and show surface temperatures from 20000 to 30000 K. Typically, they have the size of the Earth but a mass comparable to the sun. Nuclear burning had stopped in the white dwarf interior and they are stabilized by the degeneracy pressure of electrons. This Fermi gas balances the gravitational pressure until reaching the Chandrasekhar mass of about 1.46 $\mathrm{M}_{\odot}$ [Cha31a, Cha31b].

- Exceeding this maximum mass the next resulting object in the sequence of compact objects is a **neutron star**. Neutron stars are more compact than white dwarfs. Typical diameters are around 30 kilometers. The core structure of a neutron star is rather complicated but mainly the degeneracy pressure of neutrons stabilizes this CO. The typical mass range of neutron stars is between 1.2 and 1.6 solar masses. If a quark core is also assumed besides the hadronic phases (neutrons, kaons, hyperons), the maximum mass of a neutron star lies between 1.45 and 1.65 solar masses [Bur02].

  Neutron stars are typically formed as relic objects in core–collapse supernova (type II). A massive progenitor star becomes unstable due to the end of nuclear burning: whereas the exterior star shells explode to form the supernova remnant, the interior regions collapse to form a neutron star.
  A *pulsar* is a neutron star where the radiation cone hits occasionally the Earth; a *magnetar* denotes a neutron star with strong magnetic fields. Typical magnetar magnetic fields show strength about 10^{15} to 10^{16} Gauss and exceed the field strength of normal neutron stars by a factor of thousand.

- A new type of compact object is postulated that affiliate to neutron stars. They are called **quark stars** because they are dominantly stabilized by the quark phase. They have comparable masses to neutron stars but are more compact. Typical densities overpower the nuclear density. Then quarks form pairs that is comparable to Cooper pairs of BCS superconduction. This regime of *color superconduction* modifies the equation of state (EOS). However, it is still unclear what is the maximum mass and radius of a quark star. Different methods in quantum chromodynamics (QCD) offer distinct solutions: A perturbative QCD calculation yields 1.32 $\mathrm{M}_{\odot}$ with a radius about seven kilometers; a non–perturbative QCD calculation leads

to a much higher value of 3.2 $M_\odot$; the bag model results in an intermediate mass limit of 1.98 $M_\odot$ at a radius of eleven kilometers.

Neutron stars and quarks stars can nicely be distinguished by the mass–radius relation. Neutron stars follow a $M \propto R^{-3}$ relation but quark stars follow a $M \propto R^{+3}$ law. A candidate for an isolated quark star has already been found: *Chandra* detected RX J185635-3754 with a radius around only 4 to 8 km [Dra02]. This is much to small for a neutron star.

- The CO types discussed hitherto involve that a stellar black hole is strongly indicated by larger masses than approximately 2 to 3 $M_\odot$. If an observation leads to a mass determination in this regime, a **black hole candidate** is discovered. Roughly speaking, a massive stars with tens of solar masses can not prevent to collapse to a stellar black hole.
  Nomenclature follows the rules that such a black hole is called *Galactic Black Hole Candidate* (GBHC) when it is part of the Milky Way. In general, a black hole in a X–ray binary is called *Black Hole X–ray Binary* (BHXB).

Massive black holes (MBH) just fill up the mass gap between stellar and supermassive black holes. Since 2000, this new type was suggested by rotational curves of dwarf galaxies and globular clusters [Kaa00, vdM02, Ger02, Geb02, Shi03, Fil03]. It is an attractive idea that also these clusters of stars harbor central black holes, just as in normal galaxies. The suggestion is the missing link in black hole astrophysics. MBHs are also called mid–mass black holes or intermediate–mass black holes.

Supermassive black holes (SMBH) are the most massive representatives of black holes. They populate with few exceptions all centers of galaxies. A demographic analysis of galactic centers gives the result that 97% of the galaxies harbor massive dark objects (MDOs) [Mag98]. The existence of SMBHs is vital for the physics of AGN. Rotating SMBHs play the keyrole in the AGN paradigm: The activity of the galactic nucleus of Seyfert galaxies, quasars, blazars and radio galaxies can be modeled with accretion onto a huge black hole. Especially relativistic directed outflows, the jets, are generated due to the magnetic interaction of accretion flow and Kerr black hole. This model is outlined in Sec. 4.4 and 5.9 in more detail.

The mass range of SMBHs starts at 10^6 $M_\odot$ and ends at 10^{10} $M_\odot$. The most massive black holes are found in high–redshift quasars using empirical relationships between BLR size and source luminosity [Net03]. In some cases, huge masses were verified in very tiny regions of space. Amazingly, a deep look at this region reveals darkness so that only a supermassive black hole fits in.

Assuming the Schwarzschild solution, the mass range just mentioned before corresponds to a size of the solar system: Since the Schwarzschild radius satisfies $R_\mathrm{S} = 2\ r_\mathrm{g} = 2\ GM/c^2$, the size can be estimated to 0.01 respective 100 AU. Compared to the typical diameter of a galaxy, 10^5 ly $\simeq$ 10^{10} AU, this innermost dark center is really tiny.

3.3 Observational Evidence

The history of black holes demonstrated that they were found first as pure relativistic objects. Soon after this theoretical discovery speculations had arosen whether black hole solutions also exist in nature. Compact objects are such dense that due to gravitational redshift any emission is redshifted and becomes fainter with increasing compactness. Assuming a slowly rotating CO with mass M_* and surface r_*, the redshift z follows from GR to be

$$z\left(r\right) = \frac{\Delta\lambda}{\lambda_*} = \frac{1-\alpha\left(r\right)}{\alpha\left(r\right)} = \sqrt{1-\frac{2GM_*}{c^2 r}}^{-1} - 1. \tag{3.1}$$

The dimensionless quantity $\mathcal{C}_{\mathrm{CO}} \equiv GM_*/(c^2 r_*)$ is a suited parameter to measure compactness. White dwarfs ($r_* \simeq 5000$ km) at the Chandrasekhar limit satisfy $\mathcal{C}_{\mathrm{WD}} \simeq 0.0004$, neutron stars hold $\mathcal{C}_{\mathrm{NS}} \simeq 0.16$, quark stars may have $\mathcal{C}_{\mathrm{QS}} \simeq 0.37$, stellar Schwarzschild black holes[4] hold $\mathcal{C}_{\mathrm{SBH}} = 0.5$ whereas stellar extreme Kerr black holes satisfy $\mathcal{C}_{\mathrm{KBH}} = 1.0$. Of course, the last part of Eq. (3.1) does not hold for fast rotating COs like neutron stars and Kerr black holes. GR provides adequate relations for these objects, too (for KBH see Eq. (2.6) in Sec. 2.2).
This discussion proves that Kerr black holes are extremely compact: Their event horizon, see Sec. 2.3, suppresses any emission for an observer resulting in a complete darkness.

But how can astronomers observe black objects at the dark night sky? Naively, it seems hopeless that there is any chance to detect such an object. However, there are a couple of techniques – both, indirect and direct verification methods – that are presented and classified with a suited nomenclature in Sec. 3.4.
The smoking gun for the existence of a black hole candidate is the observational result that a huge mass harbors in a tiny region of space. If astronomers additionally confirm a very dim emission, black holes are favored to be there. Certainly, other "darkening effects" for the emission must be excluded e.g. extinction by dust. In observers language the a black hole candidate is called **compact dark object** (CDO) – sometimes also the term massive dark object (MDO) is used.

The first cosmic source that was associated with a (stellar) black hole was the X–ray source Cyg X–1 as anticipated in the historical overview in Sec. 3.1. The binary system consists of a blue giant star of about 30 $\mathrm{M}_\odot$ and a stellar black hole of about 10 $\mathrm{M}_\odot$. Due to the large companion star, Cyg X–1 is classified as high–mass X–ray binary (HMXB). Binary systems offer the advantage that orbital parameters can be deduced by using Keplerian laws. Therefore, the masses of the components follow from dynamical measurements. The compact component with 10 solar masses can only be modeled by a black hole (compare discussion in the former section). In a standard stellar model, it was created in gravitational collapse of a massive star or by merging of stars.
There are many other candidate objects for stellar black holes: Another GBHC is XTE J1118+480 which was detected with *Rossi X–ray Timing Explorer* (RXTE) in 2000. It

[4]For black holes the outer horizon radius is considered as surface radius.

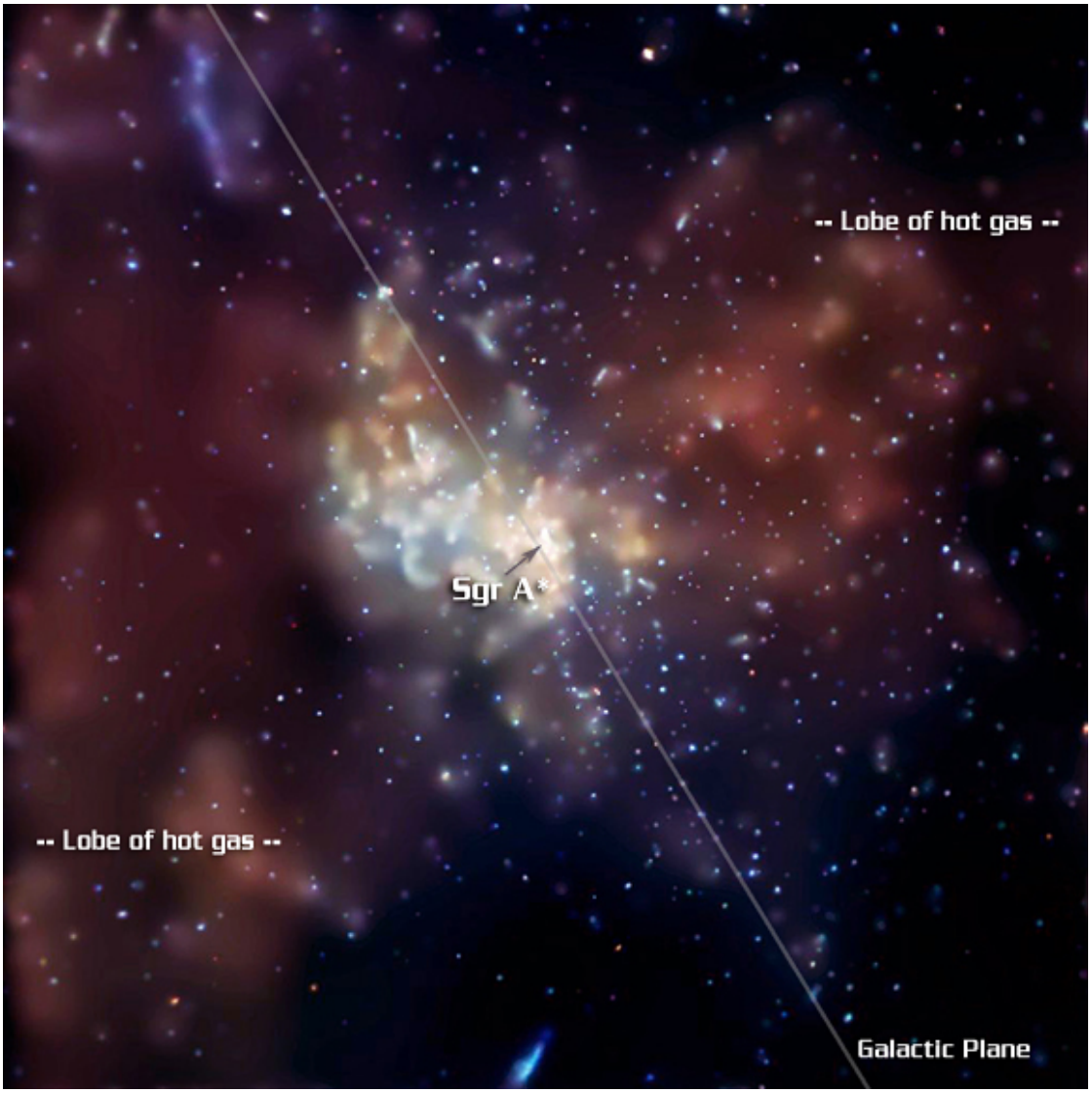

Figure 3.1: Chandra image of Sgr A* region, 8.4'×8.4', taken in the energy bands 2.0−3.3 keV (*red*), 3.3 − 4.7 keV (*green*) and 4.7 − 8.0 keV (*blue*). The supermassive black hole of about 3 million $M_\odot$ is associated with the bright central point source. The black hole is starving maybe due to explosions that cleared the Sgr A* environment from gas. The red lobes extended a few tens light years on the lower left and upper right side are possibly relics of these explosions. (Credit: NASA/CXC/MIT/F.K.Baganoff et al., January 2003)

turns out that XTE J1118+480 is actually the **nearest stellar black hole to Earth**: The distance amounts to 1.8 kpc [Wag01]. The black hole mass was determined to be

between 6.0 to 7.7 $M_\odot$. The companion star is not very massive. Hence, XTE J1118+480 belongs to the low–mass X–ray binaries (LMXB). The X–ray emission in the low–hard state can be sucessfully modelled by external Compton scattering (ECS) i.e. ambient accretion flow emission is Comptonized in a relativistic jet plasma [Geo02]. In other cases the emission of the companion star may serve as ECS input.

XTE J1650-500 is another BHXB which was identified as a black hole with mass of about four solar masses or maximally 7.3 solar masses [Oro04]. The source XTE J1720-318 is yet another candidate for a black hole of approximately five solar masses [Cad04]. Very massive stars like Wolf–Rayet stars with tens of solar masses and the "superstar" Eta Carinae with about hundred solar masses are good candidates to form a black hole at the end of their stellar life. Astronomers hope to witness the formation of a stellar black hole in the near future – just as they did in detecting neutron stars that form in supernova explosions of type II e.g. the Crab pulsar.

Since 2000, several **MBH candidates** are found as mentioned in the black hole history overview: A 500 $M_\odot$ black hole in the off–center region of M82 [Kaa00], a 4000 $M_\odot$ black hole in the globular cluster in M15 [vdM02, Ger02], a 20000 $M_\odot$ black hole in the globular cluster in G1 [Geb02], a 10^4 to 10^6 $M_\odot$ black hole in the dwarf galaxy NGC 4395 [Shi03, Fil03] and a 10^5 $M_\odot$ black hole in the dwarf galaxy POX 52 – just to name a few. However, there is an ongoing debate whether this intermediate–mass black holes really exist and about how they could form in globular clusters and dwarf galaxies.

Today, it is possible to look at these tiny regions with modern telescope techniques. Especially in case of the **Galactic Center** in a distance of 8 kpc X–ray, infrared and radio astronomers are able to study the vicinity of the center of our galaxy, see Fig. 3.1. Unfortunately, the view with optical telescopes is blocked by dust in the galactic plane. But nevertheless, the evidence is strong that a **rotating supermassive black hole** is hidden at the Galactic Center. The locus is associated with the bright and compact radio source Sgr A*. Astronomers succeeded in identifying flares in the vicinity of Sgr A* that last a few tens of seconds [Gen03, Por03]. These flares indicate unambiguously – if stable rotation on Keplerian circular orbits (ISCO) of the flare emitter is assumed – that the black hole rotates. Alternatives to the black hole such as a fermion ball or boson stars are excluded.

However, the prominent place of a supermassive black hole is the center of AGN. According to the AGN paradigm the high AGN luminosity is produced by accretion onto a SMBH. We will have a close look onto the underlying physics in the next chapter. Seyfert galaxies are rather faint AGN: Typical luminosities range from 10^{11} to 10^{12} $L_\odot$. Quasars exceed this Seyfert luminosities by a factor of hundred, $L_{QSO} \approx 10^{14}$ $L_\odot$.

Astronomers analysed the nucleus of the Seyfert galaxy type II, NGC 4258 [Pie02]. They surveyed the water maser emission of rotating gas. According to these dynamical measurements, they found 36 million solar masses for the innermost 0.13 pc.

Another Seyfert II galaxy, NGC 5252 (Hubble type S0), with a redshift of $z = 0.023$ was examined. Astronomers fitted the rotation velocity curves of interstellar gas and stars and deduced a supermassive black hole of 9.5×10^8 solar masses [Mac04].

The radio galaxy Cyg A at $z = 0.056$ is a classical double radio source, see Fig. 3.2. As a radio–loud AGN it exhibits two relativistic jets with typical velocities around $0.5c$.

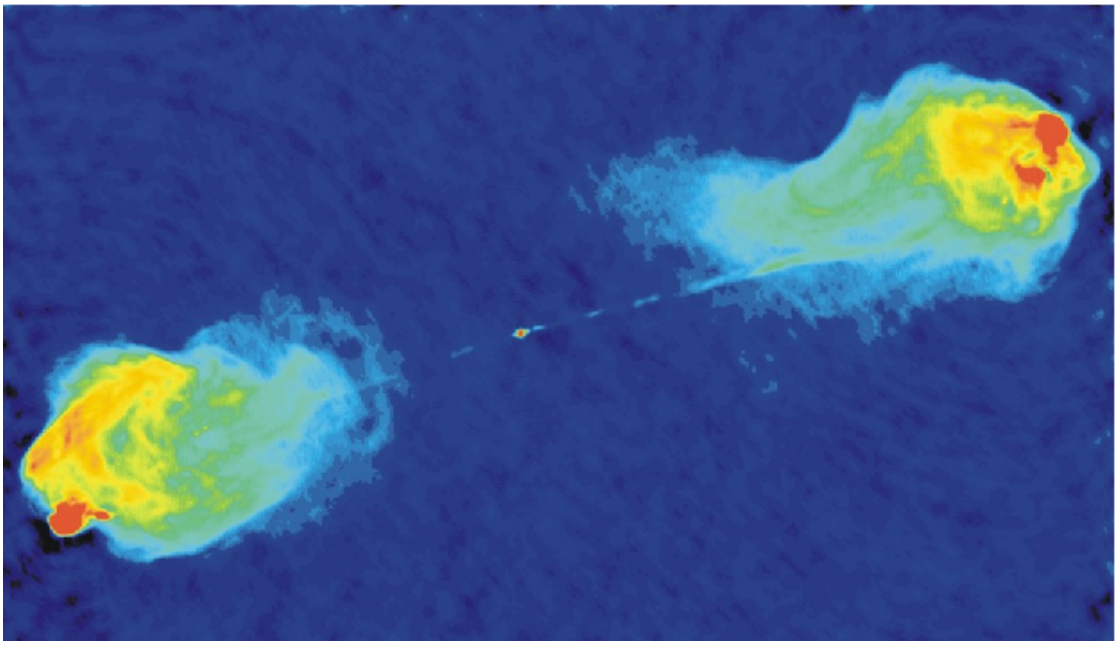

Figure 3.2: False color VLA radio image of the radio galaxy Cyg A, 2.3'×1.3', taken in the C band at 6 cm wavelength. The compact radio source in the center, the double radio jets and the extended radio lobes are clearly seen. Color–coded is the intensity: red shows brightest and blue fainter radio emission. (Credit: NRAO/AUI, Perley et al., February 1983)

The mass of the supermassive black hole in the center was determined to 2.5×10^9 $M_\odot$ [Tad03]. The bolometric luminosity is enormous: $L_B \simeq 10^{46}$ erg/s is comparable with the lower edge luminosity of quasars.

The giant elliptical (E1) M87 is the central galaxy of the Virgo supercluster in a distance 16 Mpc. In fact, this was the first candidate for a central supermassive black hole. It is the most giant black hole: 3.2×10^9 $M_\odot$ [Mac97].

3.4 Detection Methods

The identification of black hole candidates can be done astronomically by a couple of methods. After having identified a black hole candidate, astronomers are particularly interested to determine parameters of the black hole and its surroundings. Parameters of interest are black hole mass, M, black hole spin, a, inclination angle of the black hole's rotational axis to the observer, i, and accretion rate, $\dot{M}_{\rm acc}$. Later, in Ch. 5, it will turn out to be important to exactly know this parameter set. Therefore, a closer look to observational techniques is advised. A synoptical look onto the last three decades

suggests a terminology for all available black hole detection techniques. In the present work the following classification and terminology is proposed:

- kinematical verification,
- spectro–relativistic verification,
- eruptive verification,
- accretive verification,
- aberrative verification,
- obscurative verification,
- gravitational wave–induced verification.

These methods and their classification are presented now in some detail.

Kinematical method is so far most important and a widely–used method. Dynamical objects in the environment of the black hole serve as indicators for a dark mass. There are a number of variants that can be classified as kinematical method.
The simplest form is to use **Keplerian laws** which describe the motion in the deep gravitational potential of a black hole. In a sufficiently high distance the classical Keplerian laws of Newtonian physics apply; if the motion approaches the black hole, GR effects come into play. Then, the full relativistic equations are used. The Keplerian angular frequency around a Kerr black hole satisfies Eq. (2.16). The orbiting objects can be stars, gas clouds, gas or flare emitters. Stars can be used as an individual objects that are monitored e.g. $S1$ and $S2$ in case of Sgr A* [Ott03]. But stars can also be treated statistically in an ensemble. The relevant quantity to discuss is the so–called *velocity dispersion* σ. Astronomers build up a dynamical model for galactic nuclei. The observed brightness distribution is fitted to an assumed mass density distribution considering mass–luminosity relations from theory. Slit spectroscopy over the galactic nucleus gives σ in units of km/s. Unfortunately, observers use distinct definitions for σ: once it is taken at the effective radius, r_{eff},[5]; then the root–mean–square dispersion is evaluated for radii smaller than $r_{\mathrm{eff}}/8$. When CDO masses are alternatively determined (e.g. by reverberation mapping, see below) and plottet versus the observed velocity dispersion σ, one concludes an interesting result: the black hole mass, M, is correlated to σ. The **M–σ relation** can be noted as a log–linear relation [Tre02].

$$\log(M/\mathrm{M}_\odot) = \alpha + \beta \log(\sigma/\sigma_0), \tag{3.2}$$

with a suited reference value chosen to $\sigma_0 = 200$ km/s.
The slope β is estimated to 4.0 ± 0.3 [Tre02]. This undershoots significantly first results of $\beta = 5.27 \pm 0.4$ [Fer00] and $\beta = 3.75 \pm 0.3$ [Geb00]. Since then the measurements

[5] radius where surface brightness drops down to the half.

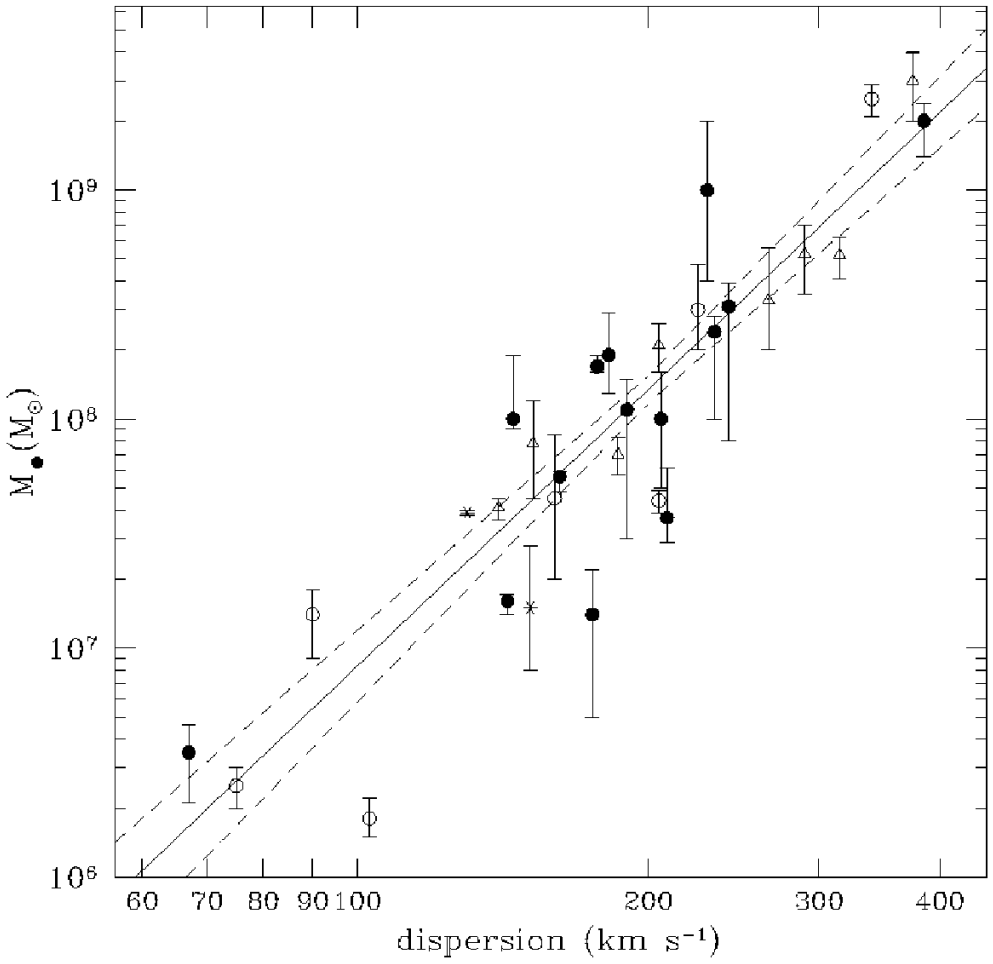

Figure 3.3: Plotting measured black hole mass M vs. velocity dispersion σ in a double–logarithmic fashion gives a correlation known as the M-σ relation. Current measurements hint for a scaling law $M \propto \sigma^4$. (Credit: [Tre02])

were finetuned and the σ's converge to a discrepancy of approximately 1.4 standard deviations. Theoretical models reproduce this observed M–σ scaling [Ada00]. Here, the initial state is a slowly rotating isothermal sphere that collapses to a supermassive black hole. But also galaxy merger scenarios reproduce the M–σ relation [Häh00]. Therefore, this scaling law can be used to estimate masses of supermassive black holes in galactic nuclei only by measuring the velocity dispersion σ, because $M \propto \sigma^4$.
Fig. 3.3 illustrates the M-σ relation which has been observed from a couple of sources.

Another kinematical method was already mentioned: **reverberation mapping**. As-

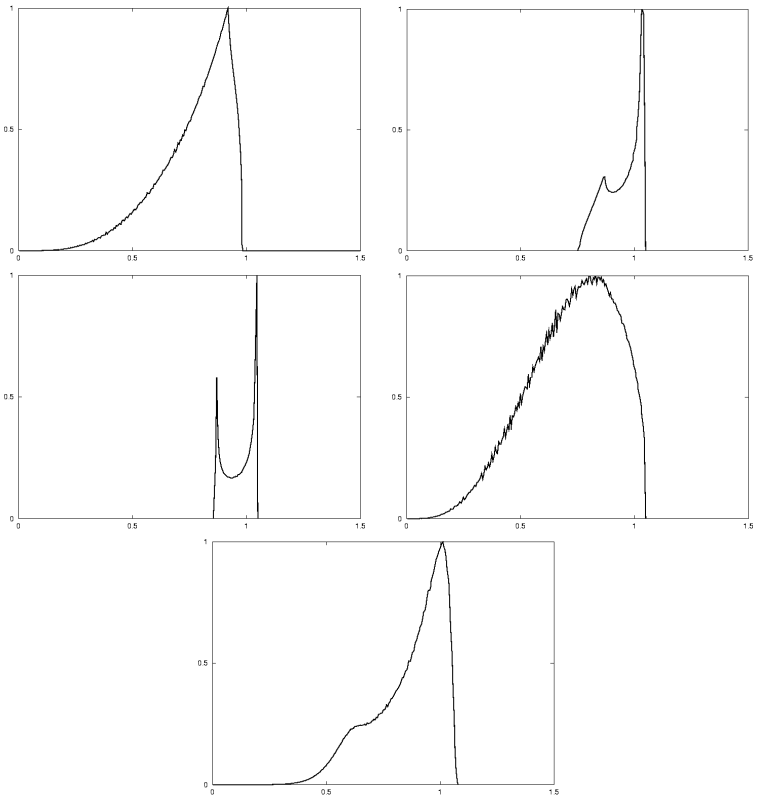

Figure 3.4: A selection of simulated relativistic emission line profiles. The line flux in arbitrary normalized units is plotted over the g-factor. $g = 1$ indicates the rest frame line. The line shapes are classified by morphology. From top left clockwise it is: triangular, double–horned, bumpy, shoulder–like and double–peaked.

tronomers utilize infalling gas clouds that are especially visible for AGN type 1, i.e. low–inclined nuclear disks. They are called *broad line regions* (BLRs) because emission lines from these clouds are significantly Doppler–broadened. The broadening is a tracer for the motion of the BLRs. BLRs are parametrized by their cloud velocity and their distance to the central black hole.
The reverberation mapping technique is based on differences in light crossing times: Astronomers detect direct radiation from the primary source, usually the AGN. With a time lag, indirect radiation hits the observer after being reflected by the BLR. This principle serves as a mapping of the BLR geometry. The dark central mass is one parameter that can be extracted by reverberation mapping.

Maser emission of galactic gas is an alternative dynamical indicator for central masses. The coherent microwave radiation of water located as 'maser clumps' in a dusty torus or molecular disk on the pc–scale was used to determine the SMBH mass of the

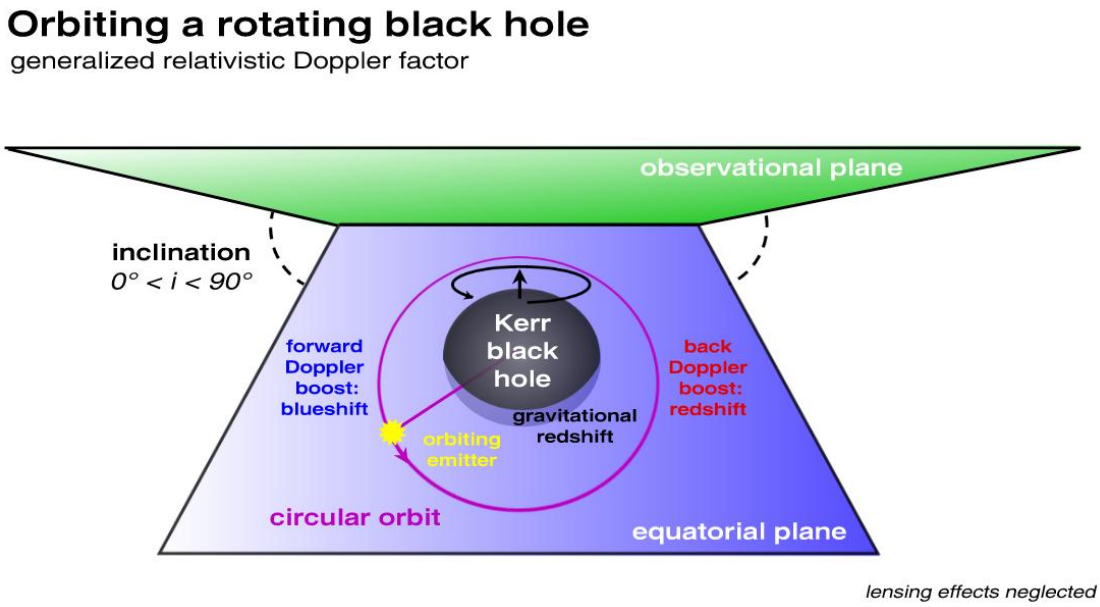

Figure 3.5: Illustration of an emitter circulating a black hole on a circular Keplerian orbit. The observer is assumed to look at intermediate inclination onto the orbital plane. The nearness to the black hole's horizon causes relativistic modulations of the intrinsic emission spectrum: Beaming and back beaming provoke periodical flickering of the orbiting source. Gravitational redshift dims the emission. The time–dependence of an intrinsic light curve is disturbed by time dilation effects. All these effects are contained in the generalized fully relativistic Doppler factor (g-factor).

Seyfert–2 NGC 4258 [Pie02] and also for NGC 3079 [Kon04]. The emission of rotating gas shows nicely the segregation in redshifted and blueshifted peaks.

Spectro–relativistic methods is a generic term for black hole detection methods that involve spectra that are influenced by GR effects. One prominent example is the relativistic broadening of X–ray emission lines such as Fe Kα line around 6.4 keV (see example profiles in Fig. 3.4). The relativistic iron emission line was first observed with the Japanese X–ray observatory ASCA at the Seyfert–1 MCG–6–30–15 [Tan95].

The Fe Kα X–ray emission line is the dominant line generated by fluorescence. It can be observed at some AGN like Seyferts and quasars type 1 but also in microquasars and X–ray binaries. Primary hard X–ray photons originating from a hot corona hit the cold optically thick standard accretion disk. This process results in a reflection bump around 20 keV in the X–ray spectrum (see also Sec. 4.1). Some Kα lines are produced at rest frame energies between 6 and 7 keV; they are part of the reflection bump. The particular feature is that relativity has certain imprints on this emission line profile due

to the proximity to the black hole. Let us assume that line emitting gas circulates stably the hole. Then the classical Doppler effect separates the rest frame line into two peaks. Additionally special relativistic beaming amplifies the blue wing of the line whereas backbeaming suppresses the red wing of the line. A further effect is of general relativistic nature, the gravitational redshift: line photons are "braked" or even trapped by the strongly curved space–time. Fig. 3.5 sketches all these effects.
The result of classical Doppler effect and relativistic effects is a broad, disturbed and asymmetric X–ray line profile. These line profile can have very different shapes. The zoo of simulated relativistic line shapes was classified into triangular, double–horned, double–peaked, bumpy and shoulder–like profiles [Mül04]. Fig. 3.4 gives an overview for typical representatives of this terminology. Details of ray tracing will be treated in Ch. 6.

X–ray astronomers try to extract the line profile from global spectra (see later Fig. 4.3). Typically, the X–ray continuum is superimposed to the emission line and must be substracted. This procedure is not straight–forward and poses some uncertainties onto the line profile. Unfortunately, the parameter space that influences the line shape is rather huge. The conclusion of theoretical studies is that the most relevant parameter is the inclination angle if line emission of flat standard accretion disks is assumed. The Kerr parameter a seems to have few influence on the line profile [Mül00]. This is especially the case when truncated standard disks (TSD) are considered. Then, the argument does not hold anymore that the Kerr parameter controls the inner disk edge, conservatively associated with the ISCO.
Another uncertainty is the radial emissivity profile. Standard accretion theory suggests a power law [Nov74, Pag74]. But it is not well understood whether other profiles are more realistic. A *cut–power law* with exponential die–out meets the requirements for truncated accretion disks and a *localized emissivity law* with Gaussian shape can be used for line emitting rings [Mül04]. A model for TSDs is later presented in Sec. 6.2.
If a X–ray source displays such a typically strong distorted and broad line profile, then the existence of a black hole is indicated.

Eruptive methods are always associated with a burst–like phenomenon. **Supernovae** (SN) and **hypernovae** (HN) are such transient eruptions at the sky. In case of an observed supernovae astronomers can not be assured that a black hole formed because also a neutron star or quark star could be the relic object. Therefore, secondary verification methods are required. SN give only a weak hint for the existence of black holes.
For hypernovae the evidence becomes stronger. HN are typically by a factor of 100 more luminous than SN. Astrophysicists believe in a link of long–term GRBs to HN. The higher energy output is released by more massive stars, like Wolf–Rayet stars. These giants of tens of solar masses are strongly favored to produce black holes at the end of their stellar life.
However, in the discussion of supernovae and hypernovae the possibility should not be neglected that the explosion may end up in a total disruption of the progenitor star!
This year, astronomers witnessed a fascinating observation: a **tidal disruption event**

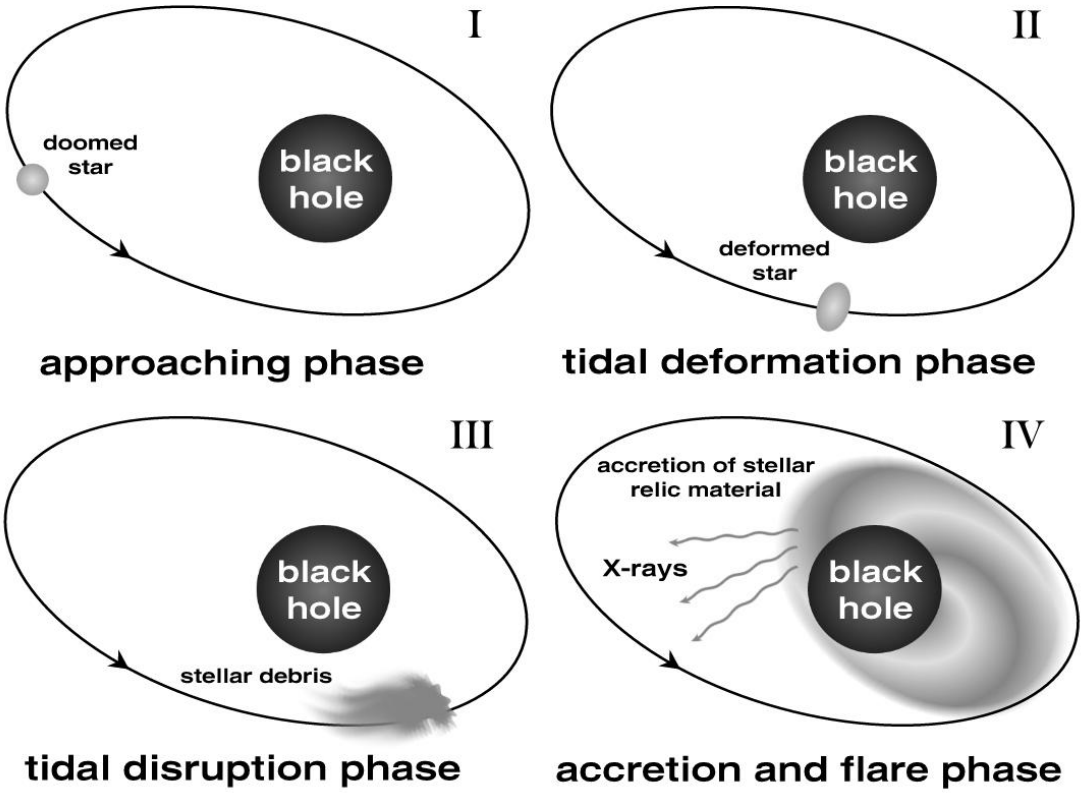

Figure 3.6: Schematic sequence of the tidal disruption event: In (I) the star spirals in and approaches the black hole. In (II) the star is extremely deformed by tidal forces. In (III) the star can not stand the forces and is disrupted. In stage (IV) the stellar relic material is accreted from the black hole and radiates away X–rays.

of a star by a black hole. The principle is that a star approaches too close to a black hole experiencing intensive tidal forces. Tidal forces are volume conserving so that the star is only extremely deformed. By means of Newtonian physics it is possible to define a *tidal radius*. This characteristic radius indicates the distance where the tidal forces overpower the self–gravitation of the star. The tidal radius for a star of mass m_* and radius R_* in the vicinity of a black hole of mass M is defined by

$$R_{\mathrm{T}} = R_* \, (M/m_*)^{1/3} \, . \tag{3.3}$$

Undergoing the tidal radius, the star can not prevent from being disrupted. In case of total disruption, the stellar debris spread over the black hole environment. Parts are

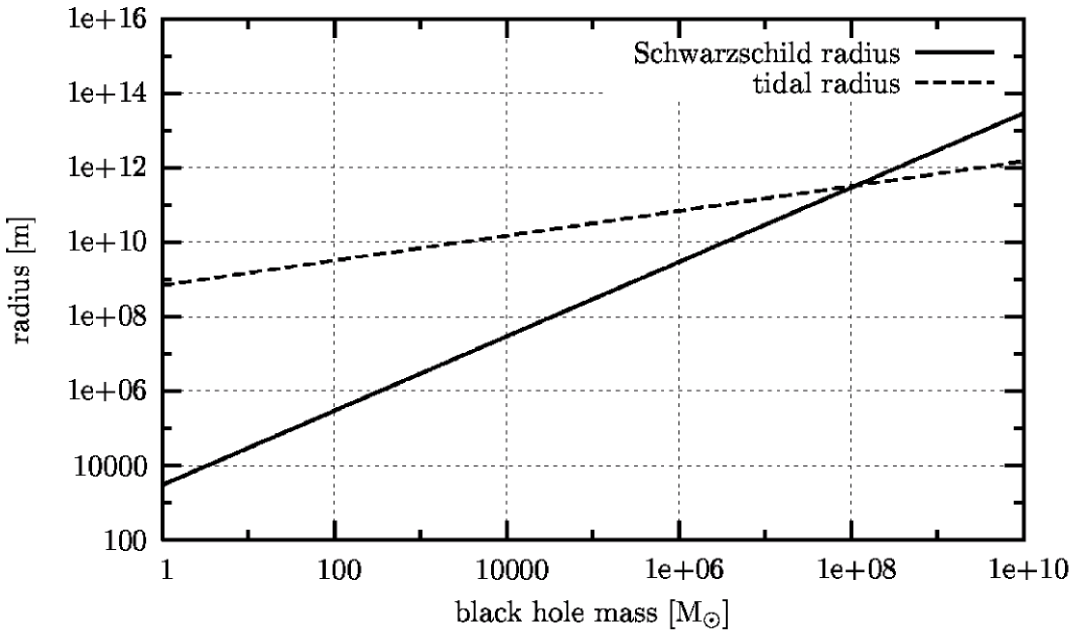

Figure 3.7: Intersection of Schwarzschild and tidal radius. For static black holes heavier than 110 million solar masses a tidal disruption event is hidden behind the event horizon.

being accreted. The local accretion burst causes X–ray flares. This scenario is outlined in Fig. 3.6. Hence, a typical signature of a tidal disruption flare and a huge drop in the post–flare spectrum hints for a black hole.

Indeed, astronomers detected such a tidal disruption flare in the X–ray source RXJ 1242.6-1119A with $z = 0.05$ [Komo04]. The post–flare spectrum dropped down by a factor of 240 and suggested a normal galaxy. This galaxy was illuminated by the flare: the black hole was fed.

It is interesting to plot the Schwarzschild radius versus the tidal radius, assuming a solar–type star ($M_* \simeq \mathrm{M}_\odot$). The result is presented in Fig 3.7. The analysis of the plot shows that not any black hole of arbitrary mass permits the visibility of the X–ray flares: The intersection point of the two lines at $M = 1.1 \times 10^8$ $\mathrm{M}_\odot$ must be interpreted that more massive black holes forbid the detection of a stellar disruption flare. The reason is that the tidal radius lies behind the event horizon radius. SMBHs heavier that 110 million solar masses do not exhibit this event for a star comparable to the sun.

The plot follows simply from this equation:

$$R_\mathrm{T} \quad = \quad R_\odot \, (M_\mathrm{BH}/\mathrm{M}_\odot)^{1/3} \tag{3.4}$$

$$= \quad 1.1\, R_{\mathrm{S}} \times \left(\frac{M_{\mathrm{BH}}}{10^8 \mathrm{M}_\odot} \right)^{-2/3} . \tag{3.5}$$

Tidal disruption event are rare phenomena: The rate for one galaxy was estimated to one event per 10^4 years!

Accretive methods As already mentioned, the AGN paradigm states that the central engine is an accreting supermassive black hole. Accretion causes the enormous luminosity by transforming rest mass energy of infalling matter into radiation. Activity of a galactic nucleus is therefore an unambiguous hint that a supermassive black hole exists. In case of stellar black holes accretion activity emerges as releasing "blobs", some kind of discontinuous jets. Many microquasars shows these outflows in radio observations (Cyg X–3, [Mio01]; GRS1915+105, [Mir94]; SS433, see Fig. 3.8) and and X–ray observations (SS433, [Mig02]). Another observational evidence is that X–ray light curves of some microquasars show nearly periodic features, the so–called **quasi–periodic oscillations** (QPOs). Typically the light curves are analyzed in Fourier space: the resulting power spectra (power density spectra, PDS) exhibit peaks at characteristic frequencies, typically lying in the range of kHz for stellar sources. One favored explanation is that the standard accretion disk undergoes periodic warpings caused by GR effects. This is known as the *Lense–Thirring precession*. In GR there is a nice analogy to electromagnetism, called gravitomagnetism. Due to that theoretical approach angular momenta (gyroscopes) interact with each other. In the case of black hole–disk system the spin of the Kerr black hole interacts with the rotating disk or more generally spoken the rotating flow in its vicinity. A typical consequence of interacting gyroscopes is a periodical precession of the disk. Hence, this motion also emerges in X–ray light curves coming from the disk. A detailed calculation of a typical QPO frequency is elaborated in Sec. 3.5.
Finally one can state that the occurrence of QPOs in X–ray binaries hints for black holes in a microquasar; but a rapidly rotating neutron star is not ruled out. Other techniques than QPOs observations must be added to detect a black hole.

Aberrative methods Mass–energy deflects light. This is a statement that *any* metrical theory of gravitation teaches, not only GR. The framework of GR provides certain techniques to calculate the amount of deflection. In Newtonian physics, light deflection can only be understood by a corpuscular model of light; this led Laplace to the hypothesis that black holes exist.
Gravitational lensing – first predicted by Einstein himself – is of special interest for cosmology. The gravitational arcs, *Einstein rings*, *Einstein crosses* of point sources like quasars reveal compact dark masses located on the line of sight just inbetween terrestrial observer and cosmic source. GR calculations by means of pseudo–Newtonian or post–Newtonian approaches permit to investigate the mass density distribution. Thereby, astronomers detect huge amounts of dark matter harboring in galaxy clusters.
Recently, this phenomenon turned out to be an advantageous tool to detect very distant sources. The weak light of high–z galaxies is magnified by factors between approximately

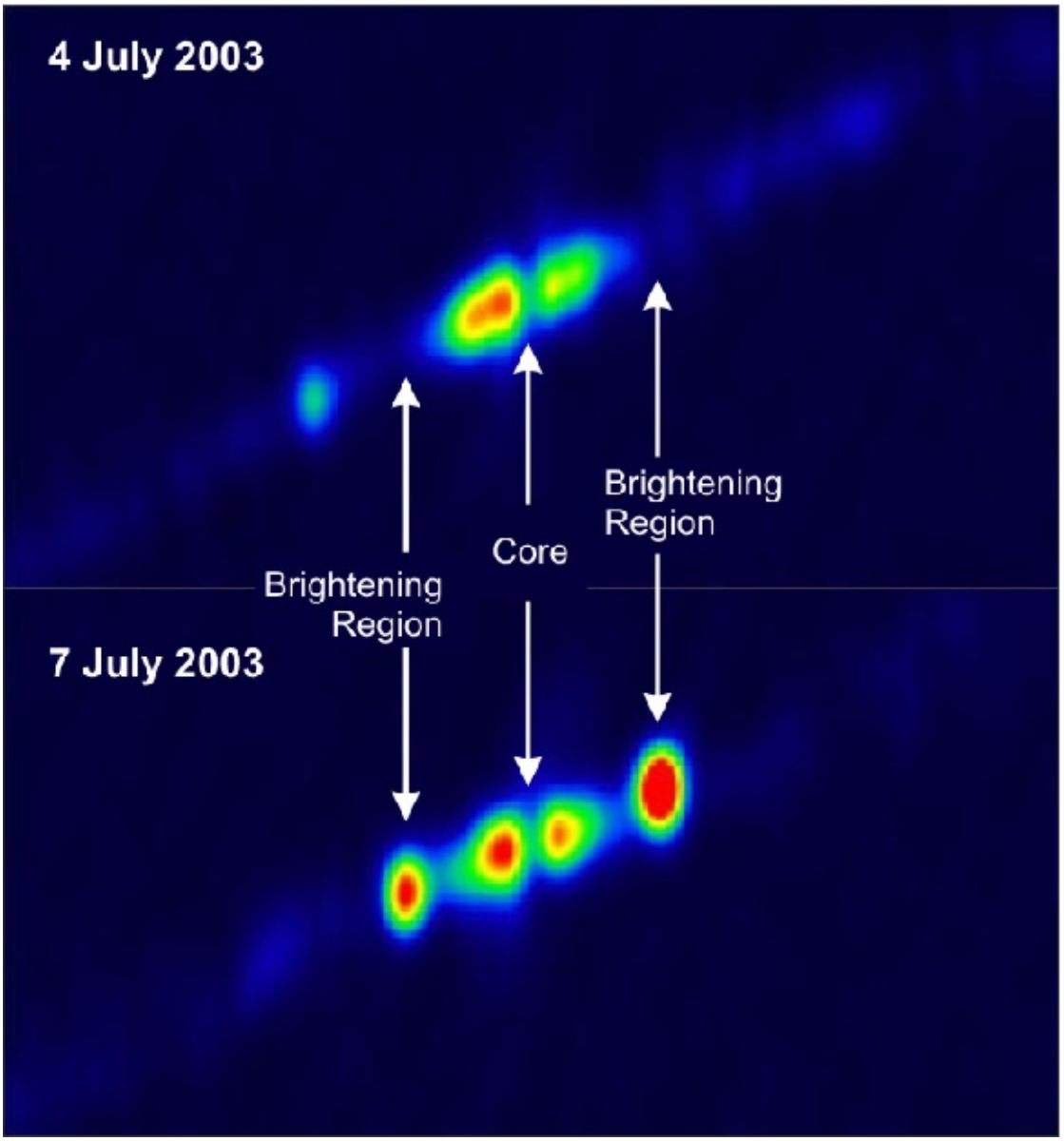

Figure 3.8: Radio image of microquasar SS433 taken at 20 cm wavelength with VLBA (L band). The field has a size of 1'×0.5' and a resolution of 7 mas along the jet axis (35 AU in a distance of 5 kpc). The jet propagates with $c/4$ causing relativistic Doppler effects. The engine of SS433 binary star is probably a stellar black hole. (Credit: NRAO/AUI, Mioduszewski et al. 2003)

10 and 100. Astronomers detect due to this lensing the current distance record starburst galaxy at $z = 10$ [Pel04]!

Considering the lower mass scale for lenses, astronomers screen the galactic halo by **microlensing events**. Stellar objects that move directly in front of a light source provide a symmetric magnification of light curves. This characteristic feature can easily be filtered by observers providing a systematic search for microlenses. In case of the Milky Way, these lenses are called MACHOs, *Massive Compact Halo Objects*. Most likely, MACHOs are brown dwarfs or M–dwarfs i.e. light cool stars that ressemble to planets (e.g. [Gau04]). Microlensing techniques can also be used to discover exoplanets. In general, microlensing hints for dim lenses. The abundance of microlensing events gives an estimate for the amount of baryonic dark matter. This is also of special interest for cosmology because the dark matter content of the universe can be estimated.
Let us now turn to gravitational lensing by black holes: Just like the lenses described above, in principle any black hole – independent of mass – can act as a lens. The effect increases with decreasing impact parameter of light rays. Black holes even allow under some circumstances u–turns of photon paths. Black hole lensing can be visualized by relativistic ray tracing techniques [Mül00]. It is interesting to consider stable circular orbits around a black hole that hold $r > r_{\mathrm{ms}}$. In Newtonian physics these circles appear either circular or elliptical depending on inclination angle of the observer. This is also the case for large orbital distances to a black hole because the space–time is asymptotically flat. But if the orbit approaches the black hole the orbit form changes dramatically: Just like the "galactic phantom images" in cosmology the circles are strongly deformed. Fig. 3.9 shows these situations for tight orbits ranging from 5.5 to 10.0 gravitational radii and for different inclination angles of the orbital plane. A really strange image occurs for nearly edge–on orientations of the orbital plane (lower right). If an astronomer detects such orbital shapes in the vicinity of a black hole candidate he could try to fit three parameters: inclination angle, i, black hole mass, M, and Kerr parameter, a. Supporting techniques other than aberrative methods can help to improve the parameter determination.
It is necessary to state that the resulting orbit forms are only *apparently* that way; intrinsically the orbiter in these rendered examples moves on a circle. Interestingly, the appearance of the "normally" spherical horizon is also deformed at high inclinations.
Hence, observations of such deformed orbits hint for the existence of a black hole. Again, a nice example is Sgr A*. Today, astronomers are able to trace orbits of stars around black holes e.g. the innermost star $S2$ at Sgr A* [Ghe00, Ott03]. These measurements are at least possible in the Milky Way if the orbiter are not too distant[6]. Fig. 3.10 shows the stellar ellipses of the innermost stars orbiting Sgr A*. In 2000, Ghez et al. deduced from these NIR observations with the Keck telescope a supermassive black hole mass of 2.6×10^6 $\mathrm{M}_\odot$.
In the future, astronomers will succeed in tracing orbits in the vicinity of other black holes, too. The challenge is to gain sufficient spatial resolution to observe the orbit form. Another handicap is gravitational redshift that dims the emission of orbiters that lie to close to the hole.
Certainly, this aberrative technique provides a proof to detect inactive black holes i.e.

[6]The Galactic Center is approximately 8 kpc or 26000 ly away.

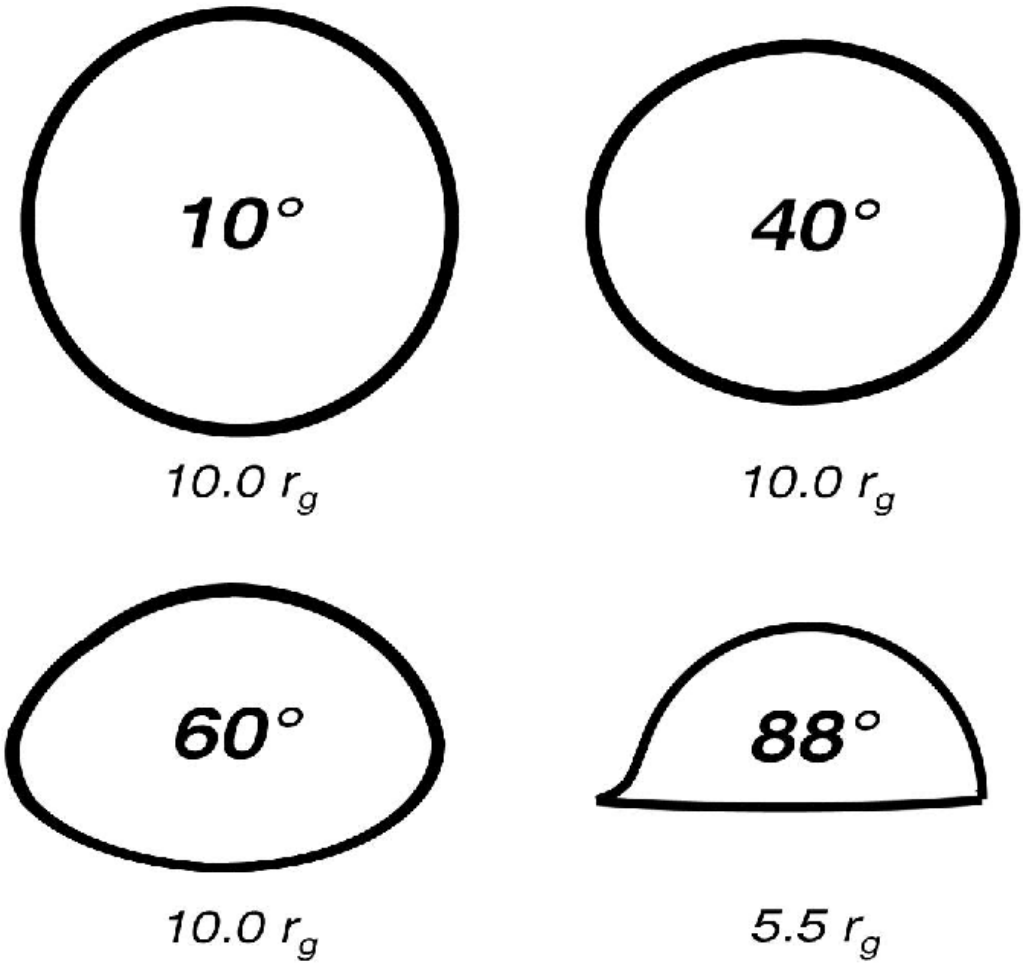

Figure 3.9: Gravitational lensing of tight circular orbits around a Kerr black hole. The black hole is approximately located in the center of each ring. The orbital plane is inclined by the denoted value (in degree) in the center of the ring. The orbital radius is given in units of gravitational radii, $r_{\rm g}$ (below each ring). As could easily expected, the strongest GR lensing effect appears for huge inclination angles and small orbital radii (*lower right image*).

starving black holes that cannot accrete due to an empty environment.

Obscurative methods Now, a detection method is presented that is unique among all others because it opens up a *direct* verification of black holes. The obscurative method is based on the fact that black holes are black. As already demonstrated gravitational redshift decreases down to the horizon, $\alpha_{\rm H} = 0 \;\rightarrow\; g_{\rm H} = 0$. The damping effect becomes

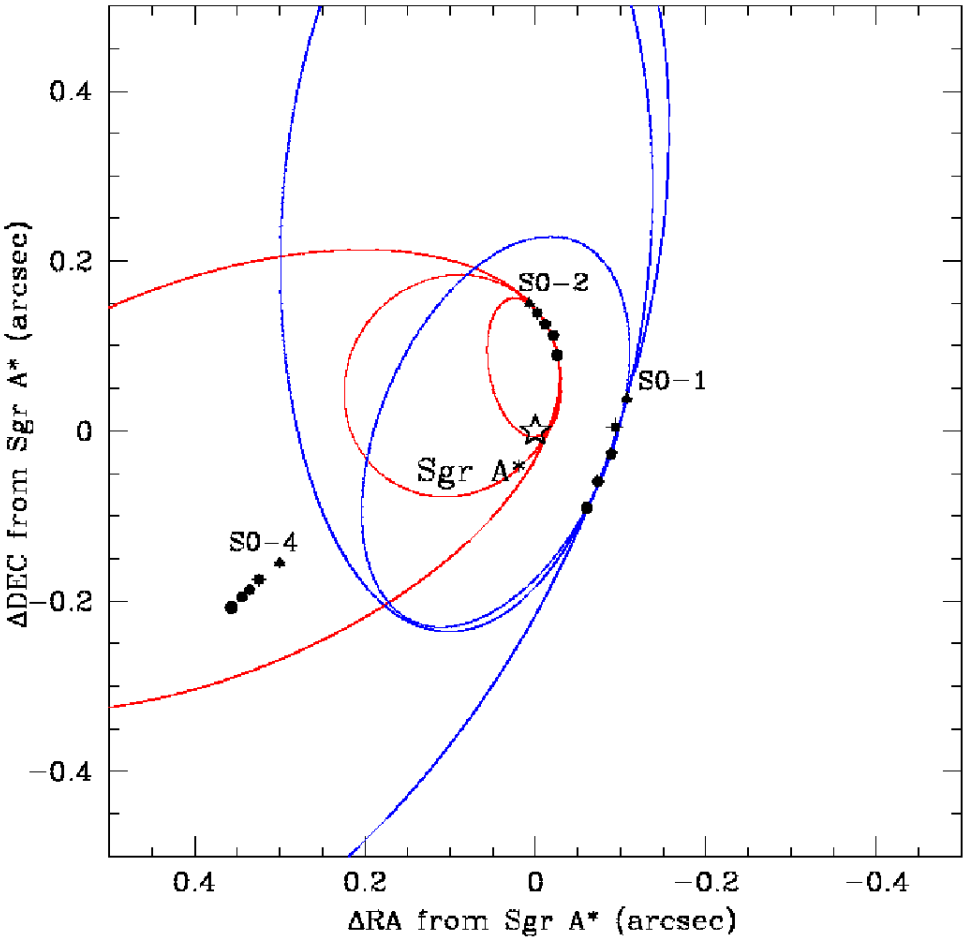

Figure 3.10: Orbital solutions of stars $S0-1$, $S0-2$ and $S0-4$ surrounding the dynamical center of the Milky Way, Sgr A*. The orbit shapes are elliptical because the distance to the black hole is too large, yet. There are no gravitational lensing effects visible. (Credit: [Ghe00])

important already outside the horizon. The result is a **Great Black Spot**[7] (GBS) as viewed from large distances. The diameter of the horizon is four gravitational radii for a Schwarzschild black hole. But the apparent diameter of the black spot may be higher depending on black hole spin and observational brightness contrast. This blackness is not urgently a disadvantage if the background is bright e.g. a luminous accretion disk. Hence, an accreting black hole ensures sufficient brightness contrast to see a black region

[7] in analogous terminology to Jupiter's *Great Red Spot* and Neptune's *Great Dark Spot*

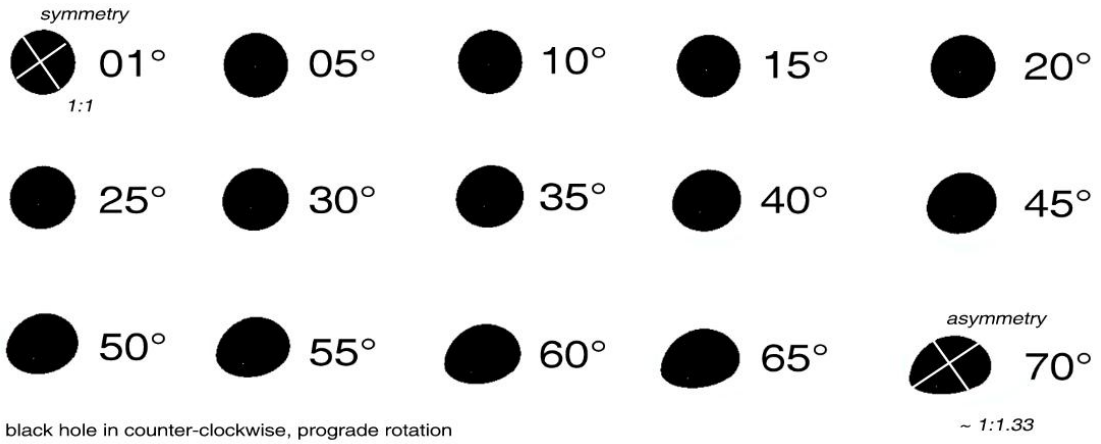

Figure 3.11: A sequence of *Great Black Spots* (GBS) of an extreme Kerr black hole, $a \simeq M$, (counter–clockwise rotation) as seen under different inclination angles. The shapes are results from relativistic ray tracing. The GBS is successively deformed with increasing inclination angle. The ratio of the crossing lines may parametrize the deformation: At low inclination the ratio is 1:1 and the GBS is symmetric (*upper left*); at high inclination this ratio deviates significantly to become 1:1.3 and even more (*lower right*).

if the surrounding gas is optically thin. A more serious problem apart from blackness is that black holes are compact and tiny: Even in case of the most supermassive black holes around 10^{10} $M_\odot$ the GBS size amounts a few hundred AU! This size comparable to the solar system shrinks to milliarcseconds if the black hole lies in a distance of 10^5 ly. Therefore, the direct detection of the black region requires sufficient spatial resolution. In case of the Galactic Center black hole associated with the compact radio source Sgr A* the predicted size of the '*black hole shadow*' is approximately 30 μas [Fal00]. The shadow size approaches the spatial resolution of modern radio interferometers using very long baseline interferometry (VLBI). However, the term *shadow* is somewhat misleading because one does not deals with a usual geometrical shadow but with an 'intrinsic darkening': photons are captured by strong space–time curvature.
The idea is to prove black holes by identifying the Great Black Spot (GBS) observationally. Precious information about the black hole is also contained in the diameter and shape of the black spot. Since mass, spin and inclination angle determine size and shape of the GBS, astronomers could fit these parameters if a detection succeeds:

- Black hole mass M determines the natural length scale in units of gravitational radii, i.e. the size of the black spot. Therefore, if the black hole distance is known and the GBS is detected, astronomers can deduce the black hole mass – except for an uncertainty based on the spin parameter.
- Likewise, the Kerr parameter a controls the size of the outer horizon, since Kerr

black holes are more compact than Schwarzschild black holes (compare Fig. 2.3). But also the symmetry of the GBS is influenced by the black hole spin. In the Schwarzschild case an axis symmetry is present, independent from the inclination angle; in the Kerr case this symmetry is broken by rotation and the shape is warped. Additionally, the warping depends on the inclination angle and is well observable for highest inclinations of the black hole's equatorial plane. This can be illustrated with ray tracing techniques, see Fig. 3.11.

- The inclination angle i of the Kerr black hole's equatorial plane determines the deformation degree of the horizon. This aspect is equally illustrated in Fig. 3.11: Any spot plotted there is based on the same Kerr parameter. Hence, only inclination controls the degree of deformation of the GBS. At low inclination the symmetry is perfect and ressembles to Schwarzschild. In this degeneracy case, an observer could not decide whether or not the black hole rotates. This changes dramatically at high inclination angles: The GBS is elongated to an asymmetric drop. The degree for asymmetry can be parametrized by the ratio of two diameters that form a cross. Perfect symmetry of the GBS gives a ratio of 1:1; broken drop–like symmetry gives ratios of 1:1.3 or even higher. Ray tracing simulations show that at maximum inclination, $i = 90°$, the horizon shape ressembles to a semicircle.

It should be stressed that the ray tracing technique shown here is based on tracing of 2D objects. The appearance of a black hole traced in 3D differs from the images presented here, but the principle method remains. Also the deformation trend of the black hole's horizon with increasing inclination stays the same.
The visibility of the GBS is naturally influenced by the black hole's environment e.g. the accretion flow. An optically thin accretion solution, $\tau < 1$, like the ADAF (see Sec. 4.2) permits visibility. At high accretion rates comparable to the Eddington rate the GBS may be obscured due to optical thickness, $\tau > 1$ (compare Sec. 4.3). Then, visibility depends on the interstellar medium on larger length scales that may obscure the GBS by extinction from dust.

In this work the direct detection technique is denoted as an obscurative method from the Latin word *obscuratio*, i.e. darkness. The GBS is clearly shown in Fig. 3.12. The appearance of a standard disk is rendered with a Kerr ray tracing solver [Mül00]. Its shows the emission distribution of the disk inclined intermediately, $i = 30°$, around an extreme Kerr black hole, $a = 0.999999\,M$, extending outwards to 30 gravitational radii. The calculation involves the generalized GR Doppler factor g that includes a purely Keplerian velocity field. The g–factor is calculated to the fourth power and plotted in grey scale: black equals zero and white equals approximately 2. In this first render step the radial emissivity profile lacks for simplicity. This distribution is always folded into any flux integral thereby causing the GBS. If astronomers succeed in observing the GBS at a cosmic black hole candidate, they prove the existence of a black hole and can deduce essentially three black hole parameters: mass M, spin a and inclination angle i.

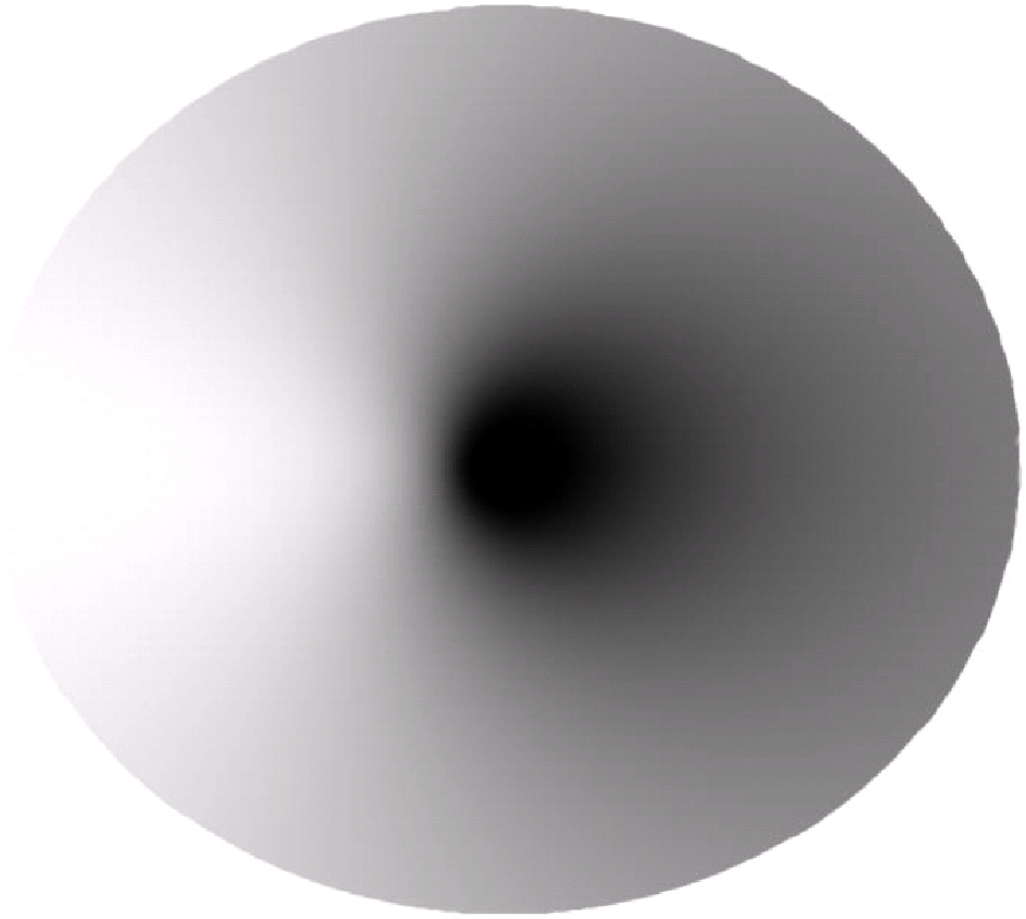

Figure 3.12: Distribution of the g-factor to the 4th power (no folding with emissivity) for an extreme Kerr black hole, $a \simeq M$. The appearance of a standard accretion disk is raytraced for an inclination angle of $i = 30°$. The disk extends from the outer horizon to 30 gravitational radii. The *Great Black Spot* is clearly visible: Any emission will be strongly suppressed by gravitational redshift due to the curved space–time.

Gravitational wave–induced methods Gravitational wave physics in the framework of GR is a growing research field. Gravitational waves are ripples of space–time that are produced when masses are accelerated. This wave phenomenon is in some analogy to electromagnetic waves that are generated by accelerated electric charges. On can imagine gravitational waves (GWs) as perturbations or dents that move along a space–time manifold. But space–time is a rather robust medium, so violent events are required

to produce GWs of sufficient amplitude. In astrophysics stellar explosions such as supernovae, hypernovae or merging COs are favored to emit GW bursts. Also the Big Bang is supposed to be such a transient source. Continuous GW emitters are compact binaries. Among these is one famous object, the **Hulse–Taylor pulsar** with catalogue name PSR 1913+16. These two neutron stars surround each other thereby emitting GWs. According to this energy loss the system collapses successively. This effect was investigated experimentally and turned out to be the best indirect proof for the existence of gravity waves [Hul74, Hul75a, Hul75b]. In fact, direct verification of GWs is one of the last outstanding verifications of GR.
GWs are also important in black hole physics: The black hole (BH) formation process is associated with GW transient emission, binary stellar black holes and binary supermassive black holes are involved, too. Hence, there is much theoretical efforts to derive GW spectra of all the GW emitters. Depending on the black hole mass the inspiral phase in a BH–BH merger event produces GWs in the frequency range between 10 to 500 Hz. These current developments in GW physics suggest that the **detection of black holes by a characteristic GW signature** produced in terrestrial detectors may become possible in the near future. If one regards the impact of gravitational waves to the local space–time this could be paraphrased as "*space–time seismology*".

3.5 Ergospheric Processes

The ergosphere as presented in Sec. 2.5 is the most fascinating region in Kerr black holes. Fig. 3.13 displays the ergosphere lying between static limit and outer event horizon. The static limit – defined in Eq. (2.14) – marks the starting point where infalling test particles cannot prevent from co–rotating with the drag of the Kerr space–time. The oblate ergosphere has maximum volume for extreme Kerr black holes, $a = \pm 1$. The angular momentum of a Kerr black hole is nothing else than an energy channel; the black hole possesses apart from mass–energy also rotational energy.

Penrose Process In a pioneering work, Roger Penrose pointed out that it could be possible to extract rotational energy from a Kerr black hole [Pen71]. The scenario may be outlined by the following gedankenexperiment: A compound particle is shot into the ergosphere. Within the ergosphere the particle decays into two particles: one may free–fall into the hole, the other one may escape to infinity. Now, the interesting feature is that the energy of a particle in the ergosphere could be *negative* as viewed from infinity. This is due to the fact that the Killing vector ∂_{t} – actually time–like outside the ergosphere – becomes space–like within the ergosphere. This metamorphosis concerns not only the Killing field but also the corresponding conserved quantity, in this case the time–component of the 4–momentum, p_{t}, i.e. the particle energy [Cha83].
Bardeen outlined that a physical observer following a time–like world line must be dragged in positive ϕ–direction if he is inside the static limit. Ergospheric observers have therefore access to "*negative energy trajectories*" which extract energy from the

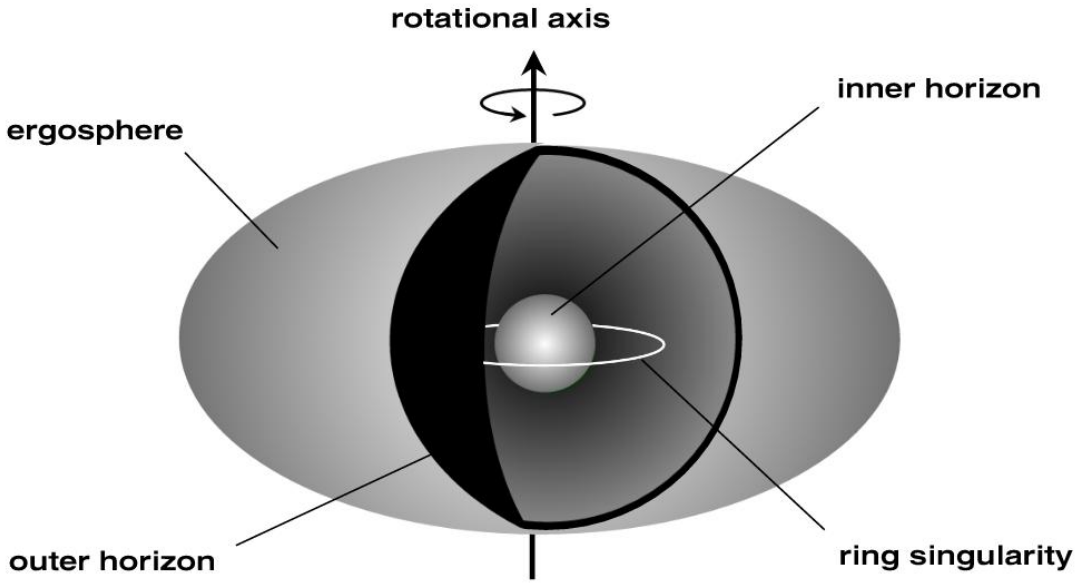

Figure 3.13: Sketch of the morphology of a Kerr black hole. The ring singularity (*white*) at $r = a$ is the source of the gravitational field and lies always inbetween the two horizons (outer: *black sphere*, inner: *gray sphere*). The oblate ergosphere (*gray ellipsoid*) envelopes the spherical horizons.

black hole [Bar72].
The classical Penrose process is based on counter–rotating particles which take negative energy states as viewed from asymptotical flatness. In scattering processes the negative energy may be transferred that could yield an energy gain as a net effect. This gain of particle energy is associated with a loss of rotational energy for the Kerr black hole. Frequently occuring Penrose processes can theoretically stop the black hole rotation.

Penrose Pair Production (PPP) A variant of the classical Penrose process is the Penrose Pair Production [Will02]. The mechanism is based on another ingredient, the *photon sphere* (see Sec. 2.6). Photons are instably trapped in the photon sphere. Other photons may now infall on radial null geodesics and hit these trapped photons. If the energy of the quanta exceeds the rest frame energy of about one MeV, gamma photons produce pairs of leptons. For rather large values of the black hole spin, $a \gtrsim 0.7$, the spherically symmetric photon sphere plunges into the oblate ergosphere (compare Fig. 2.6). Then, the PPP is expected to occur dominantly. PPP is sketched in Fig. 3.14. Williams applied this model to explain the populations of ultrarelativistic electrons in the quasars 3C 279 and 3C 273 [Will03].

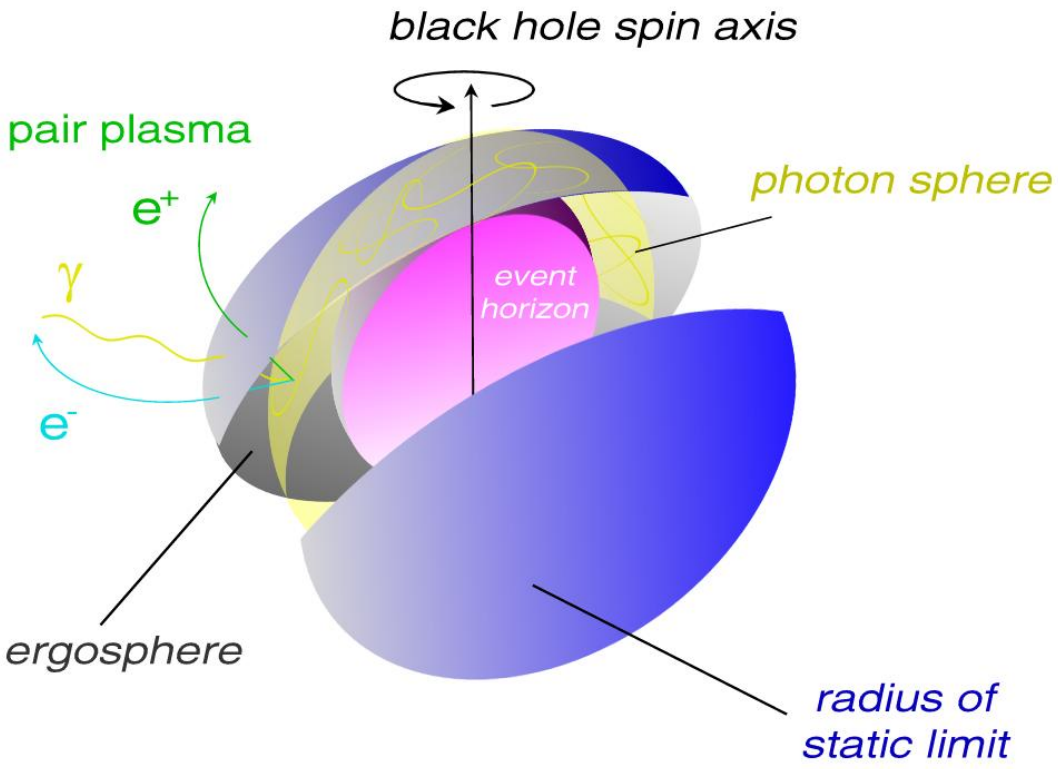

Figure 3.14: Illustration of the production of a pair plasma via Penrose processes in the ergosphere (*blue*) of a Kerr black hole (*violet*). The gamma photons annihilate in the photon sphere (*yellow*) to produce electrons (*cyan*) and positrons (*green*).

Blandford–Znajek mechanism In 1977 an essential effect was found which only operates near rotating black holes: the Blandford–Znajek mechanism [Bla77]. The two basic ingredients of this effect are an electromagnetic field and a rotating space–time. The fundamental statement is that it is possible to extract rotational energy of the black hole via electromagnetic fields. Technically it suffices to consider the energy–stress tensor of the electromagnetic field – this is a vital distinction to the GRMHD approach where also the plasma is incorporated as a fluid.
In the ansatz for the Blandford–Znajek mechanism, one regards a rotating black hole immersed in a (force–free) magnetosphere. Fig. 3.15 displays the magnetosphere of the gas planet Jupiter. Astonishingly, this is an interesting morphological analogue to black hole magnetospheres. The planet's magnetosphere was traced by synchrotron radiation at a wavelength of 20 cm which is emitted by electrons captured by Jupiter. These radio data were documented by the VLA. The morphology of this magnetosphere

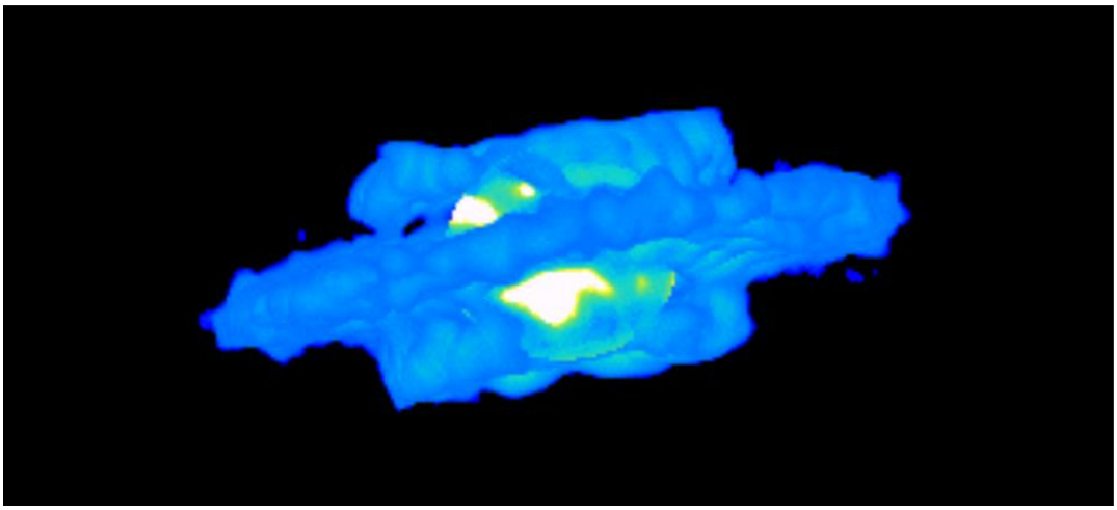

Figure 3.15: 3D reconstruction of observed synchrotron radiation in Jupiter's magnetosphere at radio wavelength of 20 cm. (Credit: NRAO/AUI/NSF, de Pater & Sault, 1998)

strongly ressembles to the black hole magnetosphere because gravitomagnetic forces produce dominantly toroidal magnetic fields in the surroundings. The seed magnetic fields are generated by external currents streaming in the accretion flow. Thereby the electric potential difference i.e. the field energy can exceed a critical limit to produce a pair plasma in cascades. The energy donator is the black hole. The resulting event is often outlined as "electromagnetic breaking" or "magnetic spin–down". Another essential consequence for the surrounding is that the plasma could probably outflow by getting a 'kick' by frame–dragging i.e. from gravitomagnetic forces. Hence, the Blandford–Znajek mechanism provides an efficient process to transform rotational energy into radiation.

Blandford & Znajek estimated the total emitted power of the black hole, $L_{\rm H}$, to be

$$L_{\rm H} \simeq 0.3 \left(\frac{a}{M}\right)^2 L_{\rm disk} \simeq 10^{38}\, W \left(\frac{a}{M}\right)^2 \left(\frac{\dot{M}}{1\,{\rm M}_\odot/{\rm yr}}\right), \tag{3.6}$$

where an completely electromagnetic disk, a paraboloidal magnetic field and low black hole spin, $a \ll M$, were assumed.
The magnetic field strength, B, is related to the black hole luminosity, $L_{\rm H}$, and was derived to be

$$B \simeq 0.2\, T \left(\frac{L_{\rm H}}{10^{38}\, W}\right)^{1/2} \left(\frac{M}{a}\right) \left(\frac{10^9\,{\rm M}_\odot}{M}\right). \tag{3.7}$$

According to these equations, Eqs. (3.6) and (5.13), one can easily deduce the magnetic field strength that can be produced from the data set $\{a, M, \dot{M}\}$. Pair production starts when the critical field strength limit is exceeded that corresponds to 1 MeV in the

rest frame energy. Astronomers believe that this is one essential feeding mechanism for leptonic jets.

Gravitomagnetism GR exibits a beautiful analogy to classical electrodynamics that lacks in Newtonian gravity: gravitomagnetism (GM). It is known that moving electric charges produce magnetic fields in their surroundings as viewed by an observer in the laboratory frame. Similarly, a moving mass produces a *gravitomagnetic field*. There are essentially two forces in this formalism, the *gravitoelectric force* and the *gravitomagnetic force*. The general expression for a mass m including both force contributions is [TPM86]

$$\left(\frac{dp_i}{d\tau}\right)_{\mathrm{GM}} = H_{ij}\, p^j = \frac{1}{\alpha}\nabla_i \beta_j p^j, \tag{3.8}$$

with the lapse function, α, and the space–like shift vector, $\vec{\beta}$. Lapse, shift and spatial 3–metric, γ_{ij}, are the basic quantities to split the space–time. This procedure is elaborated in detail in Sec. 5.4.
$\vec{H}$ denotes the gravitomagnetic vector field – some kind of GR extension of the magnetic field in electrodynamics. The equation implicitly presumes that this new field can be constructed by taking the divergence of a suitable potential, the shift vector. This is the gravitomagnetic analogue to $\vec{B} = \mathrm{rot}\vec{A}$. Hence, $\vec{\beta}$ could be taken as an angular momentum potential. Therefore, it is clear that the Schwarzschild geometry, $\vec{\beta} = 0$, has vanishing gravitomagnetic field. The Schwarzschild space–time only exhibits a gravitoelectric force term.
Evaluated in a FIDO frame, this yields

$$\left(\frac{dp_i}{d\tau}\right)_{\mathrm{GM}} = \frac{1}{\alpha}\frac{dp_i}{dt} = \underbrace{\gamma m\, g_i}_{gravitoelectric} + \underbrace{\gamma m\, H_{ij} v^j}_{gravitomagnetic}\ , \tag{3.9}$$

where γ denotes the Lorentz factor and $\vec{g} = -\vec{\nabla}\ln\alpha$ is the gravitational force, as measured locally by ZAMOs (see later in Sec. 5.4).
In particular, rotating masses produce gravitomagnetic fields. In other words gyroscopes generate GM fields. Interestingly, gyroscopes can interact via these GM fields. This is often referred as *gravitomagnetic spin–spin interaction*. The gyroscope spin couples to the GM field and starts to precess. This effect is known as **Lense–Thirring precession** and can be taken as the GR analogue to the classical Thomas precession of magnetic moments in magnetic fields. The *spin evolution equation* holds

$$\frac{d\vec{S}}{d\tau} = \frac{1}{\alpha}\left(\partial_{\mathrm{t}} - \vec{\beta}\vec{\nabla}\right)\vec{S} = -\frac{1}{2}\vec{H}\wedge\vec{S} = \vec{\Omega}\wedge\vec{S}. \tag{3.10}$$

In this equation the spin vector, $\vec{S}$, and the *precession frequency*, $\vec{\Omega}$, are introduced. In general, Ω splits into contributions from the Lense–Thirring (LT) precession and from the geodetic motion, $\vec{v}_{\mathrm{Gyr}}$, of the gyroscope with respect to the FIDO:

$$\frac{d\vec{S}}{d\tau} = \left(\vec{\Omega}_{\mathrm{GM}} + \vec{\Omega}_{\mathrm{geod}}\right)\wedge\vec{S}, \tag{3.11}$$

with the relation $\vec{\Omega}_{\rm geod} = \frac{3}{2}\,\vec{v}_{\rm Gyr} \wedge \vec{g}$.

Such spin–spin interactions are of special interest in astrophysics since e.g. a rotating black hole can interact with the nearby revolving accretion flow or with the massive rotating dusty torus on the large scale. It is useful to evaluate the **GM field of the Kerr geometry in Boyer–Lindquist coordinates**

$$\vec{H} = -\frac{2aM}{\rho^5}\left((r^2 - a^2\cos^2\theta)\,\sin\theta\,\vec{e}_\theta + \frac{2r(r^2+a^2)}{\sqrt{\Delta}}\,\cos\theta\,\vec{e}_{\rm r}\right). \tag{3.12}$$

Providing this set of equations, the strength of the Lense–Thirring precession can be estimated for a massive gas torus surrounding a supermassive Kerr black hole [Cam02]

$$|\vec{\Omega}_{\rm GM}^{\rm AGN}| \simeq \frac{1}{10^6\,{\rm yr}}\,\frac{M_{\rm torus}}{10^7\,{\rm M}_\odot}\left(\frac{10^8\,{\rm M}_\odot}{M}\right)^2\left(\frac{10^4\,M}{R_{\rm torus}}\right)^{5/2}. \tag{3.13}$$

One states that for typical values in an AGN system the Lense–Thirring frequency for a massive dusty torus on the pc–scale is very tiny, namely $|\vec{\Omega}_{\rm GM}| \simeq 3.2 \times 10^{-14}$ Hz. There is no chance to observe these long–term variations in light curves.
However, this scenario changes dramatically for stellar black hole systems i.e. microquasars (MQs). Assuming typical values in those systems – an accretion disk of 10 solar masses, a black hole of 10 solar masses (Cyg X–1) and an averaged disk distance of 1 gravitational radii (ISCO for an extreme KBH) –, we get

$$|\vec{\Omega}_{\rm GM}^{\rm MQ}| \simeq \frac{10^4}{\rm s}\,\frac{M_{\rm disk}}{1\,{\rm M}_\odot}\left(\frac{10\,{\rm M}_\odot}{M}\right)^2\left(\frac{1\,M}{R_{\rm disk}}\right)^{5/2}. \tag{3.14}$$

Therefore, microquasars such as Cyg X–1 exhibit typical Lense–Thirring frequencies in the kHz range. In fact, X–ray astronomers observe quasi–periodic oscillations (QPO) in the light curves of these stellar black hole systems. It is strongly suggested that these QPOs are associated with the Lense–Thirring effect. Today, this is one issue to explain QPO–like X–ray variability.
The Lense–Thirring effect in the case of the Earth–satellite system is currently measured by the satellite **Gravity Probe–B**. For a satellite heigth of 400 miles the LT effect amounts only 42 mas/yr [Sch60]. Unfortunately, this tiny effect is superimposed on the much stronger geodetic precession. The motion of the gyroscopes in the curved rotating space–time of the Earth shifts the gyroscope spin axis by the huge amount of 6.6". Hence, geodetic precession outnumbers the LT effect by a factor of about 160. Recently, the LAGEOS satellite experiments were able to confirm the Lense–Thirring effect in the Earth–satellite system by an accuracy of $99 \pm 10\%$ [Ciu04]. In the next year the data of Gravity Probe–B are supposed to prove this effect, too. Then, the error is going to decrease to one percent.

3.6 Black Hole Crisis

Classical black holes – in the most general case represented by Kerr–Newman black holes – were considered as a unique form of compact dark objects (CDOs) for a long time.

With the new millenium this changed: researchers found new solutions of Einstein's field equations of GR. They are called gravastars [Maz01] and holostars [Pet03a]. These new space–time solutions have amazing features: They do not possess an intrinsical singularity, nor a horizon, but they are nearly as black as black holes. Both solutions are static and have in contrast to classical black holes somewhat like a surface. However, this matter surface is very thin. The research is going on to generalize gravastar and holostar to rotating solutions. Provided that these rotating new gravitational vacua exist, they could have the power to replace the classical Kerr solution.

The motivation for black hole alternatives results from two main issues. One is the **singularity problem**: It is known that the curvature singularities of black holes and also those of the Big Bang in cosmology cause the breakdown of physics. Of course, physicists feel uncomfortable when they reach the edge of descriptivity because this equally represents the end of knowledge. A closer look to this problem may open the possibility that the emergence of intrinsical singularities signals only the breakdown of GR. Hence, it is advised to extend GR by quantum theoretical issues or to seek for a superordinated theory.

The singularity problem was intensified as Hawking and Penrose found the singularity theorems [Hawk69]. Due to these theorems intrinsical singularities are somewhat quite natural and must exist – at least *mathematically*. Up to now, the significance of these theorems is topic of an ongoing debate. The key question is if the singularity theorems prove unambiguously the existence of intrinsical singularities *in nature*.

The unprejudiced observer of this discussion finds that the question "Singularities – Yes or no?" split the scientific community in two groups. Most relativists cherish the singularity theorems and believe in the real existence of curvature singularities; but quantum and string theorists think that something happens to the idealized point or ring singularities of GR (see Sec. 2.4). The uncertainty principle suggests that idealized structures of that kind must be smoothed.

Another issue concerns the **vacuum problem**: Astrophysical black holes are vacuum solutions of the GR field equations. This means that the energy–momentum tensor vanishes *globally*. However, modern physics teaches us something new about the physical vacuum. It is not empty in the sense of a non–existence of particles. The vacuum is filled up with virtual particles that emerge and pass off. Experimental evidence for this hypothesis is the Casimir effect [Cas48, Lam97]. String theory equally suggests a more complicated version of a physical vacuum that is filled up with strings and branes. The challenge is to implement these concepts in GR and to find black hole–like solution that are possible CDO candidates.

Eventually both issues, singularity problem and vacuum problem, are linked together. One could speculate about whether a constraint to a global vacuum involves naturally curvature singularities in black hole physics. In any case the conclusion is that a re–evaluation of the singularity theorems under the modern viewpoint of physics is strongly advised.

Now, gravastars and holostars represent such alternatives to classical black holes that meet the requirements to a modern vacuum. The basic properties are now summarized briefly.

Gravastars are spherically symmetric static space–times that are given by the line element

$$ds^2 = -f(r)\,dt^2 + \frac{dr^2}{h(r)} + r^2\left(d\theta^2 + \sin^2\theta\,d\phi^2\right), \tag{3.15}$$

with some continuous metric functions $f(r)$ and $h(r)$.
A Gravastar can be divided in three zones: interior, shell and exterior. In each zone the equation of state varies:

- (I) interior: $\rho = -p$
- (II) shell: $\rho = +p$
- (III) exterior: $\rho = p = 0$

The interior of a gravastar exhibits negative isotropic pressure. Hence, it is a "de Sitter bubble" like in de Sitter universes in cosmology. This means in modern language that the gravastar core is made of dark energy which behaves like a Λ fluid. The cosmological w-parameter, $w \equiv p/\rho$, is equal to -1.
The shell consists of matter at causal limit because the sonic speed is equal to the speed of light, $c_\mathrm{s} = c$. The shell is very thin because its thickness is comparable to the Planck length, $l_\mathrm{P} = 10^{-37}$ cm. The shell is supported by the internal antigravitative negative pressure.
The exterior is determined by a "relativistic vacuum" with vanishing energy–momentum tensor.
With this ansatz one can deduce radial sectors of a gravastar that satisfy

- (I) interior: $f(r) = C\,h(r) = C(1 - H_0^2\,r^2)$
- (II) shell: $f(r) \approx h(r) \approx \epsilon \approx 10^{-25}$
- (III) exterior: $f(r) = h(r) = 1 - 2M/r$

In the exterior region one immediately identifies the *Schwarzschild factor* and concludes that the outer zone of a gravastar is identical to the outer Schwarzschild solution. The shell is located where in a Schwarzschild black hole the horizon can be found, $r_\mathrm{shell} \approx \mathrm{R_S}$. An analysis of the lapse function of this metric, $\alpha_\mathrm{G} = \sqrt{f(r)}$, shows that it does **not** vanish at the surface of gravastars: $\alpha_\mathrm{G}(r_\mathrm{shell}) \approx 10^{-13}$. Hence, gravastars are not absolutely black in contrast to black holes but they are very dark. In other words: The important consequence is that they have no event horizon. The formation process of gravastars is far away from understanding. Nevertheless, it is supposed that in gravitational collapse progenitors prevent from forming a horizon rather than undergo a *quantum phase transition* to form a gravastar. Mazur & Mottola argue that a transition to a gravitational

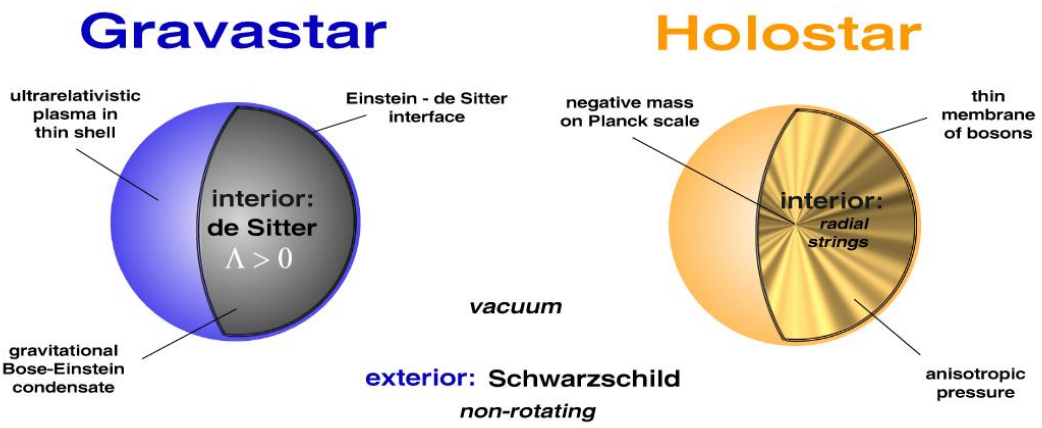

Figure 3.16: Alternatives to the static black hole solution: Gravastar vs. Holostar.

analogue of the Bose–Einstein condensate occurs (gravitational Bose–Einstein condensate, GBEC).
The internal structure is in any world point **regular**: Gravastars do not possess any singularity.

The dramatic consequence is that – in the static case – astronomers are not able to decide whether they have detected a Schwarzschild black hole or a gravastar. This is due to the fact that observationally one can not distinguish the tiny difference in the gravitational redshift between 'dark' and 'absolutely black'.
However, gravastars possess a stability problem. Generally spoken, it is not sufficient that a space–time is a solution of the field equations of GR; it should also be dynamically stable towards perturbations. A first investigation yields stability of gravastars [Vis03]. Recently, it has been shown that on one hand the gravastar solution can be extended to more general vacuum cores (e.g. quintessence–like and phantom–energy–like cores) and – more importantly – on the other hand that the gravastar solution is not stable [Vig04].

Holostars have morphologically quite similar properties like gravastars. There are also three radial sectors and holostars exhibit a thin matter surface and spherical symmetry. The main difference between the two types is that the internal pressure of holostars is anisotropic. Michael Petri found this solution in 2003 [Pet03a] and generalized the electrically neutral solution to a charged holostar [Pet03b]. Unfortunately, a rotating generalization of a holostar is still lacking.
Recently, the anisotropic negative pressure found an interpretation within the framework of string theory [Pet04]. This was motivated by the "hairs" of fuzzballs in a stringy picture of black holes [Mat04]. The interior of the holostar obeys a matter distribution

of the form

$$\rho(r) = \frac{1}{8\pi r^2}. \tag{3.16}$$

The holostar is filled with strings that satisfiy the equation of state

$$P_{\mathrm{r}} = -\rho(r), \tag{3.17}$$

where P_{r} denotes radial pressure. However, the transversal pressure component vanishes in the interior and only contributes to the holostar shell.
If it is assumed that the shell is located at radius R_{H}, the holostar radius, density and pressure can be written in compact form

$$\rho = \frac{1}{8\pi r^2}\Theta(r - R_{\mathrm{H}}) = -P_{\mathrm{r}}, \tag{3.18}$$

$$P_{\perp} = \frac{1}{16\pi R_{\mathrm{H}}}\delta(r - R_{\mathrm{H}}), \tag{3.19}$$

with the Heavyside step functional $\Theta(r)$ and the Dirac δ–distribution $\delta(r)$. It is easy to recognize that the region outside the holostar's surface, $r > R_{\mathrm{H}}$, is equal to the outer Schwarzschild solution where $\rho = P = 0$. As in case of gravastars, the holostar solution is **regular** and has **no event horizon**. Gravastars and holostars are confronted to each other in Fig. 3.16.

The new space–time solutions, gravastar and holostar, are now known for several years. But still there is great skepticism in the scientific community whether or not to accept these proposals. Studying the evolution of non–/acceptance is like history repeating: The Kerr solution in the early sixties had comparable acceptance problems because relativists and astrophysicists hoped at that time that a rotating solution of Einstein's field equation would prevent from having a horizon. The Kerr solution does not. However, nowadays Kerr black holes are viewed as essential ingredients of AGN physics.
Fig. 3.17 offers a synoptical perspective onto classical black holes and the modern (static) alternatives. *Any* of these solutions has certain advantages and disadvantages. The next step is actually clear: Serious research should test these model systems in nature. Another aspect is testing inner consistency and stability of the solutions. Maybe, astronomy offers the opportunity to rule out one solutions or more.

The meaning of static black hole alternatives for this work is marginal because still rotating generalizations of gravastars and holostars are lacking. But it is some kind of an outlook in the near future: Till today, one cannot exclude that the Kerr solution arrives to a more general space–time that is rather comparable to rotating gravastars or holostars. It is worth spending time in trying to find those generalizations. But the analysis of the Kerr solution is strongly justified until finding suited Kerr black hole alternatives.

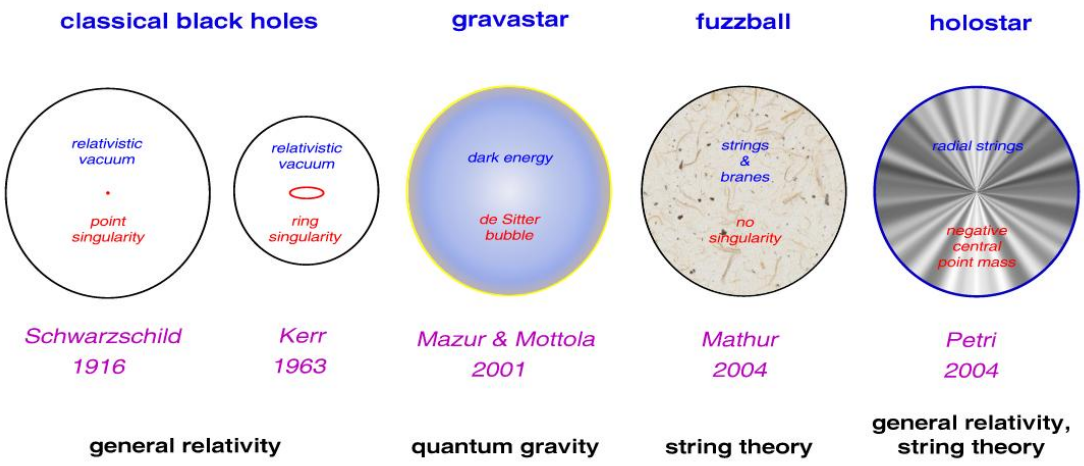

Figure 3.17: Interior black hole structure in a synopsis of theories. From left to right there is shown the internal structure of the black hole and alternatives in chronological order. The corresponding pioneers are added below each solution.

3.7 Cosmological Significance

The cosmological role of black holes is still somewhat mysterious. What came first: stars and gas of a galaxy or the central black hole? This question is often referred as the *hen–egg problem of structure formation*. This problem gets worse by another uncertain ingredient, the dark matter. In this section possible scenarios are visited.

Galaxies are surrounded by a dark matter halo. Galaxy formation is strongly dependent on this additional 'invisible' gravitational potential. The dark matter halos are outweighing its galaxy by approximately a factor of eight [Hai04]. The key question is: How does gas condense into the central regions of the dark matter halo?

In a cosmological model structure formation i.e. the formation of the first population of stars (PopIII) and galaxies depend on the initial mass density distribution. Certainly, the distribution of dark matter is at least as relevant as those from baryonic matter. Tiny inhomogeneities were amplified by gravitational instabilities.

The formation of stars from baryonic gas can be summarized as follows: The mechanism of gravitational collapse operates when exceeding the local *Jeans mass*, M_{J},

$$M_{\mathrm{J}} = \pi^{3/2} \frac{1}{\sqrt{\rho}} \left(\frac{\mathsf{R}T}{\mu G} \right)^{3/2} . \tag{3.20}$$

It depends generally on mass density, ρ, temperature, T, and average atomic weigth, μ [8]. Overdensities are preferred to become gravitationally unstable due to a lower Jeans mass. The Jeans mass is modified by centrifugal and magnetic terms when the gas rotates and is magnetized.
The collapse heats the gas. A stellar object is born when the gas reaches the temperature limits for nuclear burning processes. First of all this is lithium burning as been observable in brown dwarfs, then hydrogen burning starts.

The gravitational collapse of dark matter is quite similar. Hence, DM represents an "obstetrician" for galaxies and determines their spatial distributions, abundance and size.
The question whether stars or AGN such as quasars came first can be tackled with observational facts: Even the most distant quasars exhibit metallicities that deviate significantly from the abundances of primordial nucleosynthesis (essentially 75% hydrogen and 25% helium). The current observational constraint is given by the starburst galaxy Abell 1835 IR 1916 at $z = 10$ [Pel04]: This object lives in an epoch 480 million years after the Big bang! Its measured high star formation rate (SFR) hints rather for star formation activity than for quasar activity. This observation therefore suggests that first metals form in stellar burning processes of the first generation of stars. Afterwards, the galaxies underwent an AGN phase. What is then the conlusion for supermassive black holes that cause active galaxies by accretion according to the AGN paradigm?

There are two ways to answer this key question: Either black holes existed already in the center of starburst galaxies but were not active e.g. due to a starving phase (compare the upcoming Sec. 4.3); or central black holes **did not yet** exist in these high–z starburst galaxies.
Another outstanding question that is related to the hen–egg problem: Which process starts the AGN activity? One can think of galaxy merger events that deliver huge amounts of stellar gas. As a consequence the accretion rate steeply increases by feeding and activates the quasar switch.
The answer to the hen–egg problem is still uncertain. Improved observation techniques will surely soon tell which came first.

[8] $\mathsf{R} = 8.314511\,\mathrm{J\,mol^{-1}\,K^{-1}}$ denotes the gas constant, the product of Avogadro's constant, $\mathrm{N_A} = 6.0221367 \times 10^{23}\,\mathrm{mol^{-1}}$, and Boltzmann's constant, $\mathrm{k_B} = 1.380658 \times 10^{-23}\,\mathrm{J/K}$.

4 Accretion Physics

4.1 Global Structure – The AGN Paradigm

Today, most astrophysicists are convinced that any galaxy possesses a central supermassive black hole (SMBH). There are some individual exceptional cases with lacking SMBH that can be explained by special scenarios, e.g. merger events of galaxies. There is even observational evidence for binary supermassive black holes harboring in one galaxy, e.g. NGC 6240 [Komo03].

Observations indicate that galaxies undergo an active phase triggered by accretion onto the SMBH. The consequence is a very luminous core with a typical luminosities of about 10^{12} $L_\odot$ e.g. a normal quasar. This luminosity exceeds a normal (i.e. inactive) galaxy by far. Cores of active galaxies are generally termed as active galactic nuclei, AGN. Over the decades it turned out that the universe exhibits a complete AGN zoo. AGN are divided into Seyfert galaxies, LINERs (*low–ionization nuclear emission line regions*), ULIRGs (*ultra–luminous infrared galaxies.*), radio galaxies, BL Lac objects (*Lacertids*), blazars and quasars. The challenge is to describe this zoo in a unified scheme. Astronomers found that this is possible to a certain degree. The approach is termed as AGN paradigm that dates back to the mid–sixties. It states that the activity of any AGN is caused by an accreting supermassive black hole. The inventors of this idea were Y.B. Zel'dovich, I.D. Novikov [Zel64], E.E. Salpeter [Sal64] and Lynden–Bell [Lyn69].

Going in more detail this *accretion conjecture* can be outlined as follows: Eddington argued that there is a maximum luminosity, the **Eddington luminosity**, $L_{\rm Edd}$, in any steady spherically symmetric accretion flow. This is because at $L_{\rm Edd}$ radiation pressure pointing radially outward stops inward motion triggered gravitationally. Let us consider a plasma element: radiation pressure results from Thomson scattering on electrons in the plasma; gravitational pressure follows essentially from the heavy protons also contained in the plasma. The equilibrium condition provides then [Cam02]:

$$L_{\rm Edd} = \frac{4\pi G M \mathrm{m_p}}{\sigma_{\rm T}} \simeq 1.3 \times 10^{46}\,\mathrm{erg\,s^{-1}} \left(\frac{M}{10^8\,\mathrm{M_\odot}}\right), \tag{4.1}$$

where M is the black hole mass, $m_{\rm p}$ the proton mass and $\sigma_{\rm T}$ the Thomson cross–section. Generally, luminosity, L, can be transformed into mass accretion rate, $\dot{M}$, due to

$$L = \epsilon \dot{M}, \tag{4.2}$$

with a parameter ϵ that measures the transformation efficiency from accretion into radiation. Optically thick accretion flows on black holes fulfill $\epsilon \approx 0.1$. However, a rapidly

rotating black hole drives the efficiency up to $\epsilon \approx 0.42$ whereas nuclear fusion is rather inefficient, $\epsilon \approx 0.01$. Take $\epsilon \approx 0.1$ as a basis, one can transform the Eddington luminosity into an **Eddington accretion rate**

$$\dot{M}_{\mathrm{Edd}} \simeq 20\,\mathrm{M}_{\odot}\,\mathrm{yr}^{-1}\left(\frac{0.1}{\epsilon}\frac{L}{10^{47}\,\mathrm{erg\,s}^{-1}}\right). \tag{4.3}$$

This is the maximum accretion rate for spherical accretion. However, it is possible that this Eddington limit can be exceeded for axisymmetric accretion i.e. in accretion disks. In accretion theory a higher accretion rate than the Eddington rate, $\dot{M} > \dot{M}_{\mathrm{Edd}}$, is termed as *super–Eddington accretion*. Equally, the case $\dot{M}, \dot{M}_{\mathrm{Edd}}$ is known as *sub–Eddington accretion*.

Powerful quasars have observed luminosities of 10^{46} to 10^{47} erg/s. Hence, one can immediately deduce according to Eddingtons argument, Eq. (4.1), that quasars habor supermassive black holes with masses of 10^8 to 10^9 $\mathrm{M}_{\odot}$. Seyfert galaxies that exhibit a lower luminosity than quasars by a factor of 10 or 100 have therefore correspondingly lower SMBH masses, ranging from 10^6 to 10^7 $\mathrm{M}_{\odot}$.
The main parameter pair that controls AGN activity is $\{M, \dot{M}\}$. We will discuss the accretion unification scheme separately in Sec. 4.3. There, the observed accretion rates are linked to a specific AGN class – for supermassive black holes – or source state – for BHXB i.e. stellar black holes. The AGN lifetime can be estimated for given black hole mass and accretion rate according to

$$t_{\mathrm{AGN}} \simeq \frac{M}{\dot{M}} \simeq 10^8\,\mathrm{yr}\left(\frac{M}{10^8\,\mathrm{M}_{\odot}}\right)\left(\frac{\dot{M}}{\mathrm{M}_{\odot}\,\mathrm{yr}^{-1}}\right)^{-1} \tag{4.4}$$

Compared to sun–like stars quasars are relively short–lived objects undergoing a short active phase. The timescale is rather comparable to the age of massive stars.

Fig. 4.1 sketches all essential ingredients of the AGN paradigm. It shows the AGN in a tomographic view where length axes are scaled logarithmically for illustrative purposes. The axis of symmetry equals the axis of rotation. Coming from the outside located at the pc–scale or equivalently $10^4\,r_{\mathrm{g}}$, the first huge structure is the **cold dusty torus**. Depending on the AGN class this putative torus contains $\simeq 10^4$ $\mathrm{M}_{\odot}$ (Seyferts) to $\simeq 10^8$ $\mathrm{M}_{\odot}$ (quasars, blazars). The distance of the torus from the center depends on the AGN class, too. The dust temperature amounts ≈ 1000 K so that typically molecules like silicates, graphites and polycyclic aromatic hydrocarbons (PAHs) constitute the torus. Astronomers verify this by molecular spectral lines and infrared emission. The origin of the infrared emission is reprocession: hard radiation from the galaxy core hits the torus and is scattered to lower photon energies. From Fig. 4.1 one can recognize that it depends on the inclination of the dust torus whether the center of the AGN is obscured or not. Classically this controls the emergence of broad line regions (BLRs) in the AGN spectra. This is because broad non–relativistic emission lines originate from rapidly moving material near the AGN center. At high inclined axis of the system, the observer has no chance to look into the core in the optical since the dusty torus

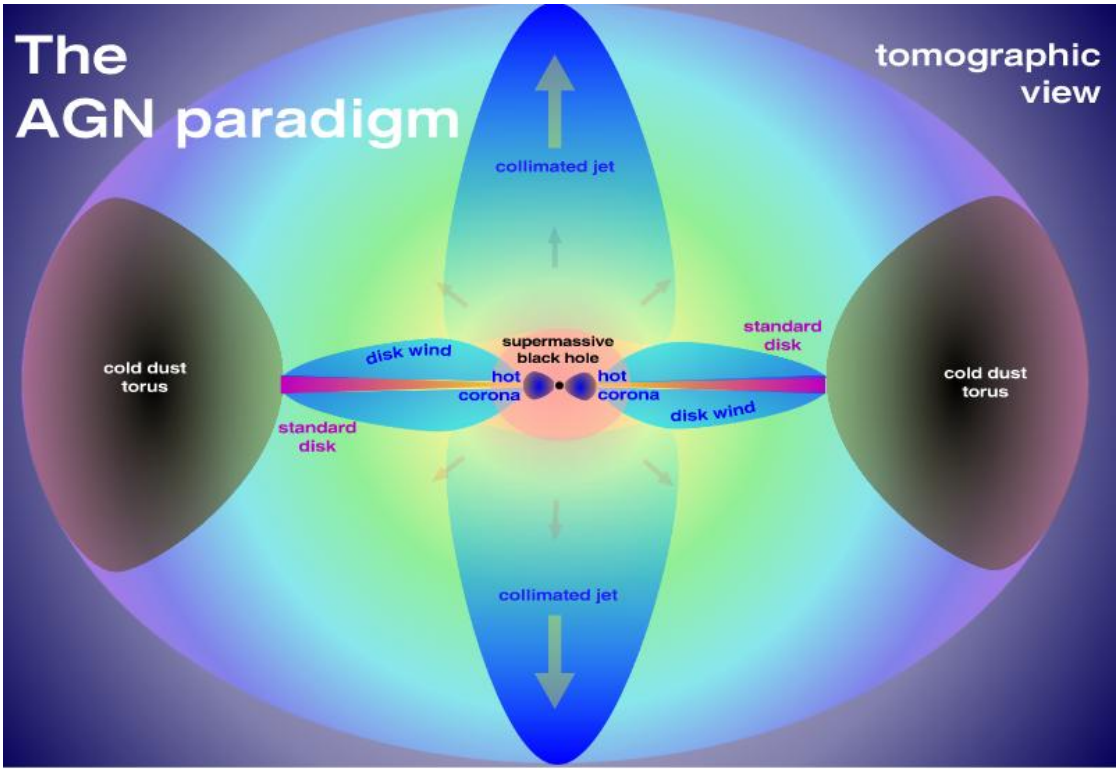

Figure 4.1: Tomographic view onto relevant AGN building blocks from the pc– down to sub–pc scale. Cold matter infalls from the putative dusty torus forming an accretion flow. The flat standard accretion disk extends towards the small length scale comparable with a few gravitational radii. Thereby, a thick and hot accretion flow is generated in the central region that is associated with a variable hot corona. The central supermassive Kerr black hole drives relativistic outflows: the jets.

lies inbetween. This orientation defines **AGN type 2**. In contrast, at low inclination angles the view into the AGN core is unobscured. BLRs are detectable in the spectra. This defines **AGN type 1**. Intermediate inclinations are coded as values between the extreme values 1.0 and 2.0, e.g. an AGN type 1.5 just lies inbetween, at 45°.

Hence, the dust torus provides distinct orientation effects resulting in the **AGN dichotomy**. However, in both cases narrow line regions (NLR) are visible because of their higher distances from the core.

The inner periphery of the torus is shaped by sublimation: intensive hard radiation from the core causes the molecular material to migrate from the solid to the gaseous phase. Therefore, astronomers hope to image this sublimation form as a cross–like feature at Seyfert–2s by means of infrared interferometry (ISO, MIDI, Spitzer telescope) [Scha03]. It is necessary that the torus configuration breaks down: Due to the Papaloizou–Pringle

instability (PPI) tori are generally unstable. Therefore, torus material infalls to the AGN core forming an accretion flow. The favored accretion solution tapping the dusty torus in inward direction is a **standard accretion disk**, SAD. It is flat due to rotation and efficient radiative cooling. The SAD is located at the pc–scale and extends down to smaller radii. One can think of rings as elementary building blocks that compose the standard disk. At sufficient tiny thickness each ring has a certain temperature, $T_{\rm i}$. Such an isothermal ring radiates like a black body (BB) with radiative power $P_{\rm bb} \propto T_{\rm i}^4$. Adjacent rings have slightly different temperature and a shifted black body spectrum. Overlaying the individual black bodies of several rings forms the *multi–color black body* spectrum [Ryb79].

The accretion flow becomes hotter with decreasing radius. SADs arround Kerr black holes are not arbitrarily stable. At the ISCO stable Keplerian rotation breaks down. The disks may also be truncated. The optically thick SAD makes a transition to the inner optically thin advective–dominated accretion flow, the ADAF. Thereby, heating evaporates the flow so that it becomes geometrically thick. The feeding from the pc–scale may end up in an **inner torus**. Typically this structure is located at the marginally stable orbit or a few $r_{\rm ms}$ (compare Sec. 2.7). The size of the ADAF and the structure of the inner accretion flow depend on the accretion rate – as we will see in Sec. 4.3. A hot reservoir of plasma that forms and varies in size is the so–called **corona** . This hard photon emitting region is the primary source that generates X–ray fluorescence lines. This line complex (Fe Kα, Fe Kβ, Ni Kα etc.) can be found as a reflection component in some AGN, especially Seyferts and quasars type 1. It forms when hot coronal photons hit the cold accretion disk and get reflected to a distant observer. However, location and shape of the corona are quite unclear. On one hand it is strongly suggested by observation that it varies from source to source; on the other hand it fluctuates in time also in one source. Some proposals for the corona geometry are outlined in Fig. 4.2. Today, it is discussed whether hot corona and cold standard disk form a slab respective sandwich geometry, a sphere+disk geometry, a torus+disk geometry or a patchy respective pill box geometry. The geometry certainly depends on the accretion regime.

Reverberation mapping technique as demonstrated in Sec. 3.4 is one method to disentangle the coronal structure. The variations in X–ray fluorescence lines – if available – carry also signatures of the corona.

The very central object and the AGN engine is the supermassive rotating black hole. It triggers not only AGN luminosity but also the **formation of relativistic jets** as elaborated in Ch. 5.

This geometrical information about the AGN structure can be deduced from multi–wavelength AGN spectra. Observations prove that each AGN emits in nearly all wavebands namely from the radio to TeV with a slight dependence on AGN class. At first sight, one recognizes that AGN continuum spectra are essentially triple–humped: One hump in the infrared, one in the blue and one in the X–ray range. The '*infrared bump*' at lowest photon energies around 10 microns originates from reprocessed photons that scatter through the dusty torus. A contribution around 100 microns comes from the starburst component of the galaxy. The central *big blue bump* (BBB) around 1000 Å is

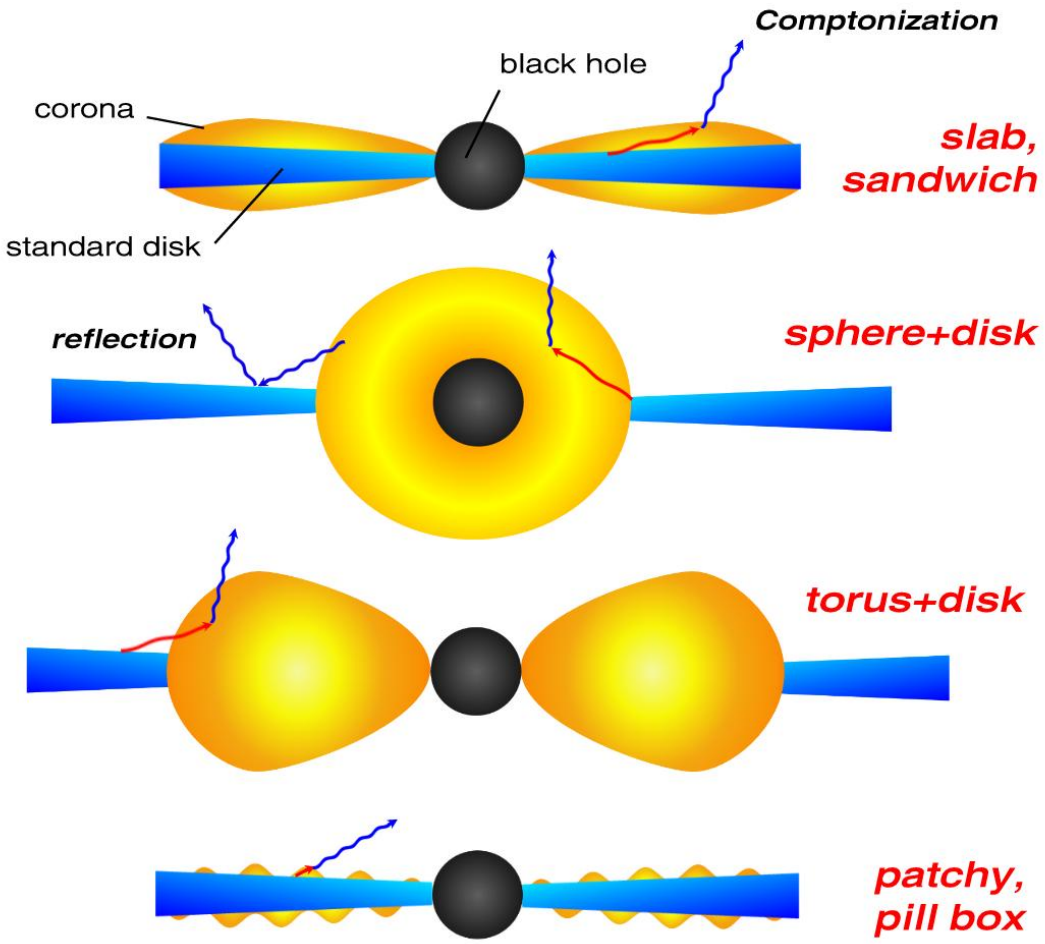

Figure 4.2: Models proposed for the geometry of cold accretion disk (*blue*) and corona (*yellow*) in the vicinity of a central black hole (*black*). Soft photons are sketched as red low–frequency waves; hot Comptonized photons are sketched as blue high–frequency waves. Reverberation mapping techniques selects a geometry for each source, each state. (adapted to [Rey03])

generated by the standard accretion disk on the pc–scale. This is the already discussed multi–color black body radiation. The thermal nature of the big blue bump was recently confirmed by a sophisticated method: Taking only the polarized flux of a small quasar sample it was shown that the BBB has a Balmer edge in absorption. Hence, the emitter is thermal and optically thick [Kis04].

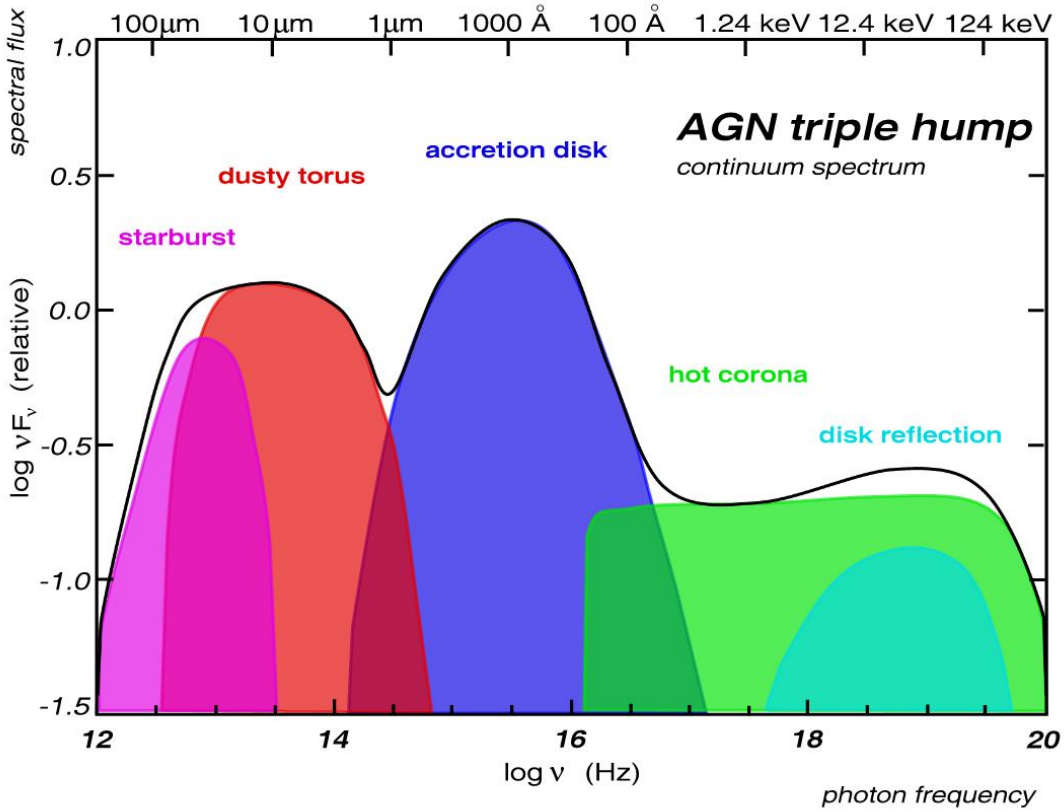

Figure 4.3: Representation of a typical triple–humped AGN continuum spectrum. Color–coded are contributions of favored sources located in the AGN. (adapted to [Man02])

The high–energy bump in the X–rays extending from about 1 keV up to 100 keV comes from the AGN core: Soft photons from the surroundings (cold accretion disk, cosmic microwave background) get inverse Compton scattered by the hot coronal plasma (**Comptonization**). This mechanism creates a characteristic Compton continuum that can be described by a power law cutting off exponentially[1]. An additional contribution, the **reflection bump** around 20 keV, overlays the Compton continuum. The reflection originates at the cold disk that acts like a mirror. Of course, this behavior depends on the ionization state of the disk just as much as the fluorescence lines. A complex of X–ray fluorescence lines around 7 keV (dominantly iron) are attributed to the reflection bump.

The sum of all these spectral components forms the typical **triple–humped AGN spectrum** in Fig. 4.3. This generic profile can be extracted from spectral energy dis-

[1]Indeed, the cut–off indicates the plasma temperature due to $h\nu_{\mathrm{cut-off}} = 3k_{\mathrm{B}}T$ [Ryb79].

tributions (SEDs) of AGN samples [Elv94].

4.2 Accretion Solutions

In this section accretion theory of black holes and solutions emerging under certain restrictions are reviewed in brief. Illustratively spoken, the whole parameter space of accretion theory can be devided into cells. Each cell is populated by a certain type of accretion flow. As a natural consequence accretion flows are classified by several acronyms that are widely–used today:

- Shakura–Sunyaev disk (SSD) or equivalently standard accretion disk (SAD)
- advection–dominated accretion flow (ADAF)
- radiatively–inefficient accretion flow (RIAF)
- convection–dominated accretion flow (CDAF)
- slim disk
- truncated disk – advective tori (TDAT)
- non–radiative accretion flow (NRAF)

These accretion solutions are briefly described in the following paragraphs. In principle, we follow in this preparation the historical path leading from Newtonian hydrodynamics over relativistic hydrodynamics to Newtonian magnetohydrodynamics and relativistic magnetohydrodynamics. The latter branch is then analyzed in Ch. 5 in more detail because it is the main topic of the present work.

Standard accretion disk (SAD) was found in 1973 [Sha73]. SADs are self–consistent analytical accretion solutions in the framework of hydrodynamics. Angular momentum of the accretion flow is transported in outward direction thereby forming a disk around the black hole. Shakura & Sunyaev considered the non–relativistic case whereas Novikov & Thorne generalized to the relativistic approach [Nov74].
Usually, one implements cylindrical coordinates $\{t, R, z, \phi\}$ in discussing SADs. One defines a half thickness of the SAD, H, in vertical direction. This thickness is controlled by hydrostatic equilibrium. For SADs, H is tiny allover the disk, i.e. $H/R \ll 1$. Therefore, it is stated that SADs are *geometrically thin*.
A vertical integration over the mass density in the vertical direction of the disk gives the surface density, $\Sigma(t, R) = \int_{-H}^{H} \rho(t, R, z)\, dz$.
The velocity field follows nearly a Keplerian profile, $\Omega \simeq \Omega_{\rm kep} \propto R^{-3/2}$. There is also a small radial drift superimposed to the rotation. Stable Keplerian rotation breaks down the marginally stable orbit. Hence, the SAD has an inner edge located at the ISCO, $r_{\rm in} = r_{\rm ms}$. In most cases, between the (outer) event horizon of a Kerr black hole located at $r_{\rm H}^{+}$ and the inner disk edge there is a gap. Only for an extreme Kerr black hole,

$a = M$, the radii coincide and the standard disk touches the horizon, $r_{\rm in} = r_{\rm ms} = r_{\rm H}^{+}$ (see Ch. 2).

The SAD is in hydrodynamical equilibrium i.e. gravitational pressure is nearly balanced by centrifugal forces causing negligible pressure gradients. The disk material is cooled efficiently by radiation. Generally in accretion theory, there is a dissipation function, $Q^{+}(t, R)$, and cooling function, $Q^{-}(t, R)$. In SADs dissipation is produced by shear, $\sigma_{R\phi} = R\, d\Omega/dR$. Considering turbulent viscosity, ν, of the accretion flow the dissipation function can be calculated to $Q^{+}_{\rm vis} = \nu\Sigma \left(R\, d\Omega/dR\right)^2$. Cooling of the flow is typically generated by radiation. The temperature scaling of cooling depends one the specific radiation mechanism. For an optically thin plasma cooling is dominantly maintained by bremsstrahlung, $Q^{-} \propto H\rho^2\sqrt{T}$. In contrast, an optically thick plasma provides $Q^{-} \propto T^4/\tau$ due to vertical radiation transfer where τ denotes the optical depth.

Now, *efficient cooling* satisfies the condition that viscous heating is completely radiated away, i.e. $Q^{+}_{\rm vis} = Q^{-}_{\rm rad}$ or equivalently $ds/dR = 0$ where s denotes the specific entropy. SADs have an entropy gradient only in the vertical direction as opposed to ADAFs. SADs are optically thick, $\tau \gg 1$. Typically they exhibit a modified black body spectrum: each disk ring with well–defined temperature contributes to the multi–color black body spectrum. This is recovered as big blue bump in AGN continuum spectra (compare Sec. 4.1).

The temperature profile of SAD is essentially decreasing in outward direction, $T \propto r^{-3/4}$. A detailed analysis gives a maximum temperature that is reached close to the inner edge [Sha73]

$$T_{\rm max} = \left(\frac{3GM\dot{M}}{8\pi\sigma r_{\rm in}}\right)^{1/4} \simeq 8.8\times10^5\,{\rm K}\left(\frac{3R_{\rm S}}{r_{\rm in}}\right)^{3/4}\left(\frac{M}{10^8\,{\rm M}_\odot}\right)^{-1/2}\left(\frac{\dot{M}}{1\,{\rm M}_\odot{\rm yr}^{-1}}\right)^{1/4}, \tag{4.5}$$

with the Stefan–Boltzmann constant, σ, the Schwarzschild radius, $R_{\rm S}$, inner disk edge, $r_{\rm in}$, black hole mass, M, and accretion rate, $\dot{M}$. Interestingly, this maximum temperature decreases with increasing black hole mass. Therefore, BHXBs are hotter than AGN if other parameters are assumed to be equal.

Historically, it turned out that SADs are not adequate to explain the hard spectra of BHXB and AGN. The idea was to incorporate hot optically thin gas that transforms cold SAD seed photons into hard Comptonized photons [Tho75].

The applications of SADs in astrophysics are manifold. They play not only in black hole accretion a major role; there are also present in systems with different CO type, e.g. in white dwarf binaries like cataclysmic variables (CVs).

Advection–dominated accretion flow (ADAF) were found in 1994 as self–similar accretion solutions in dissipative hydrodynamics [Nar94]. ADAFs are locally *inefficient* cooled by radiation. This means that the conditions $Q^{+}_{\rm vis} = Q^{-}_{\rm rad}$ respective $\frac{ds}{dR} = 0$ are abrogated. Just in contrast to SADs, ADAFs show an entropy gradient in radial direction. As a consequence, viscous heating is *not* radiated away but stored in the accretion flow as internal energy (and entropy). This increase of thermal energy in the plasma

results in a very hot flow typically for ADAFs. The internal energy is advected into the black hole. Hence, for an ADAF **advective energy transport** comes into play

$$Q^{\mathrm{adv}} = Q^{+} - Q^{-} = -\frac{\dot{M}}{2\pi R^2}\frac{P}{\Sigma}\xi, \tag{4.6}$$

with the dimensionless advection factor, ξ, and the integrated plasma pressure, P.
Heating of the plasma thickens the disk. Therefore, ADAFs are *geometrically thick*. Under these circumstances the hydrostatic equilibrium is disturbed: sub–Keplerian rotation, typically $\Omega \approx 0.4\,\Omega_{\mathrm{kep}}$, can not stand the gravitational pull. Pressure gradients are not negligible anymore. The inward pointing radial velocity is comparable to the rotation velocity.

A suitable parameter to measure radiative efficiency is the fraction $f = \left(Q^{+}_{\mathrm{vis}} - Q^{-}_{\mathrm{rad}}\right)/Q^{+}_{\mathrm{vis}}$. No radiative cooling corresponds to $f = 1$ whereas efficient radiative cooling meets $f = 0$ as in case of SADs. The self–similar ADAF solution migrates to the SAD if $f \to 0$. Then $v_{\mathrm{R}} \ll v_{\mathrm{kep}}$ and $\Omega \to \Omega_{\mathrm{kep}}$ are restored.
However, in the ADAF solution of Narayan & Yi certain boundary conditions are assumed to solve the set of equations. The flow comes from infinity, $R \to \infty$, and terminates at $R = 0$. Both assumptions are questionable because the flow comes from a finite distance and especially terminates at the horizon of the black hole not at the singularity. But it was demonstrated that the influence of the outer boundary is irrelevant [Nar97].
It turned out that ADAF solutions form at low accretion rate, $\dot{M} \ll \dot{M}_{\mathrm{Edd}}$. This is because at low accretion rate the plasma becomes very tenuous and cooling is inefficient by radiation. As a consequence the flow becomes **advection–dominated**, $Q^{\mathrm{adv}} \simeq Q^{+}$. We will return to this fact in Sec. 4.3 when discussing morphology and physics of accretion solutions depending only on $\dot{M}$.

Radiatively–inefficient accretion flow (RIAF) are the more general term for an ADAF. Any accretion flow that satisfies $f \simeq 1$ can be considered as a RIAF. Specifically, RIAF incorporates also non–analytical solutions that compare to the analytical ADAF solution. Very little energy contained in the accretion flow is converted into radiation. As a consequence RIAFs are hot, evaporated and geometrically thick, $H \simeq R$. The thermal energy is comparable to the gravitational binding energy. Or in other words: the sound speed at any radius is comparable to the local escape velocity. Hence, RIAFs are favorable candidates to produce **outflows**.
A specific numerical advantage of RIAFs is that radiative transfer can be neglected. Of course, this is due to the fact that radiatively inefficient accretion flows are tenuous due to the high content of thermal energy. RIAFs are "effective dissipators". Another numerical advantage is the geometrical thickness. Therefore, in simulations a high grid resolution is not needed as in case of flat SADs.
The low radiative efficiency is triggered by a low accretion rate. It is suggested that this picture holds for the under–luminosity of Sgr A* [Qua03].

Convection–dominated accretion flow (CDAF) If radiation does not the cooling then turbulent energy transport – **convection** – or wind may do it. It has been shown that a RIAF with small turbulent viscosity exhibit dominantly convection. Hence, the acronym CDAF for *convection–dominated accretion flow* was suggested [Igu00]. An important difference to ADAFs is that CDAFs have a flat mass density distribution, $\rho \propto R^{-1/2}$. Though CDAFs drive outflows they are neither powerful nor relativistic; it is just a wind. The release of binding energy amounts approximately 1%.

Slim disk is some kind of intermediate stationary solution between SAD and ADAF – and therefore purely hydrodynamical models. Now, cooling is maintained by a function for optically *thick* cooling. In contrast to ADAFs, for slim disks the accretion rate is rather high, $\dot{M} \simeq \dot{M}_{\rm Edd}$ or even super–Eddington. *Slim* refers to the fact that this disk type is not geometrically thin. The relative thickness holds $H/R \leq 1$. The horizontal pressure gradient – negligible for SADs – becomes dynamically important for slim disks. Horizontal transport of thermal energy is established by advection. One important feature of slim disks is the **S–shaped correlation** between $\dot{M}$ and Σ for any fixed radius. Importantly, positive slope of the S–branches correspond to stable accretion models whereas negative slope corresponds to unstable models [Abr88].
The energy balance is strongly influenced by a huge horizontal heat flux. This emerges because large entropy gradients are present at super–Eddington accretion rates in slim disk models. This phenomenon is located at the innermost transonic part of the accretion flow.
The set of equations for slim disks were also formulated on the Kerr metric [Abr96]. Hence, this approach was formulated in the framework of **general relativistic hydrodynamics** (GRHD) and prepared the developments in GRMHD.
The slim disk scenario is applied to a special type of AGN, the narrow line Seyfert–1 galaxies (NLS1s). The accretion rate is very high and amounts several tens of Eddington rates or more. The soft X–ray humps occuring in most NLS1s are considered as a natural result of super–Eddington accretion. This is because a fraction of the accretion flow is released into the hot corona whereas the rest maintains the slim disk. Saturated Comptonization in the hot corona then contributes to the soft X–ray spectrum [Wan03].

Truncated disks – advective tori (TDAT) were found as self–consistent quasi–stationary solutions in the framework of radiative hydrodynamics (RHD) [Huj00a, Huj00b]. The calculations were performed incorporating a two–component plasma including ion/electron conduction with Comptonization, synchrotron radiation and bremsstrahlung. However, Relativity is only considered in the limit of a quasi–Newtonian description, the Paczynski–Wiita potential.
Without conduction it has been shown that the accretion disk truncates close to the ISCO, whereas a hot ion torus configuration forms in direct vicinity to the black hole. *Including conduction* results in three flow regions: The outer region has Keplerian ve-

locity profile, is optically thick and satisfies a one–temperature description, $T_{\rm ion} = T_{\rm e}$. In inward direction, there is a second region, the hot torus, where the velocity profile is sub–Keplerian and the flow is optically thin. Specifically, the Compton–Y parameter is small resulting in two–temperature description, $T_{\rm ion} \gg T_{\rm e}$. The third region attaches within the ISCO. Here, the gradient of the rotational velocity decreases steeply; the flow is superthin and isothermal. In the two–temperature description of ions and electrons, both fluids cool via advection and conduction. But there is an essential distinction between the two: electrons cool additionally by Comptonization. Finally, this leads to a larger cooling time scale for ions.
The simulations with conduction showed that a significant heat flux propagates from the innermost region in outward direction. This mechanism blows up the torus. Therefore, the truncation radius, $R_{\rm tr}$, is larger than the marginally stable orbit, $r_{\rm ms} = 3\,R_{\rm S} = 6\,r_{\rm g}$, satisfying $R_{\rm tr} \simeq 9\,R_{\rm S} = 18\,r_{\rm g} = 3\,r_{\rm ms}$.
The higher accretion rate e.g. by efficient external feeding the torus shrinks and survives within the ISCO. Simultaneously, the disk truncates at lower radii, $R_{\rm tr} \simeq 4\,R_{\rm S}$.
To a certain degree the TDAT scenario is at least morphologically comparable to SSD–ADAF transitions. However, the simulations could not confirm the emergence of relativistic outflows. There were only some non–relativistic outflows that are centrifugally driven. This fact may hint for the necessity of a fully relativistic description that is formulated on the background of a *rotating* space–time.

Cosmic sources hint strongly for the existence of **truncated standard disks** (TSDs). For stellar black holes, the BHXB Cyg X–1 switches essentially between two states, the soft and the hard state. Astronomers can observe this behavior in the X–rays; *hard/soft* refers to the hardness/softness of the spectrum. In the soft state the temporal analysis showed fast variations of reflected emission on time scale of a few tens of microseconds [Gil00]. In contrast, in the hard state the variations of reflected emission are reduced to a larger time scale of about one second. The reflected emission, i.e. the reflection bump around 20 keV, originates from hard coronal photons that are reflected at a cold disk. This view can be implemented in a TDAT scenario or a ADAF–SAD configuration: The optically thin hot inner accretion flow – the corona – that is identified by an advective torus or an ADAF, produces hot photon input. These coronal photons hit the cold disk that has an inner edge at the truncation radius (TDAT) or the marginally stable orbit (SAD). Now, the observed "rapid flickering" in Cyg X–1 can be interpreted by a radially oscillating disk: Gilfanov et al. used RXTE data and performed a spectral analysis with the XSPEC software. The fit result fixed the inner disk edge at $r_{\rm in} \simeq 100\,r_{\rm g}$ in the hard state and at $r_{\rm in} \leq 10\,r_{\rm g}$ in the soft state. So, the size of the hard photon emitter – the corona – shrinks in the soft state for the benefit of the SAD. However, in the hard state the corona i.e. the inner torus or the ADAF is huge. We will return to this in the context of the accretion unification scheme elaborated in Sec 4.3.
The relevant statement is that it is *not* in any case justified to consider a SAD that extends down to the ISCO. There are many examples exhibiting an inner edge that is farther away than the marginally stable orbit. This phenomenon is called disk truncation.

Considering the supermassive accreting black holes in AGN the scenario of a truncated disk may also be valid. A nice indicator for the nearness of corona and cold disk is the existence of X–ray fluorescence lines. They are a component of the reflection bump and lie around 6 to 7 keV. If the corona–disk system is close to the black hole these emission lines are strongly broadened by relativistic effects [Mül00]. In particular, gravitational redshift enlarges the line width tearing at the red wing. Actually, any AGN should show the feature of such a relativistically broadened line. But analyzing a huge sample of Seyfert–1s proves that only a small fraction of Seyferts possess a relativistic fluorescence line. This lack of broad lines can easily explained by disk truncation: The reflector i.e. the cold standard disk is to far away from the corona so that only weak fluorescence lines are produced. So absence of relativistic emission lines suggests disk truncation and this be associated with a low accretion rate, $\dot{m} \ll 0.01$, as we will see in the next section.

Non–radiative accretion flow (NRAF) The term non–radiative accretion flow refers to the fact that in this regime any radiation effects are neglected. Insofar, NRAF are comparable to RIAFs (see paragraph above). One may make a slight semantic distinction that in NRAFs radiation physics is excluded *a priori* – although it may be relevant. Radiation physics is excluded for simplicity to do a first step to solve the flow problem. In the literature the notion NRAF was first in use by Hawley, Balbus & Stone [Hawl01]. In 2001, these authors made first approaches to the 3D ideal MHD problem with a pseudo–Newtonian potential [Pac80]. It turned out to be a standard configuration to study the decay of an initial pressure supported torus. In these MHD studies turbulence is efficiently driven by the **magneto–rotational stability** (MRI), also termed as *Balbus–Hawley instability* (BHI) [Bal91a, Bal91b]. The MRI just needs weak magnetic fields and rotation as basic ingredients. The MRI is a very efficient mechanism for transport of angular momentum: a rotating plasma particle loses due to the MRI angular momentum that is transported in outward direction. The transport of angular momentum again is a vital presumption for accretion onto the black hole. The MRI physics is presented in more detail in Sec. 5.6.

Important progress was made in 2002: The simulation of NRAFs was generalized to full GR, i.e. 3D hydrodynamics on the background of the Kerr space–time [DeV02]. De Villiers & Hawley choose the Boyer–Lindquist frame (see Sec. 2.2). Later, this framework was extended to 3D GRMHD on the Kerr geometry [DeV03a]. In this work a complete chapter is devoted to this **General Relativistic Magnetohydrodynamics, GRMHD**, see Ch. 5.

The essential features emerging in simulations of a decaying plasma torus in GRMHD are in brief: The initial torus decays and the relic object of this torus is called the *main disk body*. The main disk body is dominated by gas pressure. Matter also backflows along the torus edges forming a *coronal envelope*. In the innermost region, a torus–like object forms called *inner torus* by the authors. At the axis of symmetry there is tenuous gas located, the *axial funnel*, and at lower poloidal angles there is an outflow, the *funnel–wall jet*. In these studies, it could not be confirmed that a relativistic outflow is generated

in the ergosphere of the Kerr black hole. The funnel jet is magneto–centrifugally driven and non–relativistic. We will return to the details of this simulation in Sec. 5.9.

After these short overview of accretion solutions we can summarize that SAD, ADAF, RIAF, CDAF can be found in a framework of non–radiative Newtonian hydrodynamics; the TDAT and TSD scenario is implemented within a radiative pseudo–Newtonian approach in hydrodynamics. Efficient magnetic turbulence generated by an operating MRI can be studied within a non–radiative Newtonian MHD framework. Non–radiative GRMHD opens the possibility to study relativistic effects on the accretion flow such as frame–dragging and launching of relativistic jets. This is the current cornerstone in accretion physics in the fluid description. Although it is not clear if the simulations of relativistic jets succeeded. At least, GRMHD in the flux tubes description prove the formation of jets. However, the most general case with the most complicated physics is radiative, dissipative GRMHD. Today, there is no robust method available to treat this regime.

4.3 Accretion Unification Scheme

In this section, a unified model for black hole accretion flows is presented following Esin et al. [Esi97]. Similar phenomenological classification were also considered earlier [vdK94, Now95]. The idea is motivated from observations of black hole X–ray binaries (BHXBs) i.e. accretion flows in stellar black hole systems. The accretion rate, $\dot{m} = \dot{M}/\dot{M}_{\rm Edd}$, is the relevant parameter that controls distinct states of the accreting black hole. The normalized accretion rate, $\dot{m}$, is of special interest because then it is possible to compare accretors of different black hole mass. Distinct states can be found in the multi–wavelength spectra of black hole candidates – independent from the black hole mass. So, the accretion unification scheme is based on a "BHXB concordance model".

The terms for each state refer to the accretion rate i.e. 'high' means high accretion rate comparable to the Eddington limit (as defined in Sec. 4.1). The accretion rate correlates to the luminosity: at high $\dot{m}$, there is also a high radiation output. Accretion theory assigns to each accretion rate a characteristic morphology of the accretion flow. Of course, these geometrical prerequisites influence the spectra.

The X–ray spectra can be analyzed and compared by the photon power–law index, $\alpha_{\rm N}$, by the occurrence and characteristic of a thermal black–body like feature and by a non–thermal high–energy feature with exponential cut–off. We will see that the spectra are linked to special geometries of the accretion flow namely the already presented SAD and ADAF. The spectral state types are now consulted and interpreted in these regards in the following brief paragraphs. Fig. 4.4 gives a synoptical view onto the resulting accretion unification scheme.

Very High State In the *very high state* the source is extremely luminous in X–rays. Non–thermal and black body–like components are comparable in flux. The photon index

is $\alpha_{\rm N} \simeq 2.5$ that compares to the high state. A high–energy cut–off was not observed.
The nearness to the Eddington luminosity hints for a very high accretion rate, $\dot{m} \approx 1$. As already outlined, the slim disk model fits this regime of accretion flow solutions. The hot corona is replenished by the accretion flow.
Due to the high luminosities an outflow may exist and be radiatively driven. At high accretion rate the flow is optically thick. Therefore, most photons are trapped in the flow and dragged into the black hole by the accreting gas.

High State Spectroscopically, the *high/soft state* is dominated by a modified black body with typical temperatures around 1 keV. A high–energetic power–law tail is subluminous. The power–law index is rather constant with $\alpha_{\rm N} \simeq 2.5$.
The SAD can exclusivly explain only this state. This means that there is no ADAF or at least a very small one. All other spectral states require hot optically thin gas with high electron temperatures, $T_{\rm e} \gtrsim 10^9$ K. The accretion rate is high, $\dot{m} \gtrsim 0.09$. There may also be a boundary layer between the disk and the black hole. The boundary layer acts as a corona. However, in this case the exact disk–corona geometry is unknown (e.g. slab, sphere+disk, patchy, see also Fig. 4.2).

Low State The *low/hard state* exhibits a power–law spectrum with a photon index $\alpha_{\rm N} \sim 1.5 - 1.9$. A high–energy exponential cut–off at about 100 keV is observable. The X–ray luminosity holds $L_{\rm X} \lesssim 0.1\, L_{\rm Edd}$.
The observed luminosities suggest an accretion rate of $0.01 \geq \dot{m} \geq 0.08$. The flow geometry is similar to the quiescent state, however the ADAF is smaller. The model geometry can be termed as a sphere+disk geometry where the SAD is sandwiched by an ADAF. Under these geometrical assumptions – the proximity of hot ADAF and cold disk matter – two processes can easily occur: one is Comptonization i.e. cold seed photons from the disk hit the ADAF and gain energy by inverse Compton scattering. This generates the characteristic high–energy cut–off around 100 keV. The second process is the production of fluorescence lines: hot photons originating from the ADAF are reflected at the cold SAD. Thereby fluorescence lines form, dominantly Fe Kα at 6 to 7 keV. This scenario suggests that relativistically broadened emission lines are essentially created in the low state.
The most significant feature is an extended outflow. The low state is favored to produce the jets.

Quiescent State The *quiescent/off state* is characterized spectroscopically by a non–black body and softer photon indices than in the low state, $\alpha_{\rm N} \lesssim 1.5$. Additionally, quiescence is determined by an all–over suppressed flux that is several orders of magnitude below the Eddington luminosity. Quiescent BHXBs are the so–called *soft X–ray transients* (SXTs).
The underluminosity can be explained by a very low accretion rate, typically $\dot{m} \lesssim 0.01$. Such a process occurs by a lack of feeding from the black hole surroundings. The morphology of the accretion flow compares to the low state, but there is no jet and the

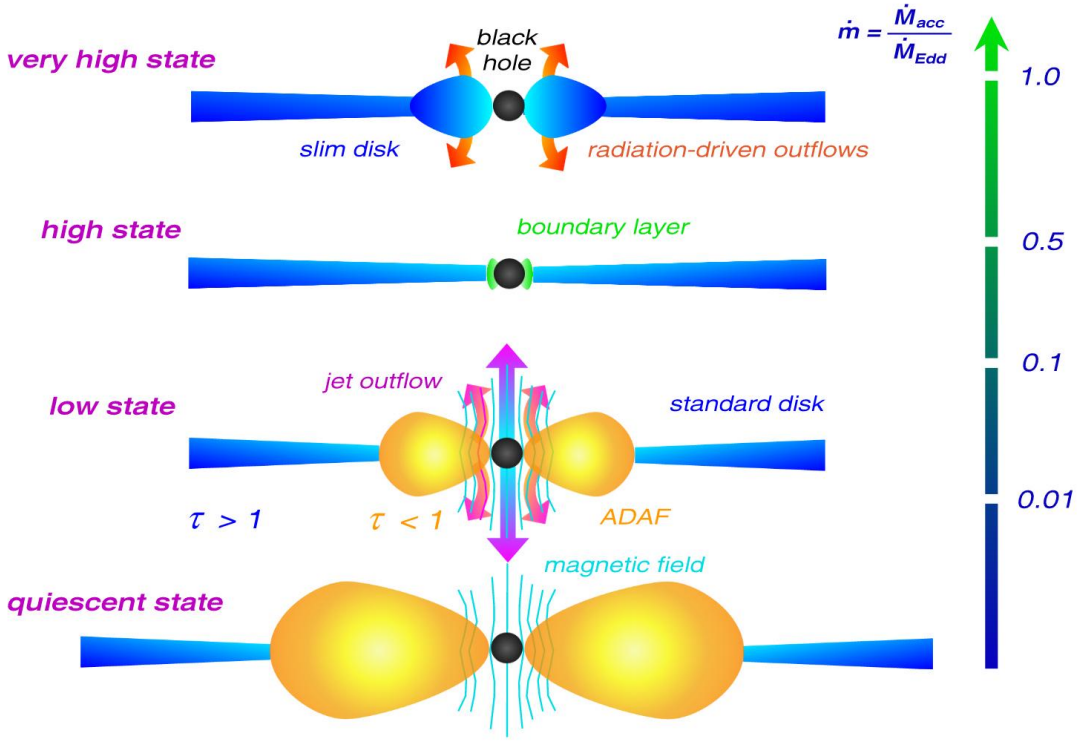

Figure 4.4: Illustration of a unified scheme for black hole accretion. The mass dependent accretion rate, $\dot{M}$, is scaled to a mass independent quantity, $\dot{m}$, by means of the Eddington accretion rate, $\dot{M}_{\mathrm{Edd}}$. Accreting black holes with arbitrary mass can thereby be compared. The accretion rate triggers distinct states that are identified by spectral features. The very high state has greatest accretion rate that decreases to high state, (possibly intermediate,) low state and quiescent state. (adapted to [Esi97])

ADAF is bigger in size. This is due to the fact that at low accretion rates the flow becomes more advection–dominated.

Sometimes, it is referred to an *intermediate state* lying between high and low (i.e. hard and soft) state. Not all states were detected at any BHXB; some switch only between two states, others spend their whole life in only one state. Transients cycle through all states.

Originally, the just presented state nomenclature was suggested while studying stellar black hole sources. But it is possible to generalize the picture to accretion flows around supermassive black holes. Thereby, it is suggested to unify both, AGN and inactive galaxy cores. Essentially, the variety of galaxy cores is only determined by the following parameters [Cam02]:

- black hole mass, M,
- black hole spin, a,
- accretion rate of the disk, $\dot{M}$,
- inclination angle of the disk to the observer, i,
- mass of the dusty molecular torus, $M_{\rm dust}$,
- seed magnetic field of the molecular torus, $B_{\rm seed}$.

Certainly, these parameters are interdependent e.g. a higher mass of the dusty torus results in a higher feeding rate of the core. Considering the measurements of black hole masses and comparing it with the activity of the galactic nucleus, it seems that a more massive black hole effectuates a more luminous core. The black hole spin determines the jet activity if an ergospheric origin by Poynting fluxes is presumed. This will be intensively analyzed in Sec. 5.9. If the rotational energy of the Kerr black hole is one energy channel that can be tapped by surrounding material this suggests that there are two AGN types: one that uses this channel (Kerr) and one that has already exploited this channel (Schwarzschild). Hence, this could explain the emergence of the radio dichotomy of AGN in radio–quiet sources (without jets) and radio–loud sources (with jets). As demonstrated above, the mass accretion rate, $\dot{M}$, controls the spectral state by feeding. The inclination angle controls the AGN appearance by simple orientation to the observer: For AGN type 1 the galaxy core and BLRs are visible; for AGN type 2 the core region is obscured by the large–scale dusty torus.

Nevertheless, there be some essential differences between stellar black hole and supermassive black hole accretion [Cam04]. Observations of putative dust tori using Faraday rotation methods suggest that AGN have **well organized global magnetic field structure**. The field structure is transported to the smaller scale towards the central black hole by the accretion process. At some time the global field is as close to the Kerr black hole as it could be dragged by the rotating space–time. Hence, the more or less aligned large–scale field structure is then rearranged by frame–dragging. Stationary accretion theory tells that ergospheric Poynting fluxes are generated that drive outflows magnetically.
The well arranged global magnetic field seems to lack in stellar black hole systems. Magnetic seed fields from the progenitor stars are too weak. Possibly, this scenario explains that there are significantly fewer and weaker jet structures in stellar systems.
Stellar black holes are easier accessible to observations in many respects: There are more nearby sources providing better spatial resolution of the system; the timescales of variabilities (e.g. QPOs) are much shorter allowing shorter monitoring times.

This section is closed with some examples for spectral states:
A special AGN type, the NLS1s, can be modeled with extreme slim disks that are endowed with an accretion rate $2.5 \ll \dot{m} \lesssim 100$ [Wan03]. These sources live in very

high states. Cyg X–1 for example switches only between high and low state due to the low eccentricity of the companion's orbit. When the black hole in Cyg X–1 approaches the companion star the mass accretion rate rises. Then, the X–ray source enters the high/soft regime.

The starving black hole at the Galactic Center is characterized by a low accretion rate. Therefore, Sgr A* is in a quiescent state. The spectrum is characterized by an underluminosity by several orders of magnitudes. If one takes an intermediate value of 3.0×10^6 $M_\odot$ and postulates accretion at the Eddington rate, its Eddington luminosity is about 3.0×10^{44} erg s^{-1} [Bag03].

4.4 Jet Engine

Jets are directed outflows of material that occur in a variety of cosmic sources: protostellar jets are produced by young stellar objects (YSOs) such as Herbig–Haro objects or T–Tauri stars. Cataclysmic variables (CVs) show jets generated in an accretion disk in the vicinity of a white dwarf. Relativistic jets can be found in long–term GRBs (hypernovae). As essential topic of this work relativistic jets are created in BHXBs and AGN. Jets can be divided in two classes depending on the size of the system: micro jets form in stellar systems whereas macro jets are generated in galactic cores.

It turned out that an accretion disk is a vital ingredient for the generation of jets. This is sometimes termed as the **jet disk symbiosis** [Fal95]. An outflow is quite a natural phenomenon simultaneously occuring with the accretion process. However, it depends on certain presumptions if the outflow is significant and more importantly if it is relativistic. We noticed in the discussion of the accretion unification scheme in the former section that e.g. the accretion rate controls the formation of outflows. The outflow's speed depends on the formation process. Highest velocities i.e. relativistic motion is caused by rotating black holes. This is topic of Sec. 5.9. It is essential to distinguish a wind from a jet. The notion jet denotes a directed and collimated outflow; in contrast, a wind is typically quasi–isotropic and uncollimated.

In the beginning, the formation process of jets was described with pure hydrodynamics. But it turned out that purely gas–pressure driven outflows do not fit the observations e.g. neither reach high relativistic speeds nor show collimation. Magnetic fields prove to be an efficient mechanism to generate outflows and to drive and collimate jets. Hence, MHD prove to be the right framework to study jets.

In the *Blandford–Payne scenario* [Bla82], there is no need for a rotating black hole but for a rotating accretion disk, typically a SAD. The accretion disk is threaded by magnetic flux tubes which extend to larger length scales. Plasma can be extracted from the disk and transported away along the field lines. Then, the outflow originates directly from the accretion flow and is purely centrifugally driven. The outflow speed is comparable to the rotation velocity. Hence, the relativistic outflows can only originate from the innermost part of the accretion disk where the orbit velocity becomes relativis-

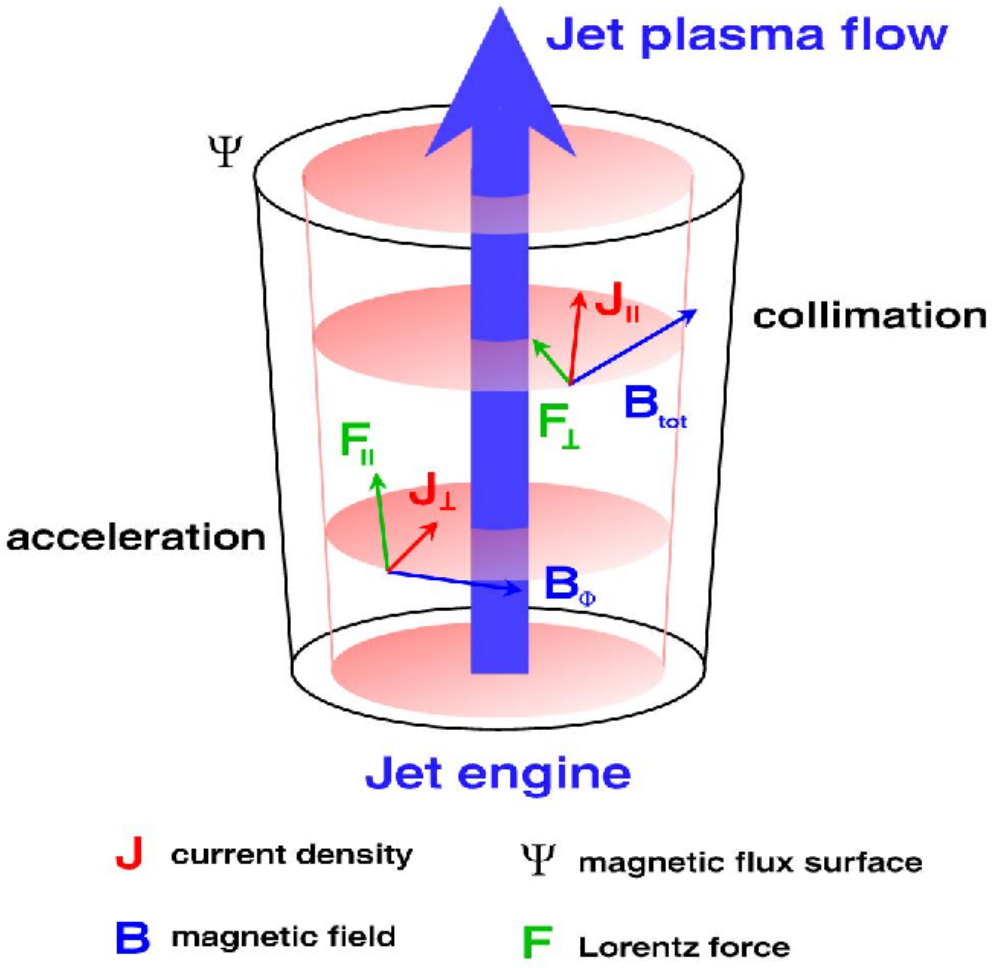

Figure 4.5: Magnetic acceleration and collimation of a jet via Lorentz forces (Illustration idea taken from *Christian Fendt, University of Potsdam*).

tic. A hot magnetically dominated corona e.g. an ADAF solution may contribute and drive the flow by gas pressure. In some distance (around 100 R_S) the acceleration and collimation of the outflow is done by the toroidal component of magnetic field. Fig. 4.5 illustrates how Lorentz forces accelerate and collimate the jet. Acceleration is generated by azimuthal magnetic fields. Finally, the macro jets of AGN form that can be observed in radio–loud quasars and radio galaxies and propagate to the kpc– and Mpc–scale. More than 25 years ago these relativistic macro jets were proposed to produce the radio emission in AGN [Bla78].
An additional acceleration process is **reconnection**. Dissipative effects in a relativistically hot pair plasma seem to play a crucial role in relativistic jets. The annihilation of

magnetic fields is transferred to the jet plasma. So, reconnection supports acceleration of the outflows. This was pointed out for the MHD winds occuring in pulsars such as in the Crab nebula [Kir03]. The importance of such dissipative effects signals that any ideal MHD approach will breakdown at a certain point. Typically, the first steps in GRMHD are based on ideal MHD as we will see in Ch. 5.

In the presence of a rotating black hole the magnetosphere of the accretion flow is immersed into the ergosphere. Then the operation of ergospheric processes starts. As outlined in Sec. 3.5, energy and angular momentum of the Kerr hole can be extracted by the via Blandford–Znajek mechanism [Bla77]: In a purely electromagnetic description it was shown that external currents delivered by a Keplerian accretion disk form a magnetosphere of leptonic pairs. This is established due to induction of an electric potential difference that provide high field strengths. Hence, the Blandford–Znajek mechanism describes a scenario for a source of relativistic electrons that feed leptonic AGN jets.

The rotating space–time turned out to be important in another perspective: Frame–dragging provides ergospheric outflows that are magnetically–driven by Poynting fluxes. The rotation of space–time is crucial to launch relativistic jets. Relativistic AGN and GRB jets are proposed to be formed in this way.

The geometrical setup is outlined in Fig. 4.6: The accretion process is triggered by the magneto–rotational instability (see Sec. 5.6). Thereby, angular momentum of the plasma is transported in outward direction causing the plasma to drift radially inward. This feeds the hot core region and generates due to radiatively inefficient cooling an ADAF in the vicinity of a rotating black hole. Differential rotation builds up strong magnetic fields, especially in the ergosphere as we will see in the flux tube simulations of Semenov et al. [Sem04a] in the next chapter. Frame–dragging thereby generates dominant toroidal magnetic fields due to $\frac{\partial \vec{B}_\phi}{\partial t} \propto \vec{B}_\mathrm{P}\,\vec{\nabla}\Omega$. The shear of spacetime even works for zero–angular momentum flows, $\lambda = 0 \rightarrow \Omega = \omega$. The gradient of the frame–dragging frequency is much steeper than the gradient of the Keplerian angular frequency: The term $\vec{B}_\mathrm{P}\,\vec{\nabla}\omega$ provides a strong source term for poloidal currents [Kha99].

In this regime, the MRI dies out because strong magnetic fields reach the equipartition threshold. The magnetized flow plunges into the ergosphere where frame–dragging operates efficiently. Here, a Poynting flux is formed i.e. a magnetic energy flux that feeds an outflow. A crucial question concerns the mixing of Poynting flux and mass flux and the consequences for the outflow. The cornerstones in jet physics so far prove that a pure mass flux does not suffice to launch relativistic jets. Jets are supposed to be *Poynting–flux dominated outflows*. But exact ratio of Poynting to mass flux is still debated. The mathematical details of relativistic jet production is topic of the next chapter. Then, the open questions of this section are revisited.

Finally, the morphology of a typical jet is demonstrated for a classical purely hydrodynamical issue. Fig. 4.7 sketches the basic structures of a non–relativistic hydro jet in some distance from the central source. The jet is injected by an *engine* e.g. a black hole and propagates through an external medium. At the front side where the jet beam hits

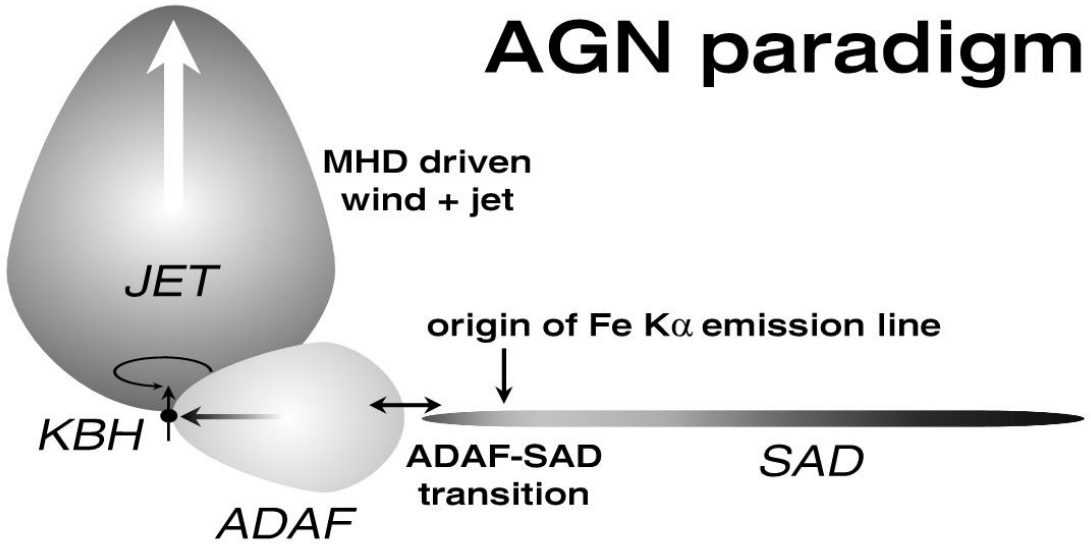

Figure 4.6: Structural ingredients for the AGN paradigm. From the outside the optically thick but geometrically thin standard accretion disk, SAD, makes a transition to the inner hot optically thin but geometrically thick accretion flow. It is often assumed that this is an advection–dominated accretion flow, ADAF. The magnetosphere of the plunging accretion flow interacts with the rotating space–time of the Kerr black hole, KBH. Thereby, relativistic outflows are created, the JETs, that are magnetically driven.

the surroundings a *bow shock* occurs. Just behind this shock there is the *contact discontinuity* where density and pressure jump discontinuously. Close to this discontinuity there is the *Mach disk* located. At this locus a backflow is generated that encloses the jet beam. This is called the *cocoon*. At the cocoon edges typically *Kelvin–Helmholtz instabilities* arise due to the distinct adjacent flow velocities. In the jet plasma there occur *internal shocks* that are obviously connected to the emission knots that are observed in a variety of jets.

This section gives an impression how the formation of relativistic GRMHD jets works phenomenologically. The numerical task is to test this scenario time–dependently on a computer. The next chapter prepares basic equations of GRMHD. Robust numerical schemes must be developed to solve this discretized set of equations. Relevant results of time–dependent GRMHD are later discussed in Sec. 5.9.

The simulated jet structures vary depending on the regime i.e. the problem is solved via hydrodynamical vs. MHD schemes or relativistic vs. non–relativistiv schemes. Observations prove basically that these structures can be found in real jets, too. Many of these simulated structures could be confirmed in observations of radio galaxies and radio–loud quasars.

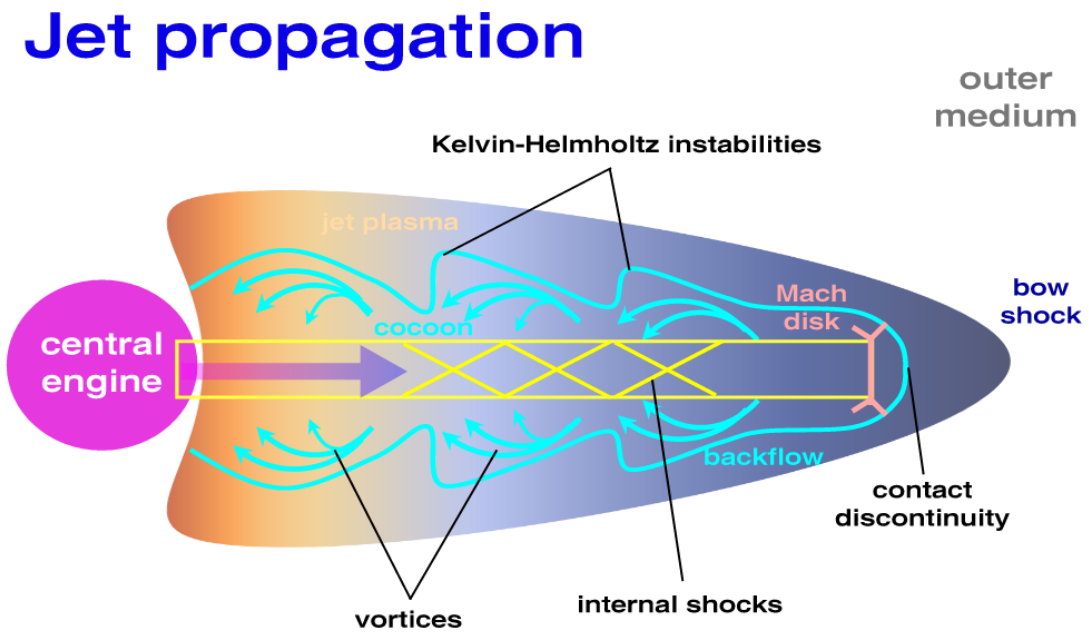

Figure 4.7: Propagating hydro–jet moving through a surrounding medium from left to right. Basic structures are highlighted. For details see descriptions in the text.

5 General Relativistic Magnetohydrodynamics

5.1 Motivation

After this review of black hole physics concerning GR on one hand and astrophysics on the other hand we are now prepared to investigate the main topic of this work: General Relativistic Magnetohydrodynamics (GRMHD). GRMHD provides a suitable framework to study time–dependent black hole hydrodynamical accretion including electrodynamic and general relativistic effects.
The motivation to construct a GRMHD framework is manifold: First of all a new branch of accretion theory is established by connecting MHD to full GR. The magneto–rotational instability (MRI) turned out to be a very efficient mechanism to magnetically induce transport of angular momentum and should be checked also in curved space–times. The observation of relativistic micro–jets (X–ray binaries, GRBs) and macro–jets (AGN) demands for a powerful model to explain these outflows. Stationary accretion theory suggests that a rotating space–time provides a powerful driver (see Sec. 4.4). The detection of supermassive compact and dark galactic centers motivates to study these effects on the background of the Kerr geometry. The accretion flow pattern in the vicinity of the black hole governs the spectra that originate from there. Of particular interest is the corona geometry, the corona–disk interrelation and the resulting spectral features e.g. X–ray fluorescent lines, Comptonized continua and their variablity. The interest in stellar black hole systems focuses on an understanding of the micro–jet structure and of GRBs. Summarizing these systems, it is sometimes referred to *relativistic magneto–rotators* (RMRs) [Gam03]. RMRs can be found in AGN, X–ray binaries, GRBs and SN type II.

It is clear that GRMHD comes into play in the innermost region of an AGN. The accretion flow is strongly influenced by the curved rotating space–time. In a first approximation cooling and heating by radiation is neglected. This may be motivated by the fact that the accretion flow moves with relativistic speeds so that radiation cannot significantly influence the flow before it is lost beyond the horizon. Therefore, the domain of NRAFs as presented in Sec. 4.2 applies here in a first relativistic approach. Astrophysical observations will evaluate the regime where this approximation holds.
The metric is considered as a *background* for the plasma flow, i.e. the energy–momentum of the flow does not couple to the metric and does not significantly deform the Kerr metric. This is a customary simplification in general relativistic hydrodynamics and magnetohydrodynamics.

5.2 Ideal GRMHD and Conserved Currents

In the formulation of the problem we will essentially follow Misner, Thorne & Wheeler (1973) [MTW73] and Camenzind [Cam86a, Cam86b] concerning the basics as well as Gammie et al. [Gam03] for general aspects of GRMHD.

Generally, GR provides a set of *locally conserved quantities*. The **basic relativistic equations in covariant form** are

$$\nabla_\mu \mathbf{T}^{\mu\nu} = 0, \tag{5.1}$$
$$\nabla_\mu N^\mu = 0, \tag{5.2}$$
$$\nabla_\mu {}^*\mathbf{F}^{\mu\nu} = 0, \tag{5.3}$$

with the energy–stress tensor, $\mathbf{T}^{\mu\nu}$, the particle 4–current, $N^\mu = n\,U^\mu$ (proper particle number density, n, and fluid 4–velocity, U^μ), and the Faraday tensor, ${}^*\mathbf{F}^{\mu\nu}$. The first equation is simply the general relativistic extension of **energy conservation** and **momentum conservation**. The second states local particle number conservation and is known as **continuity equation**. The third is the **induction equation** that is considered in more detail in the upcoming paragraph about Maxwell equations. So far, this set of equations is completely general and holds as well for relativistic hydrodynamics as for relativistic MHD for any metric. The three equations contain the whole dynamics of ideal GRMHD. It is now pursued to bring them in a suitable form for a numerical scheme.

Energy–stress tensor for one–component plasma First, the task is to specify the energy–momentum tensor, $\mathbf{T}^{\mu\nu}$, as adapted to the GRMHD problem. To study magnetized accretion flows it is necessary to take an energy–stress tensor that incorporates both, the plasma described as a perfect fluid and the electromagnetic field

$$\mathbf{T}^{\mu\nu}_{\mathrm{GRMHD}} \equiv \mathbf{T}^{\mu\nu}_{\mathrm{fluid}} + \mathbf{T}^{\mu\nu}_{\mathrm{EM}}. \tag{5.4}$$

Therefore, the total energy–stress tensor satisfies

$$\boxed{\mathbf{T}^{\mu\nu} = (\rho + e + P)U^\mu U^\nu + P\,\mathbf{g}^{\mu\nu} + \frac{1}{4\pi}\left(\mathbf{F}^\mu{}_\alpha\,\mathbf{F}^{\nu\alpha} - \frac{1}{4}\mathbf{F}_{\alpha\beta}\,\mathbf{F}^{\alpha\beta}\,\mathbf{g}^{\mu\nu}\right).} \tag{5.5}$$

Therein, $\mathbf{F}^{\mu\nu}$ denotes the Maxwell tensor that collects all components of the electric and magnetic fields. Additionally, we have isotropic pressure, P, mass density, ρ, and specific internal energy, e, that are related by an equation of state (EOS). Typically an **ideal gas** is assumed to describe the plasma. Therefore the EOS takes the form

$$P = (\gamma - 1)\,\rho\,e, \tag{5.6}$$

with an adiabatic exponent γ. Sometimes, it is useful to write the energy–momentum tensor for a perfect fluid with the specific enthalpy, h

$$\mathbf{T}^{\mu\nu}_{\mathrm{fluid}} = \rho\,h\,U^\mu U^\nu + P\,\mathbf{g}^{\mu\nu}. \tag{5.7}$$

The specific enthalpy is defined as $h = 1 + e + P/\rho$.

The regime of an one–component plasma description can be outlined as follows: A relativistic single–fluid formulation is only valid for a dense plasma. Then, the Coulomb interactions provide a redistribution of momentum to justify a one–component description. In contrast, a two–component description is recommended for a tenuous plasma e.g. in hot accretion flows. The basic equations for GRMHD of a two–component plasma in the 3+1 split are available [Kha98].

Maxwell equations In Relativity, the notions of electric and magnetic fields are reintroduced in the 3+1 split (see Sec. 5.4) and can be measured in local Lorentz frames. Then, one arrives at the covariant form of the **inhomogeneous Maxwell equations** in Special Relativity. These equations can easily be extended to other frames by substituting partial with covariant derivatives

$$\nabla_\nu \, \mathbf{F}^{\mu\nu} = 4\pi \, j^\mu, \tag{5.8}$$

$$\nabla_\nu \, {}^*\mathbf{F}^{\mu\nu} = 0. \tag{5.9}$$

These are the four Maxwell equations of electrodynamics written relativistically in compact form. The first equation, Eq. (5.8), summarizes Coulomb's and Ampère's equation whereas the second one, Eq. (5.9), summarizes Faraday's equation and the no–magnetic–monopoles equation. The second equation is also called **induction equation**. A natural consequence of this set of equations is **conservation of electric charge**

$$\nabla_\mu j^\mu = 0. \tag{5.10}$$

This corresponds to the continuity equation in relativistic hydrodynamics when a matter current density is considered[1].
$\mathbf{F}^{\mu\nu}$ in Eq. (5.8) is the electromagnetic field tensor or **Maxwell tensor**, $j^\mu = (\rho_\mathrm{c},\, j^i)^\mathrm{T}$ denotes the charge current density 4–vector with charge density, ρ_c, and purely spatial charge current 3–vector, j^i. The Maxwell tensor is also connected to a 4–potential, $\mathbf{F}_{\mu\nu} = \partial_\mu A_\nu - \partial_\nu A_\mu$. The tensor ${}^*\mathbf{F}^{\mu\nu}$ is the dual of the Maxwell tensor, the **Faraday tensor**, which can be computed by

$${}^*\mathbf{F}^{\kappa\lambda} = \frac{1}{2} \, \epsilon^{\kappa\lambda\mu\nu} \mathbf{F}_{\mu\nu}. \tag{5.11}$$

Here, the **Levi–Civita tensor**, $\epsilon^{\kappa\lambda\mu\nu}$, is introduced which is totally antisymmetric and of 4th rank. In curved space–times it holds

$$\epsilon^{\kappa\lambda\mu\nu} = \begin{cases} -1/\sqrt{-g} & \text{, even index permutation} \\ +1/\sqrt{-g} & \text{, odd index permutation} \\ 0 & \text{, otherwise.} \end{cases} \tag{5.12}$$

This is also written as $\epsilon_{\kappa\lambda\mu\nu} = \sqrt{-g}\,[\kappa\lambda\mu\nu]$.

[1] In GRMHD, one has to be careful not to mix up charge density and matter density as well as charge current and matter current!

Ideal GRMHD Magnetic induction, b^μ, and electric field, e^μ, in the fluid rest frame (comoving frame i.e. Lagrangian formulation) can be recovered as space–like 4–vectors by [Lic67, Ani89]

$$b^\mu = {}^*\mathbf{F}^{\mu\nu}\, U_\nu, \tag{5.13}$$
$$e^\mu = \mathbf{F}^{\mu\nu}\, U_\nu. \tag{5.14}$$

Now, MHD is simplified to ideal MHD. This is motivated by the fact that conductive effects are neglected in a first approximation. *Ideal* MHD means *infinite conductivity* ("flux–freezing condition") i.e. the electric field in the fluid rest frame vanishes. Hence, from the second equation, Eq. (5.14), it follows that $\mathbf{F}^{\mu\nu}\, U_\nu = 0$.

It turns out that the explicit form of the magnetic field 3–vector, $B^i = {}^*\mathbf{F}^{it}$, plays an important role in GRMHD [Komi99]. The magnetic field 4–vector can be written in terms of B^i

$$b^t = B^i U^\mu g_{i\mu}, \tag{5.15}$$
$$b^i = (B^i + b^t U^i)/U^t. \tag{5.16}$$

Using a coordinate basis, the induction equation, Eq. (5.9), splits into

$$\partial_t \left(\sqrt{-g}\, B^i\right) = -\partial_j \left(\sqrt{-g}\, (b^j U^i - b^i U^j)\right), \tag{5.17}$$
$$\frac{1}{\sqrt{-g}}\, \partial_i \left(\sqrt{-g}\, B^i\right) = 0. \tag{5.18}$$

The latter equation, Eq. (5.18), can be identified as the relativistic generalization of the no–magnetic–monopoles constraint.

In ideal GRMHD, the energy–stress tensor can be rewritten in a more convenient form (see Appendix A.1). The flux–freezing condition plus orthogonality, $b^\mu U_\mu = 0$, yields to

$$\mathbf{T}^{\mu\nu} = \left(\rho + e + P + \frac{b^2}{4\pi}\right) U^\mu U^\nu + \left(P + \frac{b^2}{8\pi}\right) \mathbf{g}^{\mu\nu} - \frac{1}{4\pi} b^\mu\, b^\nu, \tag{5.19}$$

with $b^2 = \mathbf{g}^{\mu\nu} b_\mu\, b_\nu = b^\nu\, b_\nu$. In this energy–stress tensor of ideal GRMHD the *Maxwell stress tensor*, $\mathbf{t}^{\mu\nu}_{\mathrm{M}}$, can be identified

$$\mathbf{t}^{\mu\nu}_{\mathrm{M}} = \frac{1}{8\pi} \left(b^2\, \mathbf{g}^{\mu\nu} + b^2 U^\mu U^\nu - 2\, b^\mu b^\nu\right). \tag{5.20}$$

Conserved variables The conserved quantities are related to the symmetries of the space–time. This is the fundamental statement of *Noether's theorem* which also applies in GR. The symmetries again can be expressed with Killing vectors, $\xi^\nu_{(a)}$: The higher the symmetry, the more Killing vectors exist. These fields can be extacted from the

Killing equation, a condition for vanishing Lie–derivative of the metric (isometry condition), $\mathcal{L}_\xi \, \mathbf{g}_{\mu\nu} = \nabla_\mu \, \xi_{\nu \ (a)} + \nabla_\nu \, \xi_{\mu \ (a)} = 0$. The **conserved currents**, $K^{\mu}_{\ (a)}$, follow by a contraction of the energy–momentum tensor with the available Killing fields

$$K^{\mu}_{\ (a)} = \xi^{\nu}_{\ (a)} \mathbf{T}^{\mu}_{\ \ \nu}. \tag{5.21}$$

The fundamental energy conservation, Eq. (5.1), thereby transforms to the **conservation laws**

$$\nabla_\mu K^{\mu}_{\ (a)} = 0. \tag{5.22}$$

The index (a) specifies the coordinate related to the symmetry. One sees immediately that the number of conserved currents is connected to the number of Killing fields.

This apparatus is now applied to the energy-stress tensor of GRMHD, Eq. (5.5). Further, it is specified to a stationary and axisymmetric space–time that is endowed with two Killing vectors, $\xi^{\nu}_{\ (\mathrm{t})} = \partial_{\mathrm{t}}$ for stationarity and $\xi^{\nu}_{\ (\phi)} = \partial_\phi$ for axisymmetry. The Kerr geometry is one representative of this space–time family. Then, one finds the following **conserved currents of MHD on the Kerr geometry**:
The *energy current*

$$P^\mu = \mathbf{T}^{\mu}_{\ \ \nu} \, \xi^{\nu}_{\ (\mathrm{t})}, \tag{5.23}$$

the *angular momentum current*

$$J^\mu = -\mathbf{T}^{\mu}_{\ \ \nu} \, \xi^{\nu}_{\ (\phi)}, \tag{5.24}$$

that satisfy the conditions $\nabla_\mu \, P^\mu = 0$ and $\nabla_\mu \, J^\mu = 0$ as more generally stated in Eq. (5.22). It is stressed here that Relativity provides these conservation laws in *any* case: $\exists$ a conserved energy current whether or not the accretion flow is stationary; $\exists$ a conserved angular momentum current whether or not the accretion flow is axisymmetric!
The explicit expressions of these conserved currents follow by inserting Eq. (5.19) into Eqs. (5.23) and (5.24) [Cam86a]

$$P^\mu = \bar{h} \, U_t N^\mu - \left(P + \frac{b^2}{8\pi} \right) \xi^{\mu}_{\ (\mathrm{t})} - \frac{1}{4\pi} \left(b_\nu \, \xi^{\nu}_{\ (\mathrm{t})} \right) b^\mu, \tag{5.25}$$

$$-J^\mu = \bar{h} \, U_\phi N^\mu - \left(P + \frac{b^2}{8\pi} \right) \xi^{\mu}_{\ (\phi)} - \frac{1}{4\pi} \left(b_\nu \, \xi^{\nu}_{\ (\phi)} \right) b^\mu, \tag{5.26}$$

where the specific enthalpy is generalized to the relation $\bar{h} = h + \frac{b^2}{4\pi n}$ in relativistic MHD. Eq. (5.25) states from left to right that the total energy flux is composed of particle flux, plasma flux[2] and **Poynting flux**. Eq. (5.26) can be interpreted analogously as particle angular momentum flux, plasma angular momentum flux and electromagnetic angular momentum flux.

[2] in MHD modified by additional magnetic pressure

Both conserved currents are related to conserved quantities, **total energy**, E, and **total angular momentum**, J, that are conserved along the plasma flow

$$N^\mu \nabla_\mu E = 0, \tag{5.27}$$
$$N^\mu \nabla_\mu J = 0. \tag{5.28}$$

In other words: The constants of motion, E and J, are advected with the flow.

The next step is the conservative formulation of the GRMHD problem. Before this can be done a coordinate system must be chosen. In the next section it is examined which coordinate system is suitable to the accretion physics near rotating black holes. It will turn out that we leave the customary path and prefer the use of the Kerr–Schild frame instead of the Boyer–Lindquist frame. This is motivated by GRHD. In Sec. 5.4 a formalism of numerical Relativity is introduced: the 3+1 split. We will elaborate essential formulas in the Kerr–Schild frame. Then, ideal GRMHD is revisited to present the equations in conservative form. Hence, the next two sections may be regarded as a slide–in.

5.3 A suitable Coordinate System

The Kerr solution can be expressed in different coordinate frames. In Ch. 2 the historical Cartesian form, Eq. (2.3), and the standard pseudo–spherical Boyer–Lindquist form, Eq. (2.5), were presented. Rotating black holes are usually described by the Boyer–Lindquist system. However, a closer look reveals that they are not well suited to describe black hole physics, especially near the event horizon. The reason is that these coordinates are not regular at the horizons. This is an analogous behavior to Schwarzschild coordinates that diverge at the Schwarzschild radius in the static case. Hence, using the Boyer–Lindquist frame requires some techniques like *tortoise coordinates* e.g. to adjust the boundary condition at the outer horizon in general relativistic hydrodynamical simulations (for details see Sec. 5.7).

To overcome those difficulties, one removes the coordinate singularities by a coordinate transformation. The procedure was first elaborated by Papadopoulos, Font et al. [Pap98, Fon98]. They introduced a new coordinate family, the *horizon adapted coordinates*.
Horizon adapted coordinates are generically regular and stationary at the horizon. They are derived in its most general form by the following coordinate transformations of the Boyer–Lindquist frame $\{t, r, \theta, \phi\}$ to the new system $\{\tilde{t}, r, \theta, \tilde{\phi}\}$

$$d\tilde{\phi} = d\phi + \frac{a}{\Delta}\, dr, \tag{5.29}$$
$$d\tilde{t} = dt + \left[\frac{1+Y}{1+Y-Z} - \frac{1-Z^k}{1-Z}\right] dr, \tag{5.30}$$

with $Y = a^2 \sin^2\theta/\rho^2$ and $Z = 2Mr/\rho^2$. ρ and Δ as defined in Eqs. (2.6) to (2.11). The positive integer k parametrizes the whole family of horizon adapted coordinate systems.

The algebraically simplest choice is to fix the parameter to $k = 1$: Then one arrives at the **Kerr–Schild frame** as the preferred representative of the family. The line element of the Kerr geometry reads in pseudo–spherical Kerr–Schild coordinates [Fon98, Komi04a]

$$\begin{aligned} ds^2 &= -(1-Z)\,d\tilde{t}^2 - 2Za\sin^2\theta\,d\tilde{t}\,d\tilde{\phi} + 2Z\,d\tilde{t}\,dr + \left(\frac{\Sigma\sin\theta}{\rho}\right)^2 d\tilde{\phi}^2 \\ &\quad -2a\,(1+Z)\sin^2\theta\,d\tilde{\phi}\,dr + (1+Z)\,dr^2 + \rho^2\,d\theta^2. \end{aligned} \tag{5.31}$$

One immediately recognizes that the line element is more complicated than in Boyer–Lindquist coordinates: Now, there are *three* cross terms instead of only one. This is the price that one has to pay to remove the coordinate singularity. As compared to the Boyer–Lindquist frame, the Kerr–Schild system has the new Z–function. Another function, $\tilde{Z}$, is useful, too and especially emerges for the contravariant metric, $g^{\mu\nu}$, by

$$\tilde{Z} = \tilde{\omega}^2 - (Z+1)a^2\sin^4\theta. \tag{5.32}$$

Covariant and contravariant Kerr metric in the Kerr–Schild system written in matrix form are elaborated in the Appendix A.2.

The pathology vs. the non–pathology of the Boyer–Lindquist frame vs. the Kerr–Schild frame is best illustrated in plotting and comparing the lapse functions. From Eqs. (2.6) to (2.11), the lapse function in the Boyer–Lindquist system satisfies $\alpha_{\mathrm{BL}} = \rho\sqrt{\Delta}/\Sigma$. In contrast, the lapse function in the Kerr–Schild frame holds [Komi04a],

$$\alpha_{\mathrm{KS}} = 1/\sqrt{1+Z}. \tag{5.33}$$

Fig. 5.1 illustrates in direct comparison the radial profile of both lapse functions, α_{BL}, and α_{KS}, down to the outer horizon at r_{H}^{+}. The functions are restricted to the equatorial plane and plotted for maximal rotation of the Kerr black hole. The coordinate singularity of Boyer–Lindquist coordinates represents the fact that $\alpha_{\mathrm{BL}}(r_{\mathrm{H}}^{+}) = 0$. This behavior is removed by a transformation to non–pathological Kerr–Schild coordinates. Due to this behavior the use of this alternative frame is recommended in physics of rotating black holes. We will return to the Kerr–Schild frame in Ch. 5 when discussing the 3+1 split in Sec. 5.4.

Up to now, the Kerr–Schild coordinates were exclusively in use for electromagnetic studies e.g. Papadopoulos et al. and Komissarov et al., but not for MHD: All groups concerned with GRMHD simulations on the Kerr geometry so far – Koide et al., De Villiers & Hawley as well as Gammie et al., Semenov et al. – have implemented the pathological Boyer–Lindquist frame. The difficulties arise at the horizon, at the **inner boundary** of the accretion flow problem. Theorists have to introduce tortoise coordinates to handle Boyer–Lindquist coordinates at the event horizon.

Any horizon adapted frame ensures regularity at the horizon. Implementing horizon adapted approaches has further advantages [Pap98]: One is not forced to use very high resolutions due to unphysically large gradients that evolve near the horizon. Papadopoulos et al. demonstrated the feasibility of horizon adapted techniques with spherical Bondi

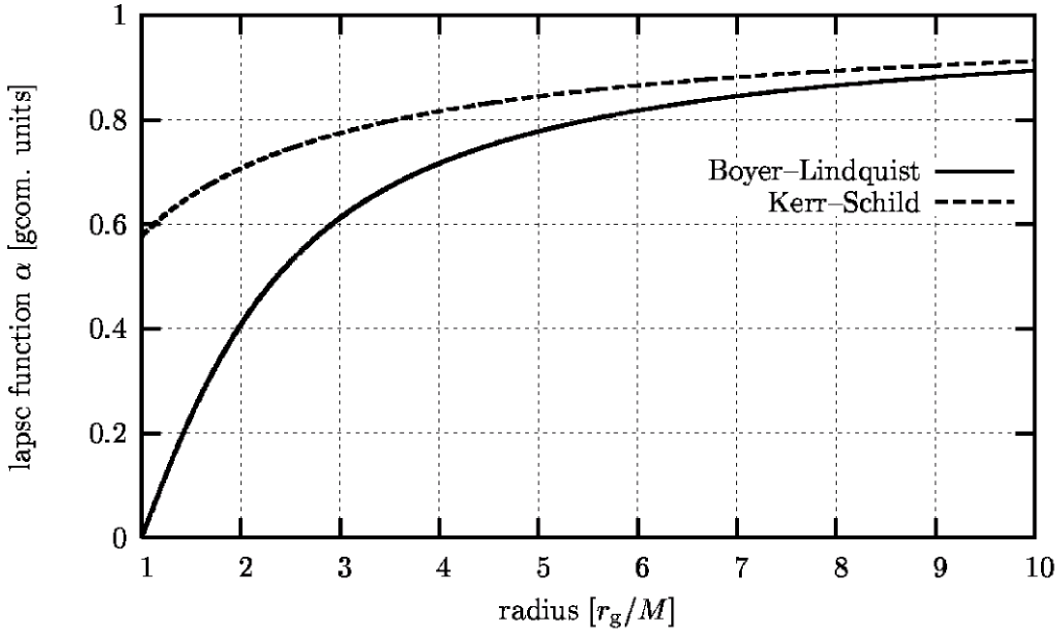

Figure 5.1: The radial profiles of the lapse functions of the Kerr geometry, once defined in the standard Boyer–Lindquist frame (*solid*) and then defined in the Kerr–Schild frame (*dashed*). Parameters are restricted to the equatorial plane, $\theta = \pi/2$, and maximum Kerr parameter, $a = M$. The coordinate singularity, $\alpha_{\rm BL}(r_{\rm H}^{+} = 1) = \rho\sqrt{\Delta}/\Sigma = 0$, is clearly indicated. In contrast, the lapse function of the Kerr–Schild frame, $\alpha_{\rm KS}(r_{\rm H}^{+}) = 1\sqrt{1+Z}$ stays finite and well–behaves at the outer horizon.

accretion flows and axisymmetric Bondi–Hoyle accretion flows. Later, the simulations were extended to non–axisymmetric relativistic Bondi–Hoyle accretion onto a Kerr black hole [Fon99]. It is stressed here that these simulations were purely hydrodynamical approaches (high–resolution shock–capturing, HRSC, scheme plus approximate Riemann solver), but *not* MHD.

Interestingly the non–axisymmetric relativistic Bondi–Hoyle simulations have shown that the flow exhibits a strong tail shock which is wrapped around the black hole due to its non–vanishing spin (see Fig. 5.2). The consequence is a rotation–induced (frame–dragging!) asymmetry in the pressure field: an overpressure evolves on the counter–rotating side. Besides, a *lift of the black hole* normal to the flow direction results. There is another plausible confirmation which confines the effects of black hole rotation to the inner regions of the black hole. The steep decay of the frame–dragging potential in radially outward direction, $\omega \propto r^{-3}$, explains this behavior very well. Beneath the distinct

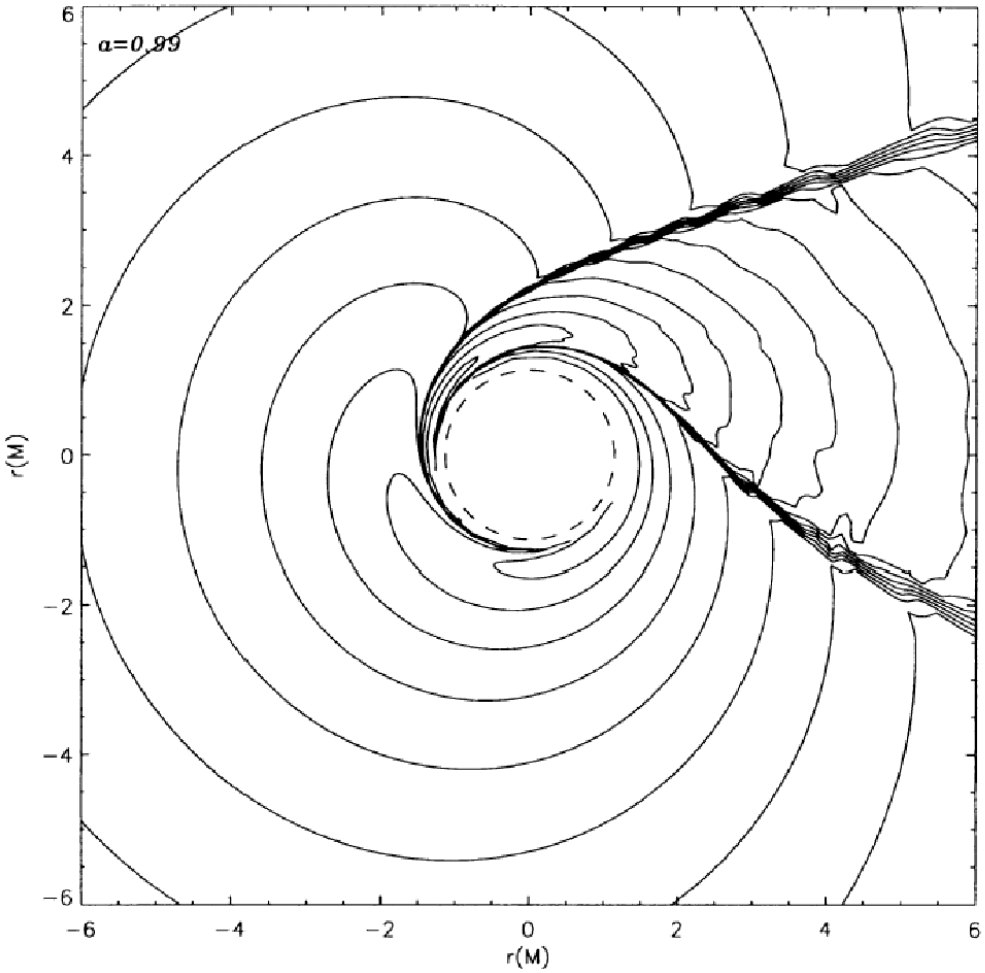

Figure 5.2: General relativistic hydrodynamics simulation on the Kerr geometry. Isocontours of the logarithm of the matter density are shown for extreme Kerr, $a = 0.99\,M$. A shock is wrapped around the Kerr black hole. The outer boundary is placed at $50.9\,M$, and the inner boundary is identical with the outer horizon at $1.14\,M$. The adiabatic index of the perfect fluid is $\gamma = 5/3$, asymptotic Mach number amounts to 5.0. (Credit: [Fon99])

behavior of the coordinate frames – Kerr–Schild vs. Boyer–Lindquist – at the horizon, it was demonstrated that both show a large amount of agreement in direct comparison with same input e.g. in resulting accretion rates.
Mass and radial momentum rates showed a spin dependence in Boyer–Lindquist but not in Kerr–Schild coordinates. Because the rates should be independent on spin it is

deduced that the Kerr–Schild system is numerically more accurate. An essential conclusion is that the Kerr–Schild frame allows a larger amount of accurate integration steps. One last computational advantage is that the regularity of the coordinate frame at the horizon allows to place the inner boundary at an arbitrary radius *beyond* the event horizon. The boundary conditions for fields can be fixed unambiguously. Thereby, unwanted numerical boundary effects are causally disconnected. In practise, unphysical reflections and "numerical heating" from the horizon can be avoided.
The Kerr–Schild frame offers an algebraic complexity due to the introduction of two additional non–vanishing metric components as compared to the Boyer–Lindquist frame. However, this complexity shall not cause numerical shortcomings. There are indeed more complicated space–times e.g. neutron stars that come along with more complicated metric tensors.
Evaluating the pros and cons one concludes that the Kerr–Schild frame offers both, computational and conceptual advantages as compared to the Boyer–Lindquist frame. It is surprising that up to now this frame is in rare use. The present discussion suggests that horizon adapted frames are strongly recommended – especially in GRMHD.

5.4 3+1 Split of Space–time

In GR, different observer generally experience distinct time measures. Therefore, the general problem emerges how to describe time dependent phenomena in Relativity. In 1962 Arnowitt, Deser and Misner overcame this problem by splitting the fourdimensional manifold into time and 3–space. The method is called 3+1 split or **ADM formalism** [ADM62]. Thereby, space–time foliates into space–like hypersurfaces of constant time, $t = \text{const}$. Each 3D slice is governed by the hypersurface metric, γ_{ij}. Hence, the hypersurfaces may be regarded as "absolute space" at different instances of time. The advance in time is parametrized by the already introduced **lapse function** (redshift factor), $\alpha = 1/\sqrt{-g^{\mathrm{tt}}}$. The third object of the ADM formalism is the space–like tangential **shift vector**, β^i. One can think of a *local fiducial observer*, the **FIDO**, who is at rest in absolute space and satisfies having the 4–velocity, $u_\mu = (-1/\sqrt{-g^{\mathrm{tt}}}, 0, 0, 0)^{\mathrm{T}}$. Then, one can interprete β^i as the components of the velocity of the spatial grid moving relative to the local FIDO as measured using the coordinate time t and spatial basis ∂_i.
An arbitrary space–time is decomposed following the instruction

$$\begin{aligned} ds^2 &= -(\alpha^2 - \beta_i\beta^i)\, dt^2 + 2\beta^i\, dx^i dt + \gamma_{ij} dx^i dx^j && (5.34)\\ &= -\alpha^2 dt^2 + \gamma_{ij}(dx^i + \beta^i dt)(dx^j + \beta^j dt). && (5.35) \end{aligned}$$

The 3+1 splitting procedure of the **Kerr space–time in Boyer–Lindquist form** – compare Sec. 2.2, Eq. (2.5) – leads to

$$\begin{aligned} \alpha_{\mathrm{BL}} &= \frac{\rho\sqrt{\Delta}}{\Sigma} \\ \beta^{\phi}_{\mathrm{BL}} &= -\omega,\ \beta^{r}_{\mathrm{BL}} = \beta^{\theta}_{\mathrm{BL}} = 0 && (5.36) \end{aligned}$$

$$\gamma_{ij}^{\mathrm{BL}} = \begin{pmatrix} \gamma_{rr}^{\mathrm{BL}} & 0 & 0 \\ 0 & \gamma_{\theta\theta}^{\mathrm{BL}} & 0 \\ 0 & 0 & \gamma_{\phi\phi}^{\mathrm{BL}} \end{pmatrix} = \begin{pmatrix} \rho^2/\Delta & 0 & 0 \\ 0 & \rho^2 & 0 \\ 0 & 0 & \tilde{\omega}^2 \end{pmatrix}, \tag{5.37}$$

with the definitions of the Boyer–Lindquist functions in Eq. (2.6).
In Boyer–Lindquist form the 3–metric of the hypersurfaces is diagonal. The Boyer–Lindquist FIDO has a purely azimuthal motion, $\beta_{\mathrm{BL}}^{\phi} \neq 0$. Due to $u_\phi = 0$, the FIDO is a **zero angular momentum observer (ZAMO)**. He sits in a *locally non–rotating frame* (LNRF) and is also called *Bardeen observer* [Bar70]. In Boyer–Lindquist coordinates the ZAMO world line becomes space–like ("tachyonic") at the event horizon; this is another manifestation of the pathological behavior of this frame at the horizon.

An alternative coordinate frame is advised to overcome the pathologies. A **coordinate transformation to the Kerr–Schild frame** (see former section and Appendix A.2) changes both, the shift vector and the hypersurface 3–metric [Komi04a]. The 3–metric becomes non–diagonal i.e. the spatial coordinates $\{r, \theta, \phi\}$ are no longer orthogonal:

$$\alpha_{\mathrm{KS}} = 1/\sqrt{1+Z} \tag{5.38}$$

$$\beta_{\mathrm{KS}}^{r} = \frac{Z}{1+Z},\ \beta_{\mathrm{KS}}^{\phi} = \beta_{\mathrm{KS}}^{\theta} = 0 \tag{5.39}$$

$$\gamma_{ij}^{\mathrm{KS}} = \begin{pmatrix} \gamma_{rr}^{\mathrm{KS}} & 0 & 0 \\ 0 & \gamma_{\theta\theta}^{\mathrm{KS}} & 0 \\ 0 & 0 & \gamma_{\phi\phi}^{\mathrm{KS}} \end{pmatrix} \tag{5.40}$$

$$= \begin{pmatrix} 1+Z & -a(1+Z)\sin^2\theta & 0 \\ -a(1+Z)\sin^2\theta & \rho^2 & 0 \\ 0 & 0 & \tilde{\omega}^2 \end{pmatrix}, \tag{5.41}$$

with the definitions of $Z = 2Mr/\rho^2$ and $\tilde{Z} = \tilde{\omega}^2 - (Z+1)a^2\sin^4\theta$.
The Kerr–Schild FIDO with $\beta_{\mathrm{KS}}^{r} \neq 0$ moves radially towards the intrinsic singularity. The motion of the Kerr–Schild FIDO in Boyer–Lindquist coordinates is [Komi04a]

$$v^\phi = 2ar/\Sigma,\ v^r = -2r\Delta/\Sigma,\ v^\theta = 0. \tag{5.42}$$

Although the Kerr–Schild FIDO has the same angular velocity as the Boyer–Lindquist FIDO, he moves radially towards the singularity.

5.5 GRMHD in Conservative Formulation

The former two sections prepared to formulate the ideal GRMHD equations from Sec. 5.2 in conservative form. The work of Papadopoulos & Font [Pap99] as well as Font [Fon00, Fon03] and Komissarov [Komi04b] may be consulted concerning conservative formulation.

Essentially, there are two possibilities to formulate the problem: In *Lagrangian formulation* the FIDO is fixed in absolute 3–space whereas in *Eulerian formulation* the FIDO moves relative to absolute space with the 4–velocity $u^\mu = \frac{1}{\alpha}\left(1,\, -\beta^i\right)^{\mathrm{T}}$. The frame is generally accelerated in GR.
If the decision comes to an 3+1 Eulerian formulation à la Wilson [Wils72] in Kerr–Schild coordinates, then Eqs. (5.38) and (5.39) will be used to express w^μ. GRHD is endowed with a 5D state vector in conservative form i.e. $\mathcal{U}_{\mathrm{GRHD}} = (D,\, M_i,\, E)^{\mathrm{T}}$. The dynamical variables are relativistic density, D, relativistic momentum 4–vector, M_μ that has only spatial components M_i ($M_\mu \perp u_\mu$), and energy, E [Fon03]. In contrast, GRMHD provides further three dynamical variables to form a **8D state vector**: $\mathcal{U}_{\mathrm{GRMHD}} = (\epsilon,\, E,\, S^i,\, B^i)^{\mathrm{T}}$ with total energy density, ϵ, total energy, E, spatial momentum flux, S^i, and spatial magnetic field, B_i. Each component consists of a matter part and an electromagnetic part.

The eight dynamical variables of GRMHD can be obtained by the following procedure: The energy density ϵ can be computed by the contraction of the density 4–vector, J^μ, with the observer's 4–velocity, u_μ,

$$\epsilon = u_\mu\, J^\mu. \tag{5.43}$$

The energy, E, follows from a parallel projection of the 4–energy–momentum current to the FIDO 4–velocity

$$E = u_\mu u_\nu\, \mathbf{T}^{\mu\nu} \tag{5.44}$$

with the simplified energy–stress tensor of GRMHD, Eq. (5.19). The evaluation of the orthogonal components of the 4–energy–momentum current supplies the momentum flux

$$S_\mu = \mathbf{P}_{\mu\lambda} u_\nu\, \mathbf{T}^{\lambda\nu} \tag{5.45}$$

where $\mathbf{P}_{\mu\nu} = \mathbf{g}_{\mu\nu} + u_\mu u_\nu$ denotes the projection tensor.
According to Sec. 5.2, Eq. (5.16) the spatial magnetic field can be computed by

$$B^i = b^i\, U^t - b^t U^i. \tag{5.46}$$

Poynting Flux The 3+1 split of the Kerr space–time (see Sec. 5.4) splits the Maxwell tensor and introduces the familiar 3–fields $\vec{E}$ and $\vec{B}$. It must be stressed that the notions of these fields are locally and e.g. with respect to the ZAMO. ZAMOs are specific observers (*tetrads*) moving with 4–velocity u perpendicular to the 3D space–like hypersurfaces.
The energy–stress tensor of GRMHD was already introduced in Eq. (5.5), compare Sec. 5.2. In contrast to Sec. 5.2 we will now split the conserved currents, $K^\mu_{\ (\mathrm{a})}$, of GRMHD into their hydrodynamic and their electromagnetic (EM) parts. Then, one finds the expressions for energy density, ϵ, momentum flux, $\vec{S}$, and stress (pressure) tensor, $\hat{t}$, with respect to the ZAMO frame [Dur88]

$$\epsilon \;=\; \gamma^2(\rho + P\vec{v}^2) + \epsilon_{\mathrm{EM}} \tag{5.47}$$

$$\vec{S} = (\rho + P)\gamma^2\vec{v} + \vec{S}_{\rm EM} = \rho_0 h\gamma^2\vec{v} + \vec{S}_{\rm EM} \tag{5.48}$$

$$\hat{t} = (\rho + P)\gamma^2\vec{v}\otimes\vec{v} + P\hat{g} + \hat{t}_{\rm EM} = \vec{S}\otimes\vec{v} + P\hat{g} + \hat{t}_{\rm EM}. \tag{5.49}$$

The new quantities introduced here are proper rest mass density, $\rho = mn$, relativistic specific enthalpy, h, the 3–metric $\hat{g}$, and **Poynting Flux**, $\vec{S}_{\rm EM}$. The Poynting flux is therefore identified as the electromagnetic part of the momentum flux.
Specifically, there are the energy density of the electromagnetic field, $e_{\rm EM}$, the Poynting flux, $\vec{S}_{\rm EM}$ and Maxwell stresses, $\hat{t}_{\rm EM}$:

$$\epsilon_{\rm EM} = \frac{1}{8\pi}\left(\vec{E}^2 + \vec{B}^2\right) \tag{5.50}$$

$$\vec{S}_{\rm EM} = \frac{1}{4\pi}\vec{E}\times\vec{B} \tag{5.51}$$

$$\hat{t}_{\rm EM} = \frac{1}{4\pi}\left(-\vec{E}\otimes\vec{E} - \vec{B}\otimes\vec{B} + \frac{1}{2}\hat{g}\left(\vec{E}^2 + \vec{B}^2\right)\right). \tag{5.52}$$

$\nabla_\mu \mathbf{T}^{\mu\nu} = 0$ leads to energy conservation $u_\nu\left(\nabla_\mu \mathbf{T}^{\mu\nu}\right) = 0$ and to the generalization of the Euler equations, $h\left(\nabla_\mu \mathbf{T}^{\mu\nu}\right) = 0$. These formulas can be evaluated in the **Kerr space–time for stationary flows** [Dur88]

$$\vec{\nabla}(\alpha^2\vec{S}) = \alpha^2\,\sigma^K_{ik}t^{ik} \tag{5.53}$$

$$\frac{1}{\alpha}\nabla_k(\alpha\,t^k{}_i) = -e\,\nabla_i(\ln\alpha) - \frac{1}{\alpha}\,S_\phi\,\nabla_i\,\omega. \tag{5.54}$$

σ^K_{ik} denotes shear, ω is the frame–dragging potential and t^{ik} is the plasma stress tensor. These two equations are fundamental to understand how a rotating black hole can drive relativistic outflows magnetically: shear couples to the angular momentum flow vector in the term $\sigma^K_{r\phi}t^{r\phi}$. The rotating Kerr space–time exhibits a huge shear, especially near the horizon. A rotating plasma in the accretion flow represents an angular momentum flow. Both result – according to the first equation, Eq. (5.53), – in a dominant Poynting flux.

Sec. 4.4 showed that in stationary theory basic mechanisms for magneto–centrifugal jet formation are basically understood. Sec. 5.9 will prove that current time–dependent GRMHD fluid simulations support this numerically. However, so far it was not achieved to prove relativistic jets with $\gamma \simeq 10$. In Sec. 5.7 we will return to this key problem while presented existing GRMHD codes. Obviously, the "string approach" of Semenov et al. (2004) could prove the appearance of "magnetic towers" and the formation of bipolar relativistic jets by Poynting fluxes [Sem04a, Sem04b]. But dissipative effects like **reconnection** were not implemented and are supposed to modify the results significantly.

Numerical scheme To implement a numerical scheme, one has to restrict the metric to a coordinate basis. Therefore, the two relativistic conservation equations, Eqs. (5.1)

and (5.2) become

$$\frac{1}{\sqrt{-g}}\,\partial_\mu\left(\sqrt{-g}\,\rho\,U^\mu\right) = 0 \tag{5.55}$$

$$\partial_t\left(\sqrt{-g}\,T^t{}_\nu\right) = -\partial_i\left(\sqrt{-g}\,T^i{}_\nu\right) + \sqrt{-g}\,\mathbf{T}^\kappa{}_\lambda\,\Gamma^\lambda{}_{\nu\kappa}, \tag{5.56}$$

with the determinant of the 4–metric, $g = \det(\mathbf{g}_{\mu\nu})$, temporal index t, spatial index i and the Christoffel symbol of the metric $\Gamma^\lambda{}_{\nu\kappa}$. g satisfies $\sqrt{-g} = \alpha\sqrt{\gamma}$ with the lapse function, $\alpha = 1/\sqrt{-g^{\mathrm{tt}}}$ (as introduced in Sec. 2.2) and the determinant of the purely spatial 3–metric, $\gamma = \det(\gamma_{ij})$. So far in GRMHD simulations the Boyer–Lindquist frame is used i.e. the Christoffel symbols of second kind, lapse, shift and 3–metric are specified to these coordinates. It is advised to use the Kerr–Schild frame as motivated in Sec. 5.3. The appropriate metric functions are presented in Sec. 5.4.

Conservative form The fundamental equations of ideal GRMHD include particle conservation, Eq. (5.55), four energy–momentum equations, Eq. (5.56), and the induction equation, Eq. (5.17), with the constraint, Eq. (5.18). These equations form a **hyperbolic system of differential equations**.

Following Gammie et al. [Gam03], the conserved variables are $\{\sqrt{-g}\,\rho\,U^t,\ \sqrt{-g}\,T^t{}_t,\ \sqrt{-g}\,T^t{}_i,\ \sqrt{-g}\,B^i\}$. These conserved variables constitute a hyperbolic system of eight differential equations for eight unknowns. Hence, in a conservative scheme it is suggested to use a **state vector** of the form $\mathcal{U} \equiv \sqrt{-g}\left(\rho U^t,\ T^t{}_t,\ T^t{}_i,\ B^i\right)^{\mathrm{T}}$. The state vector components can be identified by the local conserved quantities of the GRMHD problem. But the state vector also depends *non–linearly* on so–called primitive variables. The primitives in GRMHD are quantities with a physical meaning. They form the vector $\mathcal{P} \equiv (\rho,\ e,\ v^i,\ B^i)^{\mathrm{T}}$. Typically in Relativity, the non–linear interdependence of conserved and primitive variables requires numerical iteration. There are different iteration schemes available to recover the primitive quantities e.g. Newton–Raphson schemes [Marti91] or by iteration of quartic equations [Dun94]. Those schemes produce high computational cost and are absent in Newtonian hydrodynamics and MHD.

The time evolution of the state vector in a FIDO frame e.g. the ZAMO is updated by the use of fluxes, $\mathcal{F}$. Finally, the dynamical GRMHD problem is mapped onto a first order hyperbolic set of differential equations in conservative form:

$$\partial_t\left[\sqrt{\gamma}\,\mathcal{U}(\mathcal{P})\right] + \partial_k\left[\sqrt{-g}\,\mathcal{F}^k(\mathcal{P})\right] = \sqrt{-g}\;\mathcal{S}(\mathcal{P}), \tag{5.57}$$

where g, γ are determinant of 4–metric respectively determinant of spatial 3–metric of the space–time. Both are connected by $\sqrt{-g} = \alpha\sqrt{\gamma}$. A third quantity emerges, the source term $\mathcal{S}$. In Relativity, it contains essentially the curved metric and its derivatives. The numerical task is to solve this set of equations.

Discontinuous Galerkin finite element methods (DGFEM) are one example to solve these equations. Finite element methods (FEM) are rather new in astrophysics. Essentially, in a pioneering work it was proved that DGFEM to be suited to relativistic

hydrodynamics in astrophysics [Spi02]. It is referred to this PhD work for more details on the scheme.

5.6 Magneto–Rotational Instability

After this mathematical details now GRMHD physics is considered. Magnetically induced turbulence is a main feature in accretion physics, in particular in magnetized accretion flows around a black hole. It is necessary that the angular momentum is transported outwards so that the accretion process is built up. Real fluids are affected by viscosity. This drives purely hydrodynamical dissipative turbulence. First, Alfvén pointed out in 1942 that the coupling via magnetic fields may be important for the dynamics in case of the solar system. In the sixties, Velikhov [Vel59] and Chandrasekhar [Cha60, Cha61] developed a theory of hydromagnetic instabilities. Therefore, these pioneers prepared the modern approaches: In 1991 the **magneto–rotational instability (MRI)** was discovered by Balbus & Hawley [Bal91a, Bal91b]. The MRI proved to dictate the plasma dynamics in the weak field regime. Today, the MRI is sometimes termed as *Balbus–Hawley instability* (BHI).
The mechanism of the MRI is now investigated in more detail: key ingredients of the MRI are differential rotation and magnetic fields. The existence of magnetic fields is natural because either they are present by primordial processes or they are generated from moving electric charges. An accretion flow consists of a magnetized plasma or magneto–fluid. As described in Sec. 4.2 the accretion flow often takes the morphology of a SAD. Therefore, both MRI ingredients are available.

Considering two infinitesimal adjacent fluid elements in a differentially rotating disk the mechanism of the MRI can be outlined as follows: The two elements are connected by a common magnetic field line. One snapshot later, differential rotation enforces the two elements to separate. But the magnetic field line trys to resist, stretching elastically like a rubber band along the connection line. This effect is stabilizing. Simultaneously, the magnetic field line resists shear in tangential direction while trying to build up rigid rotation. This effect is destabilizing: The magnetic field enforces the fluid to rotate too fast for its new radial position. Hence, as a net effect, the outer fluid element is accelerated by the magnetic field line whereas the inner fluid element decelerates. A mechanical model of this issue are two point masses that are connected by a spring as displayed in Fig. 5.3.
A differentially rotating system with angular velocity $\Omega = \Omega(R)$ is in any case governed by the **stability criterion**

$$\frac{d\Omega^2}{dR} \geq 0. \tag{5.58}$$

For astrophysical disks, e.g. Keplerian disks, this criterion is generally violated. The launching of the MRI is inevitable.
A deeper analysis of the disturbance problem shows that both is relevant, radial modes and vertical modes. A finite vertical wavenumber drives axisymmetric instability: This

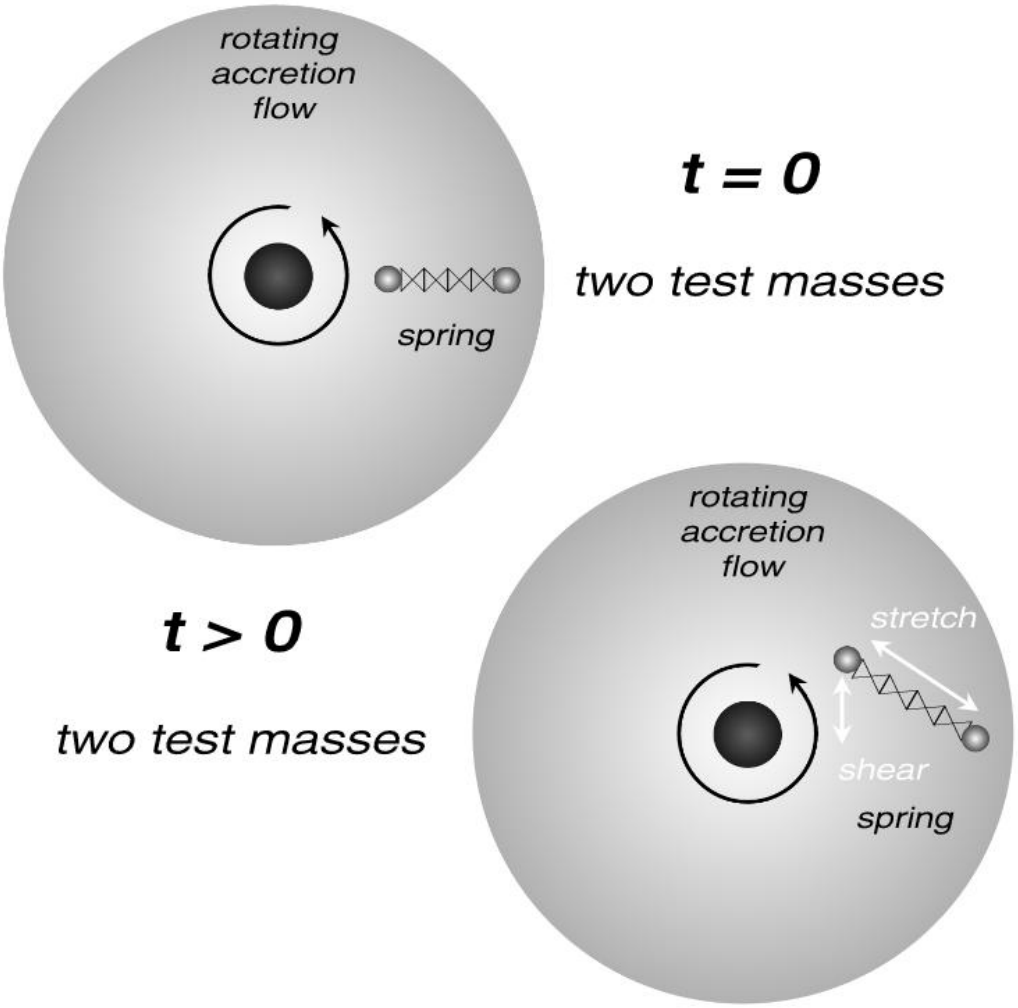

Figure 5.3: Mechanical analogy to the mechanism of the MRI. In the initial state (*top*) two test masses are connected by a spring (i.e. the common magnetic field). Later (*bottom*), the test masses are separated by rotation around the central object. But the spring resists stretching along the connection line (stabilizing). However, the spring trys to resist shear in tangential direction to enforce rigid rotation (destabilizing!).

causes the evolution of stratified interpenetrating layers with distinct angular momentum. The growth rate increases with and is of the order of the angular velocity. Interestingly, the growth rate of the MRI does **not** depend on the strength of the magnetic

field[3]. Therefore, already weak magnetic fields suffice to launch the local instability. In the strong field limit when magnetic fields reach the equipartition threshold the MRI is significantly damped. Illustratively spoken, the stabilizing effect – resistance to stretching – is dominant in this limit. Hence, it is often referred to the "*weak field instability*". Even if an accretion flow streams radially into a Kerr black hole, it will be strongly dragged in azimuthal direction when it approaches the ergosphere. Frame–dragging enhances significantly the MRI. Hence, the MRI is a quite natural effect especially in AGN harboring central supermassive Kerr black holes (compare Sec. 4.1).

One concludes that the locally operating MRI represents an efficient mechanism of **angular momentum transport**: In rotating disks of magnetized plasma the outer plasma gains angular momentum and the inner flow has angular momentum losses. This is vital to **build up the accretion process**. The MRI is the gateway to the central object. Else – without efficient transfer of angular momentum – the circulating matter would fail to hit the central object because it is reflected at the centrifugal barrier.
The efficient operation of the MRI in the weak field limit has been proven in many simulations e.g. decay of MHD plasma tori on the background of pseudo–Newtonian potentials [Bri04] or of the Kerr geometry [DeV03a].

5.7 GRMHD Codes

There is a manifold of computational possibilities to do ideal GRMHD simulations. The basic set of differential equations is fixed and presented in Sec. 5.2 in conservative form. However, conservativity is one essential difference between the existing codes. Additionally, the question arises how to discretize the system and how to work out the numerical scheme.

The discretization can be done by using finite difference methods (FDM), finite element methods (FEM) or finite volume methods (FVM). The standard issue is finite differencing. All available GRMHD codes to date are based on FDM. But it is also possible to implement FEM. A specific method, the Discontinuous Galerkin finite element method (DGFEM) was used in the framework of general relativistic ideal hydrodynamics [Spi02].
Another choice concerns the programming language especially if the code should be object–oriented (OO). In modern approaches, the code is formulated in OO style e.g. C++. The advantage is that the code is more transparent and it could be easily modified and developed further. Objects are bundled as *classes* by their function. The inheritance functionality permits to build–up clean class structures.
Highly relevant is the decision for a suitable coordinate system as discussed in Sec. 5.3. Still, the pathological Boyer–Lindquist system is widely used although it was demonstrated that horizon–adapted coordinates do a better job [Fon98]. If the Boyer–Lindquist frame is implemented nonetheless, the pathological behavior must be absorbed by implementing tortoise coordinates [MTW73]. A better formulation of the inner boundary

[3] It is only presumed that the energy density of the magnetic field is less than the thermal energy density.

at the event horizon can be achieved by using horizon–adapted coordinates e.g. the Kerr–Schild frame (presented in the Appendix A).

In the next paragraphs all[4] GRMHD codes available up to now are presented and briefly described. Today, there are essentially four groups concerned with GRMHD simulations on the Kerr geometry. All codes are restricted to the non–radiative regime and use the 3+1 split of the space–time. We will have a critical look on the capabilities of these codes. The simulated astrophysical problems are considered and compared. The physical plausibility and possible insufficiencies are discussed.

Koide et al. (1999) The first group that presented GRMHD simulations was a Japanese group [Koi99a, Koi99b]. They developed a pioneering conservative code named KGRMHD (Kerr General Relativistic Magnetohydrodynamics). The numerical method has the features

- ☐ ideal conservative GRMHD on the Kerr geometry,
- ☐ 2D (axisymmetry),
- ☐ Boyer–Lindquist coordinates with radial tortoise coordinates,
- ☐ polytrope with index $\Gamma = 5/3$,
- ☐ 210×70 mesh points,
- ☐ simplified Total Variation Diminishing (TVD) scheme.

The simulations were restricted to a quadrant with $0 \leq \theta \leq \pi/2$, axisymmetry to the z–axis and mirror symmetry to equatorial plane. The radial coordinate r extends from 1.5 to 40.0 r_{g} for Kerr, and from 2.4 to 40.0 r_{g} in the Schwarzschild metric.
The *tortoise coordinates* are introduced by $x = \log\left(\frac{r}{r_{\mathrm{H}}^{+}} - 1\right)$. This coordinate transformation compensates to some extend the Boyer–Lindquist coordinate singularity at the horizon.
The simplified TVD scheme avoids numerical oscillations. TVD scheme means that a Lax–Wendroff method plus diffusion term was used.
In the first paper [Koi99a], they studied the evolution of a disk in both, Schwarzschild and Kerr geometry. The initial condition for the accretion disk is zero radial velocity. The resulting evolution of the disk and the driving of relativistic outflows in the Kerr space–time is illustrated in Fig. 5.4.
The results can be briefly outlined: A rapidly rotating black hole, $a = 0.95$, produces a maximal jet velocity with $\beta = 0.93$ (equal to $\gamma = 2.7$). In contrast, a static Schwarzschild black hole, $a = 0$, shows a maximal outflow velocity with $\beta \lesssim 0.6$.
Later, it turned out that unfortunately the **code is unstable**. These simulations were generalized to 3D in the following period. Meanwhile simulations were presented that

[4] as far as known to the author

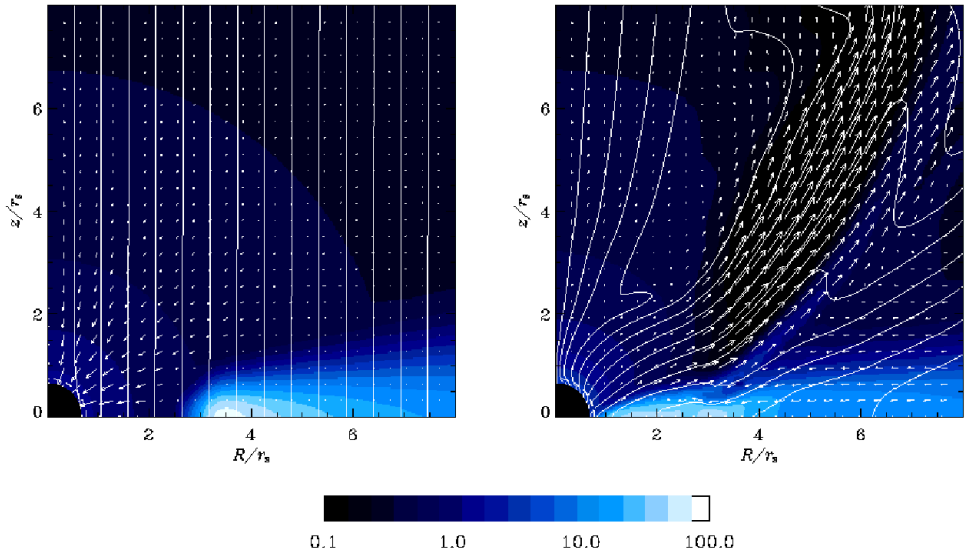

Figure 5.4: Formation of a relativistic jet in the Kerr geometry ($a = 0.95\,M$). Color codes the logarithm of the mass density. Arrows illustrate the velocity field, solid lines indicate the magnetic field. The initial state (*left–hand side*), $t = 0$, evolves to a remarkable relativistic outflow with maximal velocity $\beta = 0.93$ (equally $\gamma = 2.7$) at time $t = 65\,\tau_{\mathrm{S}}$ with the definition of the light crossing time, $\tau_{\mathrm{S}} = R_{\mathrm{S}}/c$. (Credit: [Koi99a])

ressemble to the work of Semenov et al. (see below). Magnetic flux tubes are twisted on screw lines and propel plasma from the black hole to relativistic speeds [Koi04]. However, the Lorentz factors are still too low, $\gamma \simeq 2$; it is supposed that they grow in a long–term simulation.

De Villiers & Hawley (2002) The second group that is involved in GRMHD simulations on the Kerr geometry was in Virginia, USA [DeV03a]. Indeed, one of the two collaborators, John F. Hawley discovered the MRI together with Stephen A. Balbus in 1991. Both and also co–workers like James M. Stone, Julian H. Krolik and Wayne F. Winters had deeply studied hydrodynamics and magnetohydrodynamics in 2D and 3D on the gravitational background of pseudo–Newtonian potentials for several years. The GRMHD paper in 2003 was especially prepared by a purely hydrodynamical simulation on the Kerr space–time [Hawl84, DeV02].
The numerical method of this GRMHD code has the features

- ☐ ideal *non*–conservative GRMHD on Kerr geometry,
- ☐ 3D,
- ☐ time explicit, operator–split, FDM scheme,

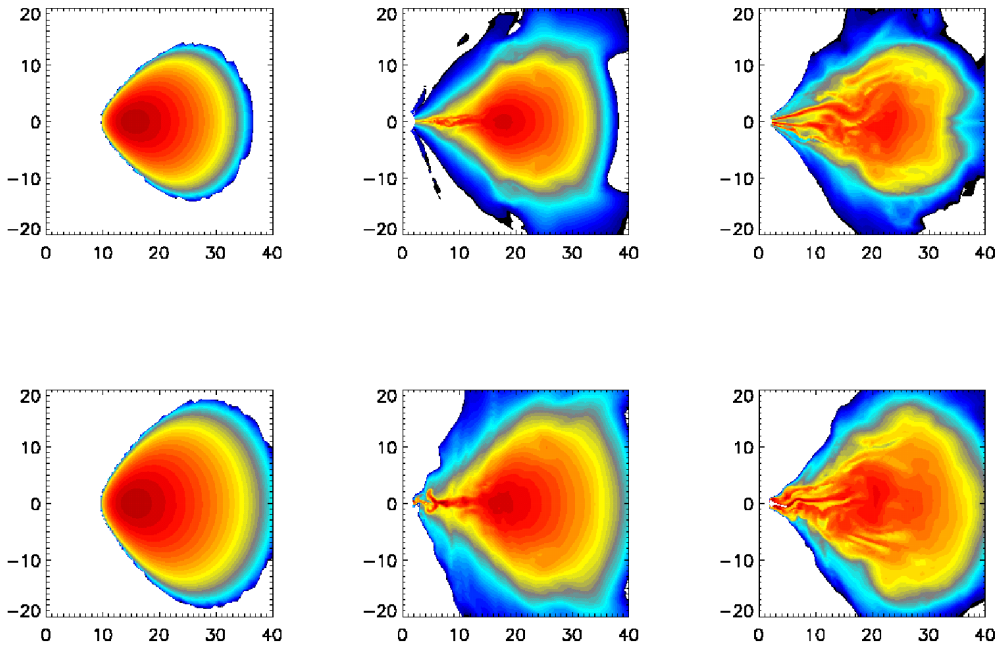

Figure 5.5: Evolution of an initial plasma torus with constant specific angular momentum in the Schwarzschild (*top row*) and the Kerr geometry (*bottom row*). The logarithm of the density is plotted color–coded. The torus configuration decays from left to right in $t = 0$, 1.5, 3.0 orbits at initial pressure maximum. The MRI launches turbulent decay of the torus and the accretion process towards the black hole. (Credit: [DeV03a])

- ☐ constrained transport (CT) formalism [Eva88] extended to method of characteristics constrained transport (MOCCT), [Hawl95], a ZEUS–like feature,
- ☐ Boyer–Lindquist coordinates (fixed spatial grid),
- ☐ perfect fluid,
- ☐ parallel coding: staggered grid → subgrids.

The code was tested on a huge variety of test problems including the special relativistic limit in 1D Minkowski, Alfvén wave propagation, fast and slow magnetosonic shocks, relativistic and non–relativistic shock tubes; on the Kerr geometry there were 1D and 2D tests undertaken like the magnetized Bondi inflow, magnetized Gammie inflow [Gam99] and a 2D magnetized torus (with constant specific angular momentum). The latter tests are in particular needed to study the evolution of the MRI.

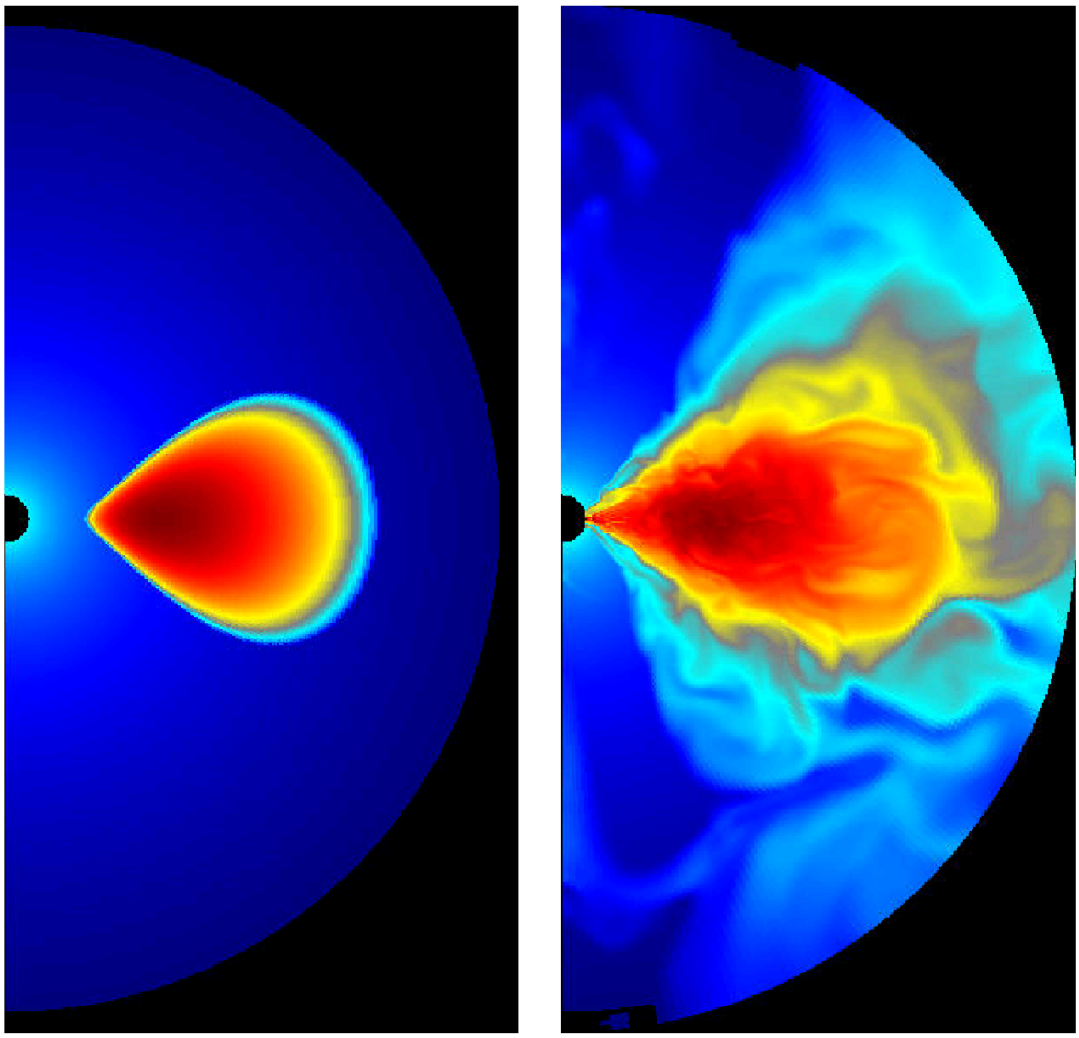

Figure 5.6: Evolution of an initial plasma torus with constant specific angular momentum in the Kerr geometry, $a = 0.5\,M$. The logarithm of the density is plotted color–coded. From $t = 0$ (*left*) to $t = 2000\,M$ (*right*), the plasma torus decays here as in Fig. 5.5. The grid resolution amounts 300×300. The interpretation of magnetically–induced turbulence due to the MRI also applies here. (Credit: [Gam03])

The authors stated themselves that the main shortcoming is the *artificial viscosity algorithm* as usually a problem in computational non–conservative hydrodynamics. A typical astrophysical standard test problem is the evolution of an initial magnetized plasma torus. The result of the GRMHD code is shown in Fig. 5.5. Further examples are given later, in Sec. 5.9, when discussing the physics of GRMHD.

Gammie et al. (2003) A very efficient conservative GRMHD code was presented in 2003 [Gam03]. The numerical method of this GRMHD code, named HARM (*High Accuracy Relativistic Magnetohydrodynamics*), has the features

- ☐ ideal *conservative* GRMHD on the Kerr geometry,
- ☐ 2D,
- ☐ constrained transport scheme [Eva88],
- ☐ Boyer–Lindquist coordinates with radial 'tortoise' coordinates ($r \to \log(r)$),
- ☐ perfect fluid,
- ☐ multi–dimensional Newton–Raphson iteration for recovery of primitives,
- ☐ slope limiter (à la MC),
- ☐ approximate Riemann solver: flux calculation by HLL scheme (**H**arten, **L**ax, van der **L**eer, [Har83]).

The advantages of HARM are that it allows longer integration times and the divergence–free constraint of the magnetic field is explicitly maintained. A deficiency is that HARM cannot handle B^2/ρ, $B^2/u \gg 1$ due to truncation errors. This was demonstrated with a magnetized Bondi flow problem.
Fig. 5.6 displays an essential result calculated with HARM. An initial torus configuration decays by magnetic turbulence as earlier been shown by De Villier & Hawley. However, we want to stress that there is no jet–like feature in the simulation.

Semenov et al. (2004) A new approach to GRMHD[5] was presented this year [Sem04a, Sem04b][6]. The authors decided to represent the plasma by its *thin magnetic flux tubes* ("*strings*"). 'Thin' means here that the pressure variations are small across the tube. The basic set of GRMHD equations remains but is extended to the so–called **string equations** describing the evolution of flux tubes in a gravitational field. This set of 1D wave equations can be solved to visualize the string dynamics in the rotating space–time. Thereby, only some individual flux tubes are calculated which is computationally very efficient.

- ☐ perfect (= ideal) GRMHD on Kerr geometry, $a = 0.9998\,M$,
- ☐ flux tube approach in 3D: string equations in *conservative* form,
- ☐ 12–dimensional state vector, flux and source,

[5] In the paper GRMHD is termed as gravitohydromagnetics (GHM).
[6] The ePrint paper contains a more detailed presentation of the equation set and numerics.

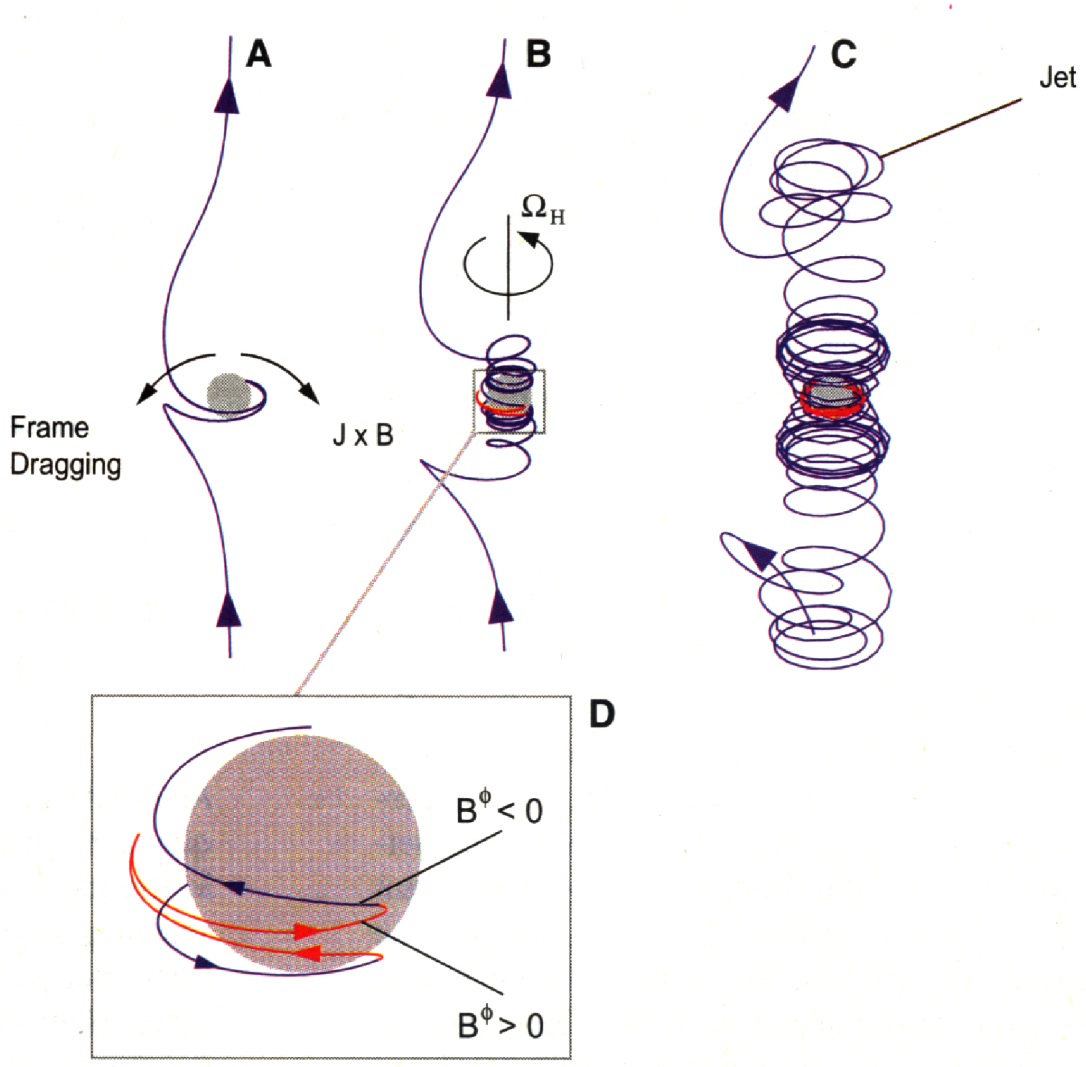

Figure 5.7: Evolving structures of a single magnetic flux tube embeded in a magnetosphere in the Kerr geometry. The frame–dragging effect wraps the initial flux tube (*a*) around the black hole spin axis. Then, the black hole ergosphere drives a Poynting flux (*b*). The result of this dynamics is a bipolar structure (*c*), a "magnetic tower": a **jet**. The red portions indicates plasma with **negative total energy** as viewed from infinity (compare Penrose process in Sec. 3.5). The gravitomagnetic dynamo is shown in the small close–up (*d*). Here, the azimuthal component of the magnetic field changes sign. The Alfvén speed amounts $12c$ to $13c$ in the regions where the ergospheric Poynting flux drives the jet. (Credit: [Sem04a])

- ☐ Boyer–Lindquist coordinates with radial 'tortoise' coordinates ($r \rightarrow -\ln(r - r_{\mathrm{H}}^{+})$),
- ☐ Solver: Total Variation Diminishing (TVD) scheme,
- ☐ three–point filter to avoid short wavelength fluctuations inside ergosphere,
- ☐ perfect fluid $\gamma = 2/3$ i.e. mid–relativistic polytrope,
- ☐ free boundary conditions at the string edges,
- ☐ no inner boundary problem: event horizon is not really a boundary!

Semenov et al. state that the main shortcoming of the code is that strings can cross without any consequence. Of course, this is not physical because reconnection is thereby not included. But from special relativistic MHD it is known that reconnection is responsible to accelerate plasma as a dissipative process: The importance of heating in Poynting–flux dominated flows was proven e.g. in case of the pulsar wind of the Crab nebula [Kir03]. However, up to now there exists no dissipative GRMHD code to tackle this problem.
The simulations cover both, initial flux tubes parallel and inclined to the black hole spin axis. In any case it turned out that the rotation of the space–time drags the flux tubes and drives bipolar structures along the black hole spin axis. This is a vital result because these **bipolar structures** are supposed to drive the jet magnetically!
A typical snapshot of the evolving structures is documented in Fig. 5.7. The total length of the simulation is mainly restricted by the plasma density since tenuous gas causes the breakdown of error control.

5.8 Conservativity and Inner Boundary

In the former section available GRMHD codes where presented. Conservative fomulations were opposed to non–conservative approaches. The main difference of the codes by Koide et al. and Gammie et al. versus the code by De Villiers & Hawley (ZEUS–like) is conservativity. Conservativity is a natural feature of Relativity as described in Ch. 5.2. In this sense Relativity *dictates* conservative formulations as natural numerical approaches.
The scientific community comments the question of conservativity in the following way: Font et al. state that conservative formulation is a necessary feature of the numerical scheme to guarantee correct evolution in regions of sharp entropy generation, especially **shocks** [Fon00].
Gammie et al. state that in 1D simulations conservative schemes are guaranteed to converge to a weak solution due to the theorems by Lax and Wendroff (1960) just as by LeVeque (1998). Besides, conservativity satisfies in any number of dimensions the jump conditions at discontinuities. This means in particular that *no artificial viscosity* is needed and the numerics does not run into troubles with relativistic shocks. The same authors noted that the ZEUS code and also its GRMHD extension by DeVilliers & Hawley are non–conservative schemes. The advantage of non–conservativity is certainly

that it permits an integration of the internal energy equation rather than a total energy equation. These schemes turn out to be more robust in flow regions where internal energy is small compared to total energy. Those conditions are especially given in highly supersonic flows that are quite common in astrophysics [Gam03].
The historical evolution of codes proves that there is a trend to implement rather conservative formulations today. The results of the simulations will tell if conservativity is suited to the specific problem. The critical comments concerning supersonic flows hint that there may be certain branches where one or the other formulation is justified.

The second point of this section involves the inner boundary of the flow problem located at the outer event horizon. In Sec. 5.3 it was demonstrated that the classical Schwarzschild ($a = 0$) respectively the Boyer–Lindquist frame exhibit a pathological behavior at the event horizon(s). As described in the former section researchers try to come along with this deficiency by using a radial tortoise coordinate. By introducing the logarithm of the radial Boyer–Lindquist coordinate the pathology is circumvented

$$r \rightarrow r_\star = -\ln(r - r_{\mathrm{H}}^+). \tag{5.59}$$

It is much more convenient to take *horizon adapted cordinates* as suggested by Font & Papadopoulos [Pap98, Fon98]. Since one could easily attach the inner boundary *behind* the event horizon. Therefore, the ghost zones lie at radii $r < r_{\mathrm{H}}^+$. The simplest way to implement horizon adapted cordinates in the Kerr geometry is the use of Kerr–Schild coordinates. They ensure regularity at both horizons as documented in Fig. 5.1.
The pay by using Kerr–Schild coordinates is that the metric tensor, $\mathbf{g}_{\mu\nu}$, contains more non–vanishing off–diagonal elements (see Appendix A). Nevertheless, this feature may not be harmful in a numerical sense. Benchmarks between Boyer–Lindquist and Kerr–Schild coordinates will evaluate suitable simulation regimes for each frame.

5.9 MRI–induced Decay of Plasma Tori

Today, accretion theory in General Relativity is constrained to the non–radiative sector. The associated accretion solutions are called non–radiative accretion flows (NRAFs). This section is dedicated to the research done so far using GRMHD simulations.

Sec. 5.7 gave an overview for existing GRMHD codes. While comparing the codes it turned out that there is now some kind of **NRAF standard problem** available: The initial configuration is a plasma torus located well–defined in the vicinity of a Kerr black hole, some tens of gravitational radii away from the outer event horizon. Starting the run of the simulation the torus is successively dismantled by the very efficient MRI as presented in Sec. 5.6. The MRI produces on one hand magnetic turbulence which destroys the torus typically by starting at its envelopes. On the other hand the MRI establishes the transport of angular momentum in outward direction. Therefore, a magnetized accretion flow is built–up. So, the accretion process starts and feeds the central black hole. Fig. 5.8 displays a snapshot after this evolution in the light of the averaged

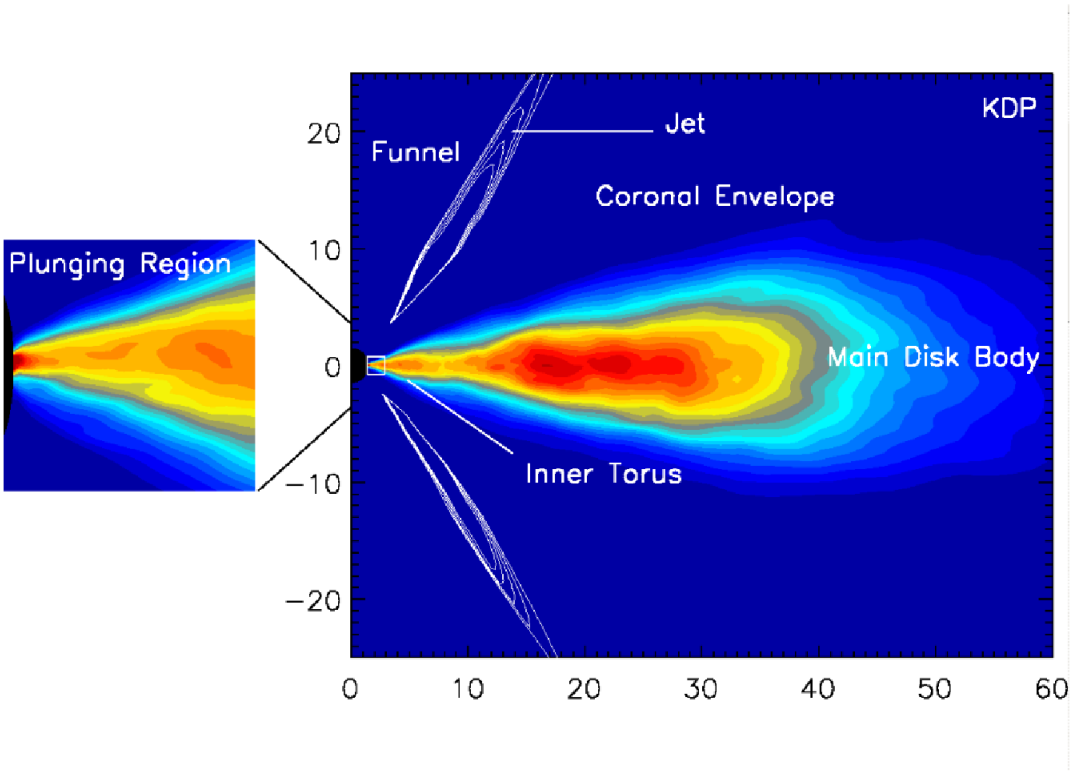

Figure 5.8: The result of the decay of an initial torus configuration simulated with non–radiative 3D GRMHD. The azimuthally–averaged density is color–coded, time–averaged on the 10th orbit. The torus decays and leaves behind a *main disk body*. The inner disk region supplies gas and magnetic field to the so–called *coronal envelope* above the main disk body. In a conical structure offside the axis of symmetry an outflow is generated which is centrifugally and magnetically driven: the *funnel–wall jet* – displayed by contour lines of positive radial momentum (*white*). The axis is divided in units of the gravitational radius, $r_{\rm g} = M$. Parameters were chosen to: Kerr parameter $a = 0.9$, plasma $\beta = p_{\rm gas}/p_{\rm mag} = 200$, constant specific angular momentum of the initial torus $l_{\rm in} = 4.57$, initial inner torus edge at 15.0 $r_{\rm g}$, pressure maximum (*red*) at 25.0 $r_{\rm g}$ (simulation KDP; Credit: [DeV03b]).

logarithmic density contours. The simulations were done with the already presented non–conservative GRMHD code (in Boyer–Lindquist frame) by De Villier & Hawley [DeV03b].
The relic torus structure is called **main disk body**. It has the morphology of a turbulent wedge which is gas pressure dominated, $\beta \gtrsim 1$. The outer region of the main disk body runs in outward direction with time due to the efficient transport of angular momentum triggered by the MRI.

Another structure is a matter backflow region at higher poloidal angles, the so–called **coronal envelope**. It is a very tenuous flow region with $\beta \simeq 1$ where the magnetic field structure is less turbulent. The animation studies clearly indicate that the coronal envelope is fed by the central region.

There is also a close–up excised in Fig. 5.8 that pictures the innermost region in front of the event horizon. De Villiers et al. state that they found an **inner torus** which plunges into the horizon. The animations show that the inner torus is *time–variable*. Considering the X–ray variability of AGN that are supposed to originate close to the hole, this is indeed a plausible feature. Therefore, one tends to link the inner torus structure to a non–steady hot corona. Then, one can interprete that the corona is built up by feeding from the surroundings, decays with time and is rebuilt. This scenario would explain the short–time variability of X–ray light curves e.g. the intraday variability (IDV) of blazars.

Near the axis of symmetry of the black hole–torus system a magnetically–dominated region of very tenuous, low–angular momentum gas accumulates. The density is typically some orders of magnitude below the main disk body. The magnetic field has essentially a radial structure. This is called the **axial funnel**. Coronal envelope and funnel are separated by the centrifugal barrier.

Along the centrifugal barrier there is an outflow, therefore termed as **funnel–wall jet**. In the light of the density, the funnel–wall jet is less dense than the main disk body but up to two orders denser than the axial funnel. The outflow is centrifugally and magnetically driven and is illustrated in Fig. 5.8 by some contour lines of positive radial momentum. The simulations with variable Kerr parameter a indicate that the funnel–wall jet is weak for small spin and increasing with black hole rotation. The outflow is not the relativistic and collimated jet which is expected from stationary theory. It is not clear whether the non–conservativity of the code prevents from building up clear jet structures. Alternatively, this may hint that the base of the jet does not start with high Lorentz factors and the acceleration and collimation operates farther outside.

The research with the code by De Villiers & Hawley is in progress: A couple of papers were presented recently that carry out further interesting features of magnetized accretion flows in the Kerr geometry. One paper is dedicated to the **unbound outflows** [DeV04]. The authors define in this context five regions: The **body of the jet** has hourglass shape and is dominated by mass flux. It is located between axial funnel and coronal envelope. The **base of the jet** marks the origin of radial outflow as illustrated in Fig. 5.9. Its stability depends on the Kerr parameter: At high spin a stable, dense ring of gas was found; at low spin the ring is rather diffuse and unstable. The **injection region** is a the coincidental locus of inner torus, funnel and envelope. It can be found at the orbit of marginal stability. The injection is not uniform, time–variable and increases in outward direction. The tenuous, high–speed outflow is called **funnel outflow**. Here, a large–scale poloidal magnetic field can be found that is sheared and spun up by frame–dragging. The consequence is a dominant toroidal magnetic field with outward–directed energy flux. This gravitomagnetic dynamo has already been demonstrated in earlier

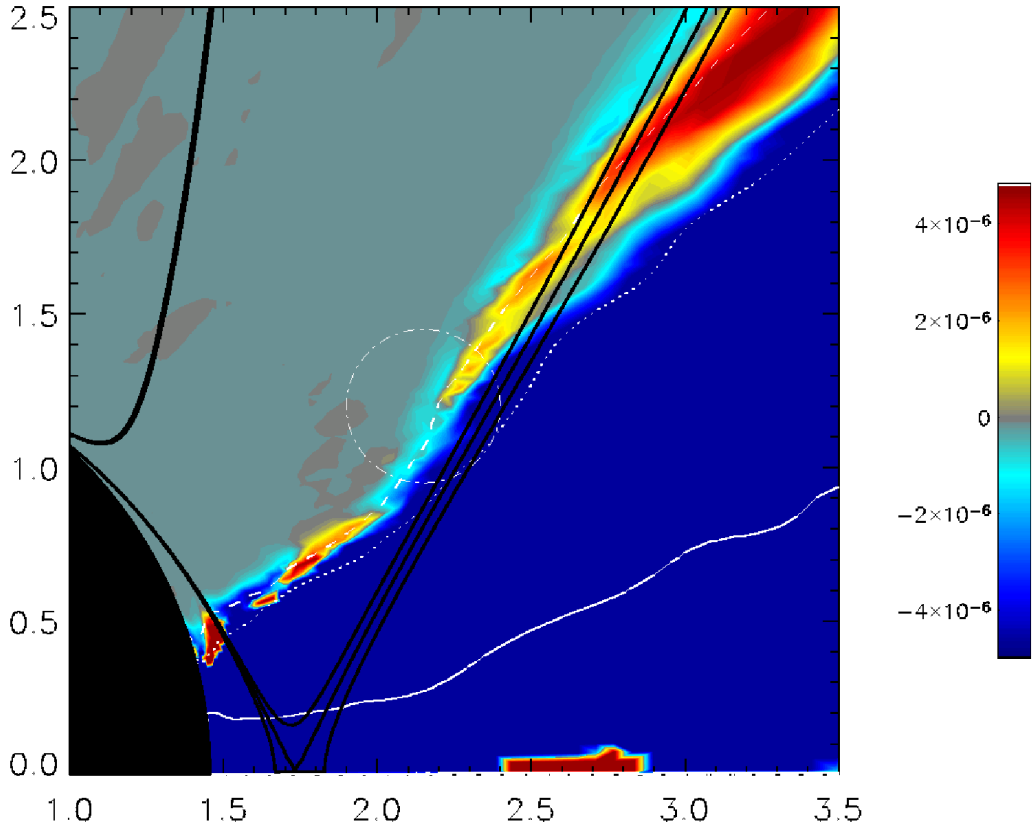

Figure 5.9: Color–coded radial azimuthally–averaged mass flux, $\langle \rho U^r \rangle_\phi$, as a result of the decay of an initial torus configuration simulated with non–radiative 3D GRMHD. The main disk body is displayed by white contour lines: $10^{-1}\,\rho_{\rm max}$ (*solid*), $10^{-2}\,\rho_{\rm max}$ (*dotted*), $10^{-3}\,\rho_{\rm max}$ (*dashed*). Below $10^{-3}\,\rho_{\rm max}$ the tenuous axial funnel is illustrated in gray color. The circle indicates the base of the jet where outgoing and ingoing material can be found. The *thick black lines* mark equipotential surfaces for marginally bound gas to display unbound outflows, $\Phi_{\rm mb} = [-0.01, 0, 0.01]$. Parameters were also chosen to the KDP model as in Fig. 5.8 (Credit: [DeV04]).

work [Kha99]. It is interesting to look at the pattern of the toroidal component of the **Lorentz force**. Fig. 5.10 hints for *magneto–centrifugal launching* of the jets. The GR Maxwell stresses correlate to the black hole spin: frame–dragging enhances Maxwell stresses and therefore the toroidal component Lorentz force. This can be compared to the GRMHD flux tube simulations by Semenov et al. [Sem04a, Sem04a]: The rotating space–time winds up the magnetic field lines and amplifies the field to become dominantly toroidal. Fig. 5.10 is simply the "force view" of this winding up. However, one must

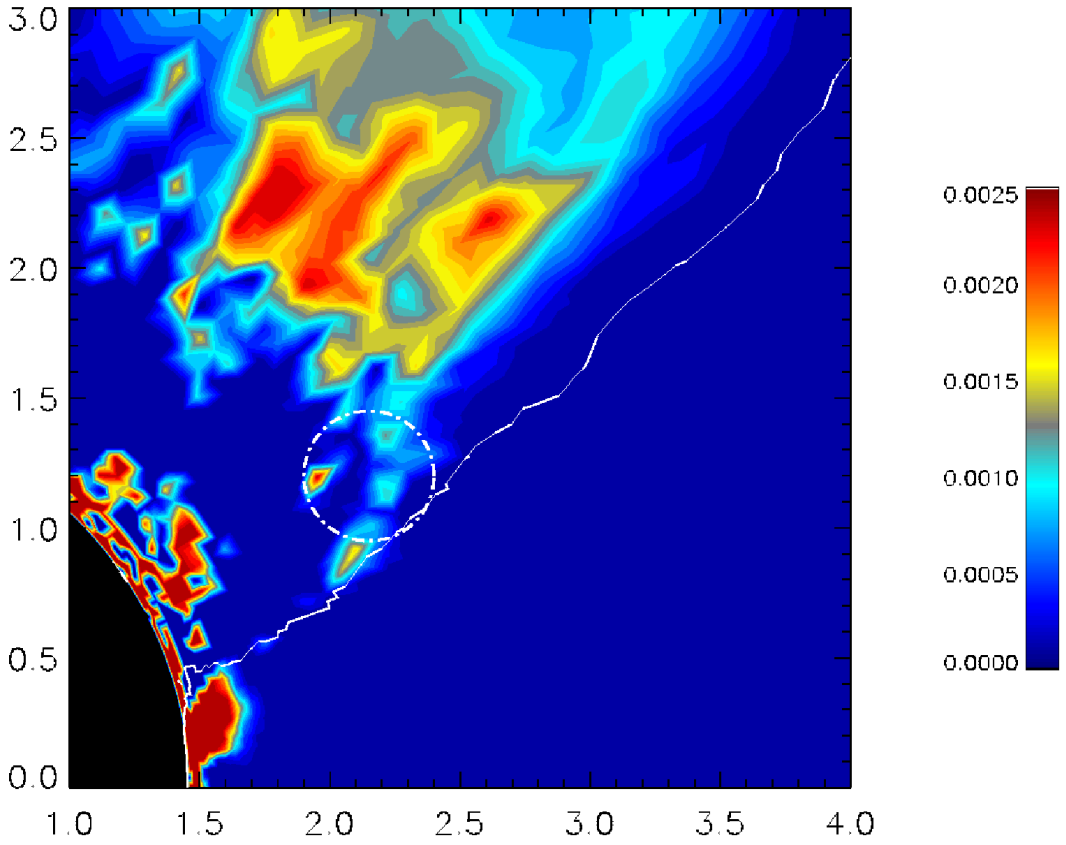

Figure 5.10: Color–coded magnitude of the azimuthally–averaged toroidal component of the Lorentz force. As in Fig. 5.9 the circle highlights the base of the jet. The distribution of the toroidal component of the force shows enhanced strength close to the event horizon and a dominance in the funnel region. These Maxwell stresses depends on the rotation of space time: it grows with Kerr parameter. The pattern suggests magneto–centrifugal launching of the jet at the base. Parameters were also chosen to the KDP model as in Fig. 5.8 (Credit: [DeV04]).

be careful in discussing these aspects in the framework of ideal GRMHD: Ideal MHD forbids the destruction of magnetic fields. But it is known from non–ideal MHD that magnetic field can be destroyed by reconnection. This is especially the case in winding–up scenarios as outlined above. Therefore, it is a natural and probably artificial feature of ideal MHD that strong magnetic fields are dammed up in the ergosphere. We conclude that dissipative GRMHD is supposed to change this behavior – also the pattern in Fig. 5.10. The magnitude of change must be proven in outstanding non–ideal simulations.

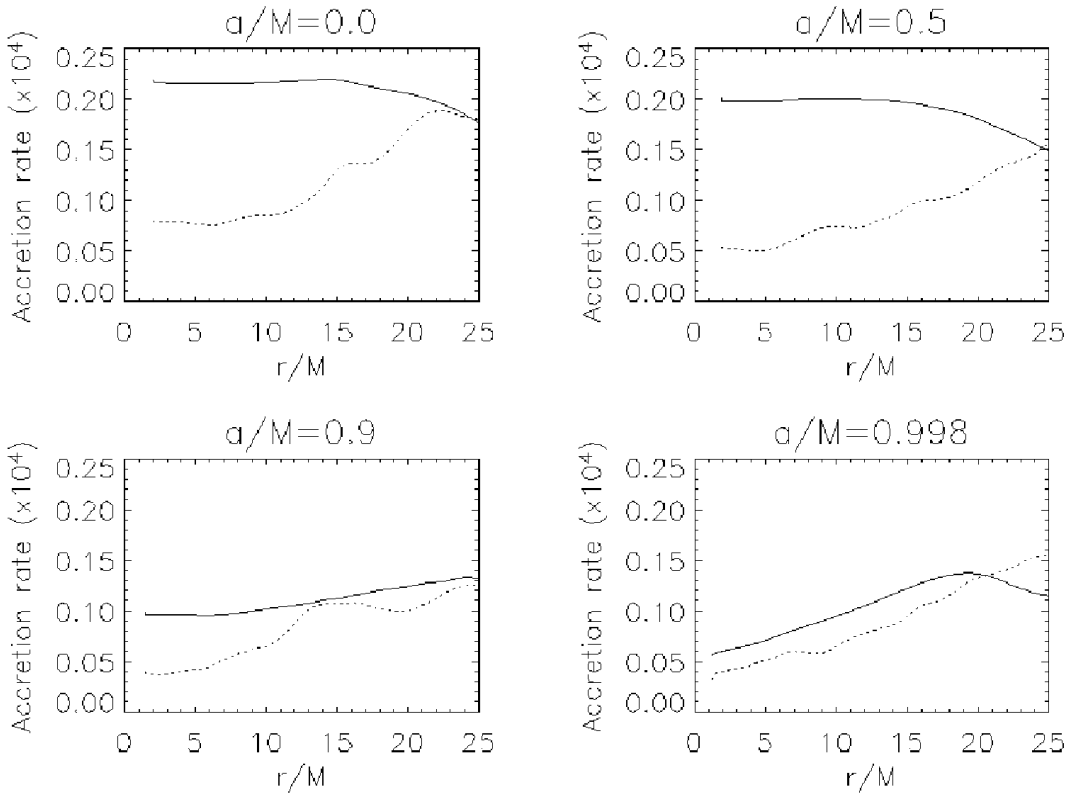

Figure 5.11: Radial dependence of the time–averaged, shell–integrated accretion rate for Kerr parameters $a/M = 0, 0.5, 0.9, 0.998$ (*solid curves*, clockwise from top left). In contrast, the *dashed curves* show the rms accretion rate fluctuations about the mean at each radius. The accretion rate is given in units of the fraction of the initial torus mass accreted per M of time. The intriguing feature is the breakdown in accretion for high black hole spins in bottom row. (Credit: [Kro04]).

Another paper treats the aspects of the **dynamics of the inner disk** [Kro04]. The most intriguing result in this analysis is that the *sharp reduction in accretion rate with increasing black hole spin* (Fig. 5.11, first documented in [DeV03b]) can be explained by a strongly spin–dependent outward–directed electromagnetic angular momentum flux. This is mediated by electromagnetic torques. For Kerr parameters $a \gtrsim 0.9\,M$ outward electromagnetic angular momentum flux and inward plasma angular momentum flux are comparable. Thereby, it can be stated that the zero–torque condition of traditional accretion theory [Pag74] is not valid. This is due to the fact that electromagnetic stresses are ubiquitous everywhere in the flow.
Poynting flux gives a further contribution to energy losses of the Kerr hole. Its rate

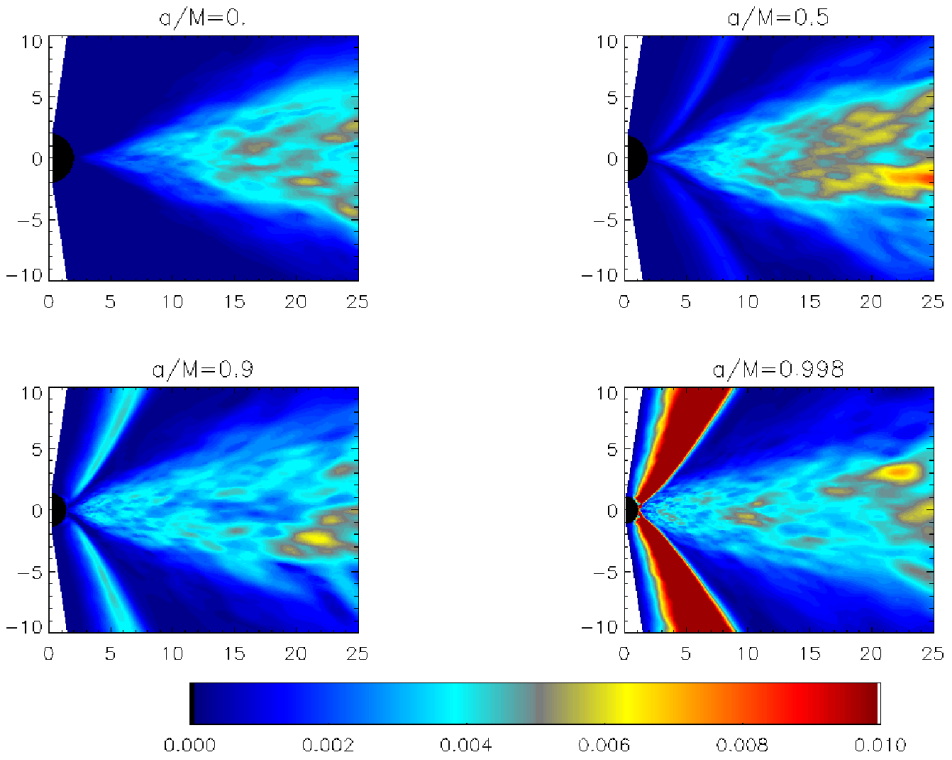

Figure 5.12: Color–coded time– and azimuthally–averaged outgoing Poynting flux for Kerr parameters $a/M = 0, 0.5, 0.9, 0.998$ (clockwise from top left) plotted in identical linear scale. The sequence clearly displays that the Poynting flux associated with the funnel–wall outflow rapidly grows with increasing black hole spin. (Credit: [Kro04]).

increases steeply with the Kerr parameter as documented in Fig. 5.12. The Poynting flux amounts more than 10% of the rest–mass accretion rate for highest Kerr parameters. Illustratively spoken, the Poynting flux changes with Kerr parameter to be with the funnel outflow and not to be with the accretion flow.
These studies confirm the suspicion that rapidly rotating black holes drive electromagnetically.

The Kerr black hole enhances the strength of the ouflows that are found in the axial funnel region. The outflows are classified in a hot, fast, tenuous and a cold, slow, dense component.

The well–defined torus solution on the Kerr geometry is a nice starting point for GRMHD fluid simulations. It is recommended to establish this as a standard test to benchmark the codes and to validate them. Especially, such a strategy allows to find

out advantages and shortcoming of each code. Additionally, researchers are able to find the best suited numerical scheme for magnetized accretion onto a Kerr black hole.
More efficient methods and better computers will allow to integrate the evolution for longer times. An interesting extension of the this test problem would be to shift the initial pressure maximum to larger radii. In particular, astrophysics proposes to study the evolution of a massive dusty torus located at the pc–scale. Unfortunately, it may take some time until simulations of this kind are feasible although in supercomputing the codes run always at the edge of hardware. Sometimes there are additional conceptual problems concerning the coding. Another problem is the underlying physics because the cold dust torus involves also molecular physics (above all H_2 chemistry) and radiation transfer. It may take some time until a complete network of this physics is available.
Hence, simulations mainly suffer from a scale problem: It is not possible to study AGN accretion physics from the pc–scale down to one gravitational radius. Numerically spoken, one deals with a *resolution problem*. Probably, researchers will solve this challenge by implementing adaptive mesh refinement (AMR) techniques. But GRMHD in general must be extended to certain branches including radiation, dissipation and large scales.

The next steps in the development of GRMHD are twofold: One branch concerns an extension to **dissipative GRMHD**. This is motivated by the fact that reconnection of magnetic fields is relevant in a variety of astrophysical systems. The other branch concerns **radiative GRMHD** i.e. the incorporation of radiation processes (thermal radiation, bremsstrahlung, cyclotron– and sychrotron radiation and its Comptonization) on curved space–times. It is expected that e.g. cooling by synchrotron radiation will have a strong impact on the dynamics of flow since the cooling time scale is very short. Robust methods including dissipative issues and covariant radiation transfer within computational fluid dynamics are still lacking. But this physics is supposed to modify significantly the non–radiative paradigms established today.

6 Kerr Ray Tracing of Accreting Black Holes

6.1 Numerical method

Kerr ray tracing is a computational method to calculate the trajectories of photons that move in the curved Kerr space–time. A typical setup in astrophysics is an emission locus given in a black hole–disk system with a known emission direction. One is interested if the emitted photons hit an observer's screen located at infinity (in asymptotical flatness). It is numerically more efficient to formulate this propagation problem vice versa (*back tracking*): One considers an observer's screen and "shoots" photons from each pixel of the screen. Each photon contributes to an image of the black hole–disk system. Some million photons form typically a high–resolution image. The Ray tracing principle is sketched in Fig. 6.1.

The equation which dictates the propagation of photons in curved space–times is the **null geodesics equation** of GR

$$\frac{d^2x^\mu}{d\tau^2} + \Gamma^\mu{}_{\nu\sigma}\frac{dx^\nu}{d\tau}\frac{dx^\sigma}{d\tau} = 0, \tag{6.1}$$

with an affine parameter, τ, and the connection coefficients $\Gamma^\mu{}_{\nu\sigma}$. Kerr ray tracing requires the Christoffel symbols of second kind to be specified for the Kerr geometry, e.g. in Boyer–Lindquist coordinates, see Eq. (2.5).
The second order differential equation can be solved by exploiting the integrals of motion: energy, E, angular momentum, J, particle rest mass[1], m, and Carter's constant, $\mathcal{C}$. The latter conserved quantity is an exclusive feature of the Kerr geometry. Other stationary and axisymmetric space–times possess only three integrals of motion. Brandon Carter found the fourth integral of motion by analyzing the problem using the Hamilton–Jacobi formalism [Car68].

Further Carter reduced by means of the four integrals of motion the second order geodesics equation to a set of four *first* order differential equations. These equations can be integrated directly with Runge–Kutta schemes or solved by the use of elliptical integrals [Fan97]. The result is a definite allocation of emission loci in the black hole–disk system to pixels on the screen for each set of conserved quantities. For details concerning Carter's work and the ray tracing algorithm it is referred to the work of Müller & Camenzind [Mül00, Mül04].

[1] This mass vanishes identically for photons. Consequently, one terms *null* geodesics.

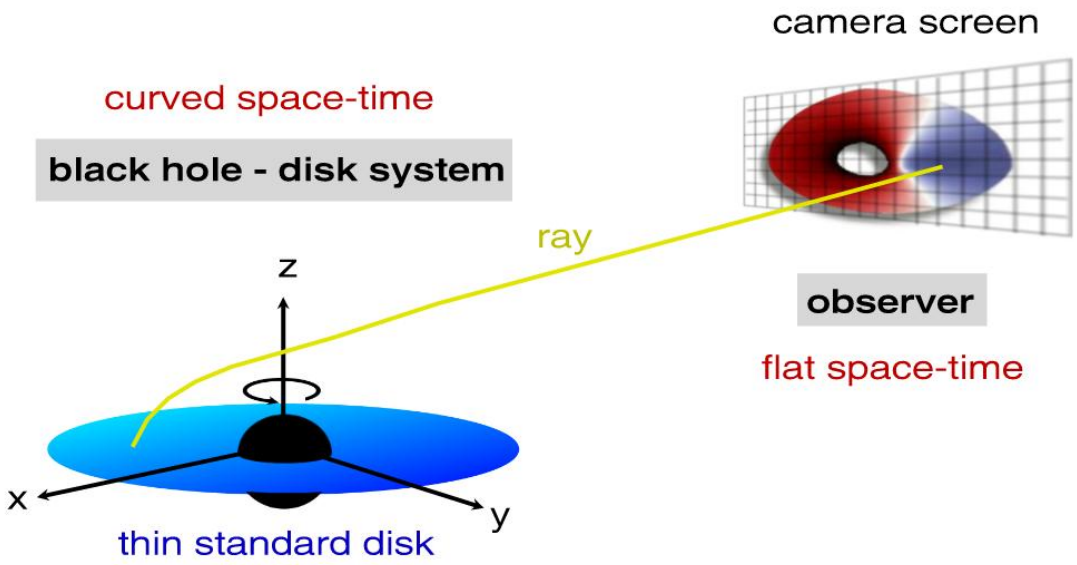

Figure 6.1: Illustration of the Kerr ray tracing technique. Physically, a light ray is emitted at the surface of a standard disk lying in the equatorial plane of a Kerr black hole. The trajectory is distorted by the curved space–time. The ray may hit the camera screen of the observer located at asymptotically flat infinity. Each ray contributes to an image of the system but the photons suffer from strong relativistic effects.

The astrophysical meaning of the ray tracing technique is in general to simulate spectra that originate from strongly curved regions e.g. compact objects. Of particular interest are relativistic emission lines, usually the X–ray fluorescence lines of iron. The line is observed in microquasars and AGN such as Seyfert galaxies and quasars type 1. This characteristic spectral component around 6 keV is reflected hard radiation coming from the hot corona and hitting the cold SAD as outlined in Sec. 4.2. In this process fluorescence photons are created that propagate almost freely to the distant observer. Usually, the intrinsic line profile in the rest frame of the plasma is assumed to be a delta distribution. But the intrinsic rest frame profile changes significantly as it is detected in infinity in the laboratory frame. Relativistic effects evoke characteristic imprints on the line profile:

- ▷ The **Doppler effect** emerges when the plasma moves relatively to the observer along the line of sight. The line is shifted when the plasma rotates towards (*blueshift*) or away from the observer (*redshift*). The Doppler effect occurs due to rotation also in Newtonian disks but it is generalized in GR.

- ▷ The **beaming effect** is a strong special relativistic effect: the radiation of an

emitter moving at relativistic speeds is collimated in the direction of motion[2]. Hence, beaming intensifies the spectral flux. One can distinguish *forward beaming*, a strong blueshift effect when the emitter approaches the observer; and *back beaming* when the emitter moves away from the observer. Both influence the line wings in flux level: forward beaming increases the blue wing whereas back beaming suppresses the red wing.

▷ The **gravitational redshift effect** is a general relativistic effect: photons propagating in gravitational fields lose energy according to the redshift factor (lapse function) $\alpha = 1/\sqrt{-g^{\mathrm{tt}}}$. It is just this effect that causes the blackness of a black hole when approaching the event horizon (see discussion of the *Great Black Spot* in Sec. 3.4).

All these effects together can be summarized in one quantity, the **relativistically generalized Doppler factor** or g–factor, satisfying

$$\begin{aligned} g &\equiv \frac{\nu_{\mathrm{obs}}}{\nu_{\mathrm{em}}} = \frac{1}{1+z} = \frac{\hat{p}^{\mathrm{t}}_{\mathrm{obs}}}{\hat{p}^{\mathrm{t}}_{\mathrm{em}}} \\ &= \frac{\alpha_{\mathrm{em}}}{\gamma\left[(1-\omega\lambda) - \alpha\, v^{(\mathrm{r})}\frac{\sqrt{\mathcal{R}_0}}{\rho\sqrt{\Delta}} - \alpha\, v^{(\theta)}\frac{\sqrt{\Theta}}{\rho} - \alpha\, v^{(\phi)}\frac{\lambda}{\tilde{\omega}}\right]_{\mathrm{em}}} \\ &= \frac{\alpha_{\mathrm{em}}}{\gamma\left[1 - \alpha\, v^{(\mathrm{r})}\frac{\sqrt{\mathcal{R}_0}}{\rho\sqrt{\Delta}} - \alpha\, v^{(\theta)}\frac{\sqrt{\Theta}}{\rho} - \lambda\,\Omega\right]_{\mathrm{em}}}. \end{aligned} \tag{6.2}$$

The g–factor follows from the Carter momenta which are boosted into the rest frame of the plasma[3]. Indices *obs* respectively *em* denote observer's respectively emitter's frame. α, ω, Δ, ρ, $\tilde{\omega}$ are the Boyer–Lindquist functions as introduced in Sec. 2.2, Eqs. (2.6). γ denotes the Lorentz factor. The plasma velocity field given in the ZAMO frame (denoted by round brackets) consists of $v^{(\mathrm{r})}$, $v^{(\theta)}$ and $v^{(\phi)}$. $\mathcal{R}_0$ and Θ represent two polynomials of fourth order[4]. They can be computed by

$$\frac{\mathcal{R}_0}{E^2} = r^4 + (a^2 - \lambda^2 - \mathcal{C})r^2 + 2\left[\mathcal{C} + (\lambda - a)^2\right] r - a^2\mathcal{C}, \tag{6.3}$$

$$\frac{\Theta}{E^2} = \frac{\mathcal{C}}{E^2} - \left[a^2\left(\frac{m^2}{E^2} - 1\right) + \lambda^2 \mathrm{cosec}^2\theta\right]\cos^2\theta. \tag{6.4}$$

The polynomials are associated with Carter's constant, $\mathcal{C}$, that is an exclusive feature of the Kerr geometry. Additionally, there is a dependence on the specific angular momentum of the photon, $\lambda = J/E$, the ratio of the two conserved quantities – angular momentum J and total energy E – along each photon path.
Simulating spectra means evaluating the **integral of the spectral flux** over each infinitesimal solid angle element, $d\Xi$, assuming a delta distribution for the intrinsic line

[2]This effect is also relevant in relativistic jets pointing towards the observer e.g. in blazars.
[3]indicated by the hat
[4]index 0 denotes photons, $m = 0$.

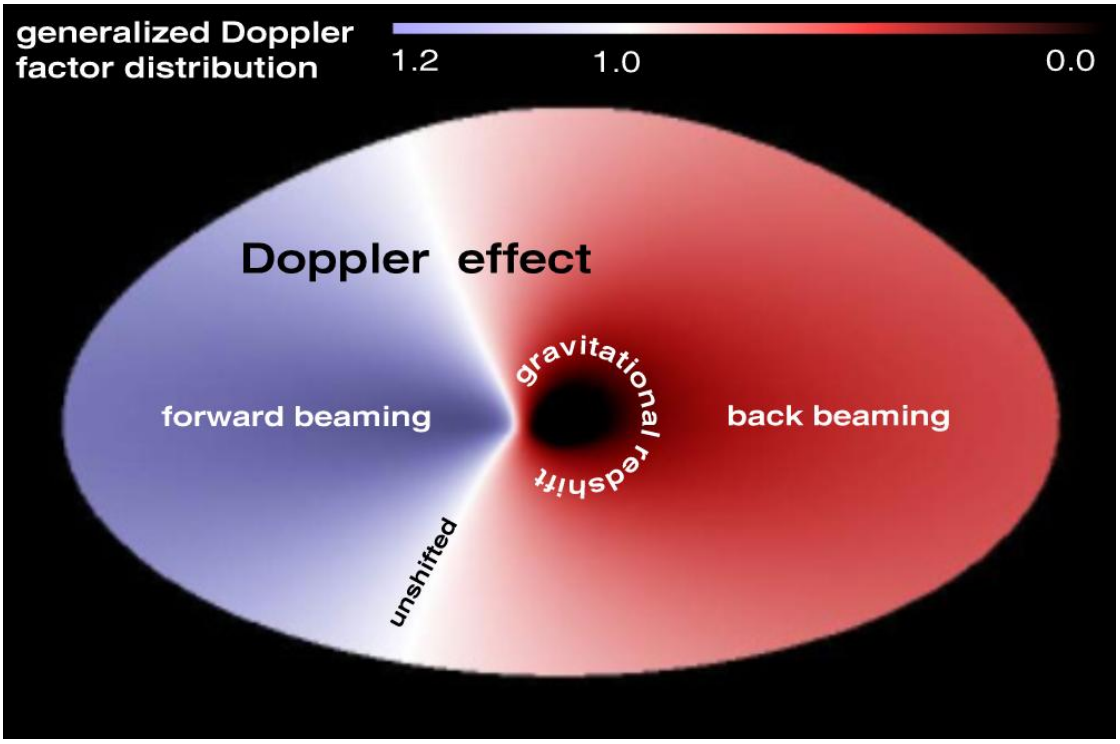

Figure 6.2: Simulated disk image around a central Kerr black hole color–coded in the generalized Doppler factor g. The distribution illustrates redshift $g < 1$ (*black* to *red*), no shift $g = 1$ (*white*) and blueshift $g > 1$ (*blue*). Regions of Doppler effect, beaming and gravitational redshift are marked. The inclination angle amounts $i = 60°$.

profile in the rest frame

$$F_{\rm obs} = \int_{\rm image} I_\nu^{\rm obs}\, d\Xi = \int_{\rm image} \epsilon(r)\, g^4\, \delta(E_{\rm obs} - gE_0)\, d\Xi. \tag{6.5}$$

Please note that the 4th power of g is a consequence of rewriting the argument in the delta distribution, $\delta(\nu_{\rm em} - \nu_0) = \delta((\nu_{\rm obs} - g\,\nu_0)/g) = g\,\delta(\nu_{\rm obs} - g\,\nu_0)$. The other three powers come from the Lorentz invariant, $I_\nu/g^3 =$ invariant. The rest frame energy of the line, E_0, must be plugged in e.g. 6.4 keV for Fe Kα X-ray lines. It appears another essential quantity, the *radial emissivity*, $\epsilon(r)$. From the theory of SADs it is motivated that the emissivity follows a power law profile with slope $p = 3.0$, $\epsilon(r) \propto r^{-p}$ [Sha73]. In recent work [Mül04], it is suggested to cut smoothly the emissivity profile at the truncation radius of the disk (see later, Sec. 6.2) or to study emitting rings with Gaussian shaped emissivities. These emissivities provide a tool to simulate distinct emitting regions. *Broken power laws* which have jumping power law index at a certain radius, $r_{\rm br}$, pose an alternative to investigate other emitters.

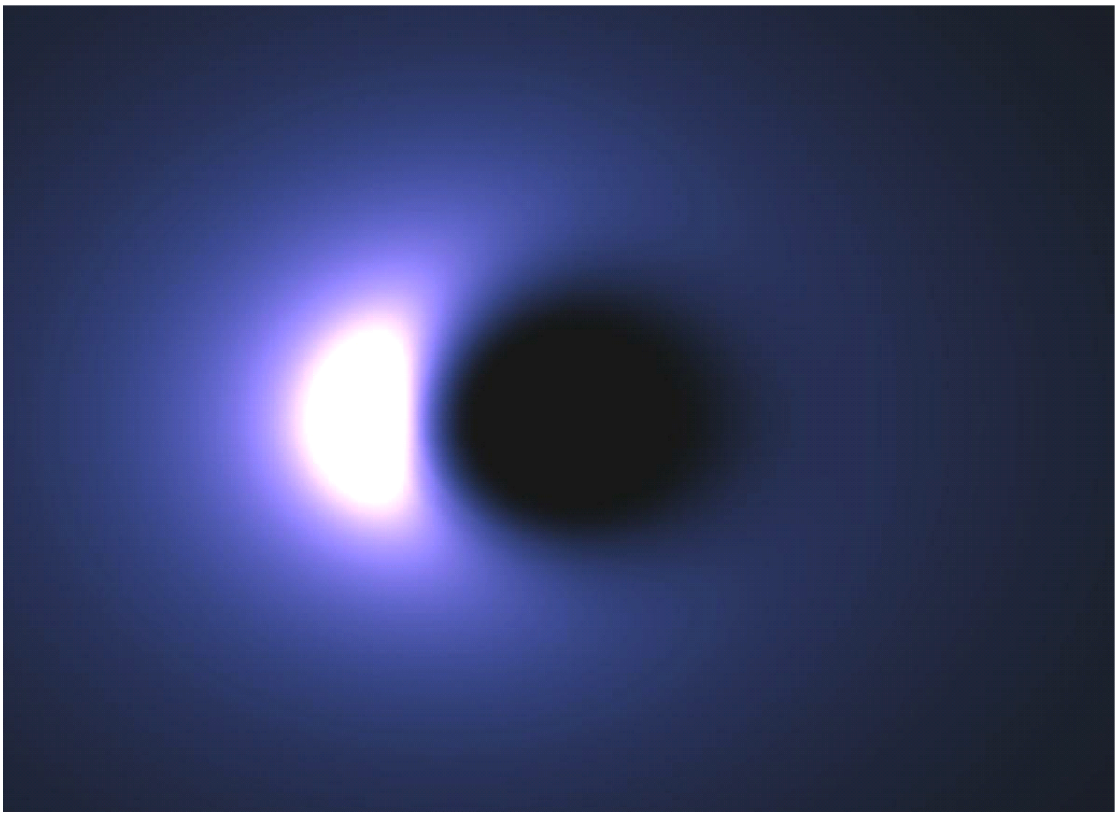

Figure 6.3: Simulated appearance of a uniformly luminous standard disk around a central Kerr black hole, $a \simeq 1$. The emission is color–coded and scaled to its maximum value (*white*). The disk is intermediately inclined to $i = 40°$. The forward beaming spot of the counterclockwisely rotating disk is clearly seen on the left whereas the right side exhibits suppressed emission due to back beaming. The black hole is hidden at the Great Black Spot in the center of the image.

Algorithm The ray tracing algorithm loops over each pixel $\{x, y\}$ on the screen. The user has to:

- ▷ specify input parameters for black hole–disk system. For black hole: Kerr parameter, a. For standard disk: inclination, i, inner edge, $r_{\rm in}$, outer edge, $r_{\rm out}$, velocity field, $\{v^{\rm r}, v^{\theta}, v^{\phi}\}$, e.g. pure Keplerian rotation, $\Omega_{\rm kep}$ (compare Eq. (2.16)); the first output is a generally lensed disk image;
- ▷ choose an emissivity law: power law, Gaussian or cut–power law to evaluate flux; the second output is an emission line or a continuum spectrum.

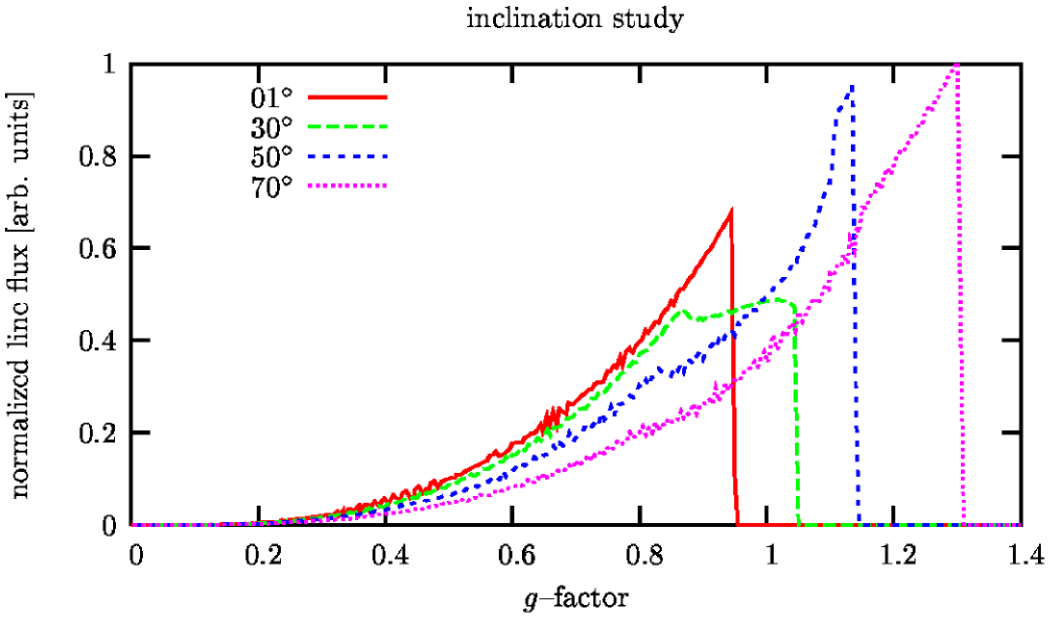

Figure 6.4: Simulation of observed line profiles with variable inclination angle of the disk, $i = 1°, 30°, 50°, 70°$. The maximum line flux is normalized to 1 and flux is plotted over the g–factor. The line in the rest frame of the plasma corresponds to $g = 1$. Other parameters are: Kerr parameter $a = 0.999999\,M$, inner disk edge $r_{\rm in} = r_{\rm H} = 1.0015\,r_{\rm g}$, outer disk edge $r_{\rm in} = 30.0\,r_{\rm g}$, single power emissivity profile, $\epsilon(r) \propto r^{-3.0}$. The plasma velocity field is purely Keplerian. Increasing inclination shifts the line to higher energies and enhances the blue wing (blueshift).

The pixel coordinates fix the conserved quantities λ and $\mathcal{C}$ [Cun73]. From the solution of the null geodesics equation a corresponding pair $\{r_{\rm em}, \theta_{\rm em}\}$ (axisymmetry!) in the emitter system is calculated. These four quantities are used to code the g–factor in Eq. (6.2) for each pixel. A result of this procedure is shown in Fig. 6.2: the distribution of the g–factor over a SAD around a Kerr black hole.

Likewise, it is possible to visualize the emission distribution over the disk. Fig. 6.3 displays a fascinating result of the appearance of a luminous standard disk around a Kerr black hole for a close observer at $r_{\rm obs} = 1000\,r_{\rm g}$. The image deviates strongly from Newtonian disks and exhibits relativistic effects from both, strong gravity and relativistic motion. An integration over such an image following the flux integral equation, Eq. (6.5), leads to relativistic line profiles or spectra emitted in the vicinity of black holes. A rather huge number of parameters determines the line profile: Kerr parameter, disk inclination,

inner disk edge, outer disk edge, velocity field, emissivity law parameters (one, two or three parameters depending on type) and truncation radius, equivalently given by the set $\{a,\, i,\, r_{\rm in},\, r_{\rm out},\, v^{(\rm r)},\, v^{(\theta)},\, v^{(\phi)},\, \epsilon(r)\}$. Therefore, a variety of line profiles results. This 'line zoo' can be classified by the morphological characteristics of the line as anticipated in Sec. 3.4, where the spectro–relativistic identification method was presented. In Fig. 3.4 it was shown that all line profiles can be put into the morphological classes: triangular, double–horned, bumpy, shoulder–like and double–peaked [Mül04].
Fig. 6.4 shows an example for a parameter study: a SAD around an extreme Kerr black hole extending down to the event horizon was assumed. Additionally, a simple single power law à la Shakura & Sunyaev was presumed, too. Then the parameter with the strongest influence on the appearance of disk and line was varied: the inclination angle of the disk. The example proves that increasing inclination angle enhances beaming.

The emission distribution over the SAD shows that a bright beaming spot (compare Fig. 6.3) evolves at the point where the plasma moves relativistically fast towards the observer. The line profiles in Fig. 6.4 prove that increasing inclination shifts the line to higher g–factors i.e. higher observed photon energies and intensifies the blue wing of the line. As an aside we state that these line profiles are triangular. Further parameter studies can be found in the work of Müller & Camenzind.
In the next section we present a new approach in Kerr black hole ray tracing: The *radial drift model* considers luminous truncated standard disks near *accreting* rotating black holes.

6.2 Radial Drift Model for Truncated Standard Disks

This section is dedicated to a contribution for accretion theory of black holes namely the radial drift model for standard disks. It was already proposed in Sec. 4.2 that the SAD does probably not extend down to the marginally stable orbit (ISCO). Efficient radiative cooling causes *disk truncation* at radii, $\mathrm{R_t}$, which are significantly larger than the ISCO [Huj00a, Huj00b]. The truncated model inspired by pseudo–Newtonian radiative hydrodynamics motivates to study truncated SADs in context of relativistic emission lines [Mül04].
Truncated standard disks (TSDs) suggest a plasma velocity field which strongly deviates from purely Keplerian motion. As outlined in Sec. 6.1 the velocity field is an input for the generalized Doppler factor, g, in Eq. (6.2). Therefore, one expects that simulated relativistic emission line profiles change notably if disk truncation is assumed.

Fig. 6.5 should be taken as a sequence which points out the evolutionary steps to modify a velocity field and adapt it to real accretion flows: The classical setup is a luminous disk, usually a SAD, but only with purely Keplerian velocity field, $v^{(\phi)} = v_{\rm K}$ (ZAMO frame). Classical ray tracing methods neglect the small radial drift overimposed to Keplerian rotation although a Shakura–Sunyaev disk demands for it as outlined in Sec. 4.2. The **radial drift model** introduced by Müller & Camenzind meets the requirements of accretion. In the middle of Fig. 6.5 the velocity field of the radial drift

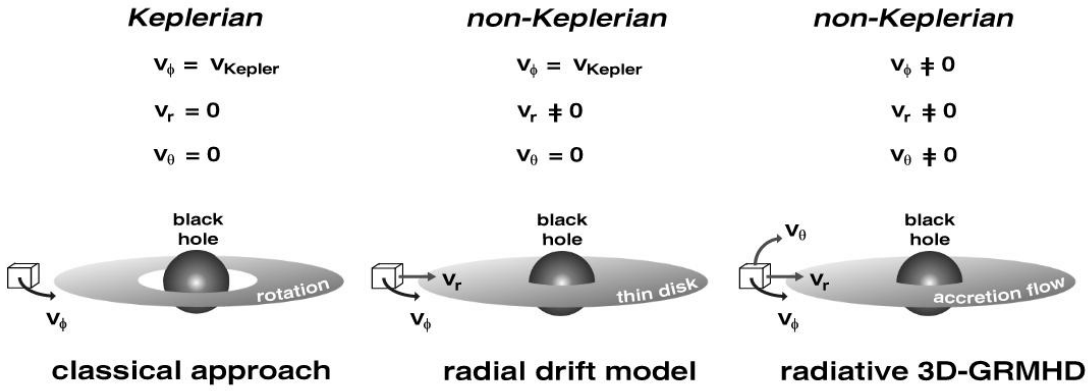

Figure 6.5: Comparison of different velocity fields in accretion disks. The *left–hand side* shows the standard velocity field: pure Keplerian rotation, $v_\phi = v_\mathrm{K}$. *In the middle*, a radial drift is superimposed to the Keplerian rotation. This accounts to accretion motion. On the *right–hand side*, a general velocity field is implemented. This flow data could be a result of a time–dependent numerical simulation i.e. radiative GRMHD in 3D.

model is sketched. On the right–hand side the most general velocity field is assumed. The parameter set $\{v_\phi, v_\mathrm{r}, v_\theta\}$ in each volume element of the black hole–disk system is a result of GRMHD calculations. The best simulations which could be done are radiative and dissipative 3D GRMHD simulations that are still not achieved – worldwide. A nice "proof of concept" on the way to link GR fluid physics to relativistic ray tracing techniques was recently done: pseudo–Newtonian MHD simulations were connected to ray tracing using transfer functions [Arm03]. It was shown that the turbulent magnetized flow produces variable X–ray spectra, especially variable X–ray iron fluorescence lines. The two numerical schemes can be linked together by plugging the velocity field of the plasma – as an output from MHD simulations – into the ray tracing algorithm as an input. This is the procedure to simulate the emission from time–dependent accretion flows (Fig. 6.6 displays the result).

Now, it is focused on the implementation of radial drift without poloidal motion. In general, the radial drift in the Boyer–Lindquist ZAMO frame satisfies [Mül04]

$$v^{(\mathrm{r})} = \frac{\sqrt{\mathcal{R}}}{\Sigma(1-\omega\lambda)}, \tag{6.6}$$

with the "radial potential" introduced by Carter

$$\frac{\mathcal{R}}{E^2} = \left[(r^2+a^2)-a\lambda\right]^2 - \Delta\left[\frac{\mathcal{C}}{E^2} + (\lambda-a)^2 + r^2\frac{m^2}{E^2}\right]. \tag{6.7}$$

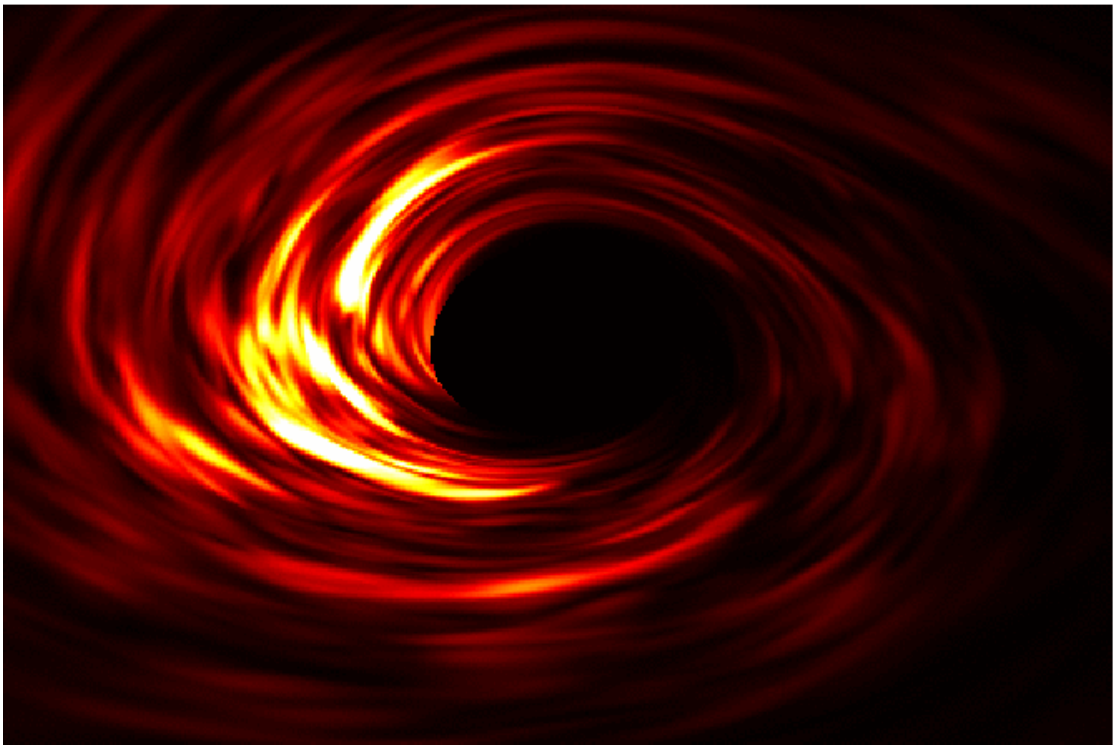

Figure 6.6: Variable emission from a pseudo–Newtonian MHD accretion disk inclined to 55°. The pseudo–Schwarzschild black hole harbors in the center. As in Fig. 6.2 the Beaming effect (*left from the hole*) and Lensing effect (*top edge of the disk*) is occur. (Credit: [Arm03])

$\mathcal{R}$ is the generalization of $\mathcal{R}_0$ in Eq. (6.3). Here an infalling plasma particle of mass m is considered, not a photon ($m = 0$) as for $\mathcal{R}_0$. Notice that Carter's constant, $\mathcal{C}$, vanishes in the equatorial plane, $\theta = \pi/2$. One can compute from Eq. (6.6) that at the event horizon the radial drift becomes unity *for any accretion flow*. In other words: The infalling plasma passes the horizon with the speed of light in any case as viewed from the ZAMO frame.

In the radial drift model it is assumed that

- ▷ for a particle that reaches a critical radius – the **truncation radius** R_t – the integrals of motion E and J i.e. $\lambda = J/E$ are fixed;
- ▷ the particle starts free–falling at R_t and follows the geodesics of the Kerr geometry;
- ▷ if $R_\mathrm{t} < r_\mathrm{ms}$ the specific angular momentum of the particle, λ, is fixed to its value at the ISCO;
- ▷ λ can only be chosen out of the interval $[\lambda_\mathrm{ms}, \lambda_\mathrm{mb}]$ [Abr78].

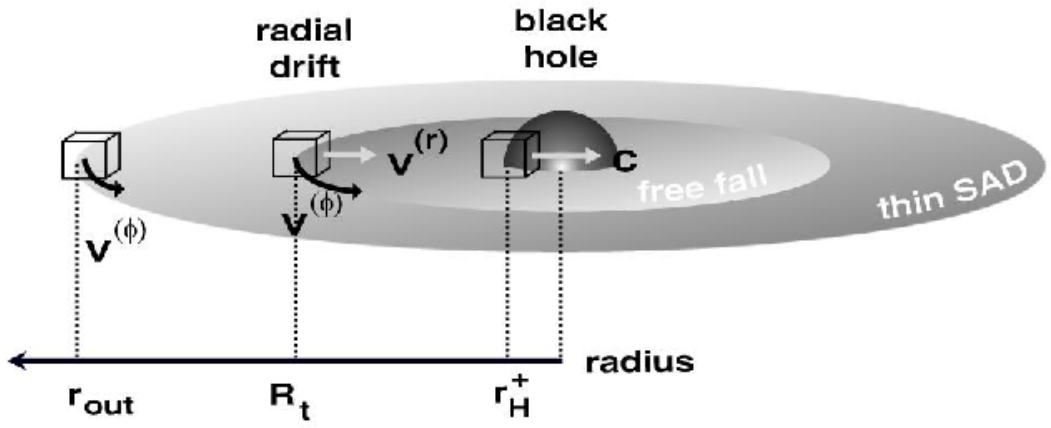

Figure 6.7: Sketch of the radial drift model for truncated standard disks (TSDs): The outer velocity field is Keplerian. At a critical radius, the truncation radius R_t, the radial inward motion of the plasma starts. The free–falling matter becomes significantly accelerated and reaches the speed of light at the outer event horizon at r_H^+ as been viewed by the ZAMO.

Paying attention to these restrictions a suitable radial drift can be chosen. The velocity field in the radial drift model for distinct regions of the disk is sketched in Fig. 6.7.

Radial emissivity profile The model is completed when truncation is also regarded in the emissivity law. The physical motivation is that emission must break down at the truncation radius. Therefore, emissivity in truncated disks differs significantly from the SAD emissivity. The emissivity is important for the evaluation of the spectral flux, Eq. (6.5).

A plausible ansatz is to suppress the power law emissivity at the inner disk edge by a steeply decreasing function. Here, it is suggested that at truncation the original SAD power law emissivity $\propto r^{-3}$ is exponentially damped by a factor $\exp(-3\,R_\mathrm{t}/r)$. This is called a **cut–power law**.

As an alternative, one can consider a *localized emissivity* which can be modeled by a **Gaussian profile**, following $\exp(-(r-R_\mathrm{t})^2/\sigma_\mathrm{r}^2)$. The parameter σ_r controls the Gaussian width and can be suitably chosen. It could also be coupled to the truncation radius by setting $\sigma_\mathrm{r} = \eta\, R_\mathrm{t}$ with a constant factor η. The interpretation of a Gaussian emissivity profile is that the emission originates from a ring. The ring thickness is fixed by σ_r. Any axisymmetric emitting region can be divided into rings. Thereby, the peak value of the Gaussian weights the emission strength. Multiple Gaussian profiles can therefore be used to model arbitrary axisymmetric emitters. However, this is rarely the case in real emitters. One could easily imagine surrounding spots that break axisymmetry. These non–stationary emitters can be modeled by considering the t– and the ϕ–integral in the

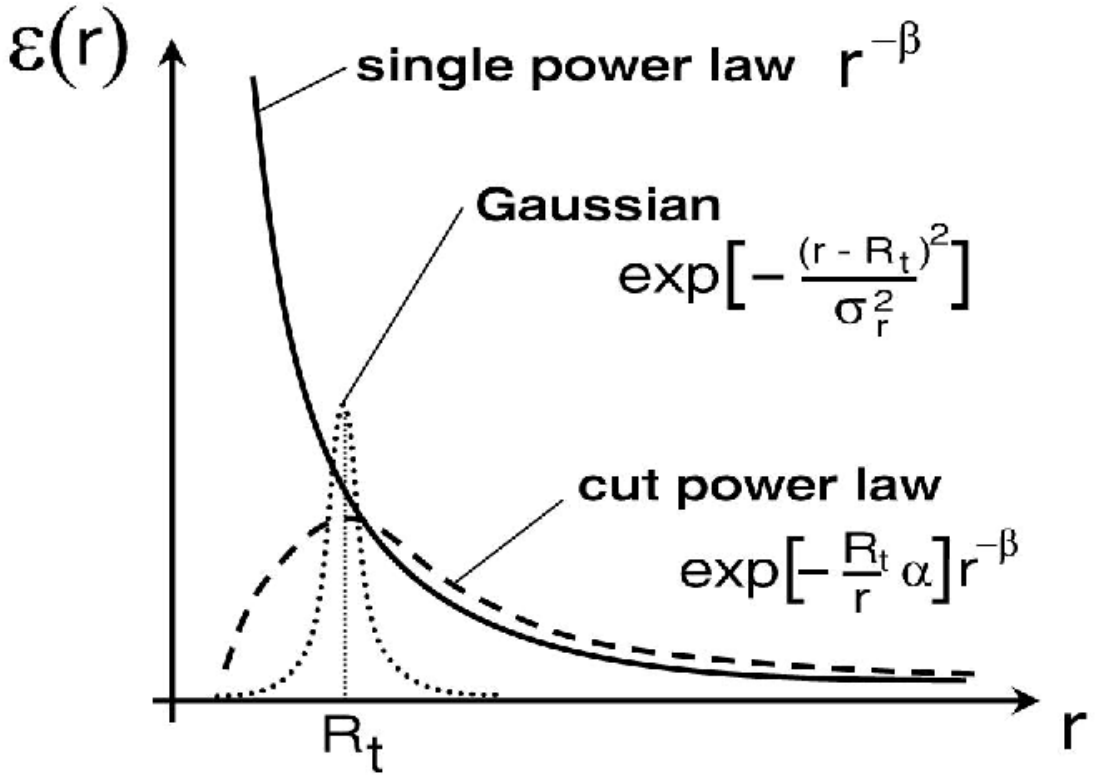

Figure 6.8: The shapes of radial emissivities of standard disks and truncated disks. The standard Shakura–Sunyaev single power law (*solid*) increases steeply to smaller radii. In contrast, the cut–power law (*dashed*) is exponentially damped at the inner edge of the disk at the truncation radius, $R_{\rm t}$. The Gaussian emissivity (*dotted*) is localized at the radius $R_{\rm t}$ of the disk, here associated with truncation.

Kerr ray tracing framework.
The shapes of these two new radial emissivity profiles are illustrated in comparison to the standard SSD single power law emissivity in Fig. 6.8.

The results of including radial drift are that **graviational redshift is enhanced** by drift. This is plausible because photons which are emitted by radially infalling particles suffer from stronger trapping and lensing effects and can hardly escape the strong gravitational pull plus the inward motion. Fig. 6.9 illustrates this while directly comparing Keplerian rotation with non–Keplerian drift motion. At the right image including drift the g–factor distribution is significantly darkend at the inner disk i.e. drift intensifies emission suppression.
The effect of drift has also imprints in line profiles. Enhancement of gravitational drift

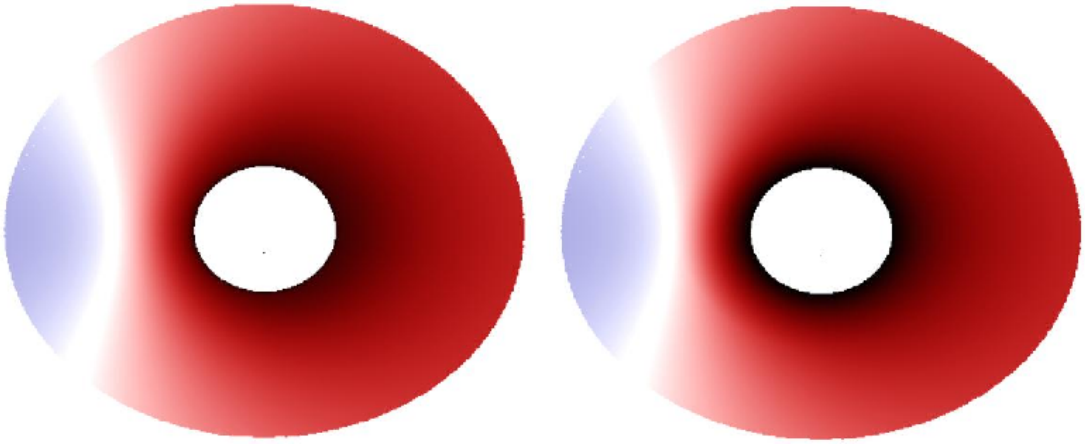

Figure 6.9: Direct comparison of purely Keplerian rotation (*left–hand side*) with non–Keplerian motion including radial drift (*right–hand side*). Drift causes darkening in the vicinity of the event horizon (*white cut–out*) i.e. gravitational redshift is enhanced by inward drift. Parameters are set to Kerr parameter $a = 0.1\,M$, inclination $i = 40°$, inner disk edge $r_{\rm in} = r_{\rm H} = 1.996\,r_{\rm g}$, outer disk edge $r_{\rm out} = 10.0\,r_{\rm g}$ and truncation radius $R_{\rm t} = 5.0\,r_{\rm g}$. Emissivity is chosen to be a exponentially damped SSD power law.

means that the red wing of the line is torn apart and the red wing flux is reduced as displayed in Fig. 6.10. It is stressed here that the lack of relativistic emission lines in observations, especially of AGN (mostly Seyfert–1s), hints for significantly *large* truncation radii, $R_{\rm t} \gg r_{\rm ms}$. A large distance between hot corona and cold disk prevents from generating fluorescence lines. So, the lack can be explained geometrically in the truncated disk scenario: on one hand the relative position of corona and disk becomes adverse so that the illumination failed; and on the other hand the proximity of hot illuminator (corona) and cold reflector (disk) is abrogated. This issue is pictured in Fig. 6.11. The accretion solution sketched there can be associated with the accretion unification scheme in Sec. 4.3: The accretion rate i.e. the feeding of the hole from the surrounding triggers the truncation. According to the GRMHD simulations by De Villiers et al. as presented in Sec. 5.9 the inner torus is time–variable for high black hole spins. The feeding of the plunging region and the decay and rebuild of the inner torus support disk truncation models. Further simulations that go away from an initial torus and follow up non–uniform feeding are supposed to confirm truncation, too.
Additionally, a contribution to this lack is the ionisation state of cold disk material. It was shown that e.g. large ionisation parameters avoid the fluorescence process [Mat93, Marto96].

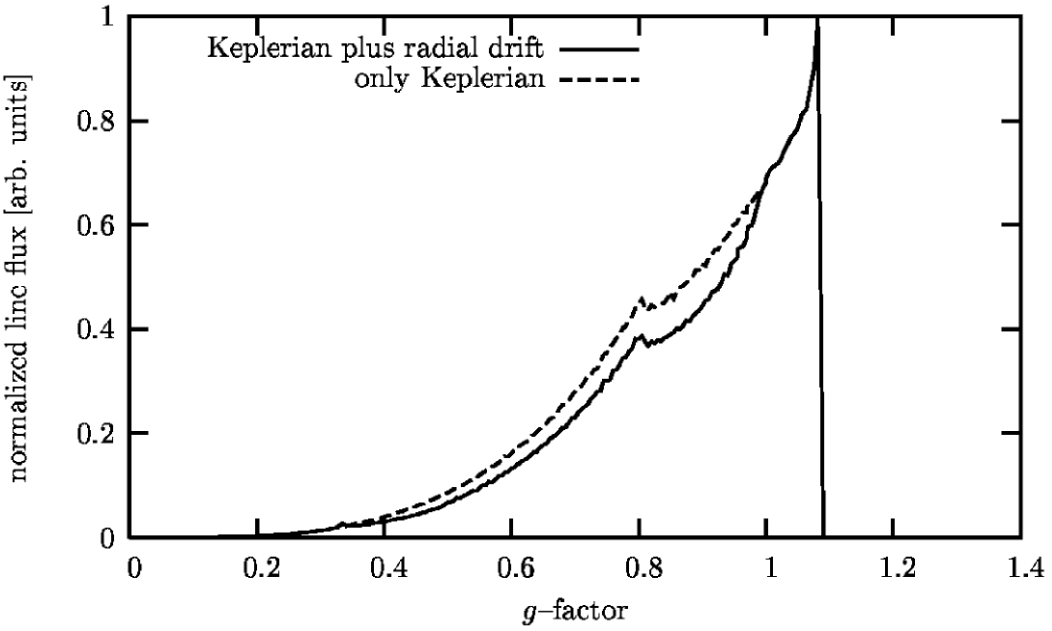

Figure 6.10: Direct comparison of purely Keplerian rotation (*dashed profile*) with non–Keplerian motion including radial drift (*solid profile*). Drift causes a more extended red wing and a significantly reduced maximum flux of the line due to enhanced gravitational redshift. Parameters are set to Kerr parameter $a = 0.8\,M$, inclination $i = 40°$, inner disk edge $r_{\rm in} = r_{\rm H} = 1.6\,r_{\rm g}$, outer disk edge $r_{\rm out} = 20.0\,r_{\rm g}$ and truncation radius $R_{\rm t} = 4.5\,r_{\rm g}$. Emissivity is chosen to be a single power SSD law $\propto r^{-3}$. As could be expected, inner disk features only change the red wing of the line.

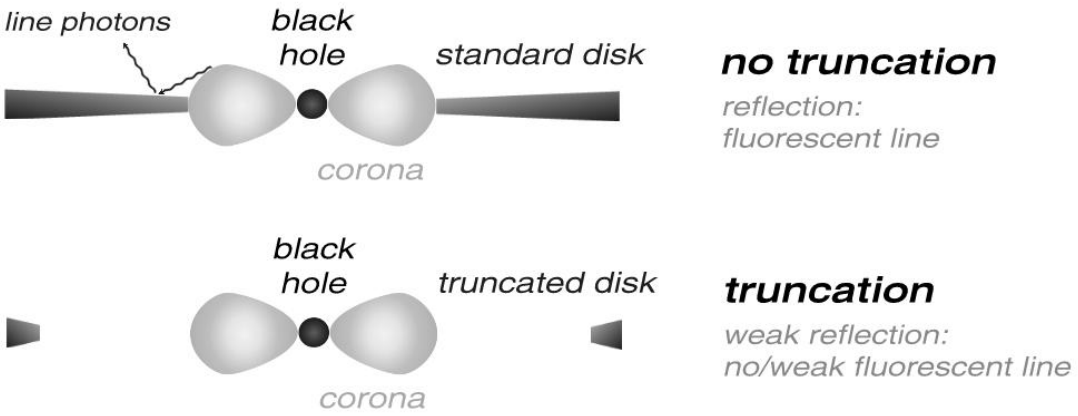

Figure 6.11: Generation and suppression of fluorescence line photons. *Top*: A sandwich–like configuration of disk and corona permits the formation of relativistic emission lines by fluorescence. *Bottom*: The fluorescence process is prevented in the truncation scenario by geometrical reasons.

7 Discussion

The present work gives an overview of black hole accretion physics. It is focused on GRMHD of Kerr black holes. Of particular interest is the formation of outflows, the relativistic jets. As asides further developments in Kerr ray tracing and a classification of black hole detection techniques are presented.

Rotation turns out to be a vital ingredient of black hole physics. Static Schwarzschild black holes do not suffice to explain the observations since they lack an ergosphere. Stationary accretion theory gives some ideas about the mechanisms that operate in the vicinity of a rotating black hole, in particular within the ergosphere: Penrose processes, Penrose pair productions, Blandford–Znajek processes, gravitomagnetism, Poynting fluxes – all these mechanisms need black hole rotation. Observations of black hole candidates that can be detected by kinematical, spectro–relativistic, eruptive, accretive, aberrative, obscurative, or – maybe in the near future – gravitational wave–induced verification methods seem to prove the existence of Kerr black holes in nature. However, the theoretical developments hint for possible different stories: alternative static space–times so far only substitutes for the Schwarzschild black hole give rise for a totally different gravitational vacuum state. They are called gravastar and holostar and meet the requirements of modern approaches to the vacuum. These solutions suggest that a "black hole" consists either of a dark energy core or a string core. Theorists have to do consistency checks and to await observational clues so that they can rule out any of the proposed solutions. Although there is few chance that one may succeed in distinguishing these CDO solutions observationally. The reason is that black holes, gravastars and holostars are all comparably dark due to the strong gravitational redshift effect. The existence of singularities, above all the idealized point or ring singularities of classical black holes collides dramatically with the concepts of quantum theory e.g. the uncertainty principle. Insofar, the current developments suggest a re–evaluation of the singularity theorems. These critical remarks concerning black holes in astrophysics are perfomed in this work to get in impression for future research directions.

Apart from these doubts that are associated with classical black holes, the Kerr space–time proves to be a well–defined and powerful model to explain a variety of phenomena associated with black hole physics. First of all, the production of relativistic jets in AGN, BHXBs and GRBs can be nicely explained by a magnetosphere that is immersed into a rotating black hole. The MRI turns out to be an efficient mechanism to launch the accretion process magnetically. In fact, black hole physics is vitally linked to MHD. This motivated for recent developments in time–dependent GRMHD i.e. the description of a magnetized plasma on the background of a Kerr black hole. Worldwide, there

are only four GRMHD codes available so far that treat this problem. The numerical schemes slightly differ e.g concerning conservativity that is naturally dictated by GR. Unfortunately, the codes following a classical fluid description failed to give a cogent prove for relativistic jet formation. A simulation result for a relativistic jet which exceeds a Lorentz factor of 10 at the jet base is still lacking. Currently, only low Lorentz factors around two are feasible. Besides this, there is an open question concerning the driver of outflows near Kerr black holes. Recent work indicates that jets are launched magneto–centrifugally via differential rotation of space–time. But the relevant mixing of mass flux and Poynting flux which both drive the outflow is still not known.
One code that seeks to solve the string equations for magnetic flux tubes gives plausible results: The flux tubes are dragged by the rotating space–time to form two diametral magnetic towers that are associated to bipolar relativistic jets. However, the code suffers from unphysical features such as a lacking dissipative description. Therefore, the dissipative reconnection of adjacent flux tubes is not included. An outlook to further developments in GRMHD points towards dissipative GRMHD and radiative GRMHD. Both regimes will be very expensive because the challenge is twofold: robust numerical methods are lacking and requirements for computational resources are high. One could imagine that scientists will work some years to come along with these problems.

The successful treatment of the non–radiative regime enriches accretion theory with new paradigms such as the NRAF. Newtonian MHD and GRMHD significantly change the knowledge of purly hydrodynamical issues (SAD, ADAF, TDAT etc.). MHD is a fast growing branch in astrophysics that turned out to be relevant also in theories for planet, star and galaxy formation and evolution.
The synoptical perspective onto observed black hole systems opens the possibility to unify them. Today, accretion theory suggests that there is no need to distinguish an accreting stellar from an accreting supermassive black hole. According to the accretion unification scheme there is a basic set of parameters that controls the appearance of a black hole system: black hole mass, black hole spin, accretion rate, inclination of the system to the observer, mass of dusty torus and seed magnetic field strength – this minimal set of input parameters may suffice to generate the zoo of black hole systems.
But certainly, there are some differences in the initial conditions: supermassive black holes harboring in nearly any galaxy are supposed to be fed by a cold dusty torus located on the pc scale. Observations reported that the large scale torus exhibits a well–arranged magnetic field structure. It is proposed that this structure survives in the accretion process down to the ergosphere. In contrast, stellar black holes in X–ray binaries lack a comparable magnetic field structure. The donator star seems not to deliver a well–arranged field. This may be the reason for the different structures seen in micro–jets vs. macro–jets.

Another aspect considered in this work concerns relativistic spectra, above all relativistically broadened emission lines. Many X–ray binaries and some AGN (Seyfert–1s, QSOs type 1) exhibit X–ray fluorescence lines around 6 keV as a component of the reflection bump. Hard photons from the corona illuminate the cold accretion disk and

produce these fluorescence photons. Since this process occurs close to the black hole relativistic imprints such as gravitational redshift and beaming deform the line profile. Therefore, the observed profile serves as diagnostical tool to fix parameters of the black hole–disk system. Parameter studies by using the Kerr ray tracing technique result in a classification of line profiles by morphology: Relativistically distorted emission line profiles can be classified as triangular, double–horned, bumpy, shoulder–like or double–peaked line.
However, many AGN type 1 lack of the fluorescence line feature. It is proposed in this work that the lack is due to disk truncation. The radial drift model for TSDs which includes accretion and new suitable emissivities alters classical approaches that only consider Keplerian motion and standard SAD emissivities. Drift motion essentially enhances the gravitational redshift effect so that the line flux is reduced. For the first time, relativistic emission lines of accreting black holes could be studied.
A better solution is definitely to couple time–dependent accretion flow simulations e.g. GRMHD issues to relativistic ray tracing techniques. A pioneering work was done in the last year – even when the flow was restricted to the equatorial plane and the black hole was approximated by an pseudo–Newtonian approach. It was thereby shown that relativistic emission line complexes – dominantly Fe Kα lines – are naturally variable due to a non–uniform and non–stationary accretion flow and time–dependent illumination by a variable corona.
The fatal problem in the relativistic emission line business is the geometry and variability of the corona i.e. the donator of hard photons. Although reverberation mapping techniques give rise to the coronal structure, there are still aggravating uncertainties involved. GRMHD issues will certainly hint for answers concerning this problem. Until that day, researchers may dream of and work hard for a code that solves radiative, dissipative GRMHD. We can be assured that nature will sweeten this time with new beautiful discoveries.

□

A Appendix

A.1 Reformulation of energy–stress tensor in ideal GRMHD

In Sec. 5.2 an alternative formulation of the energy–stress tensor of ideal GRMHD was introduced. The Maxwell tensor is explicitly used to derive an electromagnetic part of the energy–stress tensor that essentially depends on the magnetic field, b^μ, and the plasma velocity field, U^μ. First, the Levi–Cevita tensor, $\epsilon_{\kappa\lambda\mu\nu}$, satisfies the contraction properties [DeV03a]

$$\epsilon_{\delta\epsilon\gamma\alpha}\,\epsilon^{\rho\sigma\nu\alpha} = -\delta^{\rho\sigma\nu}{}_{\delta\epsilon\gamma} \tag{A.1}$$

$$\epsilon_{\delta\epsilon\alpha\beta}\,\epsilon^{\rho\sigma\alpha\beta} = -2\delta_{\delta\epsilon}{}^{\rho\sigma}. \tag{A.2}$$

The Kronecker–delta holds the conditions

$$\delta^{\alpha\beta}{}_{\mu\nu} = \delta^\alpha_\mu\delta^\beta_\nu - \delta^\alpha_\nu\delta^\beta_\mu \tag{A.3}$$

$$\delta^{\alpha\beta\gamma}{}_{\lambda\mu\nu} = \delta^\alpha_\lambda\delta^\beta_\mu\delta^\gamma_\nu - \delta^\alpha_\mu\delta^\beta_\lambda\delta^\gamma_\nu + \delta^\alpha_\mu\delta^\beta_\nu\delta^\gamma_\lambda - \delta^\alpha_\nu\delta^\beta_\mu\delta^\gamma_\lambda + \delta^\alpha_\nu\delta^\beta_\lambda\delta^\gamma_\mu - \delta^\alpha_\lambda\delta^\beta_\nu\delta^\gamma_\mu. \tag{A.4}$$

Then, an expression for the covariant Maxwell tensor is computed using these relations, the antisymmetry of the field tensor, $\mathbf{F}_{\mu\nu} = -\mathbf{F}_{\nu\mu}$ and the normalization condition of the velocity, $U_\mu U^\mu = -1$

$$\begin{aligned}
\epsilon_{\alpha\beta\mu\nu}\,B^\alpha U^\beta &= \frac{1}{2}\,\epsilon^{\alpha\delta\epsilon\gamma}\,\epsilon_{\alpha\beta\mu\nu}\,U_\delta U^\beta\,\mathbf{F}_{\epsilon\delta} \\
&= -\frac{1}{2}\,\delta^{\delta\epsilon\gamma}{}_{\beta\mu\nu}\,U_\delta U^\beta\,\mathbf{F}_{\epsilon\delta} \\
&= -\frac{1}{2}(U_\beta U^\beta\,\mathbf{F}_{\mu\nu} - U_\mu U^\beta\,\mathbf{F}_{\beta\nu} + U_\mu U^\beta\,\mathbf{F}_{\nu\beta} \\
&\quad -U_\nu U^\beta\,\mathbf{F}_{\mu\beta} + U_\nu U^\beta\,\mathbf{F}_{\beta\nu} - U_\beta U^\beta\,\mathbf{F}_{\nu\mu}) \\
&= \mathbf{F}_{\mu\nu}.
\end{aligned} \tag{A.5}$$

All terms in brackets vanish exept from the first and the latter one due to infinite conductivity, $\mathbf{F}^{\mu\nu}U_\nu = 0$, the constraint of ideal MHD. Hence, all covariant Maxwell tensors of the electromagnetic part can be written in terms of B^μ and U^μ by using the Levi–Cevita tensor

$$\begin{aligned}
\mathbf{T}^{\mu\nu}_{\mathrm{EM}} &= \frac{1}{4\pi}\left(\mathbf{F}^\mu{}_\alpha\,\mathbf{F}^{\nu\alpha} - \frac{1}{4}\mathbf{F}_{\alpha\beta}\,\mathbf{F}^{\alpha\beta}\,\mathbf{g}^{\mu\nu}\right) \\
&= \frac{1}{4\pi}\left(\mathbf{g}^{\mu\gamma}\mathbf{F}_{\gamma\alpha}\,\mathbf{F}^{\nu\alpha} - \frac{1}{4}\mathbf{F}_{\alpha\beta}\,\mathbf{F}^{\alpha\beta}\,\mathbf{g}^{\mu\nu}\right)
\end{aligned}$$

$$
\begin{aligned}
&= \frac{1}{4\pi}\left[\mathbf{g}^{\mu\gamma}\left(\epsilon_{\delta\epsilon\gamma\alpha}B^{\delta}U^{\epsilon}\right)\left(\epsilon^{\rho\sigma\nu\alpha}B_{\rho}U_{\sigma}\right)-\frac{1}{4}\left(\epsilon_{\delta\epsilon\alpha\beta}B^{\delta}U^{\epsilon}\right)\left(\epsilon^{\rho\sigma\alpha\beta}B_{\rho}U_{\sigma}\right)\mathbf{g}^{\mu\nu}\right]\\
&= -\frac{1}{4\pi}\left(\mathbf{g}^{\mu\gamma}\delta^{\rho\sigma\nu}{}_{\delta\epsilon\gamma}B^{\delta}U^{\epsilon}B_{\rho}U_{\sigma}-\frac{1}{2}\mathbf{g}^{\mu\nu}\delta^{\rho\sigma}{}_{\delta\epsilon}B^{\delta}U^{\epsilon}B_{\rho}U_{\sigma}\right)\\
&= -\frac{1}{4\pi}\left(-\frac{1}{2}\,\mathbf{g}^{\mu\nu}B^{\alpha}B_{\alpha}+B^{\mu}B^{\nu}-B^{\alpha}B_{\alpha}U^{\mu}U^{\nu}\right)\\
&= \frac{1}{2}\,\mathbf{g}^{\mu\nu}b^{2}+U^{\mu}U^{\nu}b^{2}-b^{\mu}b^{\nu}. \qquad \text{(A.6)}
\end{aligned}
$$

Here the $b^2 = \mathbf{g}^{\mu\nu}b_\mu\, b_\nu = b^\nu\, b_\nu$ is defined. Taking this reformulation of the electromagnetic part, Eq. (A.6), as well as the matter part of the energy–stress tensor of GRMHD and sorting the terms one arrives at the result given as Eq. (5.19)

$$
\mathbf{T}^{\mu\nu}_{\mathrm{GRMHD}} = \left(\rho + e + P + \frac{b^2}{4\pi}\right)U^{\mu}U^{\nu} + \left(P + \frac{b^2}{8\pi}\right)\mathbf{g}^{\mu\nu} - \frac{1}{4\pi}b^{\mu}\,b^{\nu}. \qquad \text{(A.7)}
$$

A.2 Kerr–Schild form of the Kerr geometry

In Sec. 5.3 we find a pathological behavior of the standard Boyer–Lindquist formulation of the Kerr geometry. The Kerr–Schild (KS) coordinate system offers the opportunity to circumvent this coordinate singularities at the horizon. The KS frame represents the most simple horizon adapted frame [Fon98].
According to those authors or alternatively Komissarov [Komi04a][1], the **covariant metric tensor of the Kerr geometry in Kerr–Schild form** is given by

$$
\begin{aligned}
\mathbf{g}_{\mu\nu} &= \begin{pmatrix} g_{tt} & g_{t\phi} & g_{tr} & 0 \\ g_{\phi t} & g_{\phi\phi} & g_{\phi r} & 0 \\ g_{rt} & g_{r\phi} & g_{rr} & 0 \\ 0 & 0 & 0 & g_{\Theta\Theta} \end{pmatrix}\\
&= \begin{pmatrix} -(1-Z) & -Za\sin^2\theta & Z & 0 \\ -Za\sin^2\theta & \tilde{\omega}^2 & -a(1+Z)\sin^2\theta & 0 \\ Z & -a(1+Z)\sin^2\theta & 1+Z & 0 \\ 0 & 0 & 0 & \rho^2 \end{pmatrix}, \qquad \text{(A.8)}
\end{aligned}
$$

with the function

$$
Z = 2Mr/\rho^2. \qquad \text{(A.9)}
$$

[1] signature $(-\,+\,+\,+)$

The corresponding **contravariant metric tensor of Kerr geometry in Kerr-Schild form** follows then to

$$\begin{aligned}
\mathbf{g}^{\mu\nu} &= \begin{pmatrix} g^{tt} & g^{t\Phi} & g^{tr} & 0 \\ g^{\Phi t} & g^{\Phi\Phi} & g^{\Phi r} & 0 \\ g^{rt} & g^{r\Phi} & g^{rr} & 0 \\ 0 & 0 & 0 & g^{\Theta\Theta} \end{pmatrix} \\
&= \begin{pmatrix} -(Z+1) & 0 & Z & 0 \\ 0 & 1/\tilde{Z} & a\sin^2\theta/\tilde{Z} & 0 \\ Z & a\sin^2\theta/\tilde{Z} & \frac{Z^2a^2\sin^4\theta-(Z-1)\tilde{\omega}^2}{\tilde{Z}} & 0 \\ 0 & 0 & 0 & 1/\rho^2 \end{pmatrix},
\end{aligned} \tag{A.10}$$

where a new suitable function, $\tilde{Z}$, is introduced in the present work by

$$\tilde{Z} = \tilde{\omega}^2 - (Z+1)a^2\sin^4\theta. \tag{A.11}$$

B Acknowledgements

I wish to thank...

...*Max Camenzind* to be my mentor for a couple of years.
I am grateful for interesting research and some really nice years in Heidelberg.

...*John Kirk* for his spontaneous acceptance to be referee of this work.

...*my wife Anja* for her patience and support.

...*Pascal & Dominic* that they let daddy do his PhD.

...*Jens Kleinhuis, Sven Daum and Markus Hartmann* for our friendship and some nice distractions during my PhD time.

...*Bernd Aschenbach* for interesting discussions about black holes and the "observer's view".

...*Till Neunhöffer* for a nice contact between a particle physicist and an astrophysicist.

...*Thomas Sollich* for his confidence in me and for sharing enthusiasm in distributing astrophysical knowledge.

...*Thomas Mädler* for some funny hours in our bureau.

...*Steffen Brinkmann* for advices in LaTeX and crazy philosophical debates.

...*José Gracia* for technical and mental assistance.

...*Matthias Stute* and *Martin Krause* for relaxed coffee breaks.

...*and all other theory group members* for having a nice time together.

...*my collegues* at the LSW.

...*the Persepolis* for extraordinary food support in Heidelberg.

...*my parents–in–law* for culinary and mental support.

...*my sister and my parents* for accompanying my PhD time.

Additionally, I wish to thank all the readers of my website, especially for fruitful discussions about astrophysics.
Please let me also thank all the researchers who contribute to our knowledge about nature.

C Mathematical Symbols

a: Kerr parameter, spin parameter

α: Boyer–Lindquist function: redshift factor, lapse function

α: lapse function in 3+1 split

α_{BL}: lapse function of a Kerr black hole in Boyer–Lindquist coordinates

α_{KS}: lapse function of a Kerr black hole in Kerr–Schild coordinates

α_{G}: lapse function of a gravastar

α_{N}: photon power law index

α: intercept in M–σ scaling law

b^i: spatial component of magnetic induction 4–vector

b^t: temporal component of magnetic induction 4–vector

b^μ: magnetic induction 4–vector

B^i, $\vec{B}$: magnetic field 3–vector

$\vec{B}_{\mathrm{P}}$: poloidal magnetic field 3–vector

$\vec{\beta}$: shift vector in 3+1 split

$\beta = v/c$: velocity in units of speed of light in Relativity

β: slope in M–σ scaling law

$\beta = p_{\mathrm{gas}}/p_{\mathrm{mag}}$: plasma beta

c: vacuum speed of light

c_{s}: speed of sound

$\mathcal{C}$: Carter's constant, the fourth conservative in the Kerr geometry

$\mathcal{C}$: compactness

D: relativistic density in GRHD

δ: delta distribution

Δ: horizon function

$d\Xi$: solid angle element

e: specific internal energy density

e^{μ}: electric field 4–vector

E: total energy of fluid

E_0: rest frame energy

$\vec{E}$: electric field 3–vector

ϵ: energy density

ϵ: a very tiny number

$\epsilon(r)$: radial emissivity profile

η: Gaussian emissivity parameter to couple width and truncation

$\epsilon^{\kappa\lambda\mu\nu}$: Levi–Civita tensor

$\mathbf{F}^{\mu\nu}$: Maxwell tensor

${}^{*}\mathbf{F}^{\mu\nu}$: Faraday tensor, the dual of the Maxwell tensor

$f(r)$: metric function of a gravastar

f: fraction in accretion theory to measure radiative efficiency

F_{em}: spectral flux in emitter's frame

F_{obs}: spectral flux in observer's frame

$\mathcal{F}$: flux vector of conservative formulation

g: g–factor, relativistically generalized Doppler factor

$\mathbf{g}^{\mu\nu}$: metric tensor

$\mathbf{G}$: Einstein tensor

G: Gravitational constant

γ: adiabatic index

γ: determinant of spatial 3–metric

γ: Lorentz factor, relativistic gamma

γ_{ij}: spatial 3–metric

Γ: polytropic index

$\Gamma^{\mu}{}_{\nu\sigma}$: Christoffel symbol, connection

h: Planck's constant

h: specific enthalpy

$h(r)$: metric function of a gravastar

$\bar{h}$: generalized specific enthalpy in GRMHD

H: SAD scale height

H_{ij}: gravitomagnetic field vector

i: spatial index

i: inclination angle

I_ν: spectral intensity

j: spatial index

j^μ: charge current 4–vector

j^i: charge current 3–vector

J: angular momentum

J^μ: angular momentum current 4–vector

J^i: angular momentum current 3–vector

k: spatial index

$\mathrm{k_B}$: Boltzmann's constant

$K^\mu{}_{(a)}$: conserved current with symmetry coordinate (a)

$\mathrm{L_\odot}$: solar luminosity

L_H: black hole luminosity (Blandford–Znajek mechanism)

L_disk: accretion disk luminosity (Blandford–Znajek mechanism)

$\mathcal{L}_\xi$: Lie derivative with respect to Killing vector ξ

λ: wavelength

$\lambda = J/E$: specific angular momentum

Λ: cosmological constant

m: mass of a test particle

m: mean rest mass per particle

$\mathrm{m_P}$: proton rest mass

M: black hole mass

$\mathrm{M_\odot}$: solar mass

$\dot{M}$: accretion rate

$\dot{M}_\mathrm{Edd}$: Eddington accretion rate

M_μ: relativistic momentum 4–vector in GRHD

M_i: relativistic momentum 3–vector in GRHD

$\dot{m} = \dot{M}/\dot{M}_{\mathrm{Edd}}$: accretion rate scaled to the Eddington rate

μ: atomic weigth

μ_2, μ_3: gauge functions for stationary, axisymmetric space–times

n: proper particle number density

n_μ: FIDO 4–velocity

$\mathrm{N_A}$: Avogadro's constant

N^μ: particle current 4–vector

ν: photon frequency

ν: turbulent viscosity

ν_{em}: photon frequency in emitter's frame

ν_{obs}: photon frequency in observer's frame

ω: Boyer–Lindquist function: frame–dragging frequency

$\tilde{\omega}$: Boyer–Lindquist function: cylindrical radius

Ω: angular velocity

Ω_{K}: Keplerian angular velocity

p: momentum

p: index of emissivity single power law

P: pressure

P^μ: energy current

$\mathcal{P}$: vector of primitives in conservative formulation

Φ: potential function for stationary, axisymmetric space–times

ϕ: azimuthal coordinate

ψ: potential function for stationary, axisymmetric space–times

Q^-: cooling function

Q^+: dissipation function

Q^-_{rad}: radaitive cooling function

Q^+_{vis}: viscous dissipation function

r: radial coordinate

$r_\star$: tortoise coordinate

r_{br}: break radius for broken power law emissivities

$r_{\rm eff}$: effective radius (M–σ relation)

$r_{\rm E}$: ergosphere radius

$r_{\rm g}$: gravitational radius

$r_{\rm H}^{-}$: inner horizon radius

$r_{\rm H}^{+}$: outer horizon radius

$r_{\rm in}$: inner disk radius

$r_{\rm mb}$: marginally bound radius

$r_{\rm ms}$: marginally stable radius

$r_{\rm out}$: outer disk radius

$r_{\rm ph}$: photon sphere radius

$r_{\rm ring}$: ring singularity radius

$R_{\rm S}$: Schwarzschild radius

$R_{\rm t}$: truncation radius

$R_{\rm T}$: tidal radius

$\mathrm{R}_{\odot}$: solar radius

$\mathcal{R}$: fourth order polynomial (a 'radial potential') for a particle with mass m

$\mathcal{R}_0$: fourth order polynomial (a 'radial potential') for a photon, $m = 0$

R: gas constant

$\rho = nm$: proper rest mass density

ρ: Boyer–Lindquist function

s: specific entropy

$\vec{S}$: momentum flux

S_μ: relativistic momentum 4–vector in GRMHD

S_i: relativistic momentum 3–vector in GRMHD

σ: Stefan–Boltzmann constant

σ: velocity dispersion

$\sigma_{\rm r}$: Gaussian width parameter for localized emissivity

$\sigma_{\rm T}$: Thomson cross section

$\sigma_{R\Phi}$: shear

Σ: Boyer–Lindquist function

Σ: SAD surface density

$\mathcal{S}$: source vector of conservative formulation

t: temporal coordinate

$\hat{t}$: stress tensor or pressure tensor

T: temperature

τ: proper time

τ: optical depth

τ_{S}: light crossing time

$\mathbf{t}_{\mathrm{M}}^{\mu\nu}$: Maxwell stress tensor

$\mathbf{T}$: energy–momentum tensor, energy–stress tensor

$\mathbf{T}_{\mathrm{fluid}}$: energy–stress tensor of a perfect fluid

$\mathbf{T}_{\mathrm{EM}}$: energy–stress tensor of electromagnetic field

θ: poloidal coordinate

Θ: fourth order polynomial (a 'poloidal potential') for a particle with mass m

u: observer's 4–velocity e.g. FIDO, ZAMO

U: plasma 4–velocity

$\mathcal{U}$: state vector of conservative formulation

v_R: radial velocity

v_{K}: Keplerian velocity

$v^{(\mathrm{r})}$: radial velocity component in ZAMO frame

$v^{(\theta)}$: poloidal velocity component in ZAMO frame

$v^{(\Phi)}$: azimuthal velocity component in ZAMO frame

$\vec{v}$: plasma 3–velocity

w: w–parameter of cosmology, EOS–parameter

x: Cartesian coordinate

x: pixel coordinate

$\xi^{\nu}{}_{(a)}$: Killing vector with symmetry coordinate (a)

y: Cartesian coordinate

y: pixel coordinate

Y: auxiliary function to transform to horizon adapted coordinates

z: Cartesian coordinate

z: redshift

$\tilde{z}$: Kerr–Schild function

Z: auxiliary function to transform to horizon adapted coordinates, Kerr–Schild function

Z_1, Z_2: auxiliary functions for ISCO

ζ: dimensionless advective parameter

D Acronyms

ADAF: Advection–Dominated Accretion Flow

ADD: scenario proposed by Arkani–Hamed, Dimopoulos & Dvali

AGN: Active Galactic Nuclei

AMR: Adaptive Mesh Refinement

ASCA: Advanced Satellite for Cosmology and Astrophysics

AU: Astronomical Unit

BB: Black Body

BBB: Big Blue Bump

BH: Black Hole

BHI: Balbus–Hawley Instability

BHXB: Black Hole X–ray Binary

BL: Boyer–Lindquist coordinate frame

BLR: Broad Line Region

CDAF: Convection–Dominated Accretion Flow

CDO: Compact Dark Object

CMB: Cosmic Microwave Background

CO: Compact Object

CT: Constrained Transport (formalism)

CV: Cataclysmic Variable

ECS: External Compton Scattering

EF: Eddington–Finkelstein Coordinate Frame

EM: ElectroMagnetic

EOS: Equation Of State

FDM: Finite Difference Method

FEM: Finite Element Method

FIDO: FIDucial Observer

FVM: Finite Volume Method

GBEC: Gravitational Bose–Einstein Condensate

GBHC: Galactic Black Hole Candidates

GBS: Great Black Spot

GM: GravitoMagnetism

GR: General Relativity

GRB: Gamma Ray Burst

GRHD: General Relativistic HydroDynamics

GRMHD: General Relativistic MagnetoHydroDynamics

GW: Gravitational Wave

HARM: High Accuracy Relativistic Magnetohydrodynamics (code)

HLL: numerical scheme by Harten, Lax, van der Leer

HMXB: High–Mass X–ray Binary

HN: HyperNova

HRSC: High–Resolution Shock–Capturing (scheme)

HST: Hubble Space Telescope

IDV: intraday variability

ISCO: Innermost Stable Circular Orbit

ISM: InterStellar Medium

IGM: InterGalactic Medium

ISO: Infrared Space Observatory

KBH: Kerr Black Hole

KS: Kerr–Schild coordinate frame

LINER: Low–Ionization Nuclear Emission line Region

LMXB: Low–Mass X–ray Binary

LNRF: Locally Non–Rotating Frame

LQG: Loop Quantum Gravity

LT: Lense–Thirring (effect)

ly: light year

MACHO: MAssive Compact Halo Object

mas: milliarcsecond

μas: microarcsecond

MDO: Massive Dark Object

MBH: Massive Black Hole

MIDI: MID–Infrared (instrument for VLTI)

MHD: MagnetoHydroDynamics

MOCCT: Method Of Characteristics Constrained Transport

MQ: MicroQuasar

MRI: Magneto–Rotational Instability

NIR: Near InfraRed

NLR: Narrow Line Region

NLS1: Narrow Line Seyfert–1

NRAF: Non–Radiative Accretion Flow

NS: Neutron Star

OO: Object–Orientation

PBH: Primordial Black Hole

PPI: Papaloizou–Pringle Instability

PPP: Penrose Pair Production

QCD: Quantum ChromoDynamics

QPO: Quasi–Periodic Oscillation

QS: Quark Star

QSO: Quasi–Stellar Object

RHD: Radiative HydroDynamics

RIAF: Radiatively Inefficient Accretion Flow

RMHD: Radiative MagnetoHydroDynamics

RMR: Relativistic Magneto–Rotator

RXTE: Rossi X–ray Timing Explorer

RS: Randall–Sundrum (model)

SAD: Standard Accretion Disk

SBH: Schwarzschild Black Hole

SED: Spectral Energy Distribution

SFR: Star Formation Rate

SMBH: Supermassive Black Hole

SN: SuperNova

SSD: Shakura–Sunyaev Disk

TDAT: Truncated Disks – Advective Tori

TSD: Truncated Standard Disk

TVD: Total Variation Diminishing (scheme)

ULIRG: Ultra–Luminous InfraRed Galaxy

VLA: Very Large Array

VLBI: Very Long Baseline Interferometry

VLT: Very Large Telescope

ZAMO: Zero Angular Momentum Observer

ZEUS: hydro/MHD code package

E Web Resources

- Web dictionary for Astrophysics (in German):
  `http://www.lsw.uni-heidelberg.de/users/amueller/lexdt.html`
- Talk material:
  `http://www.lsw.uni-heidelberg.de/users/amueller/astro_ppt.html`
- Selected Articles:
  `http://www.lsw.uni-heidelberg.de/users/amueller/astrodt.html`
- Further Links (Instruments & Scientists):
  `http://www.lsw.uni-heidelberg.de/users/amueller/linksdt.html`

Bibliography

[Abr78] Abramowicz, M.A., Jaroszynski, M., & Sikora, M. 1978, A&A, 63, 221

[Abr88] Abramowicz, M.A., Czerny, B., Lasota, J.P., & Szuszkiewicz, E. 1988, ApJ, 332, 646

[Abr96] Abramowicz, M.A., Chen, X.-M., Granath, M., & Lasota, J.P. 1996, ApJ, 471, 762

[Ada00] Adams, F.C., Graff, D.S., & Richstone, D.O. 2000, astro–ph/0010549, submitted to ApJL

[Ani89] Anile, A.M. 1989, Relativistic Fluids and Magnetofluids, Cambridge University Press

[Ant90] Antoniadis, I. 1990, Phys. Lett., B246, 377

[Ark98] Arkani–Hamed, N., Dimopoulos, S. & Dvali, G. 1998, Phys. Lett., B429, 263

[Arm03] Armitage, P.J., & Reynolds, C.S. 2003, MNRAS, 341, 1041

[ADM62] Arnowitt, R., Deser, S., & Misner, C. 1962, Gravitation: An introduction to current research, Whiley, New York

[Ash86] Ashtekar, A. 1986, Phys. Rev. Lett., 57, 2244

[Ash87] Ashtekar, A. 1987, Phys. Rev. D, 36, 1587

[Ash97] Ashtekar, A., & Lewandowski, J. 1997, Class. Quant. Grav., 14, A55

[Ash02] Ashtekar, A. & Krishnan, B. 2002, Phys. Rev. Lett., 89, 261101

[Bag03] Baganoff, F.K., Maeda, Y., Morris, M., et al. 2003, ApJ, 591, 891

[Bal91a] Balbus, S.A., & Hawley, J.F 1991, ApJ, 376, 214

[Bal91b] Balbus, S.A., & Hawley, J.F 1991, ApJ, 376, 223

[Bar70] Bardeen, J.M. 1970, ApJ, 162, 71

[Bar72] Bardeen, J.M., Press, W.H.& Teukolsky, S.A. 1972, ApJ, 178, 347

[Bar73] Bardeen, J.M., Carter, B., & Hawking, S.W. 1973, Commun. Math. Phys. 31, 161

[Bek78] Bekenstein, J.D., & Oron, E. 1978, Phys. Rev. D, 18, 1809

[Bek04] Bekenstein, J.D. 2004, astro–ph/0407560, Lectures delivered at the NATO Advanced Study Institute "Neutrinos and Explosive Events in the Universe"

[Bir23] Birkhoff, G. 1923, Relativity and Modern Physics, Harvard University Press, Cambridge Mass.

[Bla77] Blandford, R.D., & Znajek, R.L. 1977, MNRAS, 179, 433

[Bla78] Blandford, R.D., & Königl, A. 1978, ApJ, 232, 34

[Bla82] Blandford, R.D., & Payne, D.G. 1982, MNRAS, 199, 883

[Bol72] Bolton, C. T. 1972, Nature, 235, 271

[Boy67] Boyer, R.H. & Lindquist, R.W. 1967, J. Math. Phys., 8, 265

[Bri04] Brinkmann, S. 2004, MHD–Instabilities in Accretion Disks: Simulation and Analysis of the MRI, diploma thesis, Landessternwarte Heidelberg, Germany

[Bro03] Bromm, V., & Loeb, A., 2003, Astron. J., 596, 34

[Bur02] Burgio, G.F., Baldo, M., Sahu, P.K., Santra, A.B., & Schulze, H.-J. 2002, Phys. Lett., B526, 19

[Cad04] Cadolle Bel, M., Rodriguez, J., Sizun, P. et al. 2004, A&A, 1292

[Cam86a] Camenzind, M. 1986, A & A, 156, 137

[Cam86b] Camenzind, M. 1986, A & A, 162, 32

[Cam97] Camenzind, M. 1997, Les noyaux actifs de galaxies, Springer, Heidelberg

[Cam02] Camenzind, M. 2002, lecture notes, quasars and rotating black holes

[Cam04] Camenzind, M. 2004, private communication

[Car68] Carter, B. 1968, Phys. Rev., 174, 1559

[Cas48] Casimir, H.B.G. 1948, Proc. Kon. ned. Akad. Wetenschap. Ser., B 51, 793

[Cav02] Cavaglia, M. 2002, Int. J. Mod. Phys., A18, 1843

[Cav04] Cavaglia, M., & Saurya, D. 2002, gr–qc/0404050

[Cha31a] Chandrasekhar, S. 1931, Phil. Mag., 11, 592

[Cha31b] Chandrasekhar, S. 1931, Astrophys. J., 74, 81

[Cha60] Chandrasekhar, S. 1960, Proc. Natl. Acad. Sci., 46, 253

[Cha61] Chandrasekhar, S. 1961, Hydrodynamic and Hydromagnetic Stability, International Series of Monographs on Physics, Oxford Clarendon Press

[Cha83] Chandrasekhar, S. 1983, The Mathematical Theory of Black Holes, Oxford University Press, New York

[Cha03] Chapline, G., Hohlfeld, E., Laughlin, R.B., & Santiago, D.I. 2003, Int. J. Mod. Phys., A18, 3587

[Ciu04] Ciufolini, I., & Pavlis, E.C. 2004, Nature, 431, 958

[Coh71] Cohen, J.M., & Wald, R.M. 1971, J. Math. Phys., 12, 1845

[Cun73] Cunningham, C.T., & Bardeen, J.M. 1973, ApJ, 183, 237

[DeV02] De Villiers, J.-P., & Hawley, J.F. 2002, ApJ, 577, 866

[DeV03a] De Villiers, J.-P., & Hawley, J.F. 2003, ApJ, 589, 458

[DeV03b] De Villiers, J.-P., Hawley, J.F., & Krolik, J.H. 2003, ApJ, 599, 1238

[DeV04] De Villiers, J.-P., Hawley, J.F., Krolik, J.H., & Hirose, S. 2004, astro–ph/0407092, submitted to ApJ

[Dra02] Drake, J.J., Marshall, H.L., Dreizler, S. et al. 2002, Astrophys. J., 572, 996

[Dun94] Duncan, G., & Hughes, P. 1994, ApJL, 436, L119

[Dur88] Durrer, R., & Straumann, N. 1988, Helvetica Phys. Acta, 61, 1027

[Ein05] Einstein, A. 1905, Ann. Phys., 17, 891

[Ein15a] Einstein, A. 1915, Preuss. Akad. Wiss. Berlin, Sitzb., 778

[Ein15b] Einstein, A. 1915, Preuss. Akad. Wiss. Berlin, Sitzb., 799

[Ein15c] Einstein, A. 1915, Preuss. Akad. Wiss. Berlin, Sitzb., 844

[Elv94] Elvis, M., Wilkes, B.J., McDowell, J.C., Green, R.F., Bechtold, J., Willner, S.P., Oey, M.S., Polomski, E., Cutri, R. 1994, ApJS, 95, 1

[Esi97] Esin, A.A., McClintock, J.E., & Narayan, R. 1997, ApJ, 489, 865

[Eva88] Evans, C.R., & Hawley, J.F. 1988, ApJ, 332, 659

[Fal95] Falcke, H., & Biermann, P.L. 1995, A&A, 293, 665

[Fal00] Falcke, H., Melia, F. & Agol, E. 2000, ApJL, 528, L13

[Fan97] Fanton, C., Calvani, M., Felice, F. de & Cadez, A. 1997, PASJ, 49, 159

[Fer00] Ferrarese, L., & Merritt, D. 2000, Astrophys. J., 539, L9

[Fil03] Filippenko, A.V., & Ho, L.C. 2003, Astrophys. J., 588, L13

[Fin58] Finkelstein, D. 1958, Phys. Rev., 110, 965

[Fon98] Font, J.A., Ibáñez, J.M., & Papadopoulos, P. 1998, ApJ, 507, L67

[Fon99] Font, J.A., Ibáñez, J.M., & Papadopoulos, P. 1999, MNRAS, 305, 920

[Fon00] Font, J.A. 2000, Living Rev. Rel., 3, 2

[Fon03] Font, J.A. 2003, Living Rev. Rel., 6, 4

[Gam99] Gammie, C.F. 1999, ApJL, 522, L57

[Gam03] Gammie, C.F., McKinney, J.C., & Tóth, G. 2003, Astrophys. J., 589, 444

[Gam04] Gammie, C.F. 2004, astro–ph/0406532, accepted to ApJ

[Gau04] Gaudi, B.S., & Han, C. 2004, astro–ph/0402417, to appear in ApJ

[Geb00] Gebhardt, K., Bender, R., Bower, G., et al. 2000, ApJL, 539, L13

[Geb02] Gebhardt, K., Rich, R.M., & Ho, L. 2002, Astrophys. J., 578, L41

[Gen03] Genzel, R., Schoedel, R., Ott, T., et al. 2003, Nature, 425, 934

[Geo02] Georganopoulos, M., Aharonian, F.A., & Kirk, J.G. 2002, A&A, 388, L25

[Ger02] Gerssen, J., van der Marel, R.P., Gebhardt, K., Guhathakurta, P., Peterson, R., & Pryor, C. 2002, astro–ph/0209315, Astrophys. J. in press

[Ghe00] Ghez, A., Morris, M., Becklin, E.E., Kremenek, T. & Tanner, A 2000, Nature, 407, 349

[Gid02] Giddings, S.B., & Thomas, S. 2002, Phys. Rev., D65, 056010

[Gil00] Gilfanov, M., Churazov, E. & Revnivtsev, M. 2000, MNRAS, 316, 923

[Häh00] Hähnelt, M.G., & Kauffmann, G. 2000, MNRAS, 318, L35

[Hai04] Haiman, Z., astro–ph/0408479, published in Nature

[Har83] Harten, A., Lax, P.D., & van Leer, B. 1983, SIAM Rev., 25, 35

[Hawk69] Hawking, S.W. & Penrose, R. 1969, Proc. Roy. Soc. Lond., A 314, 529

[Hawk75] Hawking, S.W. 1975, Commun. Math. Phys., 43, 199

[Hawk04] Hawking, S.W. 2004, press release at web page *http://www.hawking.org.uk/*, publication is announced for fall 2004

[Hawl84] Hawley, J.F., Smarr, L.L., & Wilson, J.R. 1984, ApJS, 55, 211

[Hawl95] Hawley, J.F., & Stone, J.M. 1995, Comput. Phys. Comm., 89, 127

[Hawl01] Hawley, J.F., Balbus, S.A., & Stone, J.M. 2001, ApJL, 554, L49

[Hir03] Hirose, S., Krolik, J.H., De Villiers, J.-P., & Hawley, J.F. 2003, ApJ, 606, 1083

[Hul74] Hulse, R.A., & Taylor, J.H. 1974, ApJL, 191, L59

[Hul75a] Hulse, R.A., & Taylor, J.H. 1975, ApJL, 195, L51

[Hul75b] Hulse, R.A., & Taylor, J.H. 1975, ApJL, 201, L55

[Huj00a] Hujeirat, A., & Camenzind, M. 2000, A&A, 361, L53

[Huj00b] Hujeirat, A., & Camenzind, M. 2000, A&A, 362, L41

[Igu00] Igumenshchev, I.V., & Abramowicz, M.A. 2000, astro–ph/0102482, invited plenary review at the 20th Texas Symposium on Relativistic Astrophysics, Austin, Texas, 2000

[Jac87] Jacobson, T. & Smolin, L. 1987, Phys. Lett., B196, 39

[Jac88] Jacobson, T. & Smolin, L. 1988, Nucl. Phys., B299, 295

[Kaa00] Kaaret, P., Prestwich, A.H., Zezas, A., Murray, S.S., Kim, D.-W., Kilgard, R.E., Schlegel, E.M., & Ward, M.J. 2000, MNRAS, 321, L29

[Kal21] Kaluza, T. 1921, Sitzber. Deut. Akad. Wiss. Berlin (Math. Phys.), K1, 966

[Ker63] Kerr, R.P. 1963, Phys. Rev. Lett., 11, 237

[Kha98] Khanna, R. 1998, MNRAS, 294, 673

[Kha99] Khanna, R. 1999, Stellar Dynamos: Nonlinearity and Chaotic Flows, ASP Conf. Ser. 178, 57

[Kir03] Kirk, J.G. & Skjaeraasen, O. 2003, ApJ, 591, 366

[Kis04] Kishimoto, M., Antonucci, R., Boisson, C., & Blaes, O. 2004, talk contribution, to be published in Progress of Theoretical Physics Supplement

[Kle26] Klein, O. 1926, Z. Phys., 37, 895

[Koi99a] Koide, S., Meier, D.L., Shibata, K., & Kudoh, T. 1999, astro–ph/9907434, to appear in the 19th Texas Symposium on Relativistic Astrophysics

[Koi99b] Koide, S., Shibata, K., & Kudoh, T. 1999, ApJ, 522, 727

[Koi04] Koide, S. 2004, ApJL, 606, L45

[Komo03] Komossa, S., astro–ph/0306439, to appear in "The Astrophysics of Gravitational Wave Sources" (Maryland, April 2003), AIP in press, J. Centrella (ed)

[Komo04] Komossa, S., Halpern, J., Schartel, N., Hasinger, G., Santos–Lleo, M., & Predehl, P. 2004, Astrophys. J., 603, L17

[Komi99] Komissarov, S.S. 1999, MNRAS, 303, 343

[Komi04a] Komissarov, S.S. 2004, MNRAS, 350, 407

[Komi04b] Komissarov, S.S. 2004, MNRAS, 350, 1431

[Kon04] Kondratko, P.T., Greenhill, L.J., & Moran, J.M. 2004, astro–ph/0408549, to appear in ApJ

[Kro04] Krolik, J.H., Hawley, J.F., & Hirose, S. 2004, astro–ph/0409231, submitted to ApJ

[Kru60] Kruskal, M.D. 1960, Phys. Rev., 119, 1743

[Lam97] Lamoreaux, S.K. 1997, Phys. Rev. Lett., 78, 5

[Lic67] Lichnerowicz, A. 1967, Relativistic Magnetohydrodynamics, Benjamin, New York

[Lyn69] Lynden–Bell, D. 1969, Nature, 223, 690

[Mac97] Macchetto, F., Marconi, A., Axon, D.J., et al. 1997, astro–ph/9706252, ApJ in press

[Mac04] Macchetto, D. 2004, astro–ph/0405253, to be published in "The Interplay among Black Holes, Stars and ISM in Galactic Nuclei", Th. Storchi Bergmann, L.C. Ho & H.R. Schmitt, eds

[Mag98] Magorrian, J., Tremaine, S., Richstone, D., et al. 1998, Astron. J., 115, 2285

[Man02] Manners, J.C. 2002, Obscuration and X-ray Variability of Active Galactic Nuclei, PhD thesis, University of Edinburgh, Great Britain

[Marti91] Martí, J., Ibáñez, J. & Miralles, J. 1991, Phys. Rev. D, 43, 3794

[Marto96] Martocchia, A. & Matt, G. 1996, MNRAS, 282, L53

[Mat04] Mathur, S.D. 2004, gr–qc/0401115, Talk

[Mat93] Matt, G., Fabian, A.C., & Ross, R.R. 1993, MNRAS, 262, 179

[Maz01] Mazur, P.O., & Mottola, E. 2001, gr–qc/0109035

[Maz04] Mazur, P.O., & Mottola, E. 2004, Proc. Nat. Acad. Sci., 111, 9545

[Mig02] Migliari, S., Fender, R.P., & Méndez, M. 2002, Chandra press release, December 10, 2002

[Mio01] Mioduszewski, A.J., Rupen, M.P., Hjellming, R.M., Pooley, G.G., & Waltman, E.B. 2001, ApJ, 553, 766

[Mir94] Mirabel, I.F., & Rodriguez, L.F. 1994, Nature, 371, 46

[MTW73] Misner, C.W., Thorne, K.S. & Wheeler, J.A. 1973, Gravitation, Freeman, San Francisco

[Mül00] Müller, A. 2000, Emission lines of Accretion Disks around Rotating Black Holes, diploma thesis, Landessternwarte Heidelberg, Germany

[Mül04] Müller, A. & Camenzind, M. 2004, A&A, 413, 861

[Nar94] Narayan, R., & Yi, L. 1994, ApJL, 428, L13

[Nar97] Narayan, R., Kato, S., & Honma, F. 1997, ApJ, 476, 49

[Net03] Netzer, H. 2003, ApJL, 583, L5

[New65] Newman, E.T., Couch, E., Chinnapared, K., Exton, A., Prakash, A. & Torrence, R. 1965, J. Math. Phys., 6, 918

[Nor18] Nordstrøm, G. 1918, Proc. Kon. Ned. Akad. Wet, 20, 1238

[Nov74] Novikov, I.D., & Thorne, K.S. 1974, Black Holes, 343

[Now95] Nowak, M.A. 1995, PASP, 107, 1207

[Opp39a] Oppenheimer, J.R., & Snyder, H. 1939, Phys. Rev., 56, 455

[Opp39b] Oppenheimer, J.R., & Volkoff, G. 1939, Phys. Rev., 55, 374

[Oro04] Orosz, J.A., McClintock, J.E., Remillard, R.A., & Corbel, S. 2004, astro–ph/0404343, accepted to ApJ

[Ott03] Ott, T., Schoedel, R., Genzel, R., et al. 2003, ESO Messenger, 111, 1

[Pac80] Paczyński, B., & Wiita, P.J. 1980, A&A, 88, 23

[Pag74] Page, D.N., & Thorne, K.S. 1974, ApJ, 499, 191

[Pap98] Papadopoulos, P., & Font, J.A. 1998, Phys. Rev. D, 58, 024005

[Pap99] Papadopoulos, P., & Font, J.A. 1999, gr–qc/9912054

[Pel04] Pello, R., Schaerer, D., Richard, J., Le Borgne, J.-F., & Kneib, J.-P. 2004, A&A, 416, L35

[Pen65] Penrose, R. 1965, Phys. Rev. Lett., 14, 57

[Pen69] Penrose, R. 1969, Nuovo Cimento 1, special number, 252

[Pen71] Penrose, R., & Floyd, R.M. 1971, Nature Phys. Sci., 229, 177

[Pet03a] Petri, M. 2003, gr–qc/0306066

[Pet03b] Petri, M. 2003, gr–qc/0306068

[Pet04] Petri, M. 2004, gr–qc/0405007

[Pie02] Pietsch, W., & Read, A.M. 2002, astro–ph/0201267, accepted for A&A

[Por03] Porquet, D., Predehl, P., Aschenbach, B., et al. 2003, A&A, 407, L17

[Qua03] Quataert, E. 2003, astro–ph/0304099, to appear in Astron. Nachr., Vol. 324, No. S1

[Ran99a] Randall, L., & Sundrum, R. 1999, Phys. Rev. Lett., 83, 3370

[Ran99b] Randall, L., & Sundrum, R. 1999, Phys. Rev. Lett., 83, 4690

[Rei16] Reissner, H.J. 1916, Ann. Phys., 50, 106

[Rey03] Reynolds, C.S., & Nowak, M.A. 2003, Phys. Rept., 377, 389

[Rin56] Rindler, W. 1956, MNRAS, 116, 662

[Rob75] Robinson, D.C. 1975, Phys. Rev. Lett., 34, 901

[Ryb79] Rybicki, G.B. & Lightman, A.P. 1979, Radiative Processes In Astrophysics, Wiley–Interscience, New York

[Sal64] Salpeter, E.E. 1964, ApJ, 140, 796

[Scha03] Schartmann, M. 2003, Models for Dusty Tori in Active Galactic Nuclei, diploma thesis, Max-Planck-Institut für Astronomie, Heidelberg, Germany

[Sch60] Schiff, L. 1960, Phys. Rev. Lett., 4, 215

[Sch16a] Schwarzschild, K. 1916, Sitzber. Deut. Akad. Wiss. Berlin, 189

[Sch16b] Schwarzschild, K. 1916, Sitzber. Deut. Akad. Wiss. Berlin, 424

[Sem04a] Semenov, V., Dyadechkin, S., & Punsly, B. 2004, Science, 305, 978

[Sem04b] Semenov, V., Dyadechkin, S., & Punsly, B. 2004, astro–ph/0408371

[Sen82] Sen, A. 1982, Phys. Lett., 119B, 89

[Shi03] Shih, D.C., Iwasawa, K., & Fabian, A.C. 2003, MNRAS, 341, 973

[Sha73] Shakura, N.L., & Sunyaev, R.A. 1973, A&A, 24, 337

[Spi02] Spindeldreher, S. 2002, The Discontinuous Galerkin Method applied to the equations of ideal relativistic hydrodynamics, PhD thesis, Landessternwarte Heidelberg, Germany

[Sze60] Szekeres, G. 1960, Publ. Mat. Debrecen 7, 285

[Tad03] Tadhunter, C., Marconi, A., Axon, D., et al. 2003, MNRAS, 342, 861

[Tan95] Tanaka, Y., Nandra, K., Fabian, A.C., et al. 1995, Nature, 375, 659 Mue00

[Tol39] Tolman, R.C. 1939, Phys. Rev., 55, 364

[TPM86] Thorne, K.S., Price, R.H. & Macdonald, D.A. 1986, Black Holes: The Membrane Paradigm, Yale University Press, New Haven and London

[Tho94] Thorne, K.S. 1994, Black holes and time warps: Einstein's outrageous legacy, Papermac London

[Tho75] Thorne, K.S., & Price, R.H. 1975, ApJL, 195, L101

[Tre02] Tremaine, S., Gebhardt, K., Bender, R., et al. 2002, Astron. J., 574, 740

[Unr76] Unruh, W.G. 1976, Phys. Rev. D, 14, 870

[Unr84] Unruh, W.G., & Wald, R.M. 1984, Phys. Rev. D, 29, 1047

[vdK94] van der Klis, M. 1994, ApJS, 92, 511

[vdM02] van der Marel, R.P., Gerssen, J., Guhathakurta, P., Peterson, R., & Gebhardt, K. 2002, astro–ph/0209314, Astrophys. J. in press

[Vel59] Velikhov, E.P. 1959, Sov. Phys. JETP, 36, 995

[Vig04] Vigelius, M. 2004, Structure and Stability of Gravastars, diploma thesis, Landessternwarte Heidelberg, Germany

[Vis03] Visser, M. & Wiltshire, D.L. 2004, Class. Quant. Grav., 21, 1135

[Wag01] Wagner, R.M., Foltz, C.B, Shahbaz, T. et al. 2001, astro–ph/0104032, to appear in Astrophys. J., Part 1, Vol. 556

[Wal74] Wald, R.M. 1974, Phys. Rev. D, 10, 1680

[Will02] Williams, R.K. 2002, astro–ph/0203421, submitted to Phys. Rev.

[Will03] Williams, R.K. 2003, astro–ph/0306135, to appear in ApJ

[Wils72] Wilson, J.R. 1972, ApJ, 173, 431

[Wan03] Wang, J.-M., & Netzer, H. 2003, A&A, 398, 927

[Zel64] Zel'dovich, Y.B., & Novikov, I.D. 1964, Sov. Phys. Dokl., 158, 811

Index

Symbols

A

B

T

U

V

W

X

Y

Z